

Oxide Semiconductors For Energy Applications

Thesis submitted for the degree of

Doctor of Philosophy (Sc.)

in

Physics (Experimental)

By

Keshab Karmakar

Department of Physics

University of Calcutta

August, 2019

Dedicated to my beloved parents...

Acknowledgements

First of all, I would like to express my humble respect, special appreciation and thanks to my PhD supervisor Professor Kalyan Mandal for allowing me to do my research with full freedom. His valuable guidance and discussions always gives me a new angle to deal the difficulties in my research problems. He has been provided me tremendous academic support and so many wonderful opportunities.

I am grateful to S.N. Bose National Centre for Basic Sciences for providing me all research facilities and healthy research environment since I joined this research centre. I am also thankful to DST for giving me 'INSPIRE Fellowship Award' (DST/INSPIRE Fellowship/2015/IF150237).

I would like to convey my humble respect and sincere gratitude to Dr. Gobinda Gopal Khan, Assistant Professor at the Department of Materials Science and Engineering, Tripura University (A Central University) for his encouragement, guidance as a collaborator, friend and elder brother. His innovative ideas and valuable discussions has always been motivated me to face the difficulties in my research problems. I am also thankful to Dr. Ayan Sarkar, Dr. Ashutosh K Singh and Dr. Debasish Sarkar for their valuable discussions, support and encouragement as collaborators, friends.

I am really thankful to my lab mates Dr. Madhuri Mandal, Dr. Ashutosh K. Singh, Dr. Arup Ghosh, Dr. Monalisa Pal, Dr. Rupali Rakshit, Mr. Mahebab Alam, Mr. Souvanik Talukdar, Mr. Indranil Chakraborty, Mr. Subrata Ghosh, Ms. Dipika Mandal, Mr. Dipanjan Maity, Mr. Anupam Gorai and Ms. Swarnali Heit. It is my pleasure to have such cooperative labmates who provided me wonderful research environment. Especially, I want to thank Mr. Dipanjan Maity for his support, discussions in my research work.

I must thank Shakti Nath Das, Surojit Mukherjee, Samik Roy Moulik, Dipankar Roy, Amit Chanda and Urmi Chakraborty for their technical assistance in the material characterization during research works at S. N. Bose National Centre for Basic Sciences.

Without their support, encouragement, and dedication to assist me, this dissertation would not have been possible.

I must thank to my SNB friends outside my lab, Dhimadri, Samrat, Debabrata, Atanu, Jurity, Mithoon, Sayoni and Ejaj. I am also thankful to all my juniors and seniors cum friends, Sarowar, Rajkumar, Rakesh, Subhashis, Kartik, Subrata, Subhadip, Subrata, Krishnendu, Sudipta, Debashis, Ananda, Sourav, Imadul and many more. I enjoyed a wonderful time with them.

Especially, I am grateful to Mr. Somnath Ganguly for his support and encouragement throughout my journey. I am also indebt to Mrs. Sumita Choudhury, Dr. Monoj Chaudhury and their family for their tremendous support and kindness. I must thank to Mr. Parmartha Das and Mr. Bibek Narayan Dhua for their extreme support during my Higher Secondary days. I would like to thank my childhood friends Tanmoy, Satya, Prasanta, Manas, Raghunath and Rashbihari for giving me beautiful memories.

A special thanks to my family. They are the most important people for me in this world and I dedicate this thesis to them. Simply, words can't express their support, sacrifice, love and affection. I am grateful to my mother Mrs. Kabita Karmakar and father Mr. Kartick Chandra Karmakar. I am very fortunate to have my elder brother Muruli, my elder sisters Sangita and Sulekha. I am also thankful to my uncle Baisnabdas, Gobinda, my aunty Alpana and my cousin Jadao and Sukla. I am also thankful to my sister-in-law Sanchita and brothers-in law Tapan and Anup. I must thank to my nieces Samadrita (Diti), Asmit, Mou, Anwesa and Arnab for adding some colors in my life.

Keshab Karmakar

List of publications related to thesis work

- [1] A. K. Singh, D. Sarkar, **K. Karmakar**, K. Mandal and Gobinda Gopal Khan. High-Performance Supercapacitor Electrode Based on Cobalt Oxide–Manganese Dioxide–Nickel Oxide Ternary 1D Hybrid Nanotubes. *ACS Appl. Mater. Interfaces* 2016, 8, 20786–20792.
- [2] **K. Karmakar**, A. Sarkar, K. Mandal, and G. G. Khan. Stable and enhanced visible-light water electrolysis using C, N and S surface functionalized ZnO nanorods photoanodes: Engineering the absorption and electronic structure. *ACS Sustainable Chem. Eng.* 2016, 4, 5693–5702.
- [3] **K. Karmakar**, A. Sarkar, K. Mandal and G. G. Khan. Nano-engineering of p–n CuFeO₂-ZnO heterojunction photoanode with improved light absorption and charge collection for photoelectrochemical water oxidation. *Nanotechnology* 2017 28 325401.
- [4] **K. Karmakar**, A. Sarkar, K. Mandal and G. G.Khan. Investigating the role of oxygen vacancies and lattice strain defects on enhanced photoelectrochemical property of alkali metal (Li, Na and K) doped ZnO nanorods photoanodes. *ChemElectroChem* 2018, 5, 1147 -1152.
- [5] **K. Karmakar**, D. Maity, D. Pal, G. G. Khan and K. Mandal. Photo-induced Exciton Dynamics and Broadband Light Harvesting in ZnO Nanorod Templated Multilayered 2D MoS₂/MoO₃ Photoanodes for Solar Fuel Generation. (Submitted)

List of publications apart from thesis work

- [6] A. Sarkar, **K. Karmakar**, A. K. Singh, K. Mandal and G. G. Khan. Surface functionalized $\text{H}_2\text{Ti}_3\text{O}_7$ nanowires to engineer visible-light photoswitching, electrochemical water splitting, and photocatalysis. *Phys. Chem. Chem. Phys.* 2016, 18, 26900-26912.
- [7] Maheebub Alam, **Keshab Karmakar**, Monalisa Pal, and Kalyan Mandal. Electrochemical Supercapacitor Based on Double Perovskite Y_2NiMnO_6 Nanowires. *RSC Adv.* 2016, 6, 114722-114726.
- [8] Ayan Sarkar, **Keshab Karmakar** and Gobinda Gopal Khan. Designing Co-Pi modified 1D *n-p* $\text{TiO}_2/\text{ZnCo}_2\text{O}_4$ nano-heterostructure photoanode with reduced electron-hole pair recombination and enhanced (>3%) photoconversion efficiency. *J. Phys. Chem. C* 2017, 121, 25705–25717.
- [9] Dipanjan Maity, **Keshab Karmakar** and Kalyan Mandal. N-N type core-shell heterojunction engineering with layered material MoO_3 over ZnO nanorods core for photoelectrochemical watersplitting. *Journal of Alloys and Compounds* 791 (2019) 739-746.

CONTENTS

1. Introduction	
1.1 Preamble	2
1.2 Sustainable Energy Resources and The Solar Energy Challenges	3
1.2.1 Hydrogen: Next Generation Energy Carrier	6
1.3 Water Electrolysis	7
1.3.1 Photoelectrochemical Cell	7
1.3.2 Water Splitting Reactions	8
1.3.3 Efficiency Consideration of The PEC Cell	9
1.4 Energy Levels in Semiconductor and Electrolyte	10
1.5 Semiconductor and Electrolyte Inteface	12
1.5.1 Potential Distribution Across The Interface	15
1.5.2 Energy Band Diagram	19
1.5.3 pH Dependence on The Band Edges	21
1.5.4 Charge Transfer Process	22
1.6 Characteristics of Photoelectrode Materials	24
1.7 Oxide Semiconductors for PEC Cell	25
1.7.1 ZnO As Photoanode Materials for Water Splitting	26
1.8 Energy Storage and Supercapacitor	28
1.8.1 Classification of Supercapacitors	33
1.8.2 Oxide Materials for Supercapacitor	34
1.9 Objective of The Thesis	35
1.10 Organization of The Thesis	36
Bibliography	38
2. Experimental Details	
2.1 Preamble	44
2.2 Synthesis of Nanomaterials	45
2.3 Synthesis Techniques	46

2.3.1	Spin Coating Technique	46
2.3.2	Chemical Bath Deposition Technique	46
2.3.3	Electrochemical Anodization Technique	49
2.3.4	Sputtering Technique	51
2.3.5	Electrodeposition Technique	52
2.4	Phase and Morphology Characterization Techniques	55
2.4.1	X-ray Diffractometer	55
2.4.2	Electron Microscopes	57
2.4.2.1	Scanning Electron Microscope (SEM)	58
2.4.2.2	Transmission Electron Microscope (TEM)	60
2.4.3	X-ray Photoelectron Spectroscopy (XPS)	62
2.5	Optical Characterization Techniques	64
2.5.1	UV-Vis Absorption Spectroscopy	64
2.5.2	Photoluminescence (PL) Spectroscopy	65
2.6	Electrochemical Characterization Techniques	66
2.6.1	Cyclic Voltammetry	66
2.6.2	Galvanostatic Charge/discharge	68
2.6.3	Electrochemical Impedance Spectroscopy	70
	Bibliography	72
3.	Photoelectrochemical Properties of C, N and S Functionalized ZnO NRs	
	Photoanodes	
3.1	Preamble	75
3.2	Experimental Section	77
3.2.1	Substrate and Reagents	77
3.2.2	ZnO NRs Synthesis	77
3.2.3	C, N and S Functionalization of ZnO NRs	77
3.2.4	Material Characterizations	78
3.2.5	Photoelectrochemical Measurements	79
3.3	Results and Discussion	79

3.3.1	Morphology and Crystallography Study	79
3.3.2	XPS Analysis	81
3.3.3	Photoelectrochemical Performance	82
3.4	Conclusion	93
	Bibliography	96
4.	Photoelectrochemical Properties of Alkali Metal (Li, Na and K) Doped ZnO Nanorods Photoanodes	
4.1	Preamble	101
4.2	Experimental Section	103
4.2.1	Chemicals and Materials	103
4.2.2	ZnO NRs Synthesis	103
4.2.3	Doped ZnO NRs Synthesis	103
4.2.4	Material Characterizations	
4.2.5	Photoelectrochemical Studies	104
4.3	Results and Discussion	105
4.3.1	Morphology and Structural Analysis	105
4.3.2	XPS and Defect Analysis	107
4.3.3	Photoelectrochemical Performance	110
4.4	Conclusion	115
	Bibliography	117
5.	The <i>p-n</i> CuFeO₂-ZnO Nano-Heterojunction Photoanode for Photoelectrochemical Water Oxidation	
5.1	Preamble	122
5.2	Experimental Section	123
5.2.1	Reagents	123
5.2.2	Fabrication of ZnO NRs on FTO	124
5.2.3	Fabrication of <i>p-n</i> CuFeO ₂ -ZnO Nano-Heterojunction	124
5.2.4	Material Characterizations	124
5.2.5	Photoelectrochemical Studies	125

5.3	Results and Discussion	125
5.3.1	Morphology and Structural Analysis	125
5.3.2	XPS Studies	129
5.3.3	Photoelectrochemical Performance	130
5.4	Conclusion	139
	Bibliography	141
6.	1D-2D Nano-Heterojunction Photoanodes for Solar Fuel	
6.1	Preamble	145
6.2	Experimental Section	147
6.2.1	Reagents	147
6.2.2	Preparation of ZnO NRs	147
6.2.3	Preparation of ZnO/MoS ₂ and ZnO/MoO ₃ NHs	
	Photoanodes	147
6.2.4	Material Characterizations	147
6.2.5	PEC Measurements	148
6.3	Results and Discussion	149
6.3.1	Morphology and Crystallography Study	149
6.3.2	XPS Analysis	151
6.3.3	Photoelectrochemical Performance	152
6.4	Conclusion	161
	Bibliography	163
7.	Cobalt Oxide - Manganese Dioxide -Nickel Oxide Ternary 1D Hybrid Nanotubes for Supercapacitor Electrode	
7.1	Preamble	168
7.2	Experimental Section	170
7.2.1	Chemicals and Materials	170
7.2.2	Synthesis of Co ₃ O ₄ -MnO ₂ -NiO Ternary Hybrid Nanotubes	170
7.2.3	Structural Characterizations	171
7.2.4	Electrochemical Measurements	172

7.3	Results and Discussion	172
7.3.1	Structural and Morphological Analysis	172
7.3.2	XPS Analysis	175
7.3.3	Electrochemical Performance	176
7.4	Conclusion	182
	Bibliography	184
8.	Conclusion and Future Scope of The Work	
8.1	Conclusion	188
8.2	Future Scope	191

Chapter 1 | Introduction

This chapter highlights the basic introduction to the research work addressed in this dissertation. The motivation behind selecting this work in the area of solar energy harvesting using photoelectrochemical cell by designing the electrodes and the development of efficient energy storage devices (supercapacitor) by using the oxide semiconductor nanostructures are the main focus of this chapter. This chapter also deals with the related basic scientific knowledge and the review of past research works.

1.1 Preamble

The technological advancement has been reducing the difference between the living standard of human being in a village and a city. The history of science and development remind us the same thing that the technological drive due to industrial revolution facilitates the human needs and comfort. Energy supply is highly required in order to maintain this industrially revolutionized society. Therefore, energy is most important factor by which peoples amplify the development of the society. Since the beginning of the industrial revolution, the energy required for economic development and growth has been supplied mainly by coal, oil and natural gases. This revolution took place from 18th to 20th centuries, the transition period from wood to coal and petroleum. [1] These fossil fuels have a high energy density and can be transported in an easier way. Almost 80% of the total energy supply of the world comes from burning of fossil fuels. Currently, global population consumes 15 TW of energy which is expected to be doubled by 2050. [2] Fossil fuels will be unable to meet this huge supply of energy as the fossil fuels are depleting fast. According to current consumption rate, coal reserves will run as long as 150-400 years and this estimated reserve will run 40-80 years for oil and 60-160 years for natural gases. [2] Besides, it is critically hard to recover these fossil fuel resources.

On the other hand, the burning of fossil fuels causes anthropogenic environmental problems like, greenhouse effect, acid rain and high ozone concentration. The major concern of fossil fuels is CO₂ emission and its severe impact on global warming and associated climate change and biodiversity. Due to industrial revolution the atmospheric CO₂ level has risen from 280 to 400 ppm by today. [3] According to International Panel on Climate Change (IPCC), the level of CO₂ in atmosphere, more than 450 ppm brings a high risk of global warming as it will increase the average temperature of earth atmosphere by more than 2 °C. [2] This change of temperature will cause severe impact on the inhabitants on earth and the effect will be felt throughout the century.

Therefore, there is a big question on sustainable development of the society. In this stage, it is therefore extremely necessary to utilize sustainable energy resources in form of usable energy by replacing the principle energy resources available today, the fossil fuels. The utilization of clean and renewable energy resources will not only provide the total energy need in future but it will prevent severe anthropogenic impact on the environment.

1.2 Sustainable Energy Resources and The Solar Energy Challenges

In 2003, German Advisory Council on Global Change (WBGU) published a report presenting the prime concerns surrounding energy systems to the policy maker. [4] The report also suggested some criteria towards the sustainable development of energy systems to be met within 21st century. The scenario for the global transformation of energy systems presented in this report is that the stabilization of CO₂ concentration in the atmosphere, limiting a maximum of 450 ppm, a three-fold growth of energy usage by 2050 and a six-fold economic development should take into account towards sustainable society. The feasibility of execution lies on the declining use of fossil fuels, rising use of renewables and growing energy productivity. However, the lack of enough infrastructure and superior technology for harvesting of renewable energy resources in an economically competitive way will lead to the domination of energy production from the fossil fuels over the next decades. The expert panel recommended that future energy economy based on the existing and traditional fossil fuels can be shifted to renewables energy system by further development of energy infrastructure and technologies. They expect that from 2050, the renewable resources will mostly be used to meet the energy demands. In fact, the energy production from renewable energy resources will be almost 50% of the total production by 2050 and 90% by 2100.

In 1987, Brundtland Report [5] of the United Nations emphasized on **Sustainable Development** of society which is a process of development of land, cities, business, communities, etc., [1] that “meets the needs of the present without compromising the

ability of future generations to meet their own needs". Therefore, utilization of environmentally sound energy resources is critically important for sustainable development. Solar energy, wind energy, ocean current etc., are such kind of sustainable and renewable resources of energy which are advantageous because of earth abundance, intrinsic cleanliness. Practically, these resources are available till the existence of this planet. The estimated power generating capabilities from the sustainable energy resources is shown in Table 1.1. Among the all kind of renewable resources that we have, solar energy is the principal source of energy as of our planet receives 174×10^3 TW of radiation, which in other terms means that solar energy striking earth surface in 10 minutes is equivalent to total human energy consumption (15 TW) throughout the year. [6] So, if a fraction of total solar energy could be harvested then only solar energy could meet the energy challenges of human society. If 0.16% of the earth's surface is covered with 10% efficient solar cells then it would satisfy our present energy requirements. However, there remain enormous challenges with technologically sophisticated implementation to achieve it.

Table 1.1: Renewable energy resources and their power generation capabilities. [2]

Energy Resource	Power (TW)	Comments
Wind	4	Which is 10-15 % of global technical potential for on- and off- shore installations
Hydroelectric	1-2	Remaining untapped potential is 0.5 TW
Tidal and ocean current	< 2	-----
Geothermal	12	Only small fraction of this can be utilized
Biomass	10	Needs to cover 10% of the earth surface with switchgrass
Solar	>20	Needs to cover 0.16% of the earth surface with solar cells having efficiency 10 %

Nowadays photovoltaic cell, dye sensitized photovoltaic cell, large scale concentrating solar thermal power and solar heater have earned enormous research interests to fulfill the next generation energy goal for sustainable development of energy sector. Photovoltaic cells use solar energy and directly convert into electrical energy and are predominantly made of semiconductor materials based on silicon solar

cell technology or other thin films. Large scale solar concentrator requires reflecting materials which can concentrate solar heat to drive the water turbine and low temperature solar absorber is required to heat water or any other materials in household, commercial or industrial purposes.

Therefore, it is clear that solar energy conversion in usable form of energy is necessary in order to deliver at the time of deliverable, like in photovoltaic cells into electricity, in solar heater or solar concentrator into heat energy. On the next section, we will see that hydrogen as the next generation energy carrier has a tremendous potential value as it has a low impact on environment.

1.2.1 Hydrogen: Next Generation Energy Carrier

The availability of renewable energy resources varies in space and time, therefore to satisfy the human need of energy in usable form it is necessary to have a buffer medium to store the energy. Hydrogen is an energy carrier but not an energy source. [1] Hydrogen, a colorless, odorless and nontoxic gas is the lightest gas. It is the most energy dense fuel per mass. [2] Generally, one pound of hydrogen holds three times of energy (55 MJ) than one pound of gasoline. [7] Besides, hydrogen can be stored in a container or piped and transported easily like oil, natural gas. The burning of hydrogen in fuel cells produces zero emissions rather water vapor which leads feasibility towards sustainable development of future energy infrastructure. The future energy infrastructure based energetically on hydrogen, welcome in the concept of 'hydrogen economy' which was initially pointed out at the time of the first oil crisis in 1970s. John Bockris first used the term of 'hydrogen economy' during a lecture session in 1970 at General Motors (GM) Technical Center. [7] The concept of hydrogen economy necessitates the development of systems for production of hydrogen, transport, storage and usage. These four components of the hydrogen economy have been discussed in detail in a book edited by D. Scholten. [8]

Today almost 96% of hydrogen is produced from coal (18%), oil (30%), and natural gas (48%). [6] As discussed previously, the target to shift the energy infrastructure totally based on renewable resources (carbon free source) should be fulfilled in future for sustainable development. So in order to harvest solar energy (the principle renewable energy resource) to electricity solar cells or solar thermal plants are made. Then hydrogen can be produced substantially by using this electricity through water electrolysis. Hydrogen is finally feed to the fuel cell for further utilization on human need. Here, each conversion step: solar energy-electricity-hydrogen-electricity causes from energy losses which consequently increases the overall production to supply cost. Almost 70% losses occur during this conversion step as shown in Bossel's calculations. [9] Therefore, if we reduce the step involved for hydrogen generation then significant production loss will be simultaneously decreased. It is possible to avoid the first step: solar to electricity conversion for hydrogen generation in a water photolysis cell. Semiconductors are potential candidates for this purpose but efficiency of this process should be enhanced in order to meet future application.

1.3 Water Electrolysis

Electrolysis is a process of dissociating a compound to its elements by passing an electric current through it. Thereby, water electrolysis means the dissociation of water to hydrogen and oxygen by passing a current. Generally, current could not pass through pure water, we have to dissolve electrolyte so that dissociated ions can carry the electric current for water electrolysis. Since, the renewable resources have potential to meet future energy challenges, storing solar energy via electrolysis process is therefore necessary for satisfying the sustainable challenges. Photoelectrolysis is a single step process where semiconductor in an electrochemical cell creates electron-hole pair under solar irradiance and splits water into oxygen and hydrogen.

1.3.1 Photoelectrochemical Cell

Photoelectrochemical cell (PEC) is a monolithic device where solar energy is converted into more useful form of energy through photon assisted electrochemical process. Here, in the PEC cell both current and voltage could be simultaneously produced by absorbing light. In a typical PEC cell (Fig. 1.1) for water splitting, three electrodes: namely working electrode (WE), counter electrode (CE) and a reference electrode (RE) are immersed into aqueous solution of electrolyte. Working electrode is a semiconductor material, grown on some conducting substrate. The counter electrode is typically made of platinum, a corrosion resistant material and KCl saturated Ag/AgCl electrode is used as reference electrode.

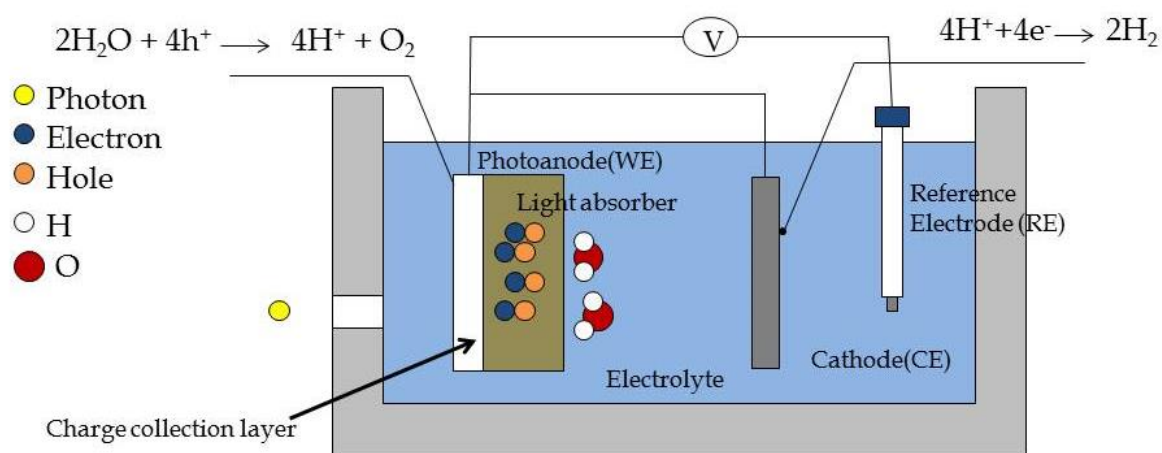
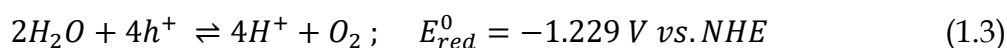
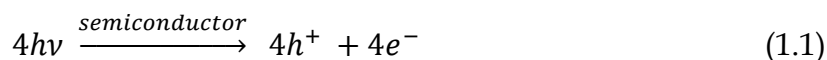


Figure 1.1: Schematic representation of the conventional three electrodes PEC cell under working condition. Upon illumination, electron-hole pair is created. Hole is responsible for water oxidation and electron is responsible for water reduction.

1.3.2 Water Splitting Reactions

The starting point of photoelectrochemical water splitting reaction is to illuminate the semiconductor electrode surface in the PEC cell. Due to illumination (Photon energy, $h\nu > E_g$) to the semiconductor electrode electron-hole pairs are created. These electron-hole pairs are then separated due to the developed electric field in the

semiconductor/electrolyte interface. In a photoanode, the electrons will drive towards the counter electrode via external circuit whereas the hole oxidizes the water to produce oxygen at the electrode/electrolyte interface. Then the electrons and diffused proton ions produced hydrogen at the counter electrode, thereby separating hydrogen, oxygen at two macroscopically different locations without post separation cost. The reactions steps are given below: [1, 2]



The overall water splitting reaction involves with four protons which generate four electron-hole pairs for every two hydrogen molecule and one oxygen molecule, which is given by:



For this reaction to occurs, external voltage supply (1.229 V) is required. The change of Gibbs free energy for this reaction is calculated by the following formula:

$$\Delta G^0 = -nF \cdot \Delta E^0 \quad (1.5)$$

where ΔG^0 and ΔE^0 are the Gibbs free energy change and the standard electric potential of the reaction. This is an endothermic process with a corresponding +237 kJ/mol of Gibbs free energy change (at standard temperature and pressure). Therefore, equivalent amount of energy must be supplied to split water.

1.3.3 Efficiency Consideration of The PEC Cell

Determination of the solar energy conversion efficiency is necessary to figure out the merit of the PEC device. Considering all the electron-hole pairs are involved in

water splitting reactions, the overall solar to hydrogen (STH) conversion efficiency is given by: [2]

$$\eta_{STH} = \frac{P_{out}^{electrical} - P_{in}^{electrical}}{P_{light}} = \frac{J_{photo}(V_{redox} - V_{bias})}{P_{light}} \quad (1.6)$$

V_{redox} is the standard thermodynamic water splitting potential in room temperature which is 1.229 V. J_{photo} is the photocurrent achieved during the applied bias potential (V_{bias}) scan during light illumination. The above expression is the so called “applied bias photon-to-current conversion efficiency” or ABPE. [10]

1.4 Energy Levels in Semiconductor and Electrolyte

Semiconductor is defined by the forbidden energy gap between the conduction and valance band edges, generally called band gap typically ranges 1 to 4 eV. The electronic structure of the semiconductor is normally delineated by energy bands. The energy bands are considered as closely spaced energy levels of the adjacent molecular orbitals making a continuum. The valence band is the highest energy band with occupied molecular orbitals, whereas the conduction band is the lowest energy band with unoccupied molecular orbitals. The bottom level of conduction band is leveled as E_C whereas the upper level of valance band is lebeled as E_V . The electrons can be excited to conduction band thermally or photochemically, creating holes in the valence band. Band gap determines cut off wavelength of the absorption of electromagnetic waves ($E_g = \frac{hc}{\lambda}$). Now, the Fermi level is defined by the energy level where the probability of having single electron per available state is 0.5. The Fermi level position can be estimated by using the following equation:

$$E_F = \frac{1}{2}(E_C + E_V) + \frac{1}{2} k_B T \ln \frac{N_{VB}^*}{N_{CB}^*} \quad (1.7)$$

where E_C, E_V, k_B, T are conduction band edge position, valence band edge position, Boltzman constant (1.38×10^{-23} J/K) and temperature respectively. N_{CB}^*, N_{VB}^* are

density of energy states in conduction and valence band, respectively which are given by:

$$N_{VB}^* = 2 \left[\frac{2\pi m_h^* kT}{h^2} \right]^{\frac{3}{2}} \quad (1.8)$$

$$N_{CB}^* = 2 \left[\frac{2\pi m_e^* kT}{h^2} \right]^{\frac{3}{2}} \quad (1.9)$$

in which, h represents Plank constant and m_e^* , m_h^* represent the effective mass of electron and hole, respectively. The equilibrium electrons and holes concentration for an intrinsic semiconductor are given by following equations:

$$n_0 = N_{CB}^* e^{-\frac{(E_{CB}-E_F)}{k_B T}} \quad (1.10)$$

$$p_0 = N_{VB}^* e^{-\frac{(E_F-E_{VB})}{k_B T}} \quad (1.11)$$

The intrinsic carrier concentration of the semiconductor is given by:

$$n_i^2 = n_0 p_0 = N_{CB}^* N_{VB}^* e^{-\frac{(E_{CB}-E_{VB})}{k_B T}} \quad (1.12)$$

which means that the carrier concentration exponentially decreases with the increase of band gap of the semiconductor.

The position of Fermi level tells us the type of the majority charge carrier as either n-type or p-type. In case of n-type semiconductor Fermi level lies near the conduction band edge whereas for a p-type semiconductor it lies near the valance band edge (Fig. 1.2). In case of intrinsic semiconductor the Fermi level lies in the mid position of the conduction and valence band. On the other hand, in electrolyte three different energy levels exist: $E_{F,red}$, E_{ox} (controlled by the electron affinity of the oxidized species), E_{red} (controlled by the ionization energy of the reduced species), respectively. The energy states of the species follows Gaussian energy distribution due to fluctuation of their energy levels as following:

$$W_{ox}(E) = \frac{1}{\sqrt{4\pi kT}} \exp\left(\frac{-(E-E_{F,red}+\lambda)^2}{4kT\lambda}\right) \quad (1.13)$$

$$W_{red}(E) = \frac{1}{\sqrt{4\pi kT}} \exp\left(\frac{-(E-E_{F,red}-\lambda)^2}{4kT\lambda}\right) \quad (1.14)$$

where, λ is reorganization energy and $E_{F,red}$ is the standard redox potential of the species involved.

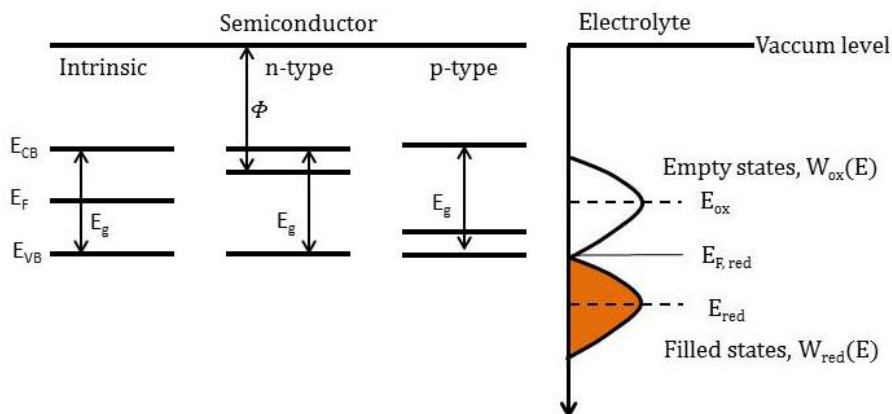


Figure 1.2: Energy band diagram of different types of semiconductor and energy distribution of electrolyte species.

1.5 Semiconductor and Electrolyte Interface

The behavior of semiconductor into an electrolyte solution is described comprehensively in several books. [2, 11] Helmholtz [12] first showed the behavior of metal/electrolyte interface as a double layer capacitor. The excess amount of charges that stayed in the metallic surface remains separated by opposite charges, aggregated in the electrolyte solution by making solvation shell. Gouy and Chapman later modified the theory with diffuse ionic double layer model which showed the behavior of potential at the surface, decreasing exponentially owing to the chemisorbed counter ions from the electrolyte solution. [13-14]

In contrast to metals, semiconductors do not have high conductivity. So diffused ionic double layer model can be introduced to show the interfacial properties. [1, 15-19] Semiconductor and electrolyte interface consists of either trapped electrons or holes at

the surface states and adsorbed ions at the semiconductor surface. The counter charges are supplied by the ionized donors or acceptors in the semiconductors. Water molecule have a large dipole moment thereby, the ions in the solution are enclosed by water molecule, forming a solvation shell (Fig. 1.3). The distance from the adsorbed ions to the closest ions into the electrolyte is called as the Helmholtz layer having width $\sim 2-5 \text{ \AA}$. Now, potential drop across the Helmholtz layer is measured by:

$$V_H = \frac{Q_s d}{\epsilon_0 \epsilon_r} \quad (1.15)$$

where, Q_s is the surface charges, d is the width of the Helmholtz layer, ϵ_0 is the free space permittivity and ϵ_r is the dielectric constant of water. Basically, the potential distribution at the metal oxide and electrolyte interface is affected by adsorption of protons, hydroxyl ions which is controlled by pH of the solution. It can be shown that Helmholtz voltage changes -59 mV per unit pH at 25°C .

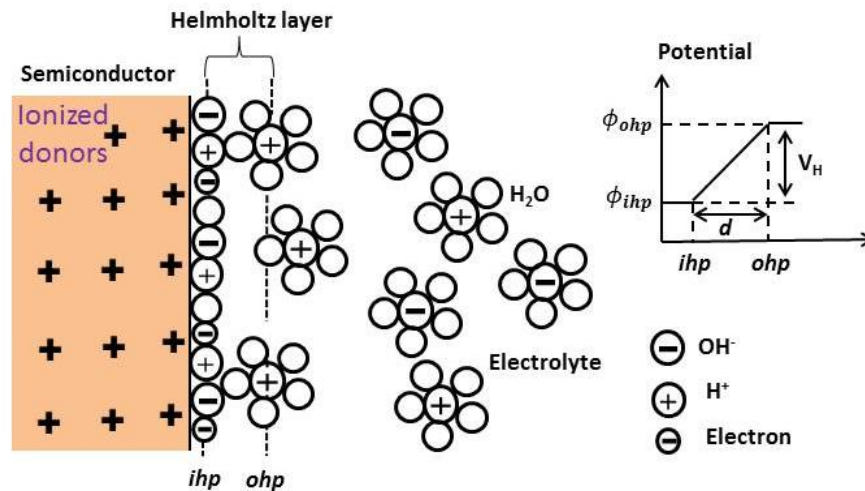


Figure 1.3: The charge distribution of the interfacial region of semiconductor and electrolyte, Helmholtz layer and potential distribution across it. [Redrawn from ref. 2]

Here, rather a simpler situation arises when metal oxide semiconductors are exposed to humid air. The mechanism is explained here. When metal oxide semiconductors are exposed to humid air, there result a space charge layer and band bending. Generally, water molecules from the air can dissociatively adsorb at the metal

oxide interface, resulting in -OH surface termination forming electronic surface states below the conduction band edge as shown in Fig. 1.4. Electrons from the bulk of the semiconductors then occupy these surface states and the ionized donors (N_D^+) stay behind the bulk of the semiconductor and formed a positive space charge layer. Therefore, an electric field is formed due the excess ionized donor states below the conduction band edges which tend to bend the conduction band edges. This process continues until the potential barrier becomes so high to transfer of electrons from the conduction band. The potential distribution and the width of the space charge layer depend on the amount of charge transfer to the surface and also the density of donor states (N_D^+).

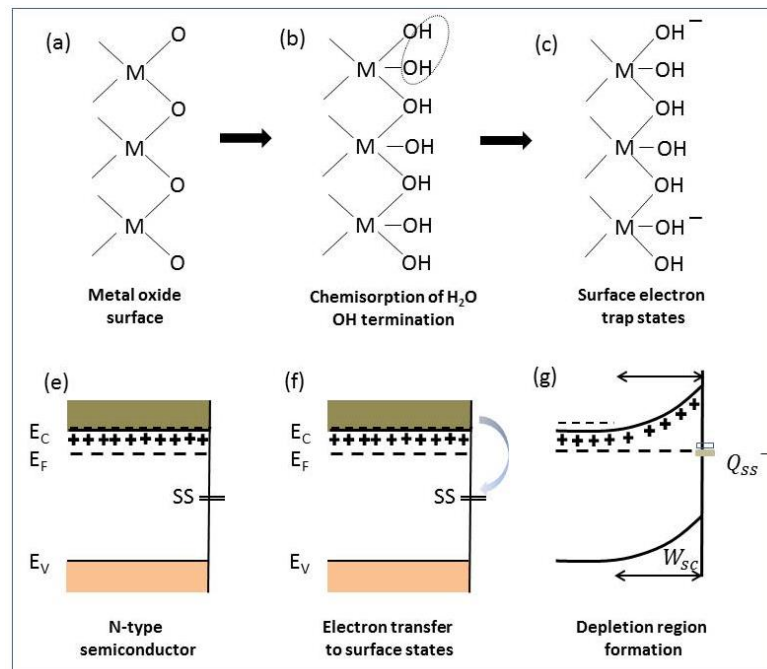


Figure 1.4: Space charge layer in metal oxide semiconductors when exposed to humid air. [Redrawn from ref. 2]

For an n-type semiconductor, immersed into electrolyte, a depletion layer is formed where the region is depleted of electrons, leaving behind a net positive charge inside the semiconductor and the counter charges are provided by the negative ions of the electrolyte. Similarly, if negative excess charges (electrons) are accumulated at the

interface and the counter charges are provided by positive ions of the electrolyte, an accumulation layer is formed. Besides, if number of adsorbed negative surface charges of an n-type semiconductor are increased beyond certain number then Fermi level crosses the middle of the band gap making surface region p-type which is called inversion layer. For better understanding, different situations for n-type and p-type semiconductors are shown schematically in Fig. 1.5.

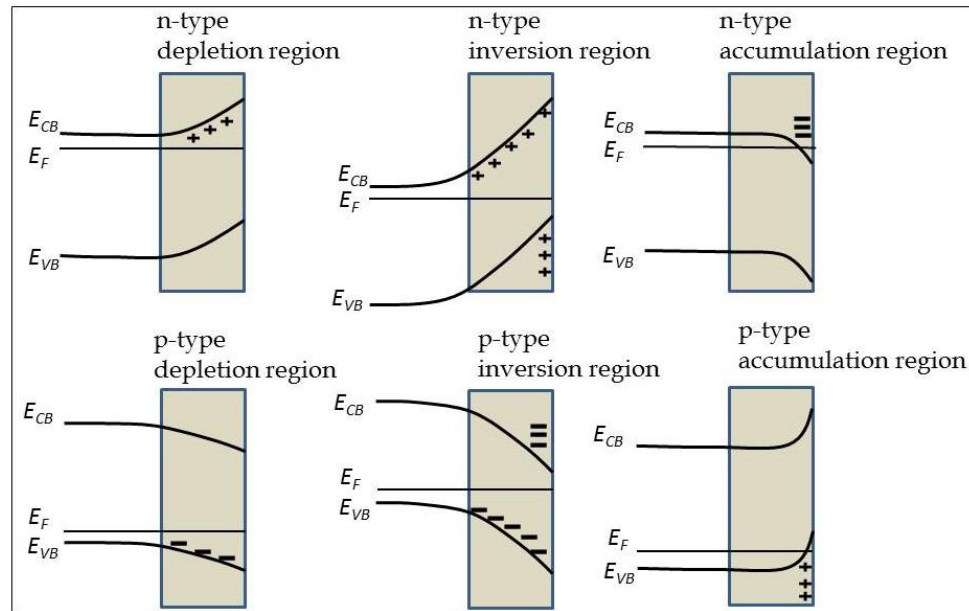


Figure 1.5: Formation of different type of space charge layers and corresponding band bending in n-type and p-type semiconductors.

1.5.1 Potential Distribution Across The Interface

Let us consider an n-type semiconductor is immersed into an electrolyte solution and attains an equilibrium such that $E_F = E_{F,red}$ by forming a space charge layer and band bending in the interfacial region. Therefore, a potential difference (ϕ) is established between the semiconductor (WE) and the reference electrode. Now, the total potential developed across the interface can be expressed as the following: [1]

$$\phi = \phi_{sc} + \phi_H + \phi_G + C \quad (1.16)$$

where ϕ_{sc} is the potential, established across the space charge layer, ϕ_H is the Helmholtz potential and ϕ_G is the potential attributed due to the diffused double layer which can be neglected for large ion concentration in the electrolyte. Moreover, the nature of the reference electrode determines the constant potential (C). Here, the charges contained in the space charge region in the semiconductor and in the Helmholtz layer are equal by their origin. So, comparison between the capacitance developed across the both region results that the space charge layer capacitance (C_{sc}) is usually much smaller than the Helmholtz layer capacitance. Under this condition ϕ_H remains constant and potential applied between the semiconductor and reference electrode will fall across the space charge region, so that:

$$\phi = \phi_A = \phi_{sc} + \phi_{FB} \quad (1.17)$$

where, ϕ_{FB} is the flatband potential and at this potential surface concentration of charges is equal to that of semiconductor bulk. The electronic charge distribution at the space charge layer establishes the differential capacitance across the interface. This can be quantitatively derived by the following approach.

The potential distribution and the width of the space charge layer depend on the amount of charge transfer to the surface and also the density of donor states (N_D^+). The potential distribution varies from surface to the bulk of the semiconductor ($x = 0$) and can be obtained by solving Poisson's equation:

$$\frac{d^2\phi}{dx^2} = -\frac{\rho(x)}{\epsilon_0\epsilon_r} \quad (1.18)$$

Here it is assumed that $k_B T$ is negligible in compared to the potential drop across the depletion region with charge density, $\rho(x) \cong eN_D^+ = eN_D$ (for n-type semiconductor, fully ionized donors) and reference potential drop across the bulk of the semiconductor to be zero ($\phi_{bulk}(x) = 0$) which is given by the following relationship:

$$\phi_{sc}(x) = -\frac{eN_D}{2\epsilon_0\epsilon_r}(x - W_{sc})^2 \quad (1.19)$$

where, ϵ_0 and ϵ_r are the permittivity of the vacuum and relative dielectric constant, respectively whereas W_{sc} is the width of the space charge layer, corresponding to the distance between surface and where the band gets flattened. Actually, the total charge density across the space charge region is given by:

$$\rho(x) = e(N_D^+ - n) \quad (1.20)$$

where, n is the free electron concentration, which is determined by the distance between conduction band minima and the Fermi level as defined by equation (1.10). It is also to be noted that inside the space charge region this distance is modified by the band bending $\phi(x)$ such that the carrier concentration :

$$n(x) = N_{CB}^* e^{\frac{-(E_{CB} - E_F - e\phi(x))}{k_B T}} = n_b e^{\frac{e\phi(x)}{k_B T}} \quad (1.21)$$

Here, $n_b = N_{CB}^* e^{\frac{-(E_{CB} - E_F)}{k_B T}}$ is the electron concentration at the bulk of the semiconductor which is equal to $N_D^+ = N_D$ for fully ionized donors for the n type semiconductor. Therefore, the charge density in the space charge region is modified by:

$$\rho(x) = eN_D(1 - e^{\frac{e\phi(x)}{k_B T}}) \quad (1.22)$$

By putting the equation (1.22) in equation (1.18) we have,

$$\frac{d^2\phi}{dx^2} = -\frac{eN_D(1 - e^{\frac{e\phi(x)}{k_B T}})}{\epsilon_0\epsilon_r} \quad (1.23)$$

By integrating the equation (1.23), we can find out the potential distribution of the space charge region. Since, there is an implicit dependence of $\phi(x)$, we can solve the above equation (1.23) by following technique:

$$\frac{d}{dx} \left(\frac{d\phi}{dx} \right)^2 = 2 \frac{d\phi}{dx} * \frac{d^2\phi}{dx^2} = -2 \frac{eN_D(1 - e^{\frac{e\phi(x)}{k_B T}})}{\epsilon_0\epsilon_r} * \frac{d\phi}{dx} \quad (1.24)$$

Since, the electric field is defined by $\xi = -\frac{d\phi}{dx}$, so

$$\xi^2 = \left(\frac{d\phi}{dx}\right)^2 = \int_0^{\phi(x)} -2 \frac{eN_D(1-e^{-\frac{e\phi(x)}{k_B T}})}{\varepsilon_0 \varepsilon_r} * d\phi \quad (1.25)$$

Now the total charge stored (Q) in the space charge region is found by solving Gauss's law as:

$$\xi = \frac{Q}{\varepsilon_0 \varepsilon_r A} \quad (1.26)$$

Here, A is the area of the semiconductor/electrolyte interface. Then the total charge stored within the space charge region is given by;

$$\begin{aligned} Q_{SC} &= \sqrt{-2\varepsilon_0 \varepsilon_r A^2 \int_0^{-\phi_{SC}} eN_D \left(1 - e^{-\frac{e\phi(x)}{k_B T}}\right) d\phi} \\ &= \sqrt{2\varepsilon_0 \varepsilon_r A^2 eN_D \left(\phi_{SC} + \frac{k_B T}{e} e^{-\frac{e\phi_{SC}}{k_B T}} - \frac{k_B T}{e}\right)} \end{aligned} \quad (1.27)$$

Under normal PEC operational condition the minimum potential drop across the space charge region is 0.1 V [2], therefore simplifying the above equation as;

$$Q_{SC} = \sqrt{2\varepsilon_0 \varepsilon_r A^2 eN_D \left(\phi_{SC} - \frac{k_B T}{e}\right)} \quad (1.28)$$

The total width of the space charge layer can be calculated by the following equation:

$$Q_{SC} = eN_D * A * W_{SC} \quad (1.29)$$

Here replacing the value of Q_{SC} from equation (1.28), we have the space charge layer width as:

$$W_{SC} = \sqrt{\frac{2\varepsilon_0 \varepsilon_r}{eN_D} \left(\phi_{SC} - \frac{k_B T}{e}\right)} \quad (1.30)$$

Again, the differential capacitance developed within the space charge can be calculated by the following;

$$\frac{1}{C_{SC}^2} = \left(\frac{dQ_{SC}}{d\phi_{SC}}\right)^{-2} = \frac{2}{\varepsilon_0 \varepsilon_r eN_D A^2} \left(\phi_{SC} - \frac{k_B T}{e}\right) \quad (1.31)$$

The flatband potential is very crucial for characterization of PEC materials as it is the potential which determine the thermodynamic ability of a semiconductor to reduce or oxidize water. It is defined by the potential required to reduce the band bending to zero or more specifically the space charge vanishes at flatband potential. Flatband potential actually indicates the Fermi level position of the semiconductors with respect to the potential of reference. This flatband potential is often measured by Mott-Schottky measurement, which shows the variation of space charge layer capacitance with external potential. Graphically, this can be determined by extrapolating the linear region to bias potential axis. A more convenient form of equation (1.31) is found by replacing ϕ_{sc} to $(\phi_A - \phi_{FB})$, obtained from equation (1.16). The carrier density of the donors can be found by determining the slope $(\frac{d(\frac{1}{C_{sc}^2})}{d\phi_{sc}})$ of the above equation which is obtained as:

$$N_d = \frac{2}{\epsilon_0 \epsilon_r e A^2} \frac{1}{\frac{d(\frac{1}{C_{sc}^2})}{d\phi_{sc}}} \quad (1.32)$$

1.5.2 Energy Band Diagram

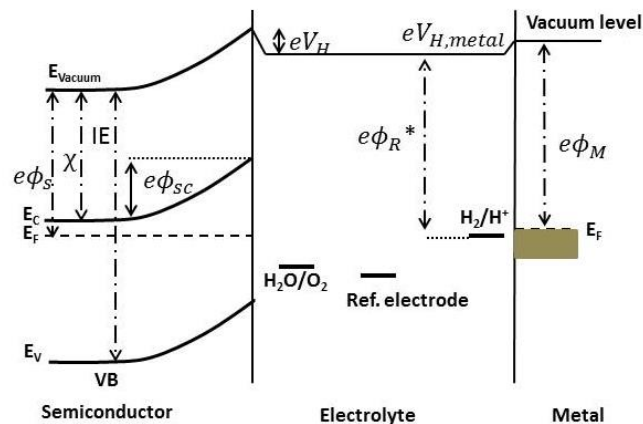


Figure 1.6: Energy band diagram of a photoanode and metallic counter electrode when immersed into conventional PEC cell. Vacuum is chosen as reference energy level. Electron affinity (χ) and ionization energy (IE) are the constant for particular material. [Redrawn from ref. 2]

Energy band diagram of semiconductor/electrolyte interface is very crucial to understand the PEC mechanism. The schematic diagram in Fig. 1.6 shows energy band diagram of an n-type semiconductor when immersed into conventional three electrode electrochemical cell. The energy of an electron in vacuum is chosen reference energy level. It is to be noted that the vacuum level also bends at both metal/electrolyte and semiconductor/electrolyte interface owing to electric field present in the PEC system. The key parameters in a PEC system are the position of band edges, the difference between conduction band edge and Fermi level, and the amount of band bending at the interface because these collectively play a significant role for the charge transfer mechanism. The energy band diagram can directly show that water splitting is either possible or not. The hole will be able to oxidize water if the valence band position is more negative than the $\text{H}_2\text{O}/\text{O}_2$ redox energy level and also the electron will be able to reduce water if position of conduction band edge is more positive than the water reduction potential. Now any applied potential can be effective to accelerate the charge transfer process. It is considered that the applied potential will affect only the space charge layer but not the Helmholtz layer because the capacitance appear in the Helmholtz layer is much higher than the space charge layer.

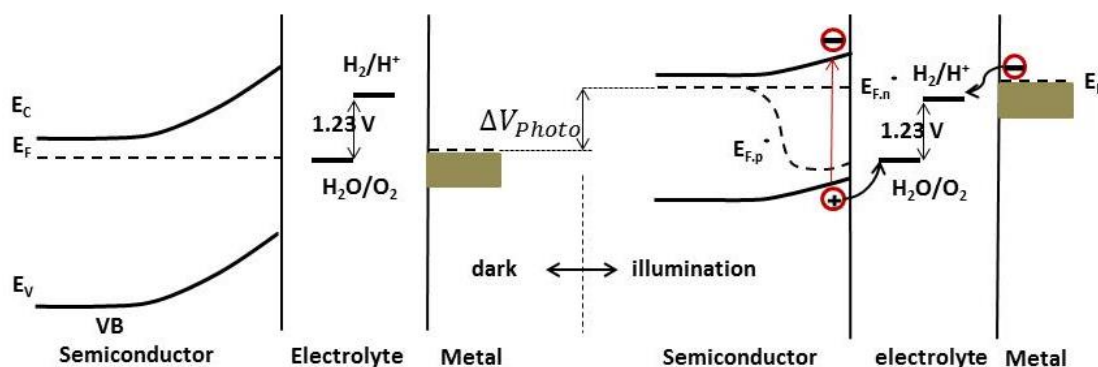


Figure 1.7: Energy band diagram of an n-type semiconductor electrode in a PEC cell. Left side: it is in equilibrium in dark, right side: in illumination condition. [Redrawn from ref. 2]

The most active species in the electrolyte solution is the redox couple $\text{H}_2\text{O}/\text{O}_2$, thereby dominating the electrochemical potential of the solution in dark. The Fermi

levels of the semiconductor and metal in equilibrium dark condition attain a value very close to the oxidation potential. But the scenario is different under illumination. Upon illumination, the Fermi level enhances by ΔV_{photo} due to creation of the electron-hole pairs. Therefore, concept of quasi Fermi level (Fig. 1.7) is important under illumination which gives the concentration of electrons and holes in the respective bands like the following:

$$n = n_0 + \Delta n = N_c e^{\frac{-(E_c - E_{F,n}^*)}{k_B T}} \quad (1.33)$$

$$p = p_0 + \Delta p = N_v e^{\frac{-(E_{F,p}^* - E_v)}{k_B T}} \quad (1.34)$$

where n_0, p_0 are the dark carrier concentration of electrons and holes. Fig. 1.6 depicts the band diagram of a n-type semiconductor under dark and illumination condition which shows that the quasi Fermi level $E_{F,n}^*$ remains horizontal due to large carrier concentration ($n_0 + \Delta n \approx n_0$) and $E_{F,p}^*$ departs from the bulk Fermi level ($p_0 + \Delta p \approx \Delta p$).

1.5.3 pH Dependence on The Band Edges

Helmholtz potential depends on pH but it does not depend on the applied bias. It is seen that Helmholtz potential changes - 59 mV per pH unit at 25 °C. This means that the band edges position also depends on the pH in the same way, shifting - 59 mV per pH unit with respect to redox potentials of the electrolyte solution. The position of the band edges is an important factor to determine the oxidation and reduction power of the photogenerated electrons and holes in semiconductor. If reduction of water is not possible due to lower energy of the conduction band, one might think that increasing the pH towards higher value to make Helmholtz potential more negative and raising E_c with respect to E_{red} will mitigate the issue. But unfortunately, the oxidation and reduction potentials also change in the same way as band edges change i.e., - 59 mV per

pH unit. Thus, band edge positions of most metal oxide semiconductors are fixed with respect to the redox potentials of water.

1.5.4 Charge Transfer Process

The charge transfer process at metal/electrolyte interface happens in an energy range very close to the Fermi level until it reaches in equilibrium with the empty acceptor states or the filled donors states of the redox species. The density of states of electrons near the Fermi level of metal is very high, therefore the electron transfer kinetics at the metal/electrolyte interface can be easily modulated by the potential difference across the Helmholtz layer. But in case of semiconductor/electrolyte interface applied potential mainly falls in the semiconductor which makes it difficult to study the electron transfer kinetics using potential perturbation techniques. H. Gerishcher [20-21] proposed a model where the charge transfer process happens via either the top of the valence band or bottom of the conduction band considering electrons and holes as individual reactants. The current in the conduction and valence band is given by:

$$J_{CB} = J_{CB}^+ - J_{CB}^- \quad (1.35)$$

$$J_{VB} = J_{VB}^+ - J_{VB}^- \quad (1.36)$$

with

$$J_{VB}^+ = ek_{VB}^+ p_s c_{red} W_{red}(E_{VB}^S) \quad (1.37)$$

$$J_{VB}^- = ek_{VB}^- N_{VB} c_{ox} W_{ox}(E_{VB}^S) \quad (1.38)$$

$$J_{CB}^+ = ek_{CB}^+ N_{CB} c_{red} W_{red}(E_{CB}^S) \quad (1.39)$$

$$J_{CB}^- = ek_{CB}^- n_s c_{ox} W_{ox}(E_{CB}^S) \quad (1.40)$$

where e is the electronic charge, k is rate constant, p_s , n_s are surface charge density of holes and electrons respectively, $c_{ox} W_{ox}(E_{VB}^S) = D_{ox}$ and $c_{ox} W_{ox}(E_{CB}^S) = D_{red}$ are the

density of states of oxidized and reduced species respectively. More analysis leads to the conduction band current and valance band current respectively as follows:

$$J_{VB} = J_{VB}^0 \left(\exp\left(-\frac{e\eta}{k_B T}\right) - 1 \right) \quad \text{and} \quad J_{CB} = J_{CB}^0 \left(1 - \exp\left(-\frac{e\eta}{k_B T}\right) \right) \quad (1.41)$$

Now it is often compare with the famous Butler-Volmer equation for the metal electrode as given by:

$$J = J_0 \left(\exp\left(\frac{(1-\alpha)e\eta}{k_B T}\right) - \exp\left(-\frac{\alpha e\eta}{k_B T}\right) \right) \quad (1.42)$$

where J_0 is the exchange current density and α is the transfer coefficient. η represent the overpotential, the potential required to initiate the reactions at the interface. A plot $\log\left(\frac{J}{J_0}\right)$ vs. η is called Tafel plot, slope of which provides the information about the reaction mechanism at semiconductor/electrolyte interface. The dark current is attributed mainly due to the majority carriers that is electrons in the conduction band for an n-type semiconductor and holes in the valance band for an p-type semiconductor. Photocurrent upon illumination increases due to the transfer of minority carriers across the interface. One most useful expression of photocurrent under reverse bias condition, derived by Gartner [22], is as follows:

$$J_G = J_0 + e\Phi \left(1 - \frac{\exp^{-\alpha W_{sc}}}{1 + \alpha L_p} \right) \quad (1.43)$$

Here, J_0 is the saturation current density, Φ is the incident light flux, α is the absorption coefficient, W_{sc} is the depletion layer width and L_p is the minority carrier diffusion length.

1.6 Characteristics of Photoelectrode Materials

Semiconductor is the heart of a PEC cell. Therefore, designing of semiconductor materials for water splitting is of primary concern. For efficient solar hydrogen production, the photoelectrode materials in PEC cell have to satisfy the following requirements:

- I. Economical
 - (a) Low material cost and abundance on earth
 - (b) Photoanode/Photocathode fabrication cost
- II. High efficiency and charge transportation
 - (a) High light absorption efficiency
 - (b) Reduced photocarrier recombination/High charge carrier separation
 - (c) High light conversion efficiency
 - (d) Low overpotential for water reduction/oxidation
 - (e) Good charge carrier transportation
- III. Stability
 - (a) High chemical stability in aqueous medium
 - (b) High stability under illumination

Generally, semiconductor always absorbs electromagnetic radiation but the main fact is that the band gap (E_g) determines the accepted frequency of absorption to generate electron-hole pairs. The band edges of the semiconductor must straddle the water oxidation and reduction potentials so that generated electron-hole pair can be able to split water. Certainly, solar light is a broad spectrum and any single semiconductor does not absorb the total spectrum of light which reduces the solar energy conversion efficiency. Apart from the high absorption efficiency, electron-hole recombination due to poor charge transportation also limits the overall PEC cell efficiency. On the other hand, no single semiconductors have the above mention properties altogether and they limit efficiency. Therefore, suitable strategies can be

adopted to mitigate the limitations involved for a single material. It is also to be noted that minimum 1.4- 1.6 eV band gap is sufficient for overall water splitting (1.229 V thermodynamic water splitting potential plus additional thermodynamic loss $\sim 0.1 - 0.5$ eV).

1.7 Oxide Semiconductors for PEC Cell

Enormous utilization of oxide semiconductors are in the forefront of research after first demonstration of watersplitting with TiO_2 by Fujishima and Honda in 1972. [23] Most of the oxides are n-type semiconductors and have been investigated as photoanodes and photocatalysts from the past several decades (Fig. 1.8). [24] Metal oxides are of relatively low cost and more stable than their metal counterparts. Moreover, the transition metal oxides have positive role in water-splitting activity due to spontaneously created oxygen vacancies in the metal oxide semiconductors which essentially develop mid band gap defect states, [24-29] acting as light absorbing donor site and also the multiple oxidation states leading to excellent photocatalytic properties. Significant reports are available on water splitting based on earth abundant metal oxide semiconductors such as TiO_2 , ZnO , Fe_2O_3 , WO_3 , [30-38] where the authors claimed the improvement in photocatalytic activity of nanostructures by minimizing all the limitations mentioned above. Still extensive research is needed to employ oxide materials in large scale application.

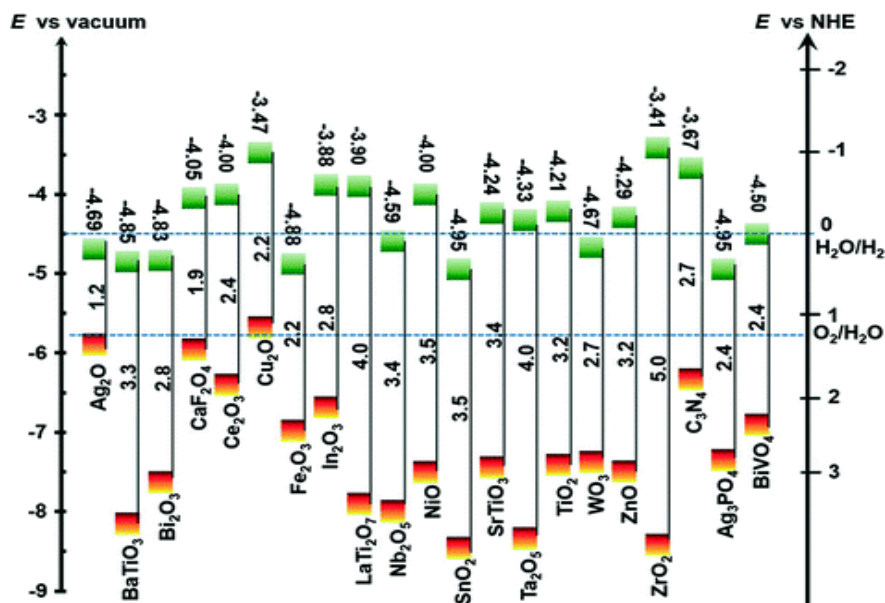


Figure 1.8: The band position of some investigated oxide materials for water splitting application. [24]

1.7.1 ZnO As Photoanode Materials for Water Splitting

According to the investigation of suitable metal oxide photocatalysts, ZnO has emerged as a promising material due to its low toxicity, earth abundance, easy synthesis process and suitable band positions for water oxidation and reduction, although the wide band gap of ZnO limits its application in the UV region only. [39-40] Now, under illumination, ZnO absorbs photons (photoexcitation) by creating an empty state in the valence band, composed of the overlapping oxygen 2p orbitals. Therefore, under illumination there are a large concentration of electrons and holes than the dark condition and new steady state is achieved by forming quasi Fermi level. Subsequently, electron-hole pairs are separated by transferring electrons towards counter electrode when the driving force is created by the space charge layer. We have already described the mechanism of space charge region formation. Basically, ZnO is an n-type semiconductor and the Fermi level is higher than the redox potential of electrolyte. As a consequence, electrons transfer to the electrolyte, making positive charge associated space charge region which is reflected in an upward band bending. Thus, band bending supports the unidirectional flow towards the counter electrode of the photoexcited

electrons. The remaining holes at surface region of ZnO act as active sites for water oxidation thereby making ZnO nanostructures will help to enhance the catalytically active sites. Furthermore, ZnO nanostructures possess short hole diffusion length. The high electron mobility of ZnO (electron and hole mobility in ZnO are 200, 180 $\text{cm}^2\text{V}^{-1}\text{s}^{-1}$ respectively) [2] supports the effective charge separation following the photoexcitation. Besides, higher electrons concentration is desirable in order to long distance transport of the photoexcited charge across the bulk. Though ZnO possesses high carrier concentration, photoconversion efficiency is lower compared to TiO_2 because of higher carrier recombination rate. [41, 42]

Now addressing several limiting parameters, different kind of strategies have been employed to enhance the water splitting performances of ZnO nanostructure based photoelectrode materials. It has been found that doping in ZnO nanostructure enhances the PEC property of the same by creating defect states within the band gap of ZnO which basically improves the visible light absorption efficiency, carrier concentration, mobility. [35, 43-45] However, defect states introduced by dopant might also enhance the probability of electron-hole recombination which might negatively impact on the PEC properties of ZnO. Another strategy that has been often implemented by researchers, the heterojunction formation or core-shell type heterostructure where the outer shell generates photo carriers by absorbing solar light and subsequently transfer the charge to the inner core material, facilitating the charge separation by suppressing the carrier recombination. [46-47] Besides, it has been found in literatures that introduction of surface passivation layer or catalyst layer reduces the surface defect states (recombination centers) and it also transfer hole to speed up water oxidation process. [47-50]

Since, the scope of presenting all the data of PEC properties investigation of ZnO based photoanodes are limited, a brief overview of overall efficiency by the same is presented here. In a report by Yang et al. [35] they synthesized N doped ZnO nanowires by hydrothermal process with variation of nitrogen concentration. They found 400

$\mu\text{A}\cdot\text{cm}^{-2}$ for N doped ZnO NWs which is much higher than bare ZnO NWs ($17 \mu\text{A}\cdot\text{cm}^{-2}$) at 1 V applied bias potential vs. Ag/AgCl. They measured PEC activity with an illumination $100 \text{ mW}\cdot\text{cm}^{-2}$ (AM 1.5) in 0.5 M NaClO_4 electrolyte solution buffered to pH 7.0 with phosphate buffer solution. Efficiency wise (STH), they showed an improvement from 0.01% for bare ZnO NWs to 0.15% for N doped ZnO NWs. On the other hand Qui et al. synthesized branched ZnO nanotetrapods and then doped with nitrogen. They observed maximum efficiency 0.31% for N doped branched ZnO nanotetrapods at 0.92 V applied potential vs. RHE which is much higher than pristine ZnO nanotetrapods (0.016% at 0.86 V vs. RHE) and branched ZnO nanotetrapods (0.045% at 0.82 V vs. RHE). [51] The PEC activity was tested in 0.5 M Na_2SO_4 electrolyte and under 1 sun illumination. Further, Lee et al. [52] implemented an useful strategy of spontaneous polarization in Li doped ZnO NWs and showed upon positive poling, STH efficiency was increased to 0.24% than Li doped ZnO NWs (0.17%) whereas upon negative poling, STH efficiency was decreased to 0.4% at 0.7 V vs. RHE. Au particle sensitized ZnO nanopencil arrays photoanode was synthesized on FTO substrate by Wang et al. [53] and they achieved a photocurrent $1.5 \text{ mA}\cdot\text{cm}^{-2}$ at 1 V vs. Ag/AgCl. Again, Y Wei et al. [54] showed 0.81% STH efficiency at 0.29 V vs. Ag/AgCl for ZnO nanorods grown on polyethylene terephthalate (PET) substrate which is modified by Ag fil of thickness 10 nm. Report by Dom and co-workers [55] investigated Cu doped ZnO as photoanode and found 0.28% STH efficiency vs. SCE. Beside N doped grapheme quantum dot synthesized by Majumdar et al. where they achieved 0.83% STH efficiency vs. Ag/AgCl. [56]

1.8 Energy Storage and Supercapacitor

Apart from the green energy harvesting, there remains another major challenges, the storage of precious energy harvested. Energy storage is one of the key challenges to maintain the sustainable energy infrastructure to supply energy according to the human requirement. The intermittent nature of the renewable energy resources still hinders them to turn out to be the foremost energy resource. Therefore, development of the

efficient energy storage devices can alleviate the intermittency issue of renewable energy sources by storing the energy, harvested from the renewable sources and making it available according to the demand. In modern days, electrical energy storage devices have become exceptionally important, as they power almost every electronic gadgets, mechatronic systems, medical instruments and so on. [57] In this context, research in the areas of different storage devices like the battery, fuel cell and supercapacitor has earned active research attention in recent time. [58-59]

Among the several types of energy storage devices, supercapacitors, also known as electrochemical capacitors or ultracapacitors have attracted increasing attention and research interests owing to their novel features including high energy and power density, long cycle life, and small size. Recently, supercapacitors are showing wide range applications, especially in electric vehicles, pacemakers, consumer electronic devices etc. Ragone plot (Fi. 1.8), (which specifies comparative operational regime) shows that no single energy storage device can emulate all power and energy region but supercapacitors and batteries, filling up the gap between conventional capacitors and fuel cells, therefore treated as ideal electrochemical energy storage systems. [60- 61]

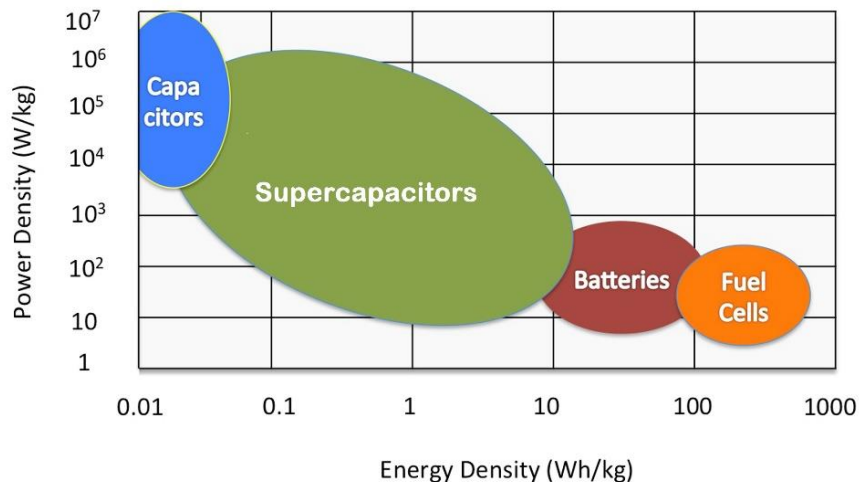


Figure 1.9: Ragone plot: comparison of specific energy and power capabilities for various kind of energy storage and conversion devices. [62]

Although the basic energy storage and conversion mechanisms are different but there are electrochemical resemblance of supercapacitors and batteries. The most common characteristics of both systems are that energy transfer takes place at electrode/ electrolyte interface, and that electron and ion transports are separated. [62] The characteristic performance of supercapacitors and batteries are different due to the inherent differences in the energy storage mechanism and electrode materials. Here, Table 1.2 summarizes the properties of batteries and supercapacitors as well as the conventional capacitors (electrolytic capacitors). [63] In case of a battery, energy is stored in form of chemical energy, whereas energy is released in the form of electrical energy when connected to an external load across the terminals of anode and cathode. The conversion of chemical energy to electrical energy is occurred via the chemical reactions of electrode materials to the ions of the electrolyte. [64] The reaction kinetics of the active material and mass transport rate determine the rate of discharge and the power performance of the batteries.

Table 1.2: *Relative properties of supercapacitors, batteries and electrolytic capacitors.*

Characteristics	Supercapacitor	Battery
Storage Mechanism	Physical	Chemical
Charge time	1~30 Sec	1~5 hrs
Discharge time	1~30 Sec	0.3~3 hrs
Energy density (Wh/kg)	1~10	20~100
Power density (kW/kg)	5~10	0.5~1
Charge/Discharge Efficiency (%)	75~95	50~90
Cycle life	> 500000	500~2000
Max. voltage determinants	Electrode and electrolyte stability window	Thermodynamics of phase reactions
Charge stored determinants	Electrode microstructure and electrolyte	Active mass and thermodynamics

Therefore, batteries predominantly provide high energy densities (150 Wh/kg is possible for LIBs), rather low power rates, and limited cycle life. The growing demand for power requirements is a serious challenge to the ability of battery design. [57] Conventional capacitors store energy physically as positive and negative charges on two parallel conductive plates and offer a high power density but a comparatively low energy density.

Conventional capacitors consist of two electrodes separated by dielectric medium. When external voltage is applied between them opposites charges are accumulated on the surface of the electrodes and separated by the dielectric material. Thus an electric field is created between the electrodes which thereby store energy. The capacitance (C) is defined by the ratio of stored charge (Q) and applied voltage (V) such that,

$$C = \frac{Q}{V} \quad (1.44)$$

For the conventional capacitors, capacitance is proportional to the area (A) of the electrode and inversely proportional to the distance (D) between the electrodes. Mathematically,

$$C = \epsilon_0 \epsilon_r \frac{A}{D} \quad (1.45)$$

Here, ϵ_0 , ϵ_r are permittivity of free space and the relative permittivity of the dielectric medium, respectively. The merit of the capacitors is determined by energy density and power density. For each case, the density can be calculated by the quantity per unit mass or unit volume. Now, the energy that is stored into the capacitor is directly proportional to its capacitance as,

$$E = \frac{1}{2} CV^2 \quad (1.46)$$

The power is defined by the energy released per unit time and the energy is released across an external load resistance, R which is connected in series with the capacitor. The internal components of the capacitors: electrodes, dielectric material also offer internal resistance. Therefore, voltage during discharge of the capacitor is determined by the equivalent series resistance (ESR). The maximum power of a capacitor is given by,

$$P = \frac{V^2}{4 \cdot ESR} \quad (1.47)$$

Supercapacitors are very special whenever rapid delivery of electrical power is required and it follows the same basic principle of conventional capacitor. The performance of a supercapacitor is figured out by its specific capacitance (C_{sp} , unit: F.g⁻¹) specific energy (E , unit: Wh.kg⁻¹), specific power (P , unit: kW.kg⁻¹), cyclic stability and rate capability. Specific capacitance, energy and power are given by following equations;

$$C_{sp} = \frac{I\Delta t}{m\Delta V} \quad (1.48)$$

$$E = \frac{1}{2} C_{sp} (\Delta V)^2 \quad (1.49)$$

$$P = \frac{E}{\Delta t} \quad (1.50)$$

Here, I is the discharge current, Δt is the discharge time and m is the mass of active material of the supercapacitor electrode. Due to the higher specific power than most batteries and a higher specific energy than conventional capacitors, supercapacitors have emerged to enable major advances in the field of energy storage. [65-67] Like the battery, a typical supercapacitor consists of a pair of polarizable electrodes, a separator, and an electrolyte. The energy in supercapacitors is stored physically by means of ion adsorption at the electrode/ electrolyte interface by forming electrochemical double layer (EDLC) which makes fundamental difference from a battery where energy is stored chemically. For this, the supercapacitor offers the ability to store/release energy in time scales of a few seconds with extended cycle life (Table 1.2). [68] The electrolytes that are used in supercapacitors can be aqueous or organic. The aqueous electrolyte offers a low internal resistance but limits the operating potential window to be about 1.0 V which is determined by the thermodynamic electrochemical window of water (1.23 V). Organic electrolytes with a broader electrochemical window can appreciably increase the electrical charge (or energy) gathered in supercapacitors than aqueous electrolytes.

1.8.1 Classification of Supercapacitors

Depending upon current research trend supercapacitors have been classified into three categories, electrical double layer capacitors (EDLCs) and pseudocapacitors (or redox supercapacitors) and hybrid capacitors. [58, 69] They are classified according to the charge storage mechanism (non Faradiac, Faradiac and the combination of the two). Faradiac process involves with oxidation and reduction reactions and the charge transfer occur at the electrode/ electrolyte interface. On the other hand, non Faradiac process does not use chemical mechanism rather charges are distributed on the surfaces of the electrodes by physical process and here making and breaking of chemical bond do not happen. EDLCs, using carbon-based active materials with high surface area, build up an electrical charge at the electrode/electrolyte interface by creating Helmholtz layer and, charge separation occurs on polarization at the electrode-electrolyte producing a double layer capacitance. [57, 70] On the other hand, pseudocapacitors utilize fast and reversible surface or near surface reactions to store charge. Several metal oxides such as RuO_2 , Fe_3O_4 , MnO_2 , NiO or Co_3O_4 , as well as electronically conducting polymers, have been studied extensively during past few decades because of their high theoretical specific capacitance. [58, 71-73] According to their charge storage mechanism, these are treated as pseudocapacitive materials and also the specific pseudo-capitance exceeds that of the carbon based EDLCs. [69] In order to delivery of high power, these materials can complement battery in electrical energy storage applications. On the other hand, carbon based materials and metal oxides are used in hybrid supercapacitors.

A noticeable enhancement in the supercapacitive responses has been observed owing to better understanding of charge storage mechanisms and the development of advanced nanostructured materials. As the pseudocapacitors store charges in the first few nanometers from surface, decrease of the particle size will increase the usage of active material. Recent reports also evince that supercapacitors based on thin films

(thickness about several tens of nanometers) exhibit high specific capacitance due to their high specific surface area.

1.8.2 Oxide Materials for Supercapacitor

Common transition metal oxides such as RuO_2 , Co_3O_4 , MnO_2 , NiO , and V_2O_5 are investigated as active pseudocapacitive materials for past several decades. [74-78] Metal oxides undergo multiple oxidation states at specific potentials, leading to enhanced capacitance. RuO_2 is widely studied as pseudocapacitive material because of its good reversibility, three distinct oxidation states accessible in potential range of 1.2 V, and an acceptable life cycle. [58] Hu, Chen, and Chang achieved a capacitance value of 1340 F/g by annealing hydrous RuO_2 at high temperature. [79] But ruthenium metal is toxic and expensive material. For this reason the researchers has been shifted the attention toward nonprecious metals that are more commercially available, including cobalt, manganese and nickel oxides. In a report [80], porous NiO nano/microspheres offer a good specific capacitance of 710 F/g at a current density of 1 A/g and it retains a 98% of the capacitance after 2000 continuous charge/discharge cycles. On the other hand, J. Lv et al. [81] showed that NiO nanoflakes on graphene foam as synthesized by hydrothermal route exhibits a very high specific capacitance 1062 F/g at a current density of 1 A/g and it retained 90.6% of the capacitance after 5000 cycles. Besides, mesoporous Co_3O_4 nanocrystals with well-controlled shapes, synthesized by solvothermal method, has showed specific capacitance 92 F/g at a current density, 5 mA/cm². [82] A high specific capacitance of 623 F/g and good cycle stability were observed for cobalt oxide aerogel based supercapacitor electrode. [83] The specific capacitance of cobalt oxide aerogel is much higher than that of loosely packed cobalt oxide nanocrystals. Cobalt hydroxide thin films were also prepared using a nonionic surfactant (Brij 56) as template. [84] The maximum specific capacitance of 1084 F/g was realized in a 2 M KOH electrolyte solution at a current density of 4 A/g. Fe-Ni/ Fe_2O_3 - NiO core/shell hybrid nanostructures offer high specific capacitance (specific capacitance 1415 F/g at a current density 2.5 A/g), excellent cycling stability and rate

capability in 1M KOH solution. [85] Again, Co-Ni/Co₃O₄-NiO core/shell nano-heterostructure electrode exhibits high specific capacitance (2013 F/g at a current density 2.5 A/g) and high energy and power density (23 Wh.kg⁻¹ and 5.5 kW.kg⁻¹) in 1M KOH solution. [86]

Nonetheless, due to poor electrical conductivity metal oxides usually suffer performance loss. Overall, a variety of materials (carbon-based materials, conducting polymers, transition-metal-oxides, and their composite materials) have been investigated as electrode materials for supercapacitors and found enhanced energy density, power density and cycling stability. The diversity of electrode materials in chemical and physical properties, preparation methods, as well as the evaluation methods renders the reported electrochemical performances highly variable. With respect to transition metal oxide based materials, it is expected to fully exploit as promising materials for supercapacitors.

1.9 Objective of The Thesis

For sustainable future, it is extremely important to harvest renewable and green energy resources, and store them in usable form of energy to supply it according to demands and also to protect our environment from toxic release of gases. As discussed previously, to achieve the energy goal for sustainable future, metal oxide semiconductors nanostructures have been proven front row materials to harvest enormous solar energy in photoelectrochemical cell in an economically viable way and also in the purpose of storing electrical energy in supercapacitors. Following the above motivation the key objectives of this thesis are:

1. Synthesis of one-dimensional (1D) nanomaterial by easy, scalable and economically viable routes.
 - (a) Synthesis of 1D ZnO NRs by easy wet chemical bath deposition technique.
 - (b) Suitable doping or surface modification/engineering of ZnO NRs by easy fabrication routes.

- (c) Fabrication of 1D ZnO NRs core based nano-heterostructures (NHs).
- (d) Synthesis of AAO template and template synthesis of compound oxide nanotubes for energy storage.
- 2. Characterization of nanostructures
 - (a) Morphological characterization.
 - (b) Crystallographic study.
 - (c) Study of chemical composition and the chemical oxidation states of constituents.
 - (a) Study of UV-Vis absorption properties.
 - (b) Study of photoluminescence properties.
- 3. Investigation of photoelectrochemical properties.
- 4. Investigation of supercapacitive properties.

1.10 Organization of The Thesis

The entire thesis has been divided into eight chapters. A brief outline of the different chapters of the thesis has been given below:

Chapter 1: Introduction

This chapter includes the importance of renewable energy infrastructure, specially focusing on solar water splitting to tackle the future energy challenges and also the importance of supercapacitor as energy storage devices by using the oxide semiconductors materials. A brief review on metal oxide semiconductors for PEC electrode and also on supercapacitor has been included herein.

Chapter 2: Experimental Details

This chapter describes the various routes for the fabrication of different semiconductor nanostructures and the several characterization tools employed to investigate their different properties.

Chapter 3: Photoelectrochemical Properties of C, N and S Surface Functionalized ZnO Nanorods Photoanodes

This chapter describes the fabrication process of C, N and S surface functionalized one dimensional (1D) ZnO nanorods photoanodes and their improved photoelectrochemical properties.

Chapter 4: Photoelectrochemical Properties of Alkali Metal (Li, Na and K) Doped ZnO Nanorods Photoanodes.

This chapter contains the detail synthesis procedure of alkali metal (Li, Na, K) doped ZnO NRs. Specifically, the role of oxygen vacancies and lattice strain behind the enhanced photoelectrochemical performance have been discussed.

Chapter 5: The p-n CuFeO₂-ZnO Nano-Heterojunction Photoanode for Photoelectrochemical Water Oxidation.

This chapter demonstrates the details of p-n junction engineering (CuFeO₂-ZnO) for improvement of STH efficiency and stability.

Chapter 6: 1D-2D Nano-Heterojunction Photoanodes for Solar Fuel.

This Chapter presents a comparative study of photoelectrochemical activity of as synthesized ZnO/MoO₃ and ZnO/MoS₂ nano-heterostructures.

Chapter 7: Cobalt Oxide - Manganese Dioxide -Nickel Oxide Ternary 1D Hybrid Nanotubes for Supercapacitor Electrode.

Chapter 7 deals with the AAO template assisted fabrication of compound metal oxide nanotubes for energy storage device (supercapacitor).

Chapter 8: Conclusion and Future Scope of The Work

This chapter addresses the overall conclusion of research work along with future scope of this work.

Bibliography

- [1] Light, Water, Hydrogen The Solar Generation of Hydrogen by Water Photoelectrolysis Craig A. Grimes, Oomman K. Varghese and Sudhir Ranjan. Springer, (2008)
- [2] Photoelectro-chemical Hydrogen Production. Roel van de Krol I Michael Graätzel. Springer, (2012)
- [3] S. Chu, Y. Cui and N. Liu, *Nat. Mater.*, **16**, 16 (2017)
- [4] World in Transition: Turning Energy Systems Towards Sustainability, German Advisory
http://www.wbgu.de/fileadmin/templates/dateien/veroeffentlichungen/hauptgutachten/jg2003/wbgu_jg2003_kurz_engl.pdf
- [5] UN General Assembly document (1987) A/42/427.
- [6] A thesis by Florian Le Formal, On the Morphology and Interfaces of Nanostructured Hematite Photoanodes for Solar-Driven Water Splitting, (2011)
- [7] National Hydrogen Association; United States Department of Energy,
<http://www.fchea.org>
- [8] D. Scholten *Hydrogen and Fuel Cells*, WILEY-CH, Weinheim, (2010)
- [9] U. Bossel, *Proceedings of the Ieee*, **94** (10), 1826 (2006)
- [10] Z.B. Chen, T.F. Jaramillo, T.G. Deutsch, A. Kleiman-Shwarsstein, A.J. Forman, N. Gaillard, R. Garland, K. Takanabe, C. Heske, M. Sunkara, E.W. McFarland, K. Domen, E.L. Miller, J.A. Turner, H.N. Dinh, *J. Mater.Res.*, **25**, 3 (2010)
- [11] R. Memming, *Semiconductor Electrochemistry*, Wiley-VCH, Weinheim (1998)
- [12] von Helmholtz HLF, *Ann Phys Chem*, **7**, 337 (1879)
- [13] R. Parsons, *Chem Rev*, **90**, 813 (1990)
- [14] JOM. Bockris, SUM. Khan, *Surface Electrochemistry. A molecular level approach*. Plenum Press, New York, (1993)

-
- [15] H. Gerischer, Solar Photoelectrolysis with semiconductor electrodes. In: Solar energy conversion: Solid-state physics aspects, Seraphin BO (Ed). Springer-Verlag New York, 115–172 (1979)
- [16] A. J. Nozik Photoelectrochemical Cells. *Phil Trans Royal Soc London Series* 295:453-470 1 (1980)
- [17] A. Heller, *Acc Chem Res*, **14**, 154 (1981)
- [18] R. Memming, Photoelectrochemical solar energy conversion. *Top Curr Chem* **143**, 79, (1988)
- [19] A. J. Nozik, R. Memming, Physical Chemistry of semiconductor-liquid interface. *J Phys Chem*, **100**, 13061 (1996)
- [20] H. Gerischer, Physical Chemistry: an advanced treatise. V.9A and V 4 Academic Press, New York (1970)
- [21] H. Gerischer, *Surf. Sci.*, **18**, 97 (1969)
- [22] Reichman, *J. Appl. Phys. Lett.*, **36**, 574–577 (1980)
- [23] A. Fujishima, K. Honda, *Nature*, **238**, 37 (1972)
- [24] Z. Zhao, Z. Wang, J. Bao, Nanomaterials for Hydrogen Generation from Solar Water Splitting. Springer, Cham (2016)
- [25] B. D. Alexander, P. J. Kulesza, I. Rutkowska, R. Solarskac, J. Augustynski, *J. Mater. Chem.*, **18**, 2298 (2008)
- [26] F. Lei, Y. Sun, K. Liu, S. Gao, L. Liang, B. Pan, Y. Xie, *J. Am. Chem. Soc.*, **136**, 6826 (2014)
- [27] J. Gan, X. Lu, J. Wu, S. Xie, T. Zhai, M. Yu, Z. Zhang, Y. Mao, I. Wang, Y. Shen, Y. Tong, *Scientific Report*, **3**, 1021 (2012)
- [28] C. Zhu, C. Li, M. Zheng, J.-J. Delaunay, *ACS Appl. Mater. Interfaces*, **7**, 22355 (2015)
- [29] G. Wang, Y. Ling, Y. Li, **4**, 6682 (2012)
- [30] K. Sivula, F. L. Formal, M. Grätzel, *ChemSusChem*, **4**, 432 (2011)
- [31] A. A. Ismail, D.W. Bahnemann, *SolarEnergyMaterials&SolarCells*, **128**, 85 (2014)

-
- [32] G. Wang, X. Xiao, W. Li, Z. Lin, Z. Zhao, C. Wang, Y. Li, X. Huang, L. Miao, C. Jiang, Y. Huang, and X. Duan, *Nano Lett.*, **15**, 4692 (2015)
- [33] J. Zhang, X. Jin, P. I. M. Guzman, X. Yu, H. Liu, H.; H. Zhang, L. Razzari, and J. P. Claverie, *ACS Nano*, **10**, 4496 (2016)
- [34] A. P. Bhirud, S. D. Sathaye, R. P. Waichal, L. K. Nikama, and B. B. Kale, *Green Chem.*, **14**, 2790 (2012)
- [35] X. Yang, A. Wolcott, G. Wang, A. Sobo, R. C. Fitzmorris, F. Qian, J. Z. Zhang, Y. Li, *Nano Lett.*, **6**, 9, 2331 (2009)
- [36] M. Liu, C.-Y. Nam, C. T. Black, J. Kamcev, and L. Zhang, *J. Phys. Chem. C*, **117**, 13396 (2013)
- [37] J. Zhang, I. Salles, S. Pering, P. J. Cameron, D. Mattia, D. Eslava, *RSC Adv.*, **7**, 35221 (2017)
- [38] A. Kafizas, L. Francàs, C. Sotelo-Vazquez, M. Ling, Y. Li, E. Glover, L. McCafferty, C. Blackman, J. Darr, I. Parkin, *J. Phys. Chem. C*, **121**, 5983 (2017)
- [39] S. B.A. Hamid, S. J. Teh and C. W. Lai, *Catalysts*, **7**, 93 (2017)
- [40] A. Bard, M. Fox, *Acc. Chem. Res.*, **28**, 141 (1995)
- [41] A.K. Chandiran, M. Abdi-Jalebi, M.K. Nazeeruddin, M. Grätzel, *ACS Nano*, **8**, 2261 (2014)
- [42] S. Hernandez, D. Hidalgo, A. Sacco, A. Chiodoni, A. Lamberti, V. Cauda, E. Tresso, G. Saracco, *Phys. Chem. Chem. Phys.*, **17**, 7775 (2015)
- [43] L. Zhang, E. Reisner, J. J. Baumberg, *Energy Environ. Sci.*, **7**, 1402 (2014)
- [44] H. J. Lee, S.-H. Shin, K. T. Nam, J. Nah, M. H. Lee, *J. Mater. Chem. A*, **4**, 3223 (2016)
- [45] M. Wang, F. Ren, J. Zhou, G. Cai, L. Cai, Y. Hu, D. Wang, Y. Liu, L. Guo, S. Shen, *Scientific Reports*, **5**, 12925 (2015)
- [46] Hsu, Y.-K.; Chen, Y.-C.; Lin, Y.-G. *ACS Appl. Mater. Interfaces*, **7**, 14157 (2015)
- [47] S. J. A. Moniz, J. Zhu, J. Tang, *Adv. Energy Mater.*, **4**, 1301590 (2014)
- [48] Y. Qiu, K. Yan, H. Deng, S. Yang, *Nano Lett.*, **12**, 407 (2012)
- [49] R. Liu, Z. Zheng, J. Spurgeon, X. Yang, *Energy Environ. Sci.*, **7**, 2504 (2014)

-
- [50] Y. -F. Xu, H. -S. Rao, X. -D. Wang, H. -Y. Chen, D. -B. Kuang, C. -Y Su, *J. Mater. Chem. A*, **4**, 5124 (2016)
- [51] Y. Qiu, K. Y. H. Deng and S. Yang, *Nano Lett.*, **121**, 407 (2012)
- [52] H. J. Lee, S.-H. Shin, K. T. Nam, J. N. and M. H. Lee, *J. Mater. Chem. A*, **4**, 3223 (2016)
- [53] T. Wang, R. Lv, P. Zhang, C. Li, J. Gong, *Nanoscale*, **7**, 77 (2015)
- [54] Y. Wei, L. Ke, J. Kong, H. Liu, Z. Jiao, X. Lu, H. Du, X.W. Sun, *Nanotech.*, **23**, 235401 (2012)
- [55] Rekha. Dom, L. R. Baby, H. G. Kim, and P. H. Borse, *International Journal of Photoenergy*, **9**, 928321 (2013)
- [56] T. Majumder, K. Debnath, S. Dhar, J. J. L. Hmar, and S. P. Mondal, *Energy Technol.*, **4**, 1 (2016)
- [57] J. Miller and P. Simson, *Science*, **321**, 651 (2008)
- [58] P. Simson and Y. Gogotsi, *Nat.Mater.*, **7**, 845 (2008)
- [59] T. Sasaki, Y. Ukyo and P. Novák, *Nat. Mater.*, **12**, 569 (2013)
- [60] P. Novak, K. Muller, K. S. V. Santanam and O. Hass., *Chem. Rev.*, **97**, 207 (1997)
- [61] D. R. Rolison, and L. F. Nazar., *MRS Bulletin*, **36**(07), 486 (2011)
- [62] M. Winter and R.J. Brodd, *Chem. Rev.* **104**, 4245 (2004)
- [63] A.G. Pandolfo and A.F. Hollenkamp, *J. Power Sources*, **157**, 11 (2006)
- [64] A. Burke, *J. Power Sources*, **91**, 37 (2000)
- [65] M. Liu, L. Gan, W. Xiong, Z. Xu, D. Zhu and L. Chen, *J. Mater. Chem. A*, **2**, 2555 (2014)
- [66] A. K. Singh, D. Sarkar, G. G. Khan and K. Mandal, *J. Mater. Chem. A*, **1**, 12759 (2013)
- [67] Y. Zhao, M. Liu, X. Deng, L. Miao, P. K. Tripathi, X. Ma, D. Zhu, Z. Xu, Z. Hao and L. Gan, *Electrochim. Acta*, **153**, 448 2015
- [68] Zhang, L. L. and X. S. Zhao. *Chem. Soc. Rev.*, **38**, 2520 (2009)
- [69] M. S. Halfer and J. C. Ellenbogen, MP 05W0000272, 2006

-
- [70] P. Jampani, A. Manivannan and P. N. Kumta, *Electrochem. Soc. Interface* **19**, 57 (2010)
- [71] N. L. Wu, *Mater. Chem. Phys.*, **75**, 6 (2002)
- [72] T. Brousse, M. Toupin, and D. Belanger, *J. Electrochem. Soc.*, **153**, A2171 (2006);
- [73] R. B. Rakhi, Wei Chen, Dongkyu Cha, and H. N. Alshareef, *Nano Lett.*, **12**, 2559 (2012)
- [74] J. P. Zheng, P. J. Cygan and T. R. Jow, *J. Electrochem. Soc.*, **142**, 2699 (1995)
- [75] S. Xiong, C. Yuan, X. Zhang, B. Xi and Y. Qian, *Chem. Euro. J.*, **15**, 5320 (2009)
- [76] S. C. Pang, M. A. Anderson and T. W. Chapman, *J. Electrochem. Soc.*, **147**, 444 (2000)
- [77] K. C. Liu and M. A. Anderson, *J. Electrochem. Soc.*, **143**, 124 (1996)
- [78] R. N. Reddy and R. G. Reddy, *J. Power Sources*, **156**, 700 (2006)
- [79] C. C. Hu, W. C. Chen and K. H. Chang, *J. Electrochem. Soc.*, **151**, A281 (2004)
- [80] C. Yuan, X. Zhang, L. Su, B. Gao and L. Shen, *J. Mater. Chem.*, **19**, 5772 (2009)
- [81] J. Lv, Z. Wang and H. Miura, *Solid State Communications*, **269** 45 (2018)
- [82] S. Xiong, C. Yuan, X. Zhang, B. Xi and Y. Qian, *Chem. Euro. J.*, **15**, 5320 (2009)
- [83] T.Y. Wei, C.H. Chen, K.H. Chang, S.Y. Lu and C.C. Hu, *Chem. Mater.*, **21**, 3228 (2009)
- [84] W.J. Zhou, J. Zhang, T. Xue, D.D. Zhao and H.L. Li, *J. Mater. Chem.*, **18**, 905 (2008)
- [85] A. K. Singh, and K. Mandal, *J. Appl. Phys.*, **117**, 105101 (2015)
- [86] A. K. Singh, D. Sarkar, G.G. Khan and K. Mandal, *Appl. Phys. Lett.*, **104**, 133904 (2014)

Chapter 2 | Experimental Details

This chapter elaborates the details of the various experimental techniques employed for the fabrication of different nanostructures like nanotubes, nanorods, and nano-heterostructures etc., along with the different characterization techniques used to study the nanostructures.

2.1 Preamble

Nanomaterials have special importance in the field of electrochemical energy conversion and storage devices. For the fabrication of electrode materials for energy conversion and storage applications, high electrochemically active surface area is desired. Nanorods (NRs) and nanotubes (NTs) have high aspect ratio and therefore, we can achieve more exposed surfaces in electrochemical cell which triggered us to synthesis nanostructures. We have already discussed in the introduction chapter, our motivation of choosing metal oxides materials for PEC application and also for supercapacitor application. In this chapter, we will briefly present an overview of the various experimental techniques that are used to synthesize 1D ZnO NRs, metal oxide NTs and various nano-heterostructures along with the different characterization technique, employed to investigate their structural, morphological properties as well as optical and electrochemical properties. We have prepared 1D ZnO NRs by simple chemical bath deposition process followed by ZnO seed layer deposition using spin coating method. We have fabricated nano-heterostructures photoanodes by electrodeposition technique, using ZnO NRs as template and also by spin coating method. On the other hand, we have used electrodeposition technique to fabricate nanowires in the porous alumina template: synthesized by anodization technique.

X-Ray Diffraction (XRD), Scanning Electron Microscope (SEM), Field Emission Scanning Electron Microscope (FESEM), Transmission Electron Microscope (TEM), High Resolution Transmission Electron Microscope (HRTEM), Energy Dispersive X-Ray Analysis (EDAX), and Selected Area Electron Diffraction (SAED) are employed for structural, morphological and phase analysis of the synthesized nanostructures. Additionally, X-ray photoelectron spectroscopy (XPS) is employed to study the chemical oxidation states of the nanostructures. Moreover, the optical properties of the nanostructures are investigated by UV-Vis absorption spectrometer and spectrofluorometer. The electrochemical properties of the samples were investigated by cyclic voltammetry (CV), linear sweep voltammetry (LSV), I-t amperometry, Mott-

Schottky (MS), electrochemical impedance spectroscopy (EIS) and galvanostatic (GV) charge/discharge software controlled conventional three-electrode electrochemical cell (potentiostat AutoLab-30) and also CHI 660E.

2.2 Synthesis of Nanomaterials

There are two general approaches by which nanomaterials and nanostructures are synthesized, top-down and bottom-up approach. Top-down approach is initiated with larger macroscopic structures and reduced to nanoscopic domain by external control like ball milling, photolithography etc. On the other hand, bottom-up approach is initiated with atoms or molecules to build up nanostructures, like electrodeposition, sputtering etc. Both approaches play a very important role in the advancement of nanotechnology. The biggest problem of top-down approach is the imperfection of the surface structure of the synthesized nanomaterials. Such kind of imperfection might have significant impact on the physical and chemical properties of the nanostructures. Besides, the crystallographic damage often occurred due to sample preparation technique associated with this approach. Therefore, these imperfections lead to extra challenges in the device design and fabrication. Though, by nature this techniques are slow and not suitable for large scale production, they will continue to play an important role in the synthesis of nanostructures. Bottom-up approach is not a newer concept; it is often used in nanotechnology. All the living beings in nature observe growth by this approach only and also it has been in industrial use for over a century; like the production of salt and nitrate in chemical industry. This route is mostly used for preparing nanostructures with the ability to generate uniform size, shape and distribution.

Synthesis of nanomaterials with uniform size, shape and further control over growth in an economical way has always been a challenge to the researchers. [1] Here in the next section, we shall describe commonly useful synthesis technique (spin coating, chemical bath deposition, anodization and electrodeposition) which have been used to prepare nanostructures, especially NRs and NTs.

2.3 Synthesis Techniques

2.3.1 Spin Coating Technique

Spin coating technique is often used to prepare thin film of micrometer to nanometer range in the industry and technology sector. (Fig. 2.1) This technique has been used from the past several decades, as it is very quick, easy and cost effective process to prepare uniform thin film. The film is prepared over a substrate uniformly by concerned coating precursor. Due to uniform rotation of the substrate, most of the precursor solution is flung off the side due to the centrifugal force developed during rotation. By controlling the rotation speed and time, thickness of the thin film is formed over the substrate.

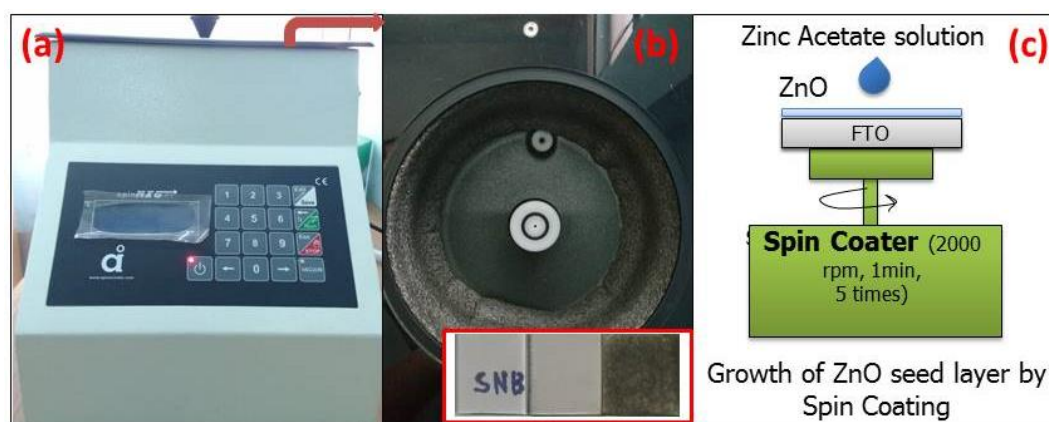


Figure 2.1: (a) spin coater, (b) inside view of the chamber, showing white color substrate holder (inset: spin coated film, first two on FTO substrate and third one on Ti substrate) and (c) spin coating process.

Typically, two steps are involved in spin coating technique which are dispense step and drying step respectively. In the dispense step, a small amount of concerned casting solution (1-10 cc) is spread off the substrate so that it can wet the substrate depending upon the nature of substrate and the viscosity of the solvent. Also the larger substrate requires large amount of casting solution. If the substrate is still not start to spinning it is called static dispense. Furthermore, if the substrate is now rotating in

smaller rotation speed, typically less than 500 rpm then it is called dynamic dispense. In particular, dynamic dispense is necessary when the wetting ability of the solution is low enough. After dispense of the casting solution, a high speed spinning, generally 1500-6000 rpm is necessary to make thin film. This step can take few seconds to several minutes. The combination of spinning speed and time will determine the final thickness of the film. Generally, high speed revolution creates higher centrifugal force making the film thinner and for this purpose sufficient time is needed. At the time of spinning the substrate, the nearest air also circulate in same speed which dries the solvent continuously. Sometimes, separate drying step is taken into account for complete removal of solvent and for the physical stability of the thin film over the substrate. [2, 3] Moreover, for the growth of the proper crystal phases, additional annealing is often required.

For example, in our case of ZnO seed layer preparation we have used 0.1 M zinc acetate, dissolved in ethanol as the casting solution and fluorine doped tin oxide coated glass as substrate. The thin film is prepared at 2000 rpm for one minute. The film is deposited for consecutive five times when dried under IR lamp. Finally, the film is heated at 350 °C for 2 hours.

2.3.2 Chemical Bath Deposition Technique

The chemical bath deposition (CBD) has a great industrial and technological value as compared to the other vapor phase routes like, evaporation, molecular beam epitaxy, spray pyrolysis etc. CBD route is a cost effective route to prepare well crystalline structure with good control over the growth of thin film along with very good reproducibility, large area scaling, and simplicity. Only hot plate, magnetic stirrer and casting solution are sufficient to prepare thin film. The details of thin film preparation by CBD method is described in review by Mane and Lokhande. [4] Furthermore, there are number of review articles available in literature, which describe the status of CBD method. [5, 6] This method depends on the deposition of the thin film

by passing a current or by chemical reaction occurred in the aqueous solution. The temperature and time are the main controlling factors for the growth of well crystalline structure and also the size of the film.

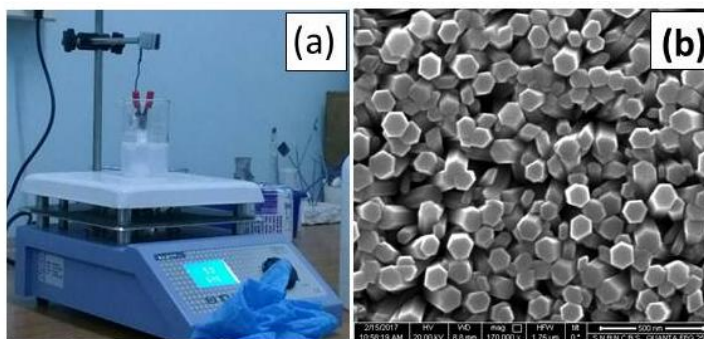


Figure 2.2: (a) Chemical bath deposition and (b) FESEM image of as synthesized ZnO NRs by CBD technique.

The evolution of the thin film starts when atomic, molecular or ionic species are aggregated together after formation of supersaturated solution followed by creation of the species and transportation of the species within the solution which is dominated at the substrate and surface of the vessel. In particular, when the ionic product exceeds the solubility product, nano-cluster is started to form. Both the homogeneous and heterogeneous nucleation is taken place into the solution. Homogeneous nucleation leads to rapid growth of nanoparticles throughout the solution which hindered the heterogeneous nucleation at the substrate solution interface, aggregating the nano cluster turning into nanoparticle and then film. This difficulty is circumvented by pre-treatment of the substrate surface which is took place by making a seed layer or ionic layer adsorption and reaction (SILAR) method. [7-9]

For an example, we have synthesized ZnO NRs array over conducting FTO substrate by CBD method followed by ZnO seed layer formation (Fig. 2.2). The details of the synthesis process will be discussed in later chapter.

2.3.3 Electrochemical Anodization Technique

The highly ordered nano porous AAO (Anodized Aluminum Oxide) template was fabricated by employing a controlled two step anodization technique [10-13] of high purity (99.99%) aluminum foil (Al) purchased from Sigma Aldrich. Before anodization, the foil ($10\text{ mm} \times 10\text{ mm} \times 1\text{ mm}$) was annealed at $400\text{ }^{\circ}\text{C}$ for 4 hours and then electropolished at 40 V for 40 sec in an acidic electrolyte for achieving smooth surface feature. The 78 ml HClO_4 , 730 ml butyl cellosolve and 100 ml of distilled water were used as electrolyte. After electropolishing, the surface was properly cleaned by acetone in a ultrasonic bath.

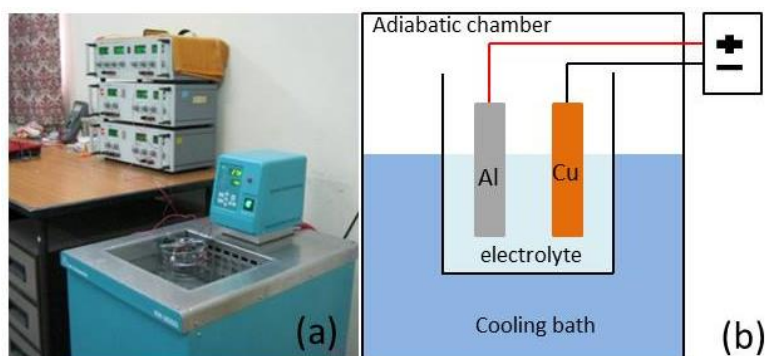


Figure 2.3: (a) Experimental set-up of the anodization of thin aluminum sheet (b) Schematic diagram of the experimental set-up for anodization of thin aluminum sheet.

The experimental set-up for anodization is shown in Fig. 2.3(a) and the schematic representation of two electrode cell is shown in Fig. 2.3(b). The positive terminal of the power supply is connected to the aluminum which acts as a cathode. On the other hand, negative terminal of the power supply is connected to copper ($\sim 1\text{ mm}$ thick) which acts as an anode. These electrodes are immersed into the electrolyte solution for anodization. To prevent the oxide layer growth on the back side of Al foil, a transparent non conducting tape was glued. Moreover, the whole electrochemical cell is kept into the adiabatic cooling bath, maintaining temperature at $11\text{ }^{\circ}\text{C}$ (Fig. 2(a)).

The first step of anodization was then carried out in 0.3 M oxalic acid electrolyte solution for 30 min at 60-65 V and a current density 200-250 A.m⁻² was maintained. After the first stage of anodization, the as grown thin porous alumina layer was removed by chemical etching using a mixture of 60 wt% phosphoric (H₃PO₄), 28 wt% sulphuric (H₂SO₄) and 12 wt% nitric (HNO₃) acid solution. Afterwards, the chemically etched Al foil was re-anodized for 6 hours keeping the anodization parameter unchanged. Finally, the uniform nanoporous AAO template was detached from the base aluminum using mercury chloride (HgCl₂) solution. The as prepared AAO template was then dipped inside the 10 wt% phosphoric acid (H₃PO₄) solution for 15 min for pore widening and pore rounding of the self-organized nanoporous template. Furthermore, the template was cleaned several times for removing the acidic inclusions. The FESEM micrographs of as synthesized AAO template are shown in Fig. 2.4.

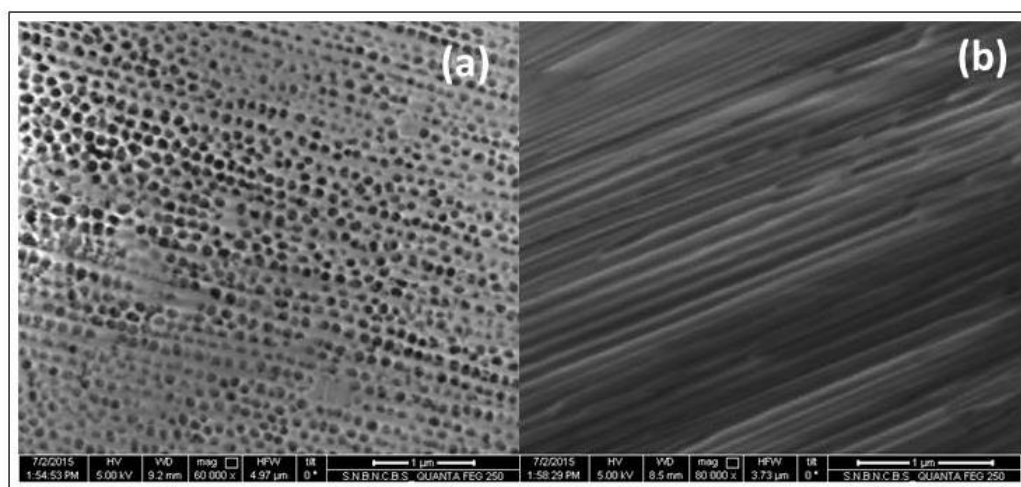


Figure 2.4: (a) FESEM micrograph of as synthesized AAO template having average pore diameter \sim 100-110 nm and (b) Cross sectional view of the same, showing densely packed tube like structure.

The conversion of aluminum into porous alumina film is an exothermic reaction. The growth mechanism of the porous alumina template is found elsewhere. [14] The type of porous alumina template and its pore distribution depends on the suitable choice of electrolyte solution (like oxalic acid, phosphoric acid, sulfuric acid etc.) and the potential provided during anodization. The growth of nanoporous AAO template with uniform pore distribution is attributed to the thermally assisted, field accelerated dissolution of oxide at the base of pores.

2.3.4 Sputtering Technique

Sputtering is a technique by which, the atoms are ejected from a material, called target and deposit onto the surface of a substrate. [15] We have deposited thin film of gold on one side of AAO template in order to make a conducting layer, employing this technique. The setup diagram of the dc sputtering unit is shown in Fig. 2.5. So in sputtering, the target material Au and the substrate AAO template are placed in vacuum chamber where the pressure is maintained at $\sim 10^{-5}$ mbar. Furthermore, a voltage is applied between them so that the target is attached to the cathode and the substrate is attached to the anode. Now, plasma is created by ionizing the sputtered gas which is typically a chemically inert gas like argon. The sputtered argon gas here bombards the gold target and sputtered of materials onto the AAO template.

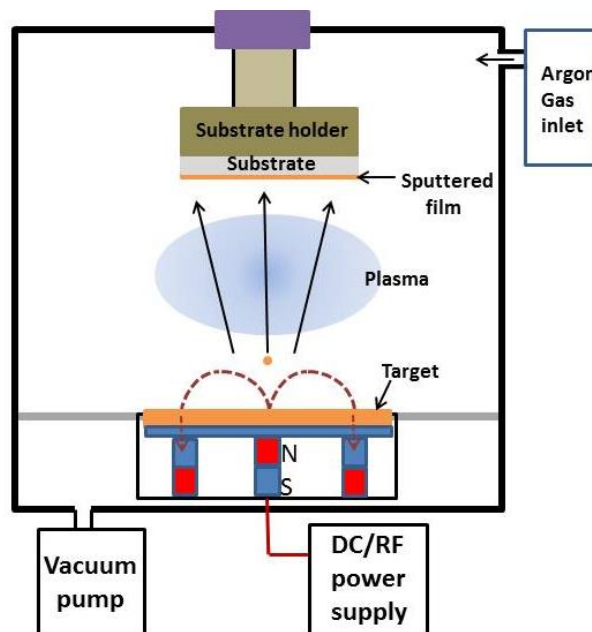


Figure 2.5: Schematic diagram of DC sputtering deposition setup.

Formation of plasma is very important factor here, because it controls the sputtering process. Once the vacuum is reached, argon gas is introduced into the chamber. This argon gas is ionized when electrons are accelerated towards the anode by the strong potential difference between anode (substrate) and cathode (Au) and collide

with neutral argon atoms. Due to ionization of neutral argon atoms, electrons are further created and again ionized the argon atoms creating a cascaded process until the gas breaks down and forms plasma. The collision process of argon ions and target are determined by the momentum and energy of the ions. The energy and momentum remain conserved throughout the collision process. Since, ions are charged particles, electric and magnetic fields can control these parameters. After collision with the target, the momentum of ions is transferred to the target atoms and ejected them from the target. Now, the ejected atoms travel to the positive substrate where they form layers of atoms. For efficient momentum transfer to happen, atomic weight of the sputtering gas should be close to that of the target material. Actually, dc sputtering is used for conducting materials. However, for non-conducting materials there is positive charge buildup on the material which stops the sputtering. In such cases, RF sputtering is efficient where a magnet is used to increase the path length of electrons, therefore, enhancing the probability of electron collision with the argon atoms and hence increases the ionization efficiency.

2.3.5 Electrodeposition Technique

Electrodeposition of metal ions is a very cost effective and commercially viable technique by which we can fabricate various types of nanostructures like thin film, nanowires (NWs), nanotubes (NTs) etc. on a conducting substrate and it is often used in nanotechnology applications from long time. It is relatively easier process as compared to the lithography processes, e.g. optical, electron beam, ion beam lithography etc. In our work, we have employed a commercial electrodeposition unit (Autolab PGSTAT 302n) in order to design NWs, NTs within the nanopores of AAO template. Moreover, we have also modified ZnO NRs surface by electrodeposition of metal ions.

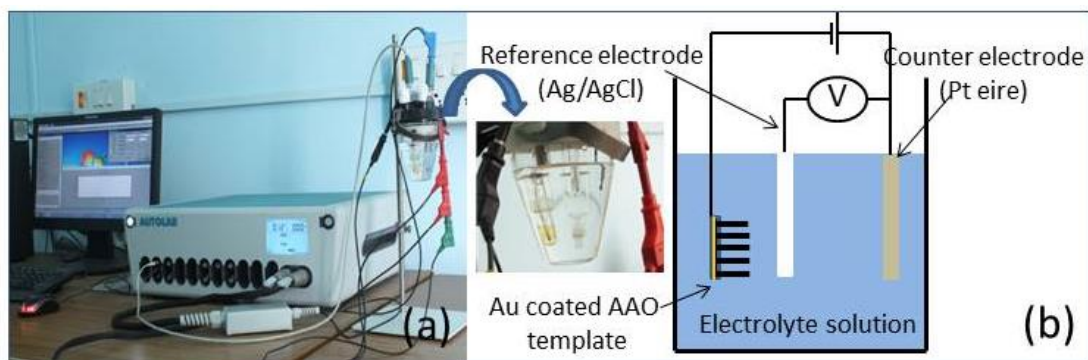


Figure 2.6: (a) Commercial electrodeposition unit; Autolab potentiostat with three electrode electrochemical cell, (b) Schematic diagram of electrochemical cell for electrodeposition within the nanopores of AAO template.

The Fig. 2.6 (a) shows the typical electrochemical set-up (Potentiostat AutoLab-30), consists of a software controlled three electrode electrochemical cell. The zoom view of the electrochemical cell is also shown in the inset of Fig. 2.6, which shows the three electrodes: working electrode (WE, black lead), counter electrode (CE, red lead) and reference electrodes (RE, blue lead). The working electrode is generally the template or the conducting substrate or nanostructure on which the desired electrochemical deposition of metal ions is carried out.

To deposit the metal ions in the nanopores of AAO template, we have used AAO template with Au sputtered (~ 100 nm) conducting base as working electrode. In case of metal deposition from the aqueous solutions of their salts, the working electrode is connected to the negative terminal of the power supply, i.e. it acts as cathode whereas high purity platinum wire ($\sim 99.99\%$, Sigma Aldrich) acts as anode, connected to positive terminal of power supply. The reference electrode is KCl saturated Ag/AgCl electrode which measures the other electrode potentials with respect to it. The cell has the volume capacity of ~ 100 cc for the electrolyte solutions.

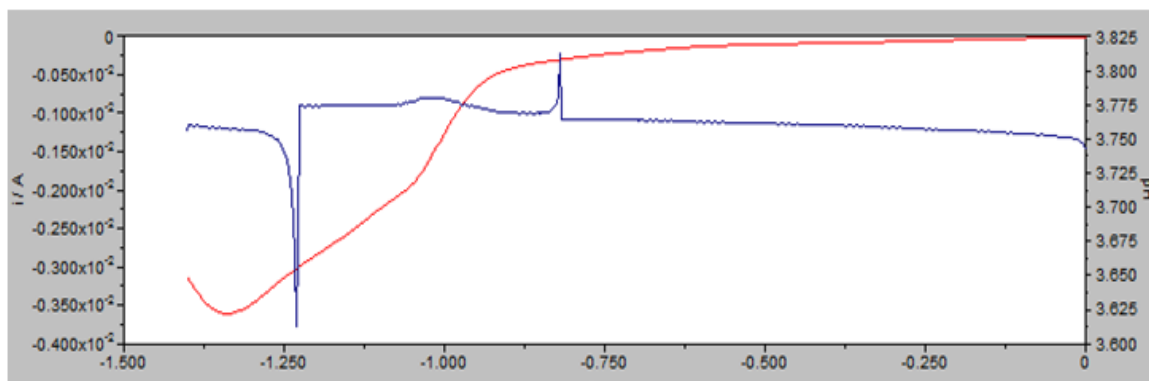


Figure 2.7: LSV profile for Ni nanowires deposition in porous AAO template (red curve) and corresponding change in pH (blue curve) of the electrolyte solution (aqueous solution of Nickel sulfate, Boric acid).

Before starting the process, particular voltage corresponding to the metal deposition should be chosen wisely in order to fabricate metallic NWs or NTs or thin films. Primary investigation of deposition potential is done by performing linear sweep voltammetry (LSV) scan which gives a current vs. voltage profile for a particular electrolyte solution and for a particular choice of electrodes. For clear vision, single LSV scan (0 V to - 1.4 V) is presented in Fig. 2.7 which shows that the current remain near zero value up to a certain applied voltage and therefore no metal ions deposition occurs. After that, the current increases suddenly with further increase of voltage and attains a maximum value. The sudden increase in current indicates deposition of metal ion at cathode. As we look up to the simultaneous pH profile of the electrolyte, it shows a spike near the potential where the sudden jump in current is observed. We choose the deposition potential just before the pH spike and very near to the start of the jump in current value.

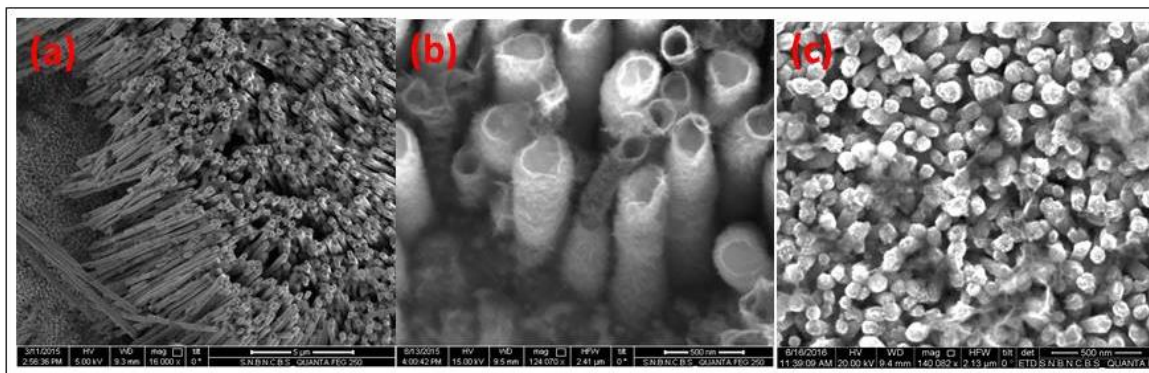


Figure 2.8: *Electrodeposition of (a) Ni NWs, (b) Ni-Co-Mn hybrid NTs and (c) Zn-Ni-Co metal deposition on ZnO NRs.*

The Fig. 2.8 shows surface morphologies of few nanostructures as synthesized by electrodeposition technique. Usually, it is found that the higher rate of ion deposition leads to formation of nanowire whereas the lower deposition rate leads to nanotube formation in template assisted electrodeposition route. The rate of electrodeposition is controlled by the deposition voltage.

2.4 Phase and Morphology Characterization Techniques

2.4.1 X-ray Diffractometer

X-ray crystallography is a method of determining the crystalline nature of a solid in which the atomic planes of the material diffract x-rays in different specific directions depending on their orientations. Now, the diffraction angle and intensity of the diffracted beams, provide a three dimensional idea of the density of electrons within the specified crystal and from this density of electrons, mean position of the atoms in the crystal can be determined.

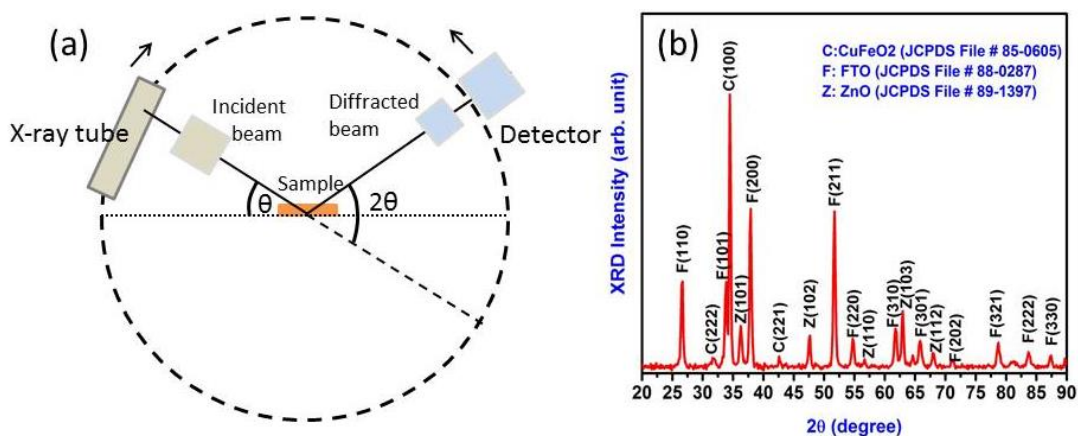


Figure 2.9: (a) Schematic diagram of X-ray diffractometer in θ - 2θ mode, (b) XRD pattern of ZnO-CuFeO₂ nano-heterostructure on FTO substrate.

X-ray diffractometer consists of three parts, an X-ray tube, a sample holder and a detector. In a practical setup as shown in Fig. 2.9 (a), a monochromatic x-rays (Cu K α , $\lambda \sim 1.54 \text{ \AA}$) beam which is produced in X-ray tube, is made to fall on a crystalline sample. These x-rays are elastically scattered by the electrons within the crystal planes and form outgoing spherical waves which will interfere constructively in few specific directions followed by Bragg's law given as,

$$2d \sin\theta = n\lambda \quad (2.1)$$

where, d is the distance between two parallel crystal plane, θ is the diffraction angle and n is an integer. These diffracted X-rays are then detected, processed and counted by detector. By scanning the sample through a range of 2θ angles, all possible diffraction directions of the lattice can be obtained due to scattering by the different plane of the material. Now, since each crystal have particular set of d spacing, therefore conversion of the diffraction peaks to d -spacings by Bragg's law allows identification of the elements/compound. Generally, this is achieved by comparison of d -spacings with standard reference patterns (JCPDS). Powder diffractometers come in two basic varieties: θ - θ in which the X-ray tube and detector move simultaneously or a θ - 2θ in which the X-ray tube is fixed, and the specimen moves at $\frac{1}{2}$ the rate of the detector to

maintain the θ - 2θ geometry. We have used X-ray Panalytical system which is a θ - 2θ system. During the data collection process, both systems maintain the geometry as shown in Fig.2.9 (a). The angles and intensities of the diffracted beams are processed and recorded electronically using the detector, connected with electronics and specialized software. The Fig. 2.9 (b) shows the obtained diffraction pattern i.e., Intensity vs. 2θ plot for the $\text{CuFeO}_2\text{-ZnO/FTO}$ sample. Here, we have also matched the crystal plane orientation as compared with standard JCPDS data file.

The grain size (τ) of the as synthesized sample can be calculated by determining the width of the diffraction peaks and using the relation as given by Debye-Scherrer,

$$\tau = \frac{0.9*\lambda}{\beta\cos\theta} \quad (2.2)$$

where, β is the full width at the half maximum of the diffraction peak at a diffraction angle of 2θ . [16]

2.4.2 Electron Microscopes

Electron Microscope (EM) is a type of microscope that uses a highly energetic beam of electrons to investigate materials on a very fine scale of submicron length. [17] The investigation can yield the surface topography of an object, the surface morphological information that is the shape and size of the particles building up the object, elemental compositions and their relative amounts, and also the crystallographic information (how the atoms are arranged in the object). The magnification power of an electron microscope is much higher than an optical microscope because the energy of the electron can be up to 100,000 times higher than the visible light photon. The original form of electron microscope, the Transmission Electron Microscope (TEM) was the first type of electron microscope to be developed first in 1931 and is used to "see through" the specimen. [18] On the other hand, the Scanning Electron Microscope (SEM) debuted in 1935 with the first commercial instruments around 1965 [19, 20]. Its late development was due to the electronics involved in "scanning" the beam of electrons across the sample.

The basic steps involved in an electron microscope are such that, a stream of electrons is generated in high vacuum by electron gun. This stream of electrons is then accelerated towards the specimen with a positive electrical potential and focused using metal apertures and magnetic lenses into a fine monochromatic beam. Finally, the effected electron beam after interaction with the specimen is detected and then is transformed into an image.

2.4.2.1 Scanning Electron Microscope (SEM)

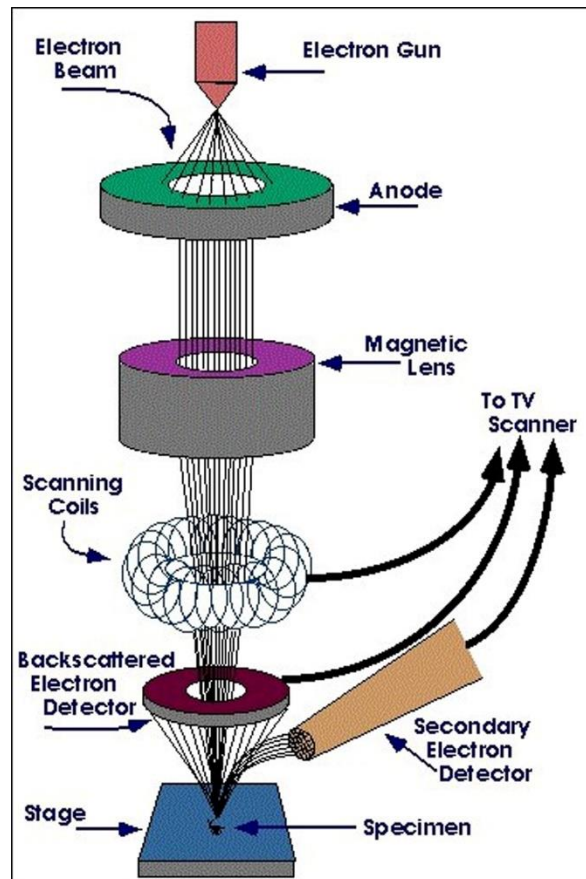


Figure 2.10: Schematic diagram of Scanning electron microscope. [23]

In case of SEM (Fig. 2.10), the electron beam is formed thermionically from a tungsten filament cathode, fitted in electron gun which is focused into a fine electron probe that is rastered over the surface of the specimen. A lanthanum hexaboride (LaB_6) single crystal is also used as electron emitters. There are other types of electron

emitters like, field emission gun (FEG and schottky emission electron gun). [21] The electron beam passes through scan coils and objective lens that deflect horizontally and vertically so that the beam scans the surface of the sample. SEM works within a voltage ranging between 2 to 50 kV whereas the diameter of the electron beam scan is 5 nanometers to few micrometer. During interaction of primary electron beam with the sample, energy dissipation of the primary electron beams occur which produces a variety of signals. These are secondary electrons, backscattered electrons, auger electrons, characteristic X-rays, cathodo-luminescence. Secondary and backscattered electrons are conventionally distinguished and collected by the detectors according to their energies. [22]

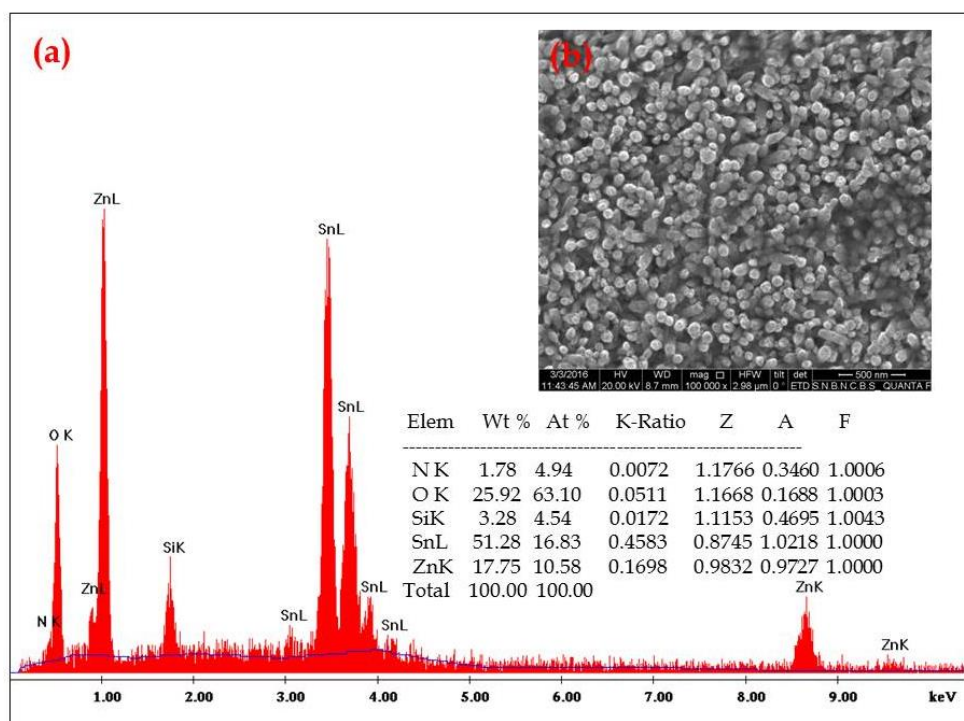


Figure 2.11: (a) EDAX spectra and (b) FESEM micrograph (inset corner) of N functionalized ZnO NRs array over FTO glass substrate.

The image displayed by SEM is due to the emission of secondary electrons by inelastic scattering of incident electrons. The probing electron beam is very narrow. SEM micrographs therefore have a large depth of field, yielding a characteristic three-

dimensional appearance which is useful for viewing the surface structure of a sample. Whereas, the elemental analysis is done by the characteristic X-rays which is produced by inelastic collisions of the incident electrons with electrons in discrete orbitals (shells) of atoms in the sample. The process is termed as energy dispersive analysis of X-ray (EDAX). Further, improvement of the spatial resolution required a field-emission cathode in the electron gun of a SEM (FESEM) which generates further narrower electron probe of low as well as high electron energy. For imaging of non-conducting samples, very often a thin gold coating on the sample is done to avoid static charge accumulation. Here, for better understanding, EDAX spectra and FESEM micrograph are presented in Fig. 2.11 (a), (b), respectively.

2.4.2.2 Transmission Electron Microscope (TEM)

In TEM, electrons beam are accelerated within a voltage range between 80-300 kV. High accelerating voltage is required so that it can pass through up to 1 μm of the specimen easily. 200-300 kV electrons are typically used for the routine imaging of the sample and comparatively less than 100 kV electrons are used for very light elements to reduce sample damage. There are mainly two different types of interactions between the electron beam and specimen, used to construct an image; which are unscattered electrons (transmitted beam) and elastically scattered electrons (diffracted beam). The transmission of unscattered electrons is inversely proportional to the sample thickness. Higher thickness of sample will transmit fewer unscattered electrons so it will appear darker, conversely thinner area of the sample will transmit more electrons, appearing as lighter thus creating dark-light contrast of the sample. This mode of TEM operation is called bright field imaging [Fig. 2.12] and the resulting micrograph is shown in Fig. 2.13 (a). The other mode of TEM imaging is electron diffraction [Fig. 2.12]. For a crystalline sample, the electron beam undergoes Bragg scattering by the parallel atomic planes. All the electrons having same energy enter the sample normal to its surface. Now, the electrons that are scattered by the same set of parallel planes can be collated using magnetic lenses to form a pattern of spots, corresponding to a specific atomic spacing.

This pattern provides the information about the orientation, atomic arrangements and phases present in the sample.

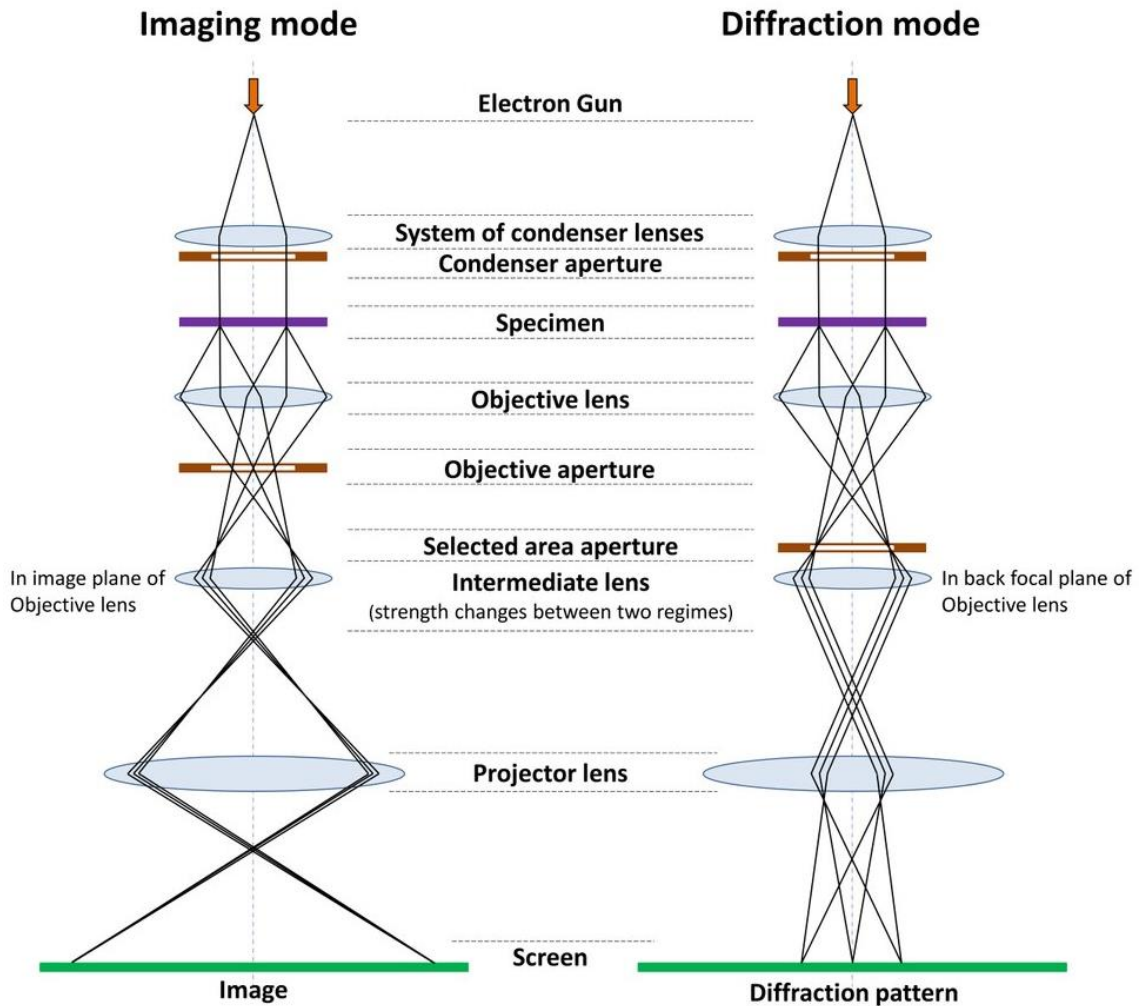


Figure 2.12: Schematic diagram of TEM. [24]

In case of high resolution TEM (HRTEM) mode we can achieve a resolution as much as 0.2 nm which is very efficient in observing the lattice fringes of the specimen under observation. Energy filtered transmission electron microscopy (EFTEM) is a technique used in TEM where electrons of particular energies are used to form an image or diffraction pattern. This technique provides information about the elemental composition of the material under observation.

Another technique that is performed in TEM is electron energy loss spectroscopy (EELS) where a material is illuminated with electrons having known narrow range of kinetic energy. These electrons undergo inelastic scattering with some energy loss. The amount of energy loss is measured in an electron spectrometer and represented in terms of what caused the energy loss. [25]

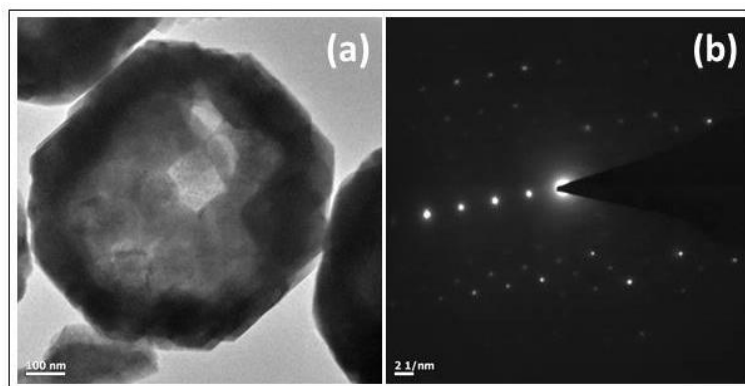


Figure 2.13: (a) TEM image, (b) SAED pattern of Fe_3O_4 nano-hollowsphere.

2.4.3 X-ray Photoelectron Spectroscopy (XPS)

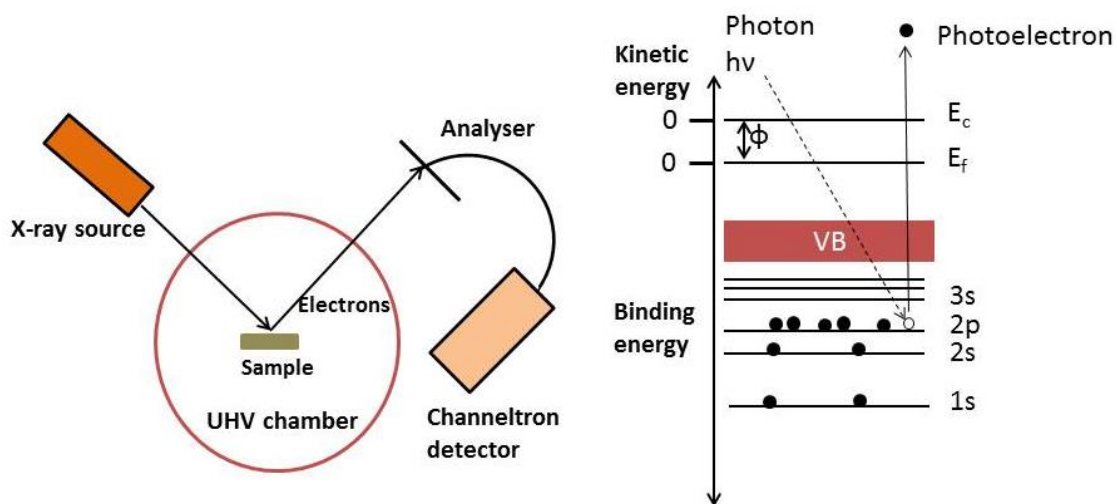


Figure 2.14: (a) Schematic diagram of an XPS spectrometer and (b) band diagram of a semiconductor under XPS measurement condition.

X-ray photoelectron spectroscopy (XPS) is a useful quantitative spectroscopic technique (Fig. 2.14) to analyze the elemental composition, chemical formula, chemical state and electronic state of constituent elements of the sample under investigation. Typically in XPS spectra, the kinetic energies and number of electrons that escape from the upper surface (1-10 nm) upon irradiation of the X-rays, are analyzed. The binding energy of each photoelectron emitted from the surface of the material can be calculated using the Ernest Rutherford equation as given below,

$$B.E_F = h\nu - K.E - \phi_{\text{spec}} \quad (2.3)$$

where, K.E is the kinetic energy of the emitted electron and ϕ_{spec} is the work function of the spectrometer.

XPS spectrum gives a plot of the number of electrons detected (Y-axis) with the binding energy of that electrons (X-axis). Each material produces its characteristics XPS peaks corresponding to the electronic configuration of the electrons in different orbitals such as 1s, 2s, 2p etc., (Fig. 2.14 (b)) and the number of electrons detected is directly proportional to the amount of that element present in the irradiated portion of the sample. As the electron counting detector in XPS instruments is typically 1 m away from the x-ray irradiated sample, so, XPS must be performed in ultra-high vacuum (UHV) condition. The schematic diagram of the XPS system is shown in Fig. 2.15.

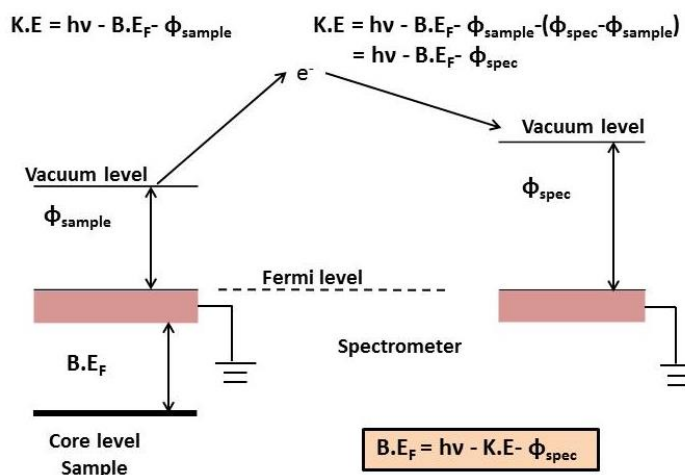


Figure 2.15: Band diagram of XPS system.

2.5 Optical Characterization Techniques

2.5.1 UV-Vis Absorption Spectroscopy

We have employed UV-Vis absorption spectroscopy, to show the absorption behavior of the sample as a function of wavelength which also provides the electronic transitions occurring in the materials. The primary requirement of the photoanodes for solar energy conversion is the higher absorbance response of the sample in the solar spectrum region, and here we have confined our interest in ultraviolet and visible region only. UV-Vis absorption spectrometer generally consists of light source, a monochromator, a sample holder and a detector as shown in the Fig. 2.16. The fraction of light transmitted after interaction with sample is estimated by Beer-Lambert law which is;

$$I = I_0 e^{-\sigma(N_1 - N_2)l} \quad (2.4)$$

where I_0 , σ , l are initial intensity of light before interaction with the sample, absorption cross section of the transition and the path length of light through the sample respectively. Besides, N_1, N_2 are the population of initial and final energy state respectively. The above equation often written in the form of Beer's law such as

$$A = \epsilon cl = -\log_{10} \left(\frac{I}{I_0} \right) \quad (2.5)$$

Here, A is the absorption, ϵ is the molar absorptivity coefficient and c is the concentration of the absorbing species. Again, the absorption coefficient of the sample is determined by normalizing the absorbance by the path length through the material such as

$$\alpha (cm^{-1}) = \frac{\ln(10) \times A}{l (cm)} \quad (2.6)$$

The optical bandgap of the material is determined by Tauc plot and Kubelka-Munk plot. [26] The extrapolation to the baseline of $(\alpha h\nu)^n$ vs $h\nu$ yield the optical bandgap of

the sample. In case of diffuse reflectance measurements Kubelka-Munk radiative transfer model can be employed to determine absorption coefficient such that,

$$f(R) = \frac{(1-R)^2}{2R} = \frac{\alpha}{s} \quad (2.7)$$

where, $f(R)$ is the Kubelka-Munk function and $R = e^{-A}$ and s is the scattering coefficient. If it is assumed that s is wavelength independent then $f(R)$ is proportional to α .

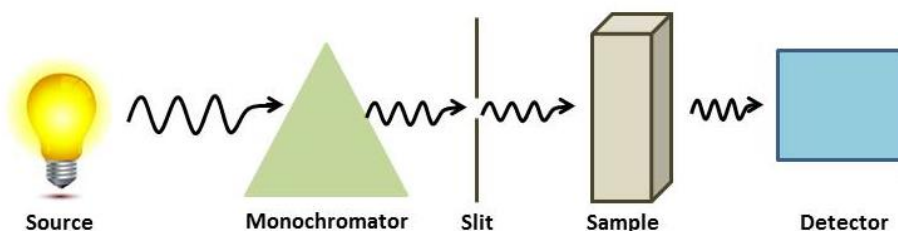


Figure 2.16: Schematic diagram of UV-Vis absorption spectroscopy instrument.

2.5.2 Photoluminescence (PL) Spectroscopy

Photoluminescence (PL) is an emission process of light in a matter after absorbing photons (electromagnetic radiation). Quantum mechanically, electrons in semiconductors materials go to the excited states after absorbing photons and then again by releasing photons they come to lower states. The period between absorption and emission is very short, which can vary from femtoseconds up to milliseconds. Steady state PL measurements of our samples were done in Horiba Jobin Yvon Fluorolog 3 spectrofluorimeter. Schematic diagram of the PL spectrometer is shown in Fig. 2.17. Photoluminescence is a very powerful tool which provides the carrier recombination behavior, information about the defects within the synthesized materials and also the band gap of the materials.

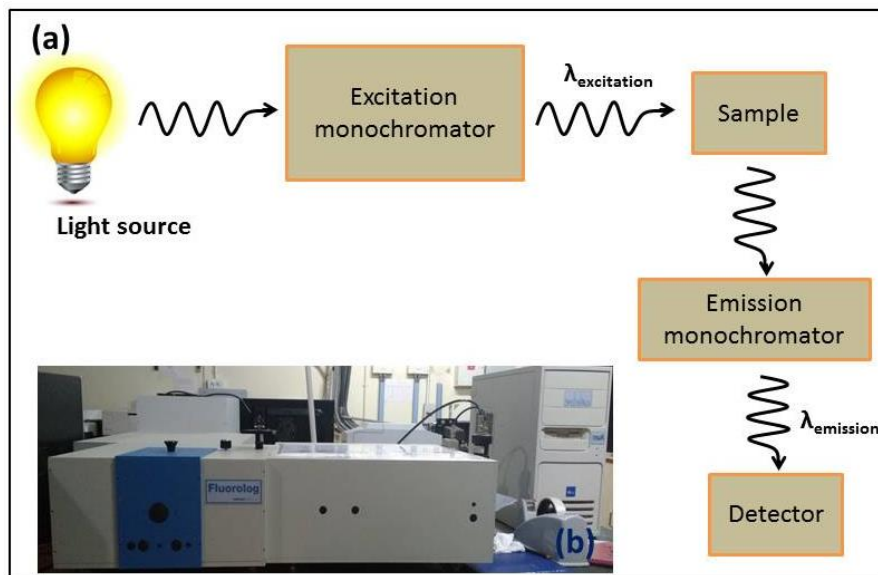


Figure 2.17: Schematic diagram of photoluminescence spectrometer.

2.6 Electrochemical Characterization Techniques

The photoelectrochemical properties of the samples were investigated by linear sweep voltammetry (LSV), *i-t* amperometry, electrochemical impedance spectroscopy and Mott-Schottky measurements using a software controlled three electrode system CHI 660E in 0.5 M Na₂SO₄ aqueous solution. The supercapacitive performance of the samples were investigated by cyclic voltammetry (CV), galvanostatic (GV) charge/discharge and electrochemical impedance spectroscopy (EIS) tests by using a software controlled conventional three-electrode electrochemical cell (potentiostat AutoLab-30) consisted of the as-prepared samples as the working electrode, saturated Ag/AgCl as the reference electrode, the Pt wire as the counter electrode and 1 M KOH solution as electrolyte, at room temperature.

2.6.1 Cyclic Voltammetry

Cyclic voltammetry is a powerful tool employed to investigate the oxidation and reduction process of molecular species which is obtained by measuring the current at the working electrode during the potential scans. [27]

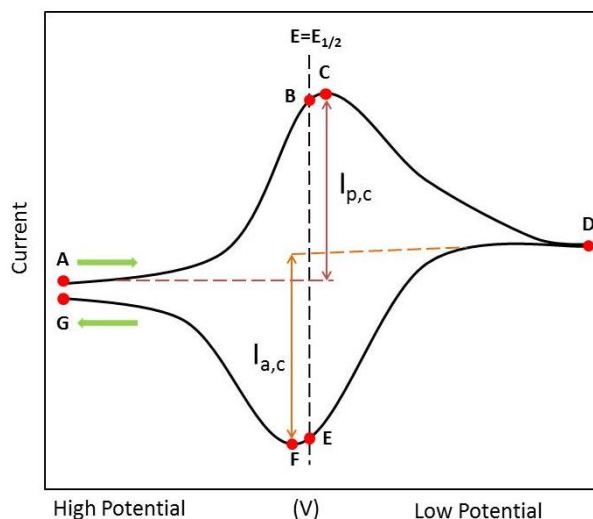


Figure 2.18: Voltammogram of a Single electron oxidation-reduction.

Fig. 2.18 shows a cyclic voltammogram curve resulting from a single electron reduction and oxidation. Consider the following reversible reaction:



Here, the molecular species is reduced by gaining electron from the working electrode surface of a three electrode electrochemical system. The transfer of electron is controlled by the concentration of species near the electrode surface and the externally applied potential to the working electrode. When the potential is scanned the concentration of the species in the solution near the electrode changes over time according to the Nernst equation as follows;

$$E = E^0 + \frac{2.3026RT}{F} \log_{10} \frac{[M^+]}{[M]} \quad (2.9)$$

where, E is the potential of the electrochemical cell, E^0 is the standard reduction potential of the species whereas R , F are the gas constant and Faraday constant respectively. Now as the potential is scanned negatively or cathodically from point A to D, $[M^+]$ is steadily depleted near the electrode and reduced to $[M]$. At point C, peak cathodic current ($I_{p,c}$) is observed and the current is dictated by the additional delivery of $[M^+]$ via diffusion from the bulk solution. The volume of the solution near the

electrode surface contains the reduced M creating the diffusion layer which continues to grow through the scan. Therefore, further mass transport of $[M^+]$ ions is hindered and simultaneous decrease of current is observed. When the switching potential D is reached oxidation process is started to occur and M is oxidized back to $[M^+]$ upon increasing the positive applied bias up to point G . Similarly anodic peak current ($I_{a,c}$) is appeared at point F . At the point B and E , the concentrations of $[M^+]$, M at the electrode surface are equal and following the Nernst equation, $E = E_{1/2}$.

A rectangular CV curve originates due to electrochemical double layer effect only. On the other hand no Faradaic reactions are involved between the active materials and the electrolyte. The measurement of specific capacitance follows the equation, [28]

$$C_{sp} = \frac{I}{mf} \quad (2.10)$$

Here, I is the current at the middle point of potential range and f is the scan rate, where m is the mass of active material. On the other hand, the pseudocapacitive responses of the active materials usually lead to the presence of redox peaks with a derivation from the rectangle shape. Therefore, the average specific capacitance is calculated using the voltammetric charge integrated from the CV curve according to the following equation: [29, 30]

$$C_{sp} (F/g) = \frac{Q}{2mV} = \frac{I}{2mf} \int_{V_c}^{V_a} I(V)dV \quad (2.11)$$

Here, Q is the total charge obtained by the integration of positive and negative scans in a CV curve, m is the mass of the active material in two electrodes, f , the scan rate, ($V=V_a - V_c$) represents the potential window.

2.6.2 Galvanostatic Charge/discharge

The galvanostatic charge/discharge (GCD) is a useful method to determine the capacitance of a material under controlled current operation. In this method, potential of the working electrode is measured with respect to a reference electrode as a function

of time when a current pulse is applied to the working electrode. The potential measured of a supercapacitor during GCD scan (Fig. 2.19), is linear or almost linear with respect to the charge/discharge time ($dV/dt = \text{constant}$) during the constant current operation, so that the state-of-charge (SOC) can be exactly pinpointed. On the other hand, most batteries show a relatively constant operating voltage due to the thermodynamics of battery reactants and their SOC could not be measured precisely [31, 32]. From this method, the specific capacitance (C_{sp}) of the active material can be calculated according to the following equation;

$$C_{sp}(F/g) = \frac{I}{m \left(\frac{dV}{dt} \right)} \quad (2.12)$$

Here I (in A), m (in g) and t (in sec) are the discharge current, mass of active materials and the discharge time respectively whereas V (in V) is the potential during the discharge process after IR drop (voltage drop due to internal resistance). Therefore, dV/dt is the slope of discharge curve. It is recommended that the specific capacitance should be calculated by taking two datum points as obtained from the discharge curve with $dV/dt = (V_{max} - 1/2V_{max})/(t_2 - t_1)$, especially in the case of the nonlinear response between potential and time for pseudocapacitive reactions [33]. Here t_2 and t_1 (in sec) are the discharge times corresponding to the maximum potential (V_{max}) and half of the voltage ($1/2V_{max}$) respectively.

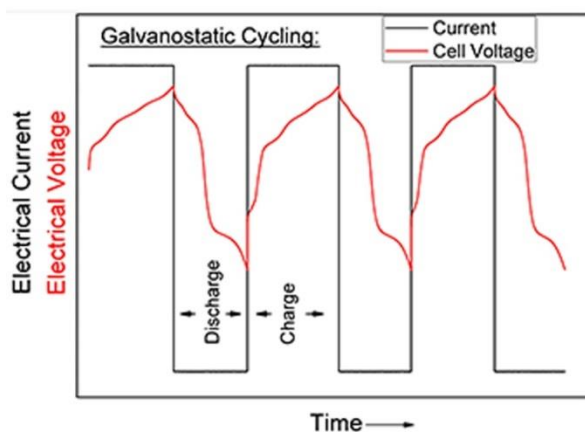


Figure 2.19: Typical galvanostatic charge/discharge cycles of standard sample.

2.6.3 Electrochemical Impedance Spectroscopy

Electrochemical impedance spectroscopy (EIS) is a powerful technique which determines frequency responses of an electrochemically active material. [34] Initially, double layer capacitance was measured by this technique but nowadays it is used to investigate the electrode processes and complex interfaces. Normally, EIS is conducted at the open circuit voltage (OCV) by applying a small amplitude of alternative potential (5 ~ 10 mV) in a range of frequency (generally 0.01 to 100kHz).

EIS connects impedance data of the real system with idealized equivalent circuit based on discrete electrical components (R, C and L) in their series and parallel combination. We can find out the equivalent series resistance, charge transfer resistance and others relevant parameters when fitted in a circuit. Fig. 2.20 (a) and (b) show the impedance behavior of ideal and real electrodes, respectively. This is called Nyquist plot.

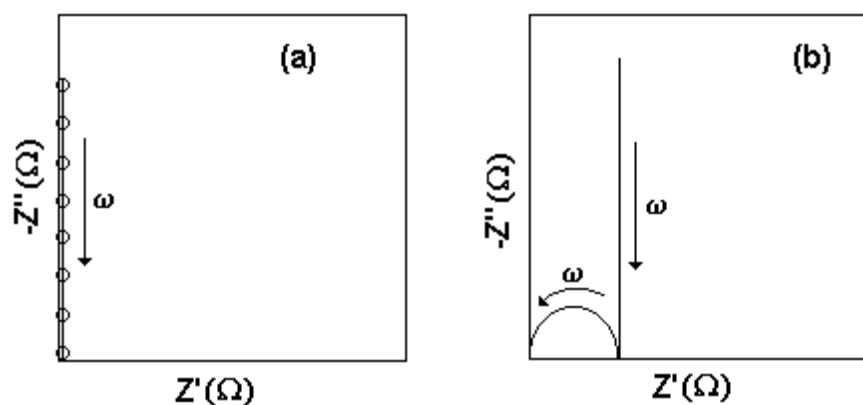


Figure 2.20: Nyquist plot: Impedance spectra of an ideal and a real capacitor electrode.

A typical Nyquist plot for a real system exhibits a semicircle over the high frequency range, followed by a linear part in the low frequency region, as shown in Fig. 2.20 (b). It is noteworthy that a large semicircle observed from a Nyquist plot is an indicative of high charge-transfer resistance, contributing to the poor electrical conductivity of materials, whereas a more vertical the line is more closing to an ideal

capacitor. [35] The resistance (Z) is defined as, $Z = Z' + jZ''$, where Z' and Z'' are the real part and the imaginary part of impedance, respectively. The capacitance is calculated from the imaginary part (Z'') of the collected EIS data according to

$$C = -\frac{1}{\omega Z''} \quad (2.13)$$

where, ω (in Hz) is the angular frequency.

Bibliography

- [1] H. Hahn, *Nanostructured Materials*, **9**, 3, (1997)
- [2] <http://www.utdallas.edu/~rar011300/CEEspinner/SpinTheory.pdf>
- [3] <https://www.ossila.com/pages/spin-coating>
- [4] R. S. Mane and C. D. Lokhande, *Mater. Chem. Phys.*, **65**, 2000, 1
- [5] S. M. Pawar, B. S. Pawar, J. H. Kim, O. S. Joo, C. D. Lokhande, *Curr. Appl. Phys.*, **11**, 117 (2011)
- [6] B. A. Ezekoye, P. O. Offor, V. A. Ezekoye, F. I. Ezema, *IJSR*, **2**, 2277 (2013)
- [7] http://www.materialsscience.pwr.wroc.pl/bi/vol28no2/articles/ms_14_2009-307kath.pdf
- [8] <http://shodhganga.inflibnet.ac.in/bitstream/10603/143535/7/07%20theoretical%20background%20of%20chemical%20bath%20deposition%20method.pdf>
- [9] http://shodhganga.inflibnet.ac.in/bitstream/10603/63785/10/10_chapter%203.pdf.pdf
- [10] Masuda, H.; Satoh, M. *Jpn. J. Appl. Phys.* 1996, 35, L126., H. Asoh, K. Nishio, M. Nakao, T. Tamamura and H. Masuda, *J. Electrochem. Soc.*, **148**, B152 (2001)
- [11] J. Sarkar, G.G. Khan and A. Basumallick, *Bull. Mats. Sci.* **30**, 271 (2007)
- [12] G. G. Khan, N. Mukherjee, A. Mondal, N. R. Bandyopadhyay and A. Basumallick, *Mats. Chem. Phy.* **122**, 60 (2010)
- [13] G. G. Khan, A. K. Singh and K. Mandal, *J. Lumin.* **134**, 772 (2013)
- [14] Woo Lee and Sang-Joon Park. *Chem. Rev.*, **114**, 7487 (2014)
- [15] http://users.wfu.edu/ucerkb/Nan242/L07-Sputtering_a.pdf
- [16] B. D. Cullity and S. R. Stock, *Elements of X-ray Diffraction*, 3rd Edition, Prentice Hall (2001)
- [17] R. Erni, M. D. Rossell, C. Kisielowski and U. Dahmen, *Phys. Rev. Lett.*, **102** (9), 096101(2009)
- [18] E. Ruska, Nobel Foundation. Retrieved 2010-01-31 (1986)
- [19] M. Knoll, *Zeitschrift für technische Physik* **16**, 467 (1935)

-
- [20] Cambridge Scientific Instrument Company, USA.
- [21] T.R. Groves, H.C. Pfeiffer, T.H. Newman and F.J. Hohn, *J. Vac. Sci. Technol. B*, **6**(6), 2028 (1988)
- [22] C.R. Brundle, C.A. Evans Jr., S. Wilson, *Encyclopedia of materials characterization*, Butterworth-Heinemann publications, (1992)
- [23] Areef Billah. (2016). Investigation of multiferroic and photocatalytic properties of Li doped BiFeO₃ nanoparticles prepared by ultrasonication. *Unpublished*.
<https://doi.org/10.13140/RG.2.2.23988.76166>
- [24] https://www.wikiwand.com/en/Transmission_electron_microscopy
- [25] http://inano.au.dk/research/research_platforms/nanoanalysis/transmission-and-scanning-electron-microscopy
- [26] Z. Chen, H. N. Dinh, E. Miller, *Photoelectrochemical Water Splitting*, Springer, (2013)
- [27] N. Elgrishi, K. J. Rountree, B. D. McCarthy, E. S. Rountree, T. T. Eisenhart, and J. L. Dempsey, *J. Chem. Educ.*, **95**, 197 (2018)
- [28] P. Simon and Y. Gogotsi, *Nat. Mater.*, **7**, 845 (2008)
- [29] A. Burke, *J. Power Sources*, **91**, 37 (2000)
- [30] L. Piraux, S. Dubois, J. L. Duvail, K. Ounadjela and A. Fert, *J. Magn. Magn. Mater.*, **175**, 127 (1997)
- [31] J. R. Miller and P. Simon, *Science*, **321**, 651 (2008)
- [32] D.J. Sellmyer, M. Zheng and R. Skomski, *J. Phys. Cond. Mat.*, **13**, R433 (2001)
- [33] H. Zhu, S. Yang, G. Ni, D. Yu and Y. Du, *Scripta Materialia*, **44**, 2291 (2001)
- [34] https://www.jlab.org/conferences/tfsrf/Thursday/Th2_1-EIS%20intro%20Reece.pdf
- [35] P. L. Taberna, P. Simon and J. F. Fauvarque, *J. Electrochem. Soc.*, **150**, A292 (2003)

Chapter 3

Photoelectrochemical Properties of C, N and S Surface Functionalized ZnO Nanorods Photoanodes

This chapter reveals the facile techniques for the fabrication of vertically aligned arrays of one dimensional (1D) arrays of ZnO nanorods (NRs) and their surface functionalization with C, N and S. The significance of the fabrication of this C, N and S surface functionalized ZnO NRs photoanodes, on the visible light driven photoelectrochemical properties is the key focus of this chapter.

A part of this content of this chapter has been published in ACS Sustainable Chemistry and Engineering [1] and is reproduced herein with permission from American Chemical Society (ACS).

3.1 Preamble

The renewable and green energy sources like solar energy have earned considerable research focus as the world is facing tremendous challenges because of the fast depletion of the fossil fuels and the ever-increasing build up of the carbon dioxide in the atmosphere. [2-4] The successful implementation of photoelectrochemical (PEC) cell to produce the hydrogen fuel by water splitting and the fixation of CO₂ into hydrocarbons by using the clean and abundant sun light are promising approaches to face this energy challenge. [5-7] For solar water splitting, the semiconductor based photoelectrodes have drawn intense attention, where the electrode can be used as anode/cathode for the water oxidation/reduction through the oxygen evolution reaction (OER)/hydrogen evolution reaction (HER). Oxide semiconductors like Fe₂O₃, TiO₂, ZnO [8-11] and their composites (oxide-oxide and metal-oxide composites) as well as the doped metal oxides have been extensively investigated as photoelectrodes for PEC water splitting. [12-22] Among the oxide semiconductors, ZnO has emerged as a promising photoelectrode material as the position of conduction and valence band of ZnO is suitable for solar water splitting, although the wide band gap of ZnO limits its application in the UV region only. [23] However, in general, an ideal photo-anode should possess the following characteristics: efficient solar light absorption for charge carrier generation, charge carrier separation, i.e., the low recombination rate of electron-hole pairs, carrier transportation/mobility, photostability during surface chemical reactions. [24,25] Considering all these parameters, different strategies have been adopted to improve the solar hydrogen synthesis efficiency of the ZnO based photoelectrodes. Formation of heterojunction or core-shell type heterostructure is one of the most effective techniques implemented by researchers, where the outer material generates charge carriers absorbing solar light and subsequently transfer the charge to the other material, facilitating the charge separation and suppress the carrier recombination. [26, 27] Secondly, the introduction of the surface passivation layers or catalyst layer can also help to achieve better water splitting activity in ZnO by reducing the surface defects (recombination centers) and helping in charge separation, where the catalyst layer acts

as a hole acceptor to speed up water oxidation process. [27, 28-30] Furthermore, doping in ZnO has also found to improve the PEC activity of the same by introducing defects within the band gap which improves light absorption efficiency and carrier mobility. [10, 31-33] However, the uniform doping in materials could also enhance the probability of electron-hole recombination via the defect states introduced by dopants and as a result doping could effectively reduce the PEC performance of the electrodes.

In this context, we have attempted a novel technique and designed the only surface functionalized or surface doped (C, N, and S functionalized/doped) ZnO nanorods (NRs) arrays photoanode to achieve better visible light absorption, low electron-hole recombination, separated charge transport and photostability for enhanced water splitting. In photoelectrodes, only the outer surface is exposed to light illumination and it is also in direct contact with the electrolyte. Hence, by proper surface functionalization of the ZnO NRs with C, N and S dopants, it is possible to tune the light absorption property of the photoanodes. Furthermore, the surface engineering would also tune the band structure and induce band bending at the electrode-electrolyte interface. Most expectedly, the surface functionalization would also tailor the surface carrier density, defect states and eventually the carrier separation and mobility in the photoelectrodes. Finally, the unique one dimensional morphology of NRs having large surface area is an efficient platform for efficient solar light harvesting and photo-electrochemical reaction. Here, as expected the C, N and S surface engineered ZnO NRs photo-anodes, fabricated by solution deposition followed by wet chemical route, exhibit better visible solar light absorption for electron-hole pair generation, better carrier separation (reduced electron-hole recombination), enhanced charge conductivity/mobility and photo-stability boosting visible light photo-electrochemical property. Surface modification in ZnO also tunes the electronic structure changing the band position and band bending at electrode-electrolyte interface leading to low electrical resistance as well as fast charge transportation of the device boosting the PEC property. The study of the mechanism of inherent PEC characteristics of the photo-

anodes opens up a new possibility to effectively tune the solar water splitting property of the oxide semiconductors.

3.2 Experimental Section

3.2.1 Substrate and Reagents

FTO (fluorine doped tin oxide, Sigma Aldrich) substrate, Zinc acetate dihydrate ($\text{Zn}(\text{CH}_3\text{COO})_2 \cdot 2\text{H}_2\text{O}$), hexamethylenetetramine ($(\text{CH}_2)_6\text{N}_4$), ethyl alcohol ($\text{C}_2\text{H}_5\text{OH}$), thiourea ($\text{CH}_4\text{N}_2\text{S}$), urea ($\text{CO}(\text{NH}_2)_2$) and dextrose ($\text{C}_6\text{H}_{12}\text{O}_6$). All the chemicals are of analytical grade and were used without further purification.

3.2.2 ZnO NRs Synthesis

ZnO NRs were grown on the conducting surface of FTO substrate by two step aqueous chemical bath deposition method. At first, the FTO substrate was thoroughly cleaned by means of ultrasonication, respectively in acetone, ethanol, and DI water, for 10 minutes each. Afterwards, a seed layer of ZnO was deposited on the FTO glass substrate by spin coating (rpm \sim 2000, for 1 minute) of 0.1 M solution of zinc acetate, prepared in ethanol. This process was repeated for five times and after each deposition, the substrate was dried under IR lamp. Finally, the substrate was rinsed with ethanol followed by DI water and then dried in air flow before subjecting to heat treatment in air at 350°C for 2 hours. In the next step, the FTO substrate containing ZnO seed layer was immersed into a chemical bath containing an equimolar aqueous solution of zinc acetate (20 mM) and hexamethylenetetramine (20 mM) and was kept for 2 hours at 90°C, under continuous magnetic stirring to grow vertically aligned ZnO NRs. Then the sample was rinsed separately in alcohol and DI water for few minutes.

3.2.3 C, N and S Functionalization of ZnO NRs

The surface of the as prepared ZnO NRs arrays was functionalized with carbon, nitrogen, and sulphur. For carbon functionalization, the pristine ZnO NRs sample was dipped into 1 M aqueous dextrose solution for 24 hours. For nitrogen and sulphur functionalization, the pristine ZnO NRs samples were dipped into 1 M aqueous

solution of urea [34] and 1 M aqueous solution of thiourea [35] for 24 hours, respectively. Afterwards, all the samples were annealed separately at 450° C for 2 hours in an argon atmosphere. Fig. 3.1 shows the schematic illustration of the proposed method to synthesis surface functionalized ZnO NRs based electrodes.

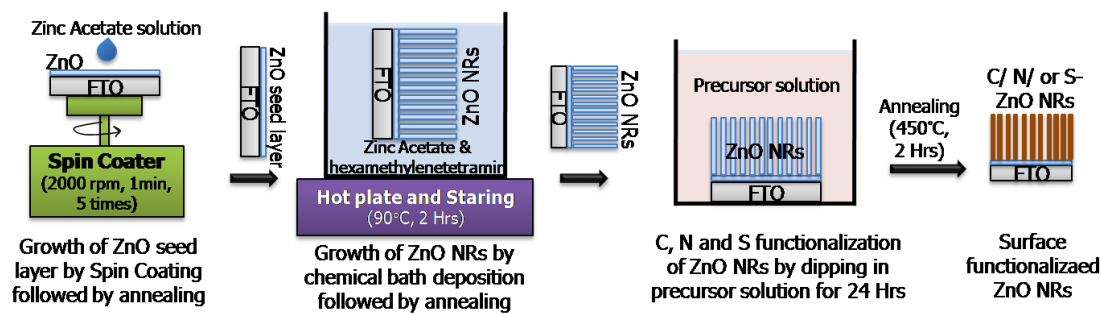


Figure 3.1: Schematic illustration for the synthesis of surface functionalized ZnO NRs.

3.2.4 Material Characterizations

The morphology and the superficial structure of the pristine ZnO NRs and the surface functionalized ZnO NRs were studied by the field emission scanning microscope (FESEM, JEOL JSM 7600F and FEI Quanta-200 Mark-2). The elemental composition of the samples was probed by the energy dispersive x-ray spectroscopy (EDS, Oxford Instruments and EDAX) equipped with the FESEM. The crystal structure of the materials were investigated by grazing incidence x-ray diffraction pattern (GIXRD, Panalytical X'Pert Pro diffractometer) using the Cu K_{α} line ($\lambda = 1.54 \text{ \AA}$) with a step size of 0.15° . The morphology and crystal structure of the NRs were also studied using a high resolution transmission electron microscope (HRTEM, JEOL JEM 2100). Besides, the ionic states and the chemical compositions of the samples were determined by x-ray photoelectron spectroscopy (XPS, VG Microtech VGX 900-W, beam line: Mg K_{α} , resolution 0.9 eV and vacuum level 2.2×10^{-10} mbar) analysis. The UV-Vis.-NIR absorption spectroscopy (Perkin Elmer Lambda 1050 UV/Vis spectrometer) and photoluminescence spectroscopy (PL, Horiba, FluoroLog-3) were also employed to study different electronic transition in the NRs.

3.2.5 Photoelectrochemical Measurements

Here, we were interested in visible light driven photo-electrochemical properties, for this purpose a visible light source ($\lambda > 420$ nm, intensity 10 mWcm^{-2}) was used and the linear sweep voltammetry (LSV), I-t amperometry, Mott-Schottky (MS), and electrochemical impedance spectroscopy (EIS) studies were performed with the help of a software controlled three electrode electrochemical workstation (CHI660E, CH Instruments). Here, the ZnO NRs samples on FTO was treated as the working electrode, platinum wire as the counter electrode and Ag/AgCl as the reference electrode in a cell containing $0.5 \text{ M Na}_2\text{SO}_4$ aqueous electrolyte of pH of 6.5.

LSV was measured in the potential window 1.4 V to 0 V at a scan rate 100 mVs^{-1} under the chopped light illumination and photo switching activity (I-t curve) of the samples were measured at a bias voltage 0.5 V vs. Ag/AgCl with consecutive on and off of the light source at a sensitivity of 10^{-3} AV^{-1} . EIS measurements were done in the frequency range of 1 MHz to 10 Hz with a dc voltage of 0 V vs. Ag/AgCl and MS were studied in a potential window -0.8 V to 0.4 V at 1 KHz frequency.

3.3 Results and Discussion

3.3.1 Morphology and Crystallography Study

The FESEM micrographs of the as prepared one dimensional dense array of ZnO and C, N and S surface functionalized ZnO NRs (C-ZnO, N-ZnO and S-ZnO), grown on FTO have been shown in Fig. 3.2 (a), (b), (c) and (d), respectively. The typical dimension of the NRs is about $75\text{-}80 \text{ nm}$. The as grown ZnO NRs have uniform hexagonal morphology which have deformed a bit after the surface functionalization processes. The GIXRD patterns of the samples, as shown in Fig. 3.2 (e), clearly indicate that the ZnO NRs are polycrystalline in nature, still the preferential growth direction of ZnO NRs is (002), which also suggest the hexagonal wurtzite structure of the ZnO NRs (JCPDS file #89-1397) with $P6_3mc$ space group symmetry. The TEM micrograph of the mechanically broken single ZnO NR is shown in Fig. 3.2(f), which again indicates that

the diameter of the NR is ~ 80 nm. The HRTEM image (Fig. 3.2 (g)) shows the highly crystalline structure of ZnO NRs where the spacing between adjacent lattice planes are 0.26 nm and 0.28 nm correspond to the distance between two (002) and (100) crystal planes of ZnO, respectively. The selected area electron diffraction (SAED) pattern obtained from the same area of measurement also clarifies the presence of (002) and (100) crystal planes of ZnO.

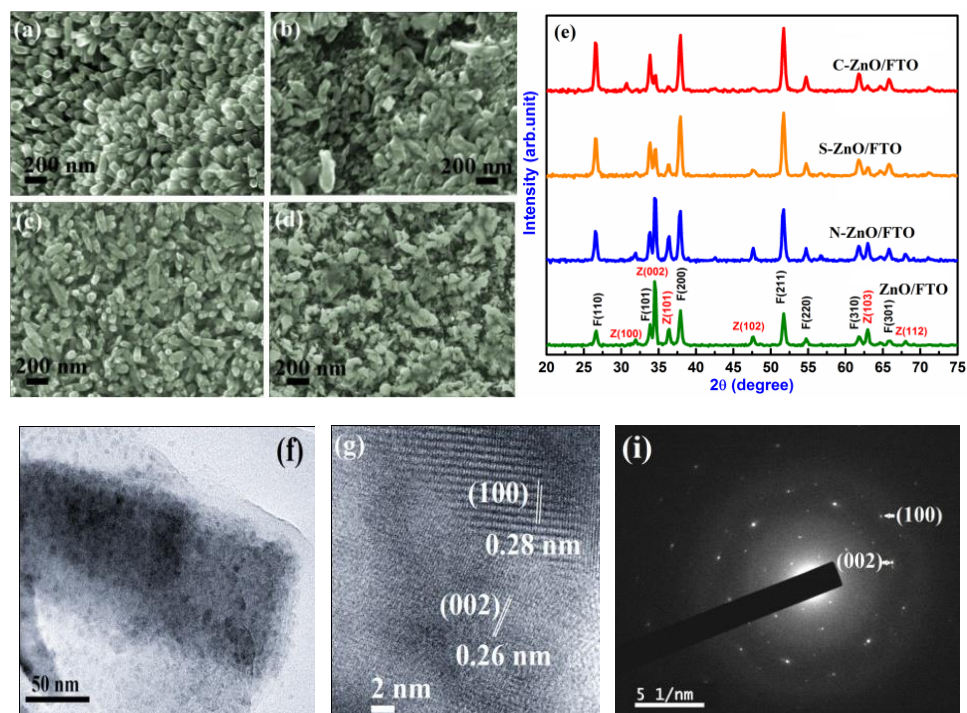


Figure 3.2: FESEM micrographs of the as prepared (a) ZnO, (b) C-ZnO, (c) N-ZnO and (d) S-ZnO NRs arrays. (e) XRD pattern of the NRs photoanodes. (f) TEM, (g) HRTEM and (i) SAED pattern of the as prepared ZnO NRs.

3.3.2 XPS Analysis

The surface sensitive XPS investigations have been conducted on the surface functionalized ZnO NRs to probe the chemical composition and the ionic states of the constituent elements of the C-ZnO, N-ZnO, and S-ZnO NRs. Figure 3.3(a) shows the high-resolution XPS spectrum of Zn 2p core level of ZnO NRs sample, which consists of a doublet positioned at 1044.91 and 1021.86 eV, having the energy difference of 23.05 eV between the two spin-orbit components, corresponds to Zn 2p_{1/2} and Zn 2p_{3/2} states in ZnO. [36, 37] Moreover, the binding energy values of Zn 2p spin-orbit components and their difference clearly indicate the +2 oxidation state of zinc.³⁶ The O 1s peak of ZnO NRs sample (shown in Fig. 3.3(b)) has been deconvoluted into two Gaussian peaks centered at 529.80 and 532.30 eV. The 529.80 eV peak corresponds to the -2 oxidation state of oxygen in Zn-O bond [38] while the 532.30 eV peak might be correlated to the presence of oxygen vacancies and/or OH⁻ species due to the adsorption of moisture at the material surface. [39, 40] Fig. 3.3(c) shows the multi-Gaussian curve fitted XPS spectrum of C 1s in the C-ZnO NRs sample. The peak centered at 284.8 eV represents the adventitious carbon and the sp³ hybridized carbon (C-C) due to the carbon functionalization. [41] The peak situated at 283.7 eV can be attributed to the Zn-C bond. [42] The peak located at 286 eV arises due to the Zn-O-C bond. [38-42] Multi-Gaussian fitting of the XPS spectrum of N 1s core level (Fig. 3.3(d)) shows four peaks positioned around 403.45, 400.80, 397.60, and 395.25 eV. The 403.45 eV peak may be attributed to N-N bonding. [43] The 400.80 peak generally represents to the N-H bonds which are supposed to be formed by the combination of acceptor nitrogen (N_O) and interstitial hydrogen atoms during the synthesis of N-ZnO nanowires in hydrogen-existing condition. [44, 45] While the 397.60 and 395.25 eV peaks correspond to N³⁻ in Zn-N bond. [44-46] The S 2p XPS spectrum, shown in Fig. 3.3(e), indicates a single distinct peak centered at 162.3 eV, which corresponds to Zn-S bonds of the S-ZnO NRs samples indicating the S doping at the surface of the ZnO NRs. [41]

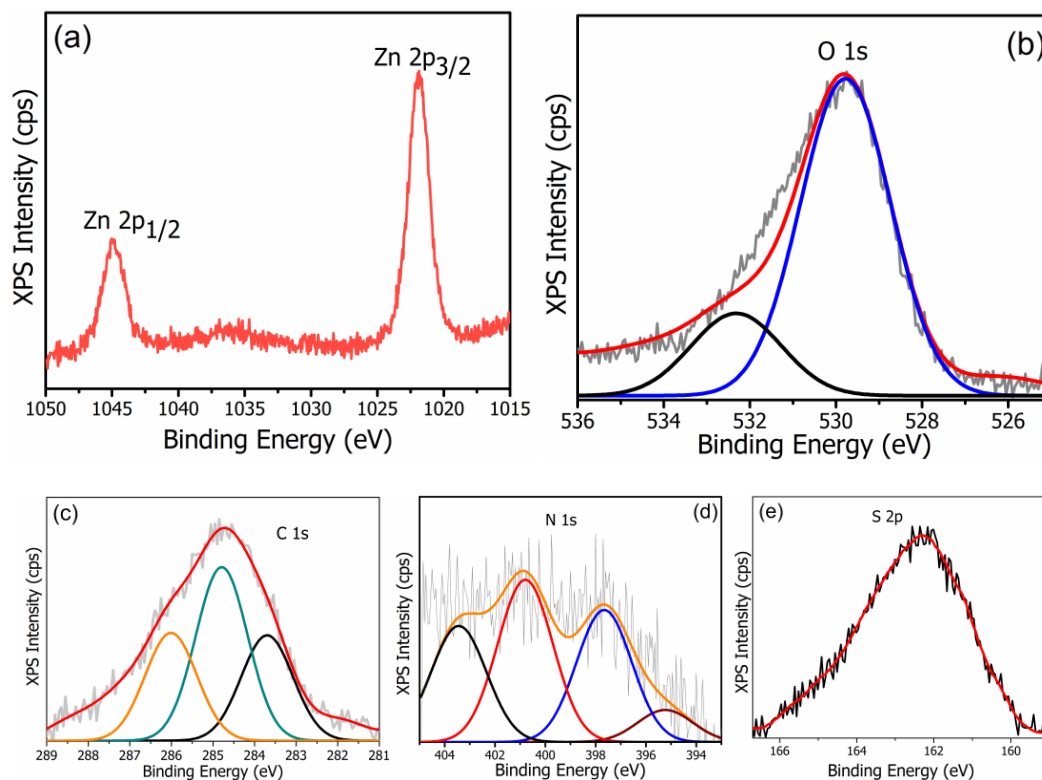


Figure 3.3: High-resolution XPS spectrum of the (a) Zn 2p of ZnO NRs, (b) O 1s of ZnO NRs, (c) C 1s of C-ZnO NRs, (d) N 1s of N-ZnO NRs and (e) S 2p of S-ZnO NRs.

3.3.3 Photoelectrochemical Performance

The visible light driven PEC water splitting/water oxidation performance of the arrays of ZnO, C-ZnO, N-ZnO and S-ZnO NRs grown on FTO has been subsequently tested in the PEC cell under light illumination ($10 \text{ mW}\cdot\text{cm}^{-2}$, wavelength $> 420 \text{ nm}$). Fig. 3.4(a) shows the representative chopped-light current density vs. potential (J - V) curves for various ZnO NRs based photoanodes obtained by linear sweep voltammetry (LSV) in the potential window of 1.4 to 0V at the scan rate of $100 \text{ mV}\cdot\text{s}^{-1}$. The increase in photocurrent density of the electrodes with the increase of positive applied bias, suggests the standard n -type nature of the electrode materials. In all these photoanodes, the increase in the photocurrent density with illumination suggests the photogeneration and conduction of carriers. The photocurrent densities of all surface functionalized ZnO NRs electrodes exhibit an enhancement compared to the pristine ZnO NRs arrays, which is ascribed to the increased visible light absorption due to surface

functionalization/doping, as evident from the adsorption studies conducted latter. The C-ZnO NRs photoanode is found to exhibit best PEC performance with a photocurrent density of $14.8 \mu\text{A}\cdot\text{cm}^{-2}$ at 0.3 V vs. Ag/AgCl, which is significantly (18 times) higher than that of the as prepared ZnO NRs arrays ($0.8 \mu\text{A}\cdot\text{cm}^{-2}$). The sharp increase in the photocurrent densities observed for C-ZnO and N-ZnO NRs compared with S-ZnO and pure ZnO NRs, in the whole potential scan range, clearly suggests the efficient charge separation in the C-ZnO and N-ZnO NRs upon illumination. Moreover, the photoresponse of the NRs photoanodes over time have been investigated by performing amperometric *I-t* studies. The *I-t* curves obtained from the different NRs photoanodes with visible-light on/off cycles at $10 \text{ mW}\cdot\text{cm}^{-2}$ at 0.5 V are shown in Fig. 3.4(b). Here the dark current is found to be as low as $0.2 \mu\text{A}\cdot\text{cm}^{-2}$. Upon the illumination of visible light on the C-ZnO, N-ZnO, and S-ZnO NRs the photocurrent is found to increase in a spike and reaches the steady state very quickly. The C-ZnO NRs shows the best photoresponse performance, whereas the pristine ZnO NRs exhibit the weakest photoresponse to visible-light. However, for the potential application of the photoanodes in PEC device, the stable operation of the photoanodes is a fundamental requirement. Herein, the stability of the photoanodes has been tested under light illumination for 3 hours (see Fig. 3.4(c)). At a bias voltage of 0.5 V vs. Ag/AgCl, the photocurrent of the bare ZnO NRs photoanode decreases by 19% during the first 3 hours, while the photocurrents for the C-ZnO, N-ZnO, and S-ZnO NRs are found to decrease by 4%, 7%, and 14%, respectively, after 3 hours of operation. Therefore, the surface functionalization/doping not only enhance the photocurrent density but also improve the stability of the photoanodes. Here, C and N functionalization clearly improves the stability of ZnO NRs remarkably. It is also interesting to notice that for C and N-ZnO NRs the photocurrent becomes completely stable within few seconds after the light illumination. Significantly the enhanced stability of the surface functionalized NRs is most likely due to efficient charge carrier separation and transport, which prevents the corrosion of the photoanodes upon the light illumination. [27] It is evident

that the surface engineering of ZnO NRs also leads to low onset potential for solar water splitting.

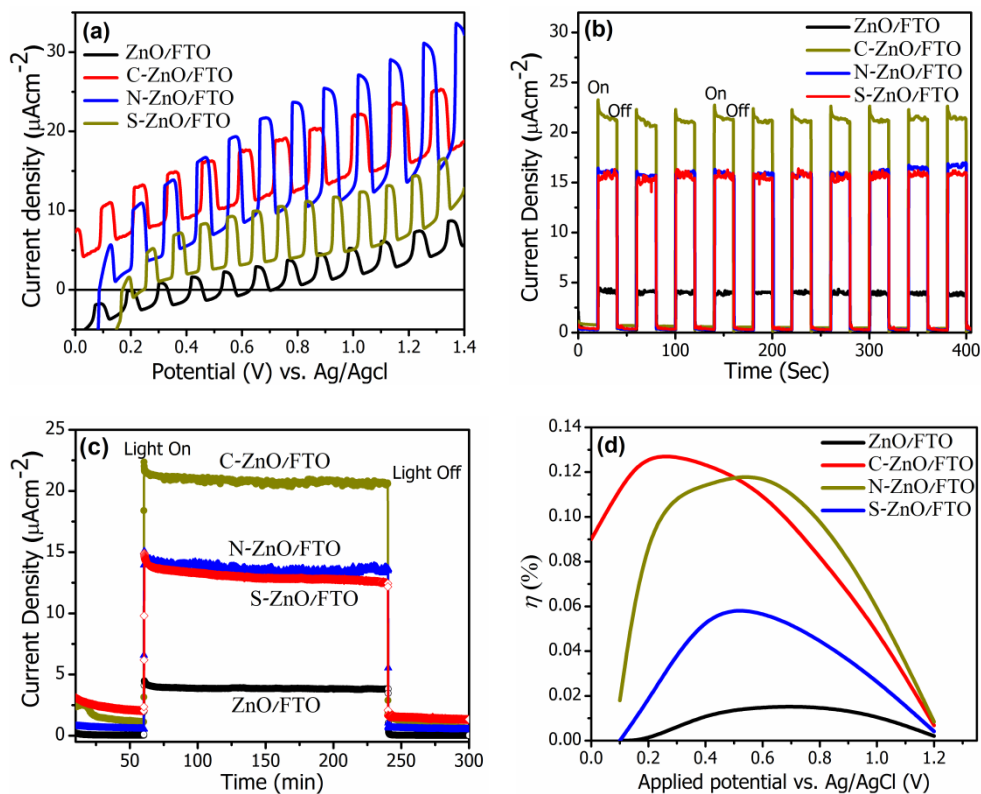


Figure 3.4: (a) Photocurrent densities vs. applied potential and (b) photocurrent density vs. time plot of the ZnO, C-ZnO, N-ZnO and S-ZnO NRs electrodes measured at 0.5 V vs. Ag/AgCl under chopped visible light illumination (10 mW. cm⁻², wavelength > 420 nm). (c) Photocurrent stability of different photoanodes measured at 0.5 V vs. Ag/AgCl. (d) Photoconversion efficiency of different photoanodes under same visible light illumination.

The PEC water splitting performance of the photoelectrodes are generally characterized based on their photoconversion efficiency (η%). [47] The photoconversion efficiency or solar-to-hydrogen (STH) efficiency of the photoelectrodes upon illumination of light is estimated by the following equation, [48]

$$\eta\% = \frac{J_{ph} \times (1.229 - V)}{P_{in}} \times 100\% \quad (3.1)$$

Where J_{ph} is the photocurrent density at measured bias, V is the applied potential vs. Ag/AgCl, P_{in} is the power of the illuminated light (10 mW. cm⁻²). STH efficiency as a function of the applied bias is plotted in Fig. 3.4(d). The as prepared ZnO NRs sample

exhibits an optimal conversion efficiency of 0.02% at 0.7 V vs. Ag/AgCl, whereas the optimal conversion efficiencies of S and N-ZnO NRs are 0.06 and 0.11%, respectively at 0.5 V vs. Ag/AgCl. The C-ZnO NRs photoanode exhibits the best photoconversion efficiency of 0.13% at a very low bias of 0.3 V vs. Ag/AgCl. It is evident that the surface functionalization of ZnO NRs substantially enhances the photoconversion efficiency by boosting the maximum photocurrent. However, at high current density, hydrogen and oxygen generation can be visualized in terms of the formation of gas bubbles at the Pt electrode and photoanodes, respectively. A comparative study on the performance of the surface functionalized ZnO NRs with other reported ZnO nanostructure based photoelectrodes have been summarized in Table 3.1. It is evident from Table 1 that the surface functionalized ZnO NRs exhibit enhanced STH efficiency.

For an in-depth understanding of the PEC process, the intrinsic electronic properties of the photoanodes including, electronic band structure, carrier density, charge carrier generation upon light illumination and carrier separation and transport and electrode-interface band bending have also been investigated. Electrochemical impedance measurements conducted on the ZnO and surface functionalized ZnO NRs electrodes in the dark provide an idea about the flat-band potentials (V_{fb}) obtained from the Mott-Schottky plots (Fig. 3.5(a)) using Mott-Schottky equation: [49-51]

$$\frac{1}{C_s^2} = \frac{2}{e\epsilon\epsilon_0 A^2 N_d} \left(V - V_{fb} - \frac{kT}{e} \right) \quad (3.2)$$

where C_s is space charge layer capacitance, e is the electronic charge, ϵ is the dielectric constant of the semiconductor; 10 for ZnO, [10] ϵ_0 is the permittivity of the free space, V is applied potential, V_{fb} is the flat band potential, A is the area of the electrode and kT/e is a temperature dependent correction term. Therefore, V_{fb} can be determined by setting $\frac{1}{C_s^2}$ to be zero, which is extrapolation of X-axis intercepts in the Mott-Schottky plots. The positive slope for all the photoanodes (Fig. 3.5(a)) indicates the n -type behavior of the semiconductors with electrons as majority charge carriers. The position of the V_{fb} of the different photoanodes indicates the position of the Fermi level of the semiconductor at the electrode-electrolyte interface. [50, 52] However, the values of the V_{fb} of different

photoanodes are summarized in Table 3.2, at a pH of 6.5 of the electrolyte. For the as prepared ZnO NRs the value of V_{fb} is -0.23 V vs. NHE, [52] where $E(\text{NHE}) = E(\text{Ag}/\text{AgCl}) + 0.197$ (unit in V). It is important to note that the position of V_{fb} strongly depends upon the experimental conditions (e.g., the frequency, pH of the electrolyte and other experimental parameters) [27, 53] as well as on the morphology, and even on the post-synthesis treatments of the photoanodes. [27] It is evident that the surface functionalization of ZnO NRs has shifted the bottom of the conduction band to more negative energy, where the C functionalization has shifted the flat band edge position remarkably. However, the band gaps (E_g) of the semiconductor photoanodes have been estimated from the analysis of the UV-Vis. absorption spectra as shown in Fig. 3.5(b) and the values of E_g are summarized in Table 3.2. Finally, the mapping of the energy band diagram (Fig. 3.5(c)) of the photoanodes have been performed based on the calculated values of the band gap energy and the data on band edge positions (V_{fb}) obtained from the PEC measurements. Moreover, the UV-Vis. absorption spectra of the photoanodes also provide information about the light absorption property of the electrodes. The surface functionalized ZnO NRs feature much higher visible light absorption than that of the pristine ZnO NR (Fig. 3.5 (b)), along with the sharp absorption edge in the UV region, which actually is the signature of band edge absorption. The UV region absorption edges of the different functionalized ZnO NRs are found to be red shifted compared to the pristine ZnO NR sample (381 nm for the pristine sample). Clearly, C-ZnO NRs exhibit significantly enhanced visible light absorption property among the photoanodes. It is evident that the surface functionalization/doping could introduce mid-bandgap defect states, which lead to the enhanced visible band absorption in the photoanodes. Furthermore, the unique aligned 1D morphology of the surface functionalized ZnO NRs might also boost the light-trapping efficiency. [27]

Table 3.1: Summary of the performance of some ZnO nanostructure based photoanodes.

Sample Name	Incident radiation	Efficiency
ZnO NRs ^[Present work]	Wavelength > 420 nm, 10 mW/cm ²	0.02%
N-ZnO NRs ^[Present work]	Wavelength > 420 nm, 10 mW/cm ²	0.11%
C-ZnO NRs ^[Present work]	Wavelength > 420 nm, 10 mW/cm ²	0.13%
S-ZnO NRs ^[Present work]	Wavelength > 420 nm, 10 mW/cm ²	0.06%
N-ZnO NWs ^[10]	AM 1.5 G, 100 mW/cm ²	0.15%
TiO ₂ shell on ZnO NWs ^[11]	AM 1.5 G, 100 mW/cm ²	0.09%
Branched ZnO NRs ^[28]	AM 1.5 G, 100 mW/cm ²	0.04%
Al-doped ZnO NWs ^[30]	AM 1.5 G, 100 mW/cm ²	0.04%
Li doped ZnO NWs ^[32]	AM 1.5 G, 100 mW/cm ²	0.17%
Nanostructured ZnO Thin Films ^[53]	AM 1.5 G, 100 mW/cm ²	0.10%

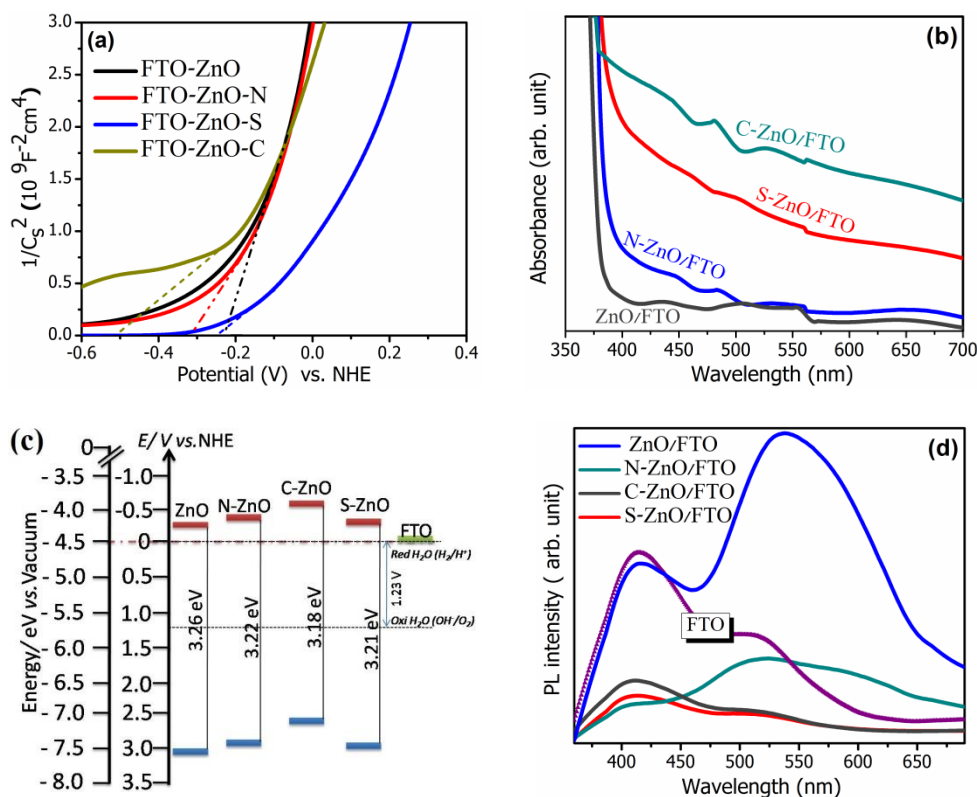


Figure 3.5: (a) Mott-Schottky plots for different photoanodes measured in 0.5 M Na_2SO_4 (pH 6.5) at 1 kHz. (b) UV-Vis. absorption spectra of ZnO, C-ZnO, N-ZnO and S-ZnO photoelectrodes. (c) Schematic of the band edge positions with respect to the vacuum level and the NHE for different photoanodes at pH 6.5, drawn using the measured values of flat band potential and band gap energy. (d) PL emission spectra of different photoelectrodes recorded under the excitation of 330 nm light.

The carrier density (N_d) of the photoanodes can also be estimated from the slope of the Mott-Schottky plots according to the following equation: [54]

$$N_d = \frac{2}{e\epsilon\epsilon_0 A^2} \frac{1}{d \left(\frac{1}{C_s^2} \right)} \frac{1}{dV} \quad (3.3)$$

The calculated carrier density values of different photoanodes are listed in Table 3.2. For the n -type semiconductors, the surface electron density (N_s) is found to decrease with the applied anodic potentials (V) as [55]

$$N_s = N_b \exp \left[-e \left(\frac{V - V_{fb}}{KT} \right) \right] \quad (3.4)$$

where, N_b is bulk electron density of the semiconductor electrode. It is evident from Table 3.2 that the surface functionalization has significantly enhanced the surface electron density of the C-ZnO, N-ZnO and S-ZnO/FTO photoanodes, as the surface functionalization can only tune the surface electronic structure of the semiconductors and cannot influence the bulk electron density in this work. It is obvious that the surface functionalization causes shifting of conduction band edge into more negative energy and introduces a large number of surface electrons for enhanced charge transport and also facilitates the electron transfer from the photoanode to the FTO substrate and counter electrode providing high performance toward hydrogen production. However, the relatively higher carrier density of the photoanodes (for ZnO in $\sim 10^{20} \text{ cm}^{-3}$) might be because of the contribution of FTO underneath.

Table 3.2: The flat band potential (E_{FB}), band gap (E_g) and the charge carrier density (N_d) of different ZnO NRs photoanodes.

Photoanode	V_{fb} (V) vs. NHE	Band gap (eV)	Carrier density (cm^{-3})
ZnO/FTO	-0.23	3.26	9.4×10^{20}
C-ZnO/FTO	-0.51	3.18	4.7×10^{21}
N-ZnO/FTO	-0.33	3.22	4.5×10^{21}
S-ZnO/FTO	-0.25	3.21	1.2×10^{22}

In order to further investigate the charge transfer and carrier recombination in the photoanodes, the photoluminescence (PL) emission property of the photoanodes have been studied. The PL emission spectra recorded at the excitation of 330 nm (Fig. 3.5(d)) exhibits two major peaks around 415 nm and 550 nm, respectively. The 415 nm peak is mostly associated with the FTO substrate underneath, whereas the ZnO NRs electrodes exhibit broad emission peak centered around 550 nm

related to defect emissions or oxygen vacancies. [56] It is obvious from Fig. 3.5(d) that the as prepared ZnO NRs show the strongest defect related emission, indicating large recombination of photo generated carriers in the pristine ZnO NRs. The intensities of the PL emission peaks centered at 550 nm for C-ZnO, S-ZnO, and N-ZnO NRs are found to decrease by 92%, 93%, and 76%, respectively, with respect to that of pure ZnO NRs, whereas the optical (visible light) absorption is found to decrease gradually (Fig. 3.5(b)) for C-ZnO, S-ZnO, and N-ZnO NRs. This quenching of luminescence of the surface functionalized ZnO NRs clearly demonstrates the significant reduction in electron-hole recombination in the photoanodes and also indicates towards the efficient charge carrier transportation to FTO from surface functionalized ZnO NRs. [27]

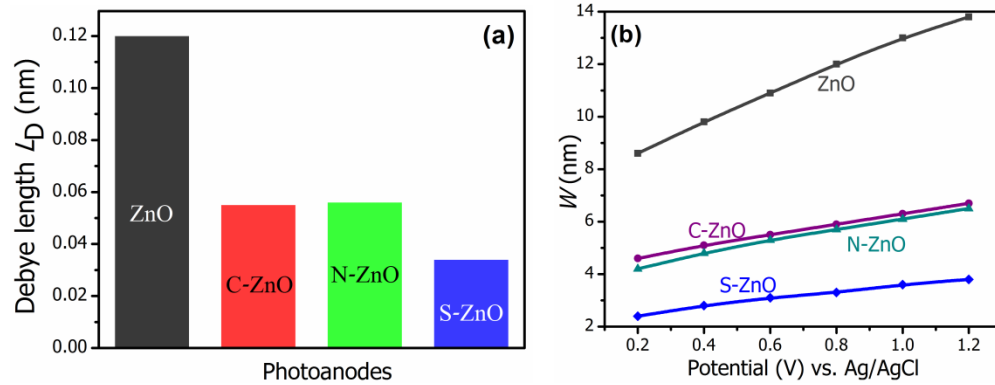


Figure 3.6: (a) Variation of Debye length in different photoanodes. (b) Variation of depletion layer width with potential vs Ag/AgCl for different photoanodes.

However, after having an idea about the probabilities of charge carrier recombination in these photoanodes, the charge carrier diffusion lengths i.e., Debye length, L_D , which is the length over which the local electric field affects the distribution of free charge carriers, for the electrodes have also been calculated according to the following equation: [57, 58]

$$L_D = \left(\frac{\epsilon \epsilon_0 kT}{e^2 N_d} \right)^{1/2} \quad (3.5)$$

Where, k is the Boltzmann constant (1.38×10^{-23} J K⁻¹) and T is the absolute temperature (K). The Debye length for different photoanodes is shown in Fig. 3.6(a), which clearly

demonstrates that the Debye length in semiconductor electrode decreases as the carrier density increases. Furthermore, the Schottky barrier model demonstrates that the charge carrier transit time through the depletion layer is proportional to the square of Debye length, [59] hence the shortest Debye length of S-ZnO NRs (Fig. 3.6(a)) indicates its lowest charge transit time through the depletion region for better electron-hole separation. It is also evident from the earlier PL study on S-ZnO NRs. The lower transit times in the surface functionalized samples compared to pristine ZnO NRs facilitate fast charge transport and better electron-hole separation in the surface modified samples, which in turn enhance their photo-electrochemical activity. Herein, the depletion region width (W) for each photoanode has also been plotted against different applied potentials (Fig. 3.6(b)) using the following equation: [10]

$$W = \left(\frac{2\epsilon\epsilon_0(V-V_{fb})}{eN_d} \right)^{1/2} \quad (3.6)$$

Assuming W to be very small compared to the dimension of the NRs, the potential drop ($\Delta\phi$) arising due to the separation of the charge carriers near the surface and subsurface layers within the NRs, may be expressed as: [60]

$$\Delta\phi = \frac{kTW^2}{2eL_d^2} \quad (3.7)$$

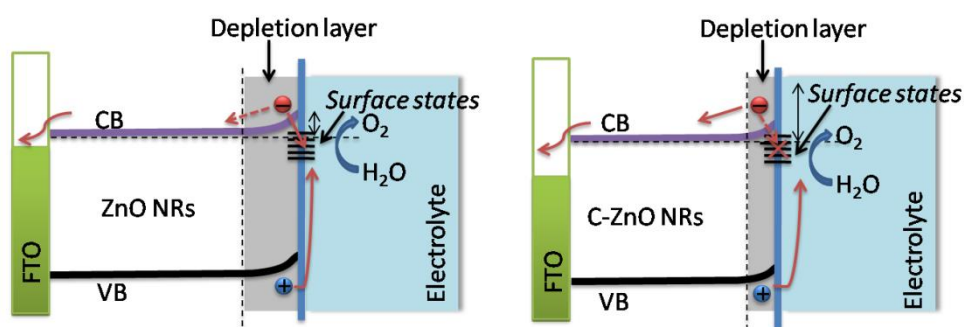


Figure 3.7: Schematic of the band alignment and the mechanism of charge separation/recombination and transfer processes in the pristine ZnO and C-ZnO NRs photoanodes in contact with the electrolyte.

Based on the above experimental results we can demonstrate the inherent mechanism of the enhanced photoelectrochemical property of the surface engineered ZnO NRs, as shown in Fig. 3.7. In pure ZnO NRs, low light absorption and high electron-hole recombination due to the presence of surface defects/states reduces its electrochemical efficiency. In the case of C-ZnO/FTO NRs electrode, it is found that it also exhibits best optical absorption among the photoanodes (evident from UV-Vis absorption study) and very low recombination of photo generated carriers (evident from PL study). Furthermore, the shift in the conduction band edge to more negative energy increases the band edge difference between C-ZnO and FTO and hence better charge carrier transportation from the photoanode to FTO. Hence, the excellent light absorption, low carrier recombination along with the fast transportation (mobility) of the photo generated carrier help the C-ZnO NRs photoanode to achieve enhanced STH efficiency. For S-ZnO NRs, the optical absorption is higher than N-ZnO and the recombination of the photo generated carriers in S-ZnO NRs is lower than N-ZnO NRs. Still, the STH efficiency of the S-ZnO NRs is found to be poor compared with N-ZnO NRs, which is most expectedly because of the better electron transportation from N-ZnO NRs to FTO compared with that of S-ZnO NRs to FTO, which might resist the proper carrier separation and mobility in the S-ZnO NRs photoanode, reducing its photo-electrochemical activity.

Furthermore, the electrochemical impedance spectroscopy (EIS) measurements on the ZnO NRs based electrodes have also been conducted under light illumination in order to study the charge transfer process of photoanode-electrolyte interface. Fig. 3.8(a) shows the Nyquist plots of the pure and surface functionalized ZnO NRs photoanodes, plotted at a bias of 0 V vs Ag/AgCl over the frequency range of 10 Hz to 100 kHz, and the inset of Fig. 3.8(a) represents the equivalent circuit fitted with a resistance-capacitance (RC) model to estimate the resistance parameters of the device. In the equivalent circuit, R_s represents the equivalent series resistance of the devices, which is calculated and plotted in Fig. 3.8(b). [61] It is found that the C-ZnO NRs device exhibits

the lowest R_s value, indicating good overall conduction of the photoanode. Here, R_{ct} represents the charge transfer resistance of the photoanodes (Fig. 3.8(b)). It is known that the arc diameter (calculated based on the fitted curves) in Nyquist plot represents the charge transfer at the interface between photoelectrode and the electrolyte. [62] The reduction of the arc diameter in EIS Nyquist plot indicates efficient charge transfer at the electrode-electrolyte interface. Here, R_{ct} of the photoanodes are plotted in Fig. 3.8(b), which clearly indicates the best charge transfer property of the C-ZnO NRs photoanode followed by N-ZnO, S-ZnO, and pure ZnO NRs. The charge transfer property of ZnO NRs is poorest amongst the photoanodes. This study suggests that the surface functionalization significantly improves the charge transfer at the semiconductor electrode/electrolyte interface.

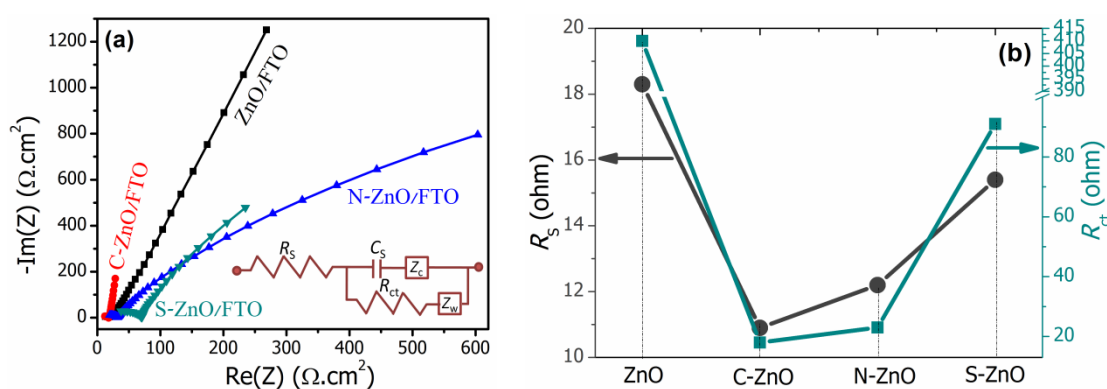


Figure 3.8: (a) Nyquist plots for the ZnO, C-ZnO, N-ZnO and S-ZnO NRs photoanodes. Inset of (a): shows the equivalent circuit fitted resistance and capacitance to estimate the resistance parameters of the device. (b) Variation of the equivalent series resistance (R_s) and charge transfer resistance (R_{ct}) of different photoanodes.

3.4 Conclusion

In summary, highly dense vertical arrays of pure and C, N, and S surface functionalized/doped ZnO NRs have been successfully fabricated on the conducting FTO surface by a facile aqueous chemical bath deposition followed by wet chemical method. The visible light driven photoelectrochemical activity in terms of solar water

splitting property of the surface engineered ZnO NRs photoanodes has been found to enhance remarkably along with the significant reduction in onset potential for water oxidation. The photocurrent densities of C-ZnO, N-ZnO and S-ZnO NRs photoanodes are 14.8, 13 and 6 $\mu\text{A cm}^{-2}$ (at 0.3 V vs. Ag/AgCl, 0.5 M Na_2SO_4 solution, 10 mW. cm^{-2} , wavelength >420 nm), which are 18, 16, and 7 times higher than that of pristine ZnO NRs ($0.8 \mu\text{A cm}^{-2}$), respectively. The photoconversion efficiency of the C-ZnO, N-ZnO, and S-ZnO NRs photoanodes are 0.13%, 0.11% and 0.06% which are 6.5, 5.5 and 3 times higher than that of pure ZnO NRs (0.02%) measured under the light illumination of 10 mW cm^{-2} with wavelength >420 nm. Interestingly the photoresponse of the surface functionalized ZnO NRs photoanodes is found to enhance significantly, where for C and N-ZnO NRs the photocurrent becomes completely stable within few seconds after the light illumination. After the first three hours of operation at a bias of 0.5 V vs. Ag/AgCl the photocurrent of the bare ZnO NRs photoanode is found to decrease by 19%, whereas the photocurrent for the C-ZnO and N-ZnO NRs decreases by 4% and 7% only, which suggests better stability of the surface functionalized electrodes for highly efficient PEC water oxidation. The excellent performance of the surface functionalized ZnO NRs toward PEC water splitting is mainly because of the enhanced visible light absorption and superior charge separation (low electron-hole recombination) coupled with high surface charge carrier density and greatly facilitated charge transfer and transport properties. Studies indicate that the surface functionalization significantly shifts the bottom edge of the conduction band of the photoanodes to the more negative energy region along with the greatly reduction of the depletion layer width causing effective the band bending at electrode-electrolyte interface boosting the charge carrier separation. Surface functionalization also reduces the Debye length of the semiconductor considerably along with the remarkable decrease in charge transfer resistance, helping to achieve better PEC property. Therefore, this present study not only demonstrates a facile approach of surface functionalization for highly efficient PEC water oxidation but also investigates insights into the mechanism of the photoelectrochemical process in these photoanodes, which highlights a general

approach to boost the water splitting based on semiconductor photoanodes. The comparative study demonstrates that the C-functionalization on ZnO NRs is most effective for the enhancement of PEC properly followed by N and S functionalization.

Bibliography

- [1] K. Karmakar, A. Sarkar, K. Mandal, and G. G. Khan, *ACS Sustainable Chem. Eng.* **4**, 5693 (2016).
- [2] A. Fujishima, K. Honda, *Nature*, **238**, 37 (1972).
- [3] M. Pagliaro, A. G. Konstandopoulos, R. Ciriminna, G. Palmisano, *Energy Environ. Sci.*, **3**, 279 (2014).
- [4] H. B. Gray, *Nat. Chem.*, **1**, 7 (2009).
- [5] R. Liu, Z. Zheng, J. Spurgeon, B. S. Brunschwig, X. Yang, *Energy Environ. Sci.*, **7**, 2504 (2014).
- [6] A. Listorti, J. Durrant, J. Barber, *Nat. Mater.* **8**, 929 (2009).
- [7] A. Nozik, *J. Annu. Rev. Phys. Chem.* **29**, 189 (1978).
- [8] K. Sivula, F. L. Formal, M. Grätzel, *ChemSusChem* **4**, 432 (2011).
- [9] J. Zhang, X. Jin, Guzman, M. P. I. X. Yu, H. Liu, H. Zhang, L. Razzari, J. P. Claverie, *ACS Nano*, **10**, 4496 (2016).
- [10] X. Yang, A. Wolcott, G. Wang, A. Sobo, R. C. Fitzmorris, F. Qian, J. Z. Zhang, Y. Li, *Nano Lett.* **6**, 9, 2331 (2009).
- [11] M. Liu, C. -Y. Nam, C. T. Black, J. Kamcev, L. Zhang, *J. Phys. Chem. C* **117**, 13396 (2013).
- [12] M. M. Momeni, M. Hakimian, A. Kazempour, *Surface Engineering* **32**, 514 (2016).
- [13] M. M. Momeni, Y. Ghayeb, *Journal of Alloys and Compounds*, **637**, 393 (2015).
- [14] M. M. Momeni, Y. Ghayeb, M. Davarzadeh, *Journal of Electroanalytical Chemistry* **739**, 149 (2015).
- [15] M. M. Momeni, Y. Ghayeb, *Journal of Electroanalytical Chemistry* **751**, 43 (2015).
- [16] M. M. Momeni, Y. Ghayeb, *J Mater Sci: Mater Electron* **27**, 3318 (2016).
- [17] M. M. Momeni, Y. Ghayeb, *J. Appl. Electrochem* **45**, 557 (2015).
- [18] M. M. Momeni, Y. Ghayeb, *J. Solid State Electrochem* **20**, 683 (2016).
- [19] M. M. Momeni, Y. Ghayeb, *Appl. Phys. A* **122**, 620 (2016).
- [20] M. M. Momeni, *Mater Res Innov* **20**, 317 (2016).

-
- [21] M. M. Momeni, I. Ahadzadeh, *Mater Res Innov* **20**, 44 (2016).
- [22] M. M. Momeni, Y. Ghayeb, Z. Ghonchehi, *Ceramics International* **41**, 8735 (2015).
- [23] A. Bard, M. Fox, *Acc. Chem. Res.* **28**, 141 (1995).
- [24] J. Tang, J. R. Durrant, D. R. Klug, *J. Am. Chem. Soc.* **130**, 13885 (2008).
- [25] Z. Zhang, L. Zhang, M. N. Hedhili, H. Zhang, P. Wang, *Nano Lett.* **13**, 14 (2013).
- [26] Y.-K. Hsu, Y.-C. Chen, Y.-G. Lin, *ACS Appl. Mater. Interfaces*, **7**, 14157 (2015)
- [27] S. J. A. Moniz, J. Zhu, J. Tang, *Adv. Energy Mater.* **4**, 1301590 (2014)
- [28] Y. Qiu, K. Yan, H. Deng, S. Yang, *Nano Lett.* **12**, 407 (2012)
- [29] R. Liu, Z. Zheng, J. Spurgeon, X. Yang, *Energy Environ. Sci.*, **7**, 2504 (2014)
- [30] Y. -F. Xu, H. -S. Rao, X. -D. Wang, H. -Y. Chen, D. -B. Kuang, C. -Y. Su, *J. Mater. Chem. A*, **4**, 5124 (2016)
- [31] L. Zhang, E. Reisner, J. J. Baumberg, *Energy Environ. Sci.*, **7**, 1402 (2014)
- [32] H. J. Lee, S.-H. Shin, K. T. Nam, J. Nah, M. H. Lee, *J. Mater. Chem. A*, **4**, 3223 (2016)
- [33] M. Wang, F. Ren, J. Zhou, G. Cai, L. Cai, Y. Hu, D. Wang, Y. Liu, L. Guo, S. Shen, *Scientific Reports* **5**, 12925 (2015)
- [34] J. J. Macías-Sánchez, L. Hinojosa-Reyes, A. Caballero-Quintero, W. de la Cruz, E. Ruiz-Ruiz, A. Hernández-Ramírez, J. L. Guzmán-Mar, *Photochem. Photobiol. Sci.* **14**, 536 (2015)
- [35] J. Cho, Q. Lin, S. Yang, J. G. Simmons Jr., Y. Cheng, E. Lin, J. Yang, J. V. Foreman, H. O. Everitt, W. Yang, J. Kim, J. Liu, *Nano Res.* **5**, 20 (2012)
- [36] S. Ghosh, G. G. Khan, S. Varma, K. Mandal, *J. Appl. Phys.* **112**, 043910 (2012)
- [37] C. D. Wagner, W. M. Riggs, L. E. Davis, J. F. Moulder, G. E. Muilenberg, *Handbook of X-ray Photoelectron Spectroscopy*, edited by G. E. Muilenburg (Perkin Elmer, Eden Prairie, (1979)
- [38] X. Zhang, J. Qin, R. Hao, L. Wang, X. Shen, R. Yu, S. Limpanart, M. Ma, R. Liu, *J. Phys. Chem. C*, **119**, 20544 (2015)
- [39] B. Yang, P. Feng, A. Kumar, R. S. Katiyar, M. Achermann, *J. Phys. D: Appl. Phys.* **42**, 195402 (2009)

-
- [40] T. Ghoshal, S. Biswas, S. Kar, A. Dev, S. Chakrabarti, S. Chaudhuri, *Nanotechnology*, **19**, 065606 (2008)
- [41] National Institute of Standards and Technology (NIST), Gaithersburg, x-ray Photoelectron Spectroscopy Database, Version 4.1 (2012); <http://srdata.nist.gov/xps>
- [42] A.S. Alshammari, L. Chi, X. Chen, A. Bagabas, D. Kramer, A. Alromaeha, Z. Jiang, *RSC Adv.* **5**, 27690 (2015)
- [43] G. Wang, X. Xiao, W. Li, Z. Lin, Z. Zhao, C. Wang, Y. Li, X. Huang, L. Miao, C. Jiang, Y. Huang, X. Duan, *Nano Lett.* **15**, 4692 (2015)
- [44] A. P. Bhirud, S. D. Sathaye, R. P. Waichal, L. K. Nikama, B. B. Kale, *Green Chem.*, **14**, 2790 (2012)
- [45] J. Gao, X. Zhang, Y. Sun, Q. Zhao, D. Yu, *Nanotechnology*, **21**, 245703 (2010)
- [46] F. Zong, H. Ma, C. Xue, W. Du, X. Zhang, H. Xiao, J. Ma, F. Ji, *Materials Letters*, **60**, 905 (2006)
- [47] Z. Li, W. Luo, M. Zhang, J. Feng, Z. Zou, *Energy Environ. Sci.* **6**, 347 (2013)
- [48] G. Wang, H. Wang, Y. Ling, Y. Tang, X. Yang, R. C. Fitzmorris, C. Wang, J. Z. Zhang, Y. Li, *Nano Lett.* **11**, 3026 (2011)
- [49] M. S. Prévot, N. Guijarro, K. Sivula, *ChemSusChem.*, **8**, 1359 (2015)
- [50] M. Ongaro, A. Mardegan, A. M. Stortini, M. Signoretto, P. Ugo, *Nanotechnology*, **26**, 165402 (2015)
- [51] Y. Ma, S. R. Pendlebury, A. Reynal, F. L. Formal, J. R. Durrant, *Chem. Sci.*, **5**, 2964 (2014)
- [52] M. A. A. Aviles, Wu. Y., *J. Am. Chem. Soc.* **131**, 3216 (2009)
- [53] A. Wolcott, W. A. Smith, T. R. Kuykendall, Y. Zhao, J. Z. Zhang, *Adv. Funct. Mater.* **19**, 1849 (2009)
- [54] M. Ye, J. Gong, Y. Lai, C. Lin, Z. Lin, *J. Am. Chem. Soc.* **134**, 15720 (2012)
- [55] M. K. Nazeeruddin, A. Kay, I. Rodicio, R. H. Baker, E. Muller, P. Liska, N. Vlachopoulos, M. Gratzel, *J. Am. Chem. Soc.* **115**, 6382 (1993)
- [56] W. I. Park, D. H. Kim, S. -W. Jung, G. -C. Yi, *Appl. Phys. Lett.* **80**, 4232 (2002)

- [57] C. Fabrega, D. M. Satoca, S. Ampudia, A. Parra, T. Andreu, J. R. Morante, *J. Phys. Chem. C* **117**, 20517 (2013)
- [58] W. Yuan, J. Yuan, J. Xie, C. M. Li, *ACS Appl. Mater. Interfaces* **8**, 6082 (2016)
- [59] X. Wang, J. Xie, C. M. Li, *J. Mater. Chem. A* **3**, 1235 (2015)
- [60] A. Hagfeldt, M. Gratzel, *Chem. Rev.* **95**, 49 (1995)
- [61] B. Klahr, S. Gimenez, F. F. Santiago, T. Hamann, J. Bisquert, *J. Am. Chem. Soc.*, **134**, 4294 (2012)
- [62] Y. -F. Xu, H. -S. Rao, X. -D. Wang, H. -Y. Chen, D. -B. Kuang, C.-Y. Sua, *J. Mater. Chem. A*, **4**, 5124 (2016).

Chapter 4

Photoelectrochemical Properties of Alkali Metal (Li, Na and K) Doped ZnO Nanorods Photoanodes

The photoelectrochemical properties of alkali metals (Li, Na and K) doped ZnO nanorods array photoanodes, synthesized by chemical bath deposition process have been demonstrated in this chapter. The significance of defect engineering because of doping of alkali metals (Li, Na and K) on the visible light driven photoelectrochemical properties of doped ZnO nanorods has been investigated.

A part of this content of this chapter has been published in the journal of *ChemElectroChem* [1] and is reproduced herein with permission from Wiley Publication.

4.1 Preamble

Generation of solar fuels and direct conversion of solar energy into electricity by photoelectrochemical (PEC) cell are the remarkable green approaches to harvest renewable energy. [2, 3] The naturally abundant metal oxide semiconductors have shown immense potential for energy conversion in PEC cell. Among various oxide semiconductors, ZnO has been extensively investigated as photoanode for PEC water splitting because of its favourable band-edge positions, superior chemical and thermal stability, relatively higher exciton binding energy of ~ 60 meV which is higher than the room temperature thermal energy (kT), non-toxicity and low cost. [4, 12] Still, the overall photoconversion efficiency of ZnO is considerably inadequate because of its large band gap energy, poor visible light absorption, low carrier separation efficiency, higher recombination rate of the photogenerated electron-hole pairs and sluggish carrier transport. [6, 9, 13-16] Proper defect engineering can provide a suitable solution to overcome these limitations. Recently, tuning of oxygen-vacancy defects present in various oxide semiconductors like In_2O_3 , Fe_2O_3 , BiVO_4 , WO_3 and TiO_2 have been found to have a dominating role to enhance their photoelectrochemical properties. [17-22] Oxygen-vacancies in oxides, reportedly improve the solar light harvesting efficiency through narrowing the bandgap and enhancing the electron conductivity. [17, 19, 21, 23] The surface oxygen-vacancies present within the bandgap can also contribute in photocurrent, providing photogenerated carriers to the conduction band under illumination [5, 22, 24, 26] and also increase the carrier lifetime serving as the active sites for electron trapping to improve the carrier separation and transportation. [17, 18, 21, 27, 28] Furthermore, it is also reported that the introduction of lattice strain defects in oxides matrix can tune their electronic structure, favouring fast charge/ion transportation and mobility. [29] Therefore, it is obvious that the defect engineering has a crucial role in tailoring the PEC property of oxides.

In this backdrop, key focus of this work is to investigate the role of oxygen-vacancies and lattice strain defects on photoelectrochemical property of alkali metal (Li, Na and K) doped ZnO NRs for the improvement of their PEC performance. It has

already been reported by our group that the group-IA alkali metals such as Li, Na and K effectively create sub-bandgap defect states in ZnO and their solubility in ZnO host lattice varies significantly with their ionic radii. [30] The density functional theory (DFT) study also indicates that the electronic properties of ZnO nanotubes are highly sensitive to the group-IA alkali metal doping and increases the work function of ZnO nanotubes. [31] Hence, various intrinsic properties of ZnO, such as electronic, optoelectronic and magnetic properties, which depend on the defect states, can be easily manipulated by the proper doping of these alkali metals. Although the defect mediated physical and chemical properties of ZnO have been studied for a long time, still the role of oxygen-vacancies on its photoelectrochemical properties have not been investigated properly, to the best of our knowledge. Recently, it has been reported that the incorporation of lower valence ions replacing Zn ions introduces holes in ZnO matrix and therefore, oxygen vacancies are formed spontaneously leaving two electrons to compensate the hole formation. [32-38] Following this, here monovalent alkali-metal doped 1D ZnO NRs are fabricated by easy, scalable and economic wet chemical route, expecting tuning of the oxygen-vacancies in ZnO. Moreover, the lattice strain developed in ZnO because of the dopants is also expected to modify the electronic structure of the material. Here, the as prepared ultrathin 1D nanostructure also provide large surface area for enhanced light absorption because of light scattering by nanostructures resulting enhanced PEC reactions. Moreover, the NRs are also expected to offer large surface oxygen-vacancies and short diffusion path for photogenerated holes for water oxidation. [22] Here, alkali metal doping is found to increase the oxygen-vacancies in ZnO NRs remarkably, where the oxygen-vacancies act as absorption sites for the visible light boosting the photo-induced carrier generation and enhanced PEC property. Furthermore, oxygen-vacancies also serve as the active sites for charge trapping, preventing recombination of photogenerated electron-hole pairs in the valence band resulting in an enhanced hole migration for water oxidation. This study demonstrates that the incorporation of alkali metal ions also promote the interfacial band bending of the electrodes resulting efficient electron transportation required for enhanced photoelectrochemical activity.

4.2 Experimental Section

4.2.1 Chemicals and Materials

FTO (fluorine doped tin oxide, Sigma Aldrich) substrate having surface sheet resistance value $\sim 7 \Omega/\text{cm}^2$, zinc acetate dihydrate ($\text{Zn}(\text{CH}_3\text{COO})_2 \cdot 2\text{H}_2\text{O}$, Loba Chemie), hexamethylenetetramine ($(\text{CH}_2)_6\text{N}_4$, Loba Chemie), ethyl alcohol ($\text{C}_2\text{H}_5\text{OH}$, Tedia), sodium acetate (CH_3COONa , Merck), potassium acetate (CH_3COOK , Merck), lithium acetate (CH_3COOLi , Merck). All the chemicals are of analytical grade and were used without further purification.

4.2.2 ZnO NRs Synthesis

ZnO NRs array was synthesized on the conducting surface of FTO glass substrate by a simple two-step bath chemical deposition process which was described in chapter 3 (Experimental Section).

4.2.3 Doped ZnO NRs Synthesis

For the synthesis of Li, Na and K doped ZnO NRs, their respective precursor, 20 mM lithium acetate, 20 mM sodium acetate and 20 mM potassium acetate were added to the aqueous solution of 20 mM zinc acetate and 20 mM hexamethylenetetramine. The same chemical bath process was carried out at 90°C for 2 h under continuous magnetic stirring to fabricate the alkali doped ZnO NRs on the conducting face of the FTO substrate having ZnO seed layer on it. Finally, all these samples were rinsed in ethanol and DI water separately for 20 min to remove the residuals from the samples and dried under the IR irradiation. Finally the samples were separately annealed at 600°C for 2 h in air.

4.2.4 Material Characterizations

The crystal structure of the samples was investigated by grazing incidence X-Ray diffraction pattern (GIXRD, Panalytical X'pert Pro diffractometer), obtained using a Cu

K_{α} line ($\lambda=1.54 \text{ \AA}$) with step size 0.15° . The morphology and geometrical dimension of the samples were investigated by field emission scanning electron microscopy (FESEM, FEI Quanta 200) and elemental composition were found by analysing energy dispersive X-ray spectroscopy (EDS), equipped with the FESEM. Finally the ionic states of the constituent elements were found by the X-ray photoelectron spectroscopy (XPS, Omicron Multiprobe Electron Spectroscopy System XM 500, X-ray source: monochromatic Al K_{α} line and vacuum level 2.5×10^{-10} mbar). Room temperature photoluminescence (PL) emission spectra of the samples were collected from Horiba Fluorolog-3 spectrofluorometer and the absorption edges of the samples were determined from the room temperature UV-Vis-NIR absorption study (Perkin Elmer, Lamda 1050 UV/Vis spectrometer).

4.2.5 Photoelectrochemical Studies

For the photoelectrochemical measurements, a software controlled three-electrode electrochemical workstation (CH Instruments, CHI660E) was used. The as prepared NRs samples were used as the working electrode, while a highly pure platinum wire and an Ag/AgCl were used as the counter and the reference electrode, respectively. All the electrochemical and photoelectrochemical measurements were carried out with an aqueous electrolytic solution of 0.5 M Na_2SO_4 , having pH 6.5. The linear sweep voltametry (LSV) measurement for each of the as prepared NRs samples was performed within a voltage range of 0 to 1.4 V, at a scan rate of 100 mV.s^{-1} with chopped visible light illumination (wavelength $> 420 \text{ nm}$ and intensity 10 mW.cm^{-2}). Each photo-switching activity was measured at an applied bias of 0.5 V vs. Ag/AgCl. The Mott-Schottky (MS) measurements were performed in a potential range of -0.8 V to 0.2 V vs. NHE at the frequency of 1 kHz.

4.3 Results and Discussion

4.3.1 Morphology and Structural Analysis

Top view FESEM images of the dense arrays of pristine ZnO, Li-ZnO, Na-ZnO and K-ZnO NRs grown on FTO by a facile two-step aqueous chemical process are shown in Fig. 4.1(a)-(d), respectively. All the as prepared NRs have hexagonal structure with diameter varying in between ~80-90 nm. However, the perfect hexagonal morphology of the ZnO NRs is found to get deformed slightly because of doping.

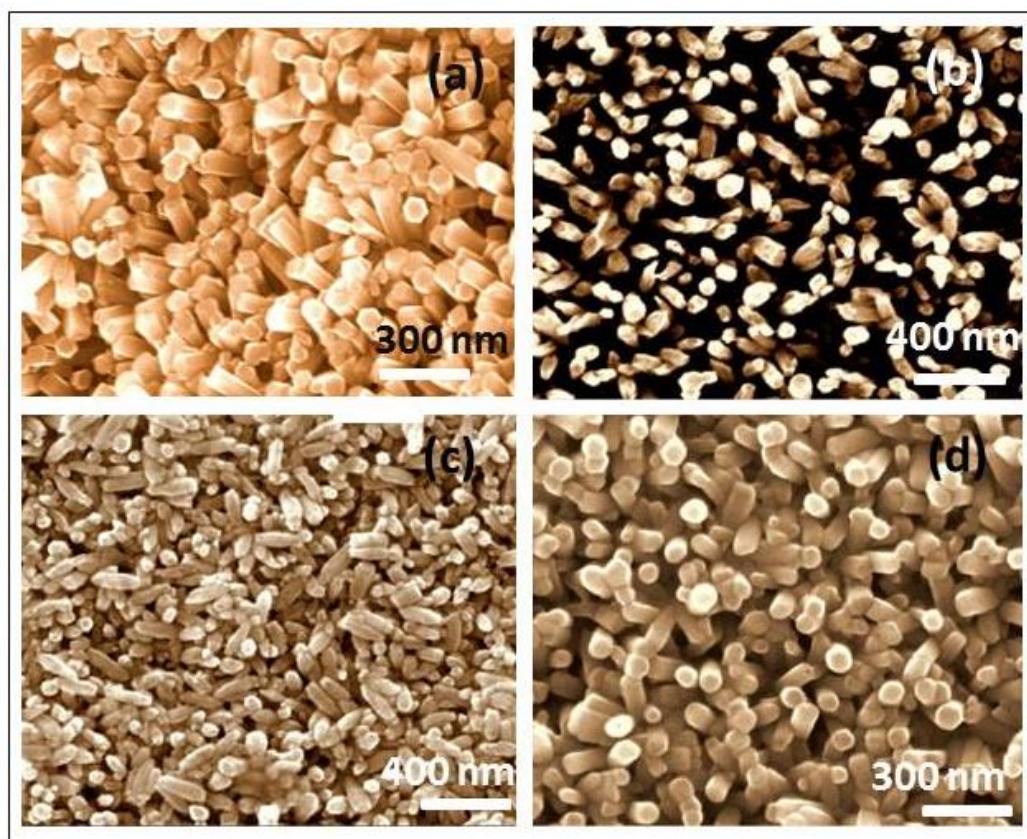


Figure 4.1: FESEM micrographs of (a) ZnO, (b) Na-ZnO, (c) Li-ZnO and (d) K-ZnO NRs.

XRD pattern (Fig. 4.2(a)) clearly indicates that (002) is the preferred growth direction of the NRs which have hexagonal wurtzite structure. The similar diffraction patterns for pristine and doped NRs indicate that no additional phase was introduced because of the doping. However, magnified view of the (002) diffraction peaks (Fig.

4.2(b)) for all the samples shows shifts in the peak positions for the doped ZnO NRs compared to the pristine ZnO NRs, which indicate insertion of alkali ions in ZnO host. The micro-strain developed in the host material because of the mismatch in the ionic radii of the host and dopants, is calculated based on the Williamson-Hall (W-H) method: [39, 40]

$$\varepsilon = \frac{\beta_{hkl}}{4 \tan \theta} \quad (4.1)$$

where, β_{hkl} is the full width at half maxima for a particular diffraction peak and 2θ is the position of the diffraction peak in XRD pattern. This calculation indicates that the lattice strain in the ZnO NRs increases because of alkali-doping (Fig. 4.2(b)), where K-ZnO NRs develops largest lattice strain.

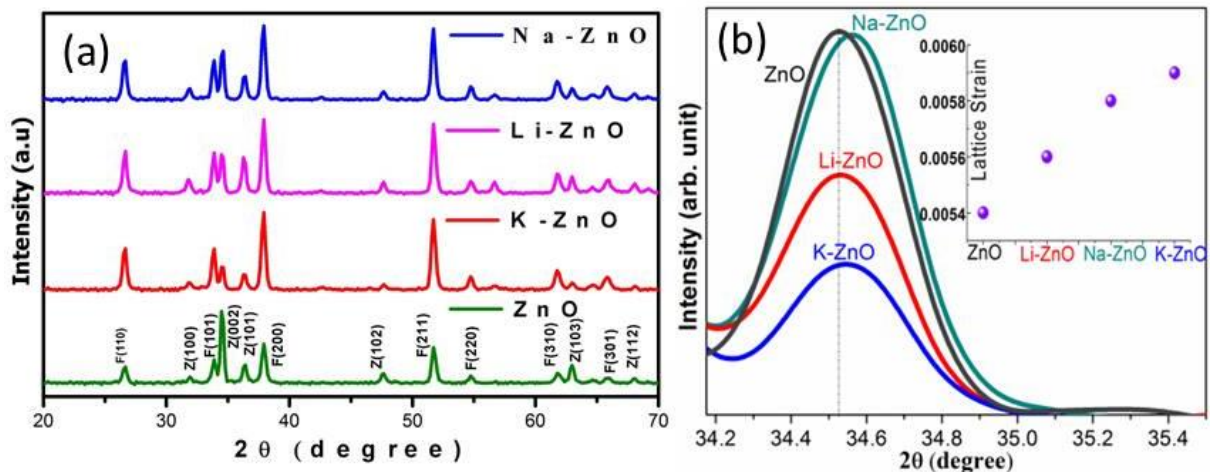


Figure 4.2: (a) XRD pattern of pure ZnO NRs and Li, Na and K doped ZnO NRs. (b) magnified view of (0 0 2) diffraction peak and the plot of estimated lattice strain (inset).

4.3.2 XPS and Defect Analysis

The chemical composition and the defect profile of the alkali doped ZnO NRs and pristine ZnO NRs are further investigated by XPS. The core level Zn 2p spectrum (Fig. 4.3(a)) with two peaks located at 1044.67 and 1021.55 eV corresponding to Zn 2p_{1/2} and Zn 2p_{3/2}, respectively, with a spin orbit splitting energy difference of 23.1 eV, demonstrates the +2 oxidation state of Zn. [41, 42] Fig. 4.3(b) shows Li 1s core level spectrum, where the sharp peak located at 55.9 eV corresponds to Li-O bond formation through substituting the Zn²⁺ by Li⁺. [43] The Na 1s core level spectrum (Fig. 4.3(c)) exhibits a hump around 1071.1 eV, which represents the Na-O bond formation because of the substitution of Na⁺ at Zn²⁺ sites. [44] The deconvoluted core level spectrum (Fig. 4.3(d)) of K 2p shows two major peaks around 293.9 and 295.8 eV corresponding to the K 2p_{3/2} and K 2p_{1/2}, respectively, which indicate to the substitution of K⁺ at Zn²⁺ sites. [30] It is evident from the XPS studies that the dopant ions will mostly incorporate within the ZnO host by substituting the Zn²⁺ ions.

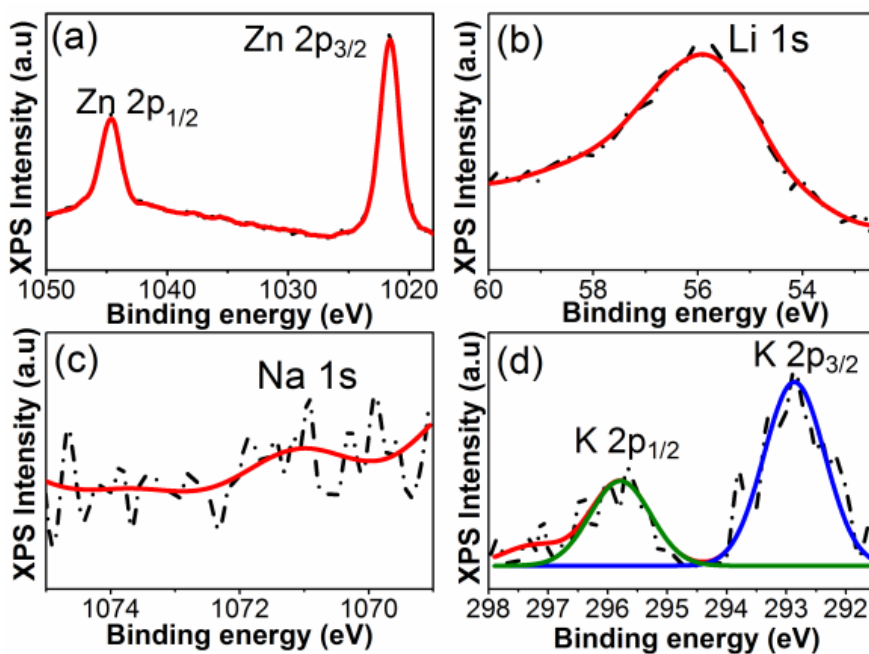


Figure 4.3: High-resolution XPS spectrum of (a) Zn 2p, (c) Li 1s, (d) Na 1s, (e) K 2p.

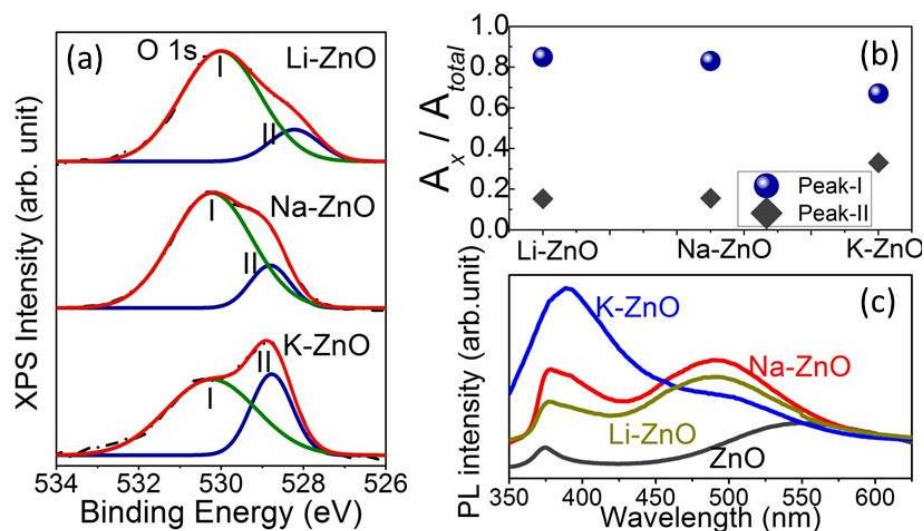


Figure 4.4: (a) O 1s for the doped ZnO NRs. (b) The peak area ratios of peak-I and peak-II to the total area. (c) Room temperature PL emission spectrum of the alkali metal doped ZnO NRs

Each of the O 1s core level spectra (Fig. 4.4(a)) of the doped ZnO NRs exhibits a broad peak, which can be deconvoluted into two peaks located at 531.6 (peak-I) and 529.9 (peak-II) eV. Here the lower energy peak (529.9 eV) is attributed to the O²⁻ ions bonded with Zn ions mostly (also with dopant ions), whereas the higher binding energy peak at 531.6 eV (peak-I) can be related to the oxygen-vacancy defects in doped ZnO NRs. [45-48] Therefore, the change in the intensity of ‘peak-I’ should have a direct relation with the variation of concentration of oxygen-vacancies present in doped ZnO NRs. [48, 49] The higher intensities of ‘peak-I’ for both the Li and Na-ZnO NRs compared to K-ZnO NRs indicate that the concentrations of oxygen-vacancies are higher in Li and Na-ZnO NRs than that in the K-ZnO NRs. The O 1s peak area ratios (A_x/A_{total}) of peak ‘x’ to the total area (A_{total}) of the doped ZnO NRs are shown in Fig. 4.4(b), where ‘x’ stands for peak-‘I’ or ‘II’. The values for $A_I : A_{total}$ are estimated as 0.85, 0.83 and 0.67 for the Li, Na and K-ZnO NRs, respectively. Results indicate that Li and Na-ZnO NRs have nearly equal concentration of oxygen-vacancies, which is considerably higher than that of K-ZnO NRs. Furthermore, the room temperature PL emission spectra (Fig. 4.4(c)) of the as prepared NRs are also recorded to probe the defect profile of the as prepared materials. It is evident that the weak PL emission of

pristine ZnO NRs significantly improves after alkali metal doping. The NRs exhibit a near band edge (NBE) emission in the UV region and defect emission at higher wavelength visible light region. Each of Li-ZnO and Na-ZnO NRs samples show quite a sharp NBE emission peak, whereas the same emission peak for K-ZnO NRs is found to be wider, indicating the presence of many new NBE states in K-ZnO NRs. The appearance of higher intensity NBE emission peak in K-ZnO NRs also suggests that they are enriched with NBE defects, which are most probably generated because of the large lattice strain in the sample. Doped ZnO NRs also exhibit a sharp sub-bandgap defect emission around 490 nm and this controversial deep level emission (DLE) of ZnO NRs is generally ascribed to the oxygen-vacancy defects. [50-52] The higher intensity DLE peaks in the Na and Li-ZnO NRs compared to K-ZnO NRs again indicate that the concentration of oxygen-vacancies is significantly higher in Na and Li-ZnO NRs compared to K-ZnO NRs. Moreover, the higher intensity of the DLE peak than the UV-emission peak for each of the Na and Li-ZnO NRs samples compared to that of K-ZnO NRs sample, indicate that the oxygen-vacancies also act as the trapping sites for electrons during photoemission, where the photogenerated electrons mostly recombine through oxygen-vacancies when large concentration of oxygen-vacancy is present in the material. In support of this, recent studies have shown that the substitutional doping of alkali ions in wide bandgap oxides generates hole in the neighboring lattice points of oxygen atoms, which promotes the removal of the oxygen, realizing two electrons to compensate the holes created in the matrix. [31] The creation of the oxygen-vacancy also boosts the formation of further oxygen-vacancies in the matrix. [32] Simultaneously, the doping of lower valence elements in oxide semiconductors is also found to induce the spontaneous oxygen-vacancy formation [33-38] and here also, we have evidenced the formation of large concentration of oxygen-vacancies because of alkali metal doping in ZnO NRs. Furthermore, the 1D arrays of nanostructure having large surface area will offer huge platform for the formation of surface oxygen-vacancies also.

4.3.3 Photoelectrochemical Performance

Photoelectrochemical performance of the as prepared NRs have been investigated by linear sweep voltametry (LSV), recorded under chopped visible light illumination (wavelength > 400 nm, 10 mW.cm^{-2}) (Fig. 4.5(a)). Pristine ZnO NRs show very weak photoresponse with significantly low photocurrent. Among the doped NRs, Na-ZnO and Li-ZnO NRs exhibit significantly enhanced photocurrent, where the photoresponse of K-ZnO NRs is the weakest one. Notably, K-ZnO NRs exhibit the highest dark current density, followed by the Na-ZnO and Li-ZnO NRs. It has already been found that the K-doping introduces the maximum lattice strain in the ZnO matrix whereas Li doping introduces the minimum lattice strain. It is reported that the favourable lattice strain can tune the electronic structure of the materials and consequently boost the electronic/ionic transportation and mobility. [38] Therefore, it is believed that the lattice strain developed in ZnO because of alkali doping is favouring better electronic transportation, resulting in high dark currents. Moreover, here, K-ZnO NRs also contain large concentration of NBE defects compared to the other doped ZnO NRs, which would most expectedly change the near conduction band electronic structure of K-ZnO NRs resulting in a large electron concentration in the conduction band, boosting the dark current density. [27, 28] On the other hand, Li-ZnO NRs, which develop lowest amount of lattice strain defects among the doped NRs, is found to exhibit the lowest dark current also. Therefore, it is evident from the experimental results that the lattice strain have a crucial role in changing the electronic structure, favouring the improved charge transfer and mobility in alkali doped ZnO NRs. [29]

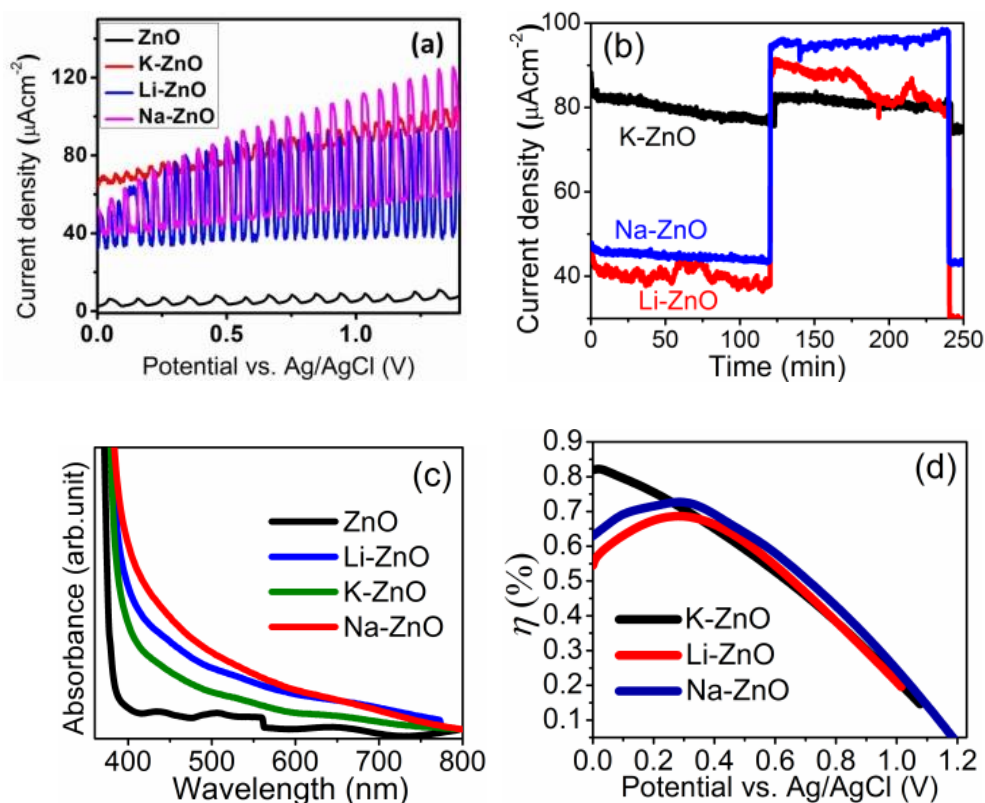


Figure 4.5: (a) Photoinduced current vs. potential curves (LSV curves) for ZnO and doped ZnO NRs. (b) Photoswitching and photocurrent stability plots of the doped ZnO NRs recorded at 0.5 V vs. Ag/AgCl. (c) UV-Vis absorption spectra and (d) photoconversion efficiency plots for the as prepared NRs electrodes.

Photo-switching and stability of photocurrent of the doped NRs are shown in Fig. 4.5(b), recorded at 0.5V vs. Ag/AgCl. Figure 4.5(b) also shows that the Na-ZnO NRs exhibit the best photocurrent stability among the NRs. Photocurrent densities of Na-ZnO, Li-ZnO and K-ZnO NRs are found to increase by 152%, 135% and 10%, respectively, with respect to their corresponding dark currents. For a better understanding of photoresponse of the NRs, the photo absorption characteristics of NRs are studied and Fig. 4.5(c) shows the UV-Vis absorption spectra of the NRs. It is evident that the Na-ZnO and Li-ZnO NRs exhibit superior visible light absorption, whereas the K-ZnO NRs show the weakest visible light absorption among the doped NRs. All the NRs also exhibit sharp absorption in the UV region, which corresponds to the band

edge absorption. Bandgap energy estimated from the absorption edges indicates that the bandgap of ZnO NRs decreases because of the alkali metal doping (Table 4.2).

The enhanced visible light absorption of the doped NRs is because of the introduction of new sub-bandgap defect states due to doping. Now, the earlier XPS and PL studies have confirmed that oxygen-vacancies are the major defects present in the sub-bandgap of doped ZnO NRs. Therefore, the superior visible light absorption by Na-ZnO and Li-ZnO NRs is resulted because of the presence of large concentration of oxygen-vacancies; mainly, as the surface oxygen-vacancies present in the sub-bandgap have been demonstrated as the deep donor in ZnO, which can absorb visible light and contribute to the increase in the donor densities of ZnO for enhanced conductivity after illumination. [19, 21, 53, 54] Here, earlier PL study also indicates that the oxygen-vacancies in doped ZnO NRs are also deep level defects. Therefore, the best photoresponse of the Na-ZnO NRs is because of its superior visible light absorption due to the presence of large concentration of oxygen-vacancies and favourable electron transportation and mobility because of the moderate lattice strain in Na-ZnO NRs. On the other hand, the poor visible light response of K-ZnO NRs is because of the low concentration of oxygen-vacancies, although the highest amount of lattice strain defects makes K-ZnO NRs a good conductor because the lattice strain is found to be favourable for electronic transportation and mobility only. Therefore, the experimental results reveal that the oxygen-vacancies are responsible for visible light absorption and enhanced photocurrent in alkali doped ZnO NRs, whereas the lattice strain developed because of doping mainly tunes the electronic structure of the material improving the electronic transportation and mobility.

The photoconversion efficiency ($\eta\%$) of the NRs photoanodes as a function of the applied voltage (equation 3.1, chapter 3) is plotted in Fig. 4.5(d). It is found that the Na-ZnO, Li-ZnO and K-ZnO NRs exhibit the maximum efficiency of 0.73%, 0.69% and 0.70%, respectively, at 0.3V vs. Ag/AgCl, which is found to increase remarkably compared to the as prepared pristine ZnO NRs (0.02% @ bias voltage of 0.7 V vs Ag/AgCl, chapter 3). [6] The $\eta\%$ values of the doped NRs are also found to be

significantly large compared to the recently reported values for different doped ZnO nanostructures based photoanodes (Table 4.1).

Table 4.1: Summary of the photoconversion efficiency of different doped-ZnO nanostructures based photoelectrodes.

Sample Name/Photoelectrode	Incident radiation	Efficiency
ZnO NRs [6]	Wavelength > 420 nm, 10 mW/cm ²	0.02%
N-ZnO NRs [6]	Wavelength > 420 nm, 10 mW/cm ²	0.11%
C-ZnO NRs [6]	Wavelength > 420 nm, 10 mW/cm ²	0.13%
S-ZnO NRs [6]	Wavelength > 420 nm, 10 mW/cm ²	0.06%
N-ZnO NWs [3]	AM 1.5 G, 100 mW/cm ²	0.15%
Branched and N doped ZnO ^[55]	AM 1.5 G, 100 mW/cm ²	0.31%
Al-doped ZnO NWs ^[56]	AM 1.5 G, 100 mW/cm ²	0.04%
Li doped ZnO NWs ^[57]	AM 1.5 G, 100 mW/cm ²	0.17%
N-GQD ZnO NR ^[58]	170 mW/cm ² .	0.83%
ZnO:Cu Electrodes ^[59]	AM 1.5 G, 100 mW/cm ²	0.28%

However, study of the electronic band position, charge separation and transportation of the doped ZnO NRs are also very important to understand their enhanced PEC performance. The flat-band potentials (E_{fb}) of the photoanodes are estimated from the Mott-Schottky plots (Fig. 46(a)) obtained from the impedance measurement studies conducted in 0.5 M Na₂SO₄ aqueous solution (pH 6.5). The estimated E_{fb} of the pristine ZnO NRs electrode (-0.23 V NHE, chapter 2) [6] is found to be shifted towards the

negative potential because of alkali metal doping. The schematic of the band edge positions of the photoelectrodes obtained based on the calculated values of E_{fb} and bandgap energies are shown in Fig. 4.6(b).

Table 4.2: The estimated flat-band potential (E_{fb}) and bandgap for different ZnO NRs photoanodes grown on FTO.

Photoanode	E_{fb} (V) vs. NHE	Bandgap (eV)
ZnO/FTO	-0.23	3.28
Li-ZnO/FTO	-0.33	3.18
Na-ZnO/FTO	-0.56	3.17
K-ZnO/FTO	-0.44	3.19

It is evident from Fig. 4.6(b) that the shift of the conduction band edges towards the more negative energy will induce an efficient band bending at the doped NRs/FTO interface leading to an easy separation and transportation of the photogenerated electrons and reduced electron-hole pair recombination resulting in an enhanced photoelectrochemical activity of the alkali doped NRs. Here, the band bending at Na-ZnO NRs/FTO interface is maximum, which suggests better transportation of photogenerated electrons in Na-ZnO NRs than the other doped NRs. Moreover, previous PL study also suggests that the photogenerated electron-hole pairs mostly recombine through the sub-bandgap oxygen-vacancies. Therefore, as the oxygen-vacancies act as the trapping sites/recombination centres for photogenerated electrons, the photogenerated minority carries in the valance band of the doped ZnO NRs will have enough time to reach the surface of the NRs for oxygen evaluation reaction because of the electrode/electrolyte band bending (Fig. 4.6(c)). Therefore, the excellent PEC property of the Na-ZnO NRs is because of its excellent visible light absorption due to the presence of large concentration of oxygen-vacancies, better electron transportation due to large Na-ZnO NRs/FTO interfacial band bending and reduced photo generated charge carrier recombination because of oxygen-vacancy trapping. Similarly, the interfacial band alignment between K-ZnO NRs/FTO allows fast

transportation of the photogenerated electron but because of its poor light absorption and carrier separation, K-ZnO NRs exhibit comparatively poor photoelectrochemical property among the doped NRs.

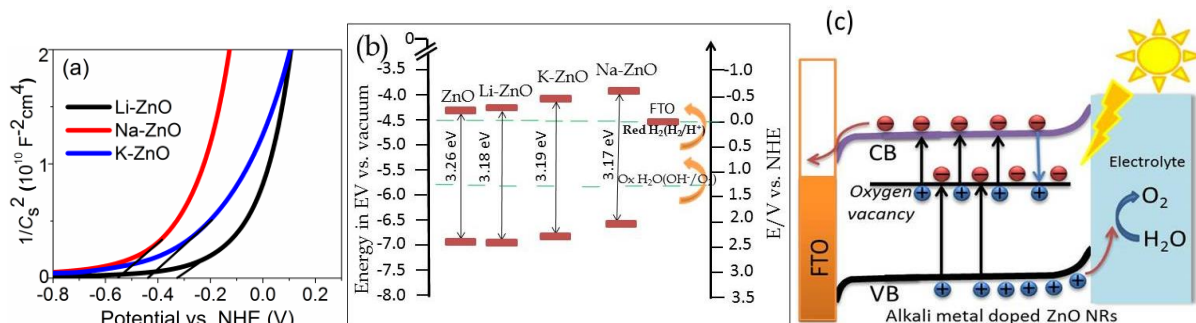


Figure 4.6: (a) Mott-Schottky plots for the alkali-doped ZnO NRs. (b) Schematic of band positions of the FTO, ZnO and alkali-doped ZnO NRs and (c) The mechanism of band bending and photo carrier generation/recombination in alkali metal doped ZnO NRs.

4.4 Conclusion

A facile wet chemical method was successfully employed to fabricate highly dense arrays of alkali metal (Li, Na and K) doped ZnO NRs. The alkali metal doped ZnO NRs are found to exhibit remarkable photoelectrochemical property with enhanced oxygen evolution reaction. The alkali metal doping introduces significant lattice strain and large concentration of oxygen-vacancy defects in ZnO host. Lower valence alkali metal doping introduces holes in the matrix and therefore the neighbouring oxygen leaves the site, leaving behind two electrons to compensate the holes created in the system; creating oxygen-vacancies. The oxygen-vacancies act as the sub-bandgap donor sites, which generate photoelectrons during light illumination, resulting in the enhanced photocurrent. Along with the light absorption, the oxygen-vacancies also act as the recombination centre for the photogenerated electrons, which helps in the diffusion of the photogenerated minority carriers in valence band, facilitating the charge separation and thus reduce electron-hole recombination. Here, the lattice strain is found to tailor the electronic structure of the NRs, favouring

enhanced electronic/ionic transportation and mobility only. Alkali metal doping also reduces the effective band gap energy of the NRs and also shift the conduction/valence band edges towards more negative energy. Thus the alkali metal doping also alters the NRs/FTO interfacial band alignment, resulting in the easy transportation and separation of photo carriers and thereby resulting in the enhanced photoelectrochemical property. These findings demonstrate in depth understanding on the defect mediated photoelectrochemical property of alkali metal doped ZnO NRs for its application in water splitting.

Bibliography

- [1] K. Karmakar, A. Sarkar, K. Mandal and G. G. Khan. *ChemElectroChem*, **5**, 1147 (2018)
- [2] B. D. Alexander, P. J. Kulesza, I. Rutkowska, R. Solarz, J. Augustynski, *J. Mater. Chem.* **18**, 2298 (2008)
- [3] M. Grätzel, *Nature*. **414**, 338-344 (2001)
- [4] X. Yang, A. Wolcott, G. Wang, A. Sobo, R. C. Fitzmorris, F. Qian, J. Z. Zhang, Y. Li, *Nano Lett.* **9**, 2331 (2009)
- [5] A. Sarkar, A. K. Singh, G. G. Khan, D. Sarkar, K. Mandal *RSC Adv.*, **4**, 55629 (2014)
- [6] K. Karmakar, A. Sarkar, K. Mandal, G. G. Khan, *Nanotechnology*, **28**, 325401 (2017)
- [7] K. Karmakar, A. Sarkar, K. Mandal, G. G. Khan, *ACS Sustainable Chem. Eng.*, **4**, 5693 (2016)
- [8] P.-Y. Kuang, J.-R. Ran, Z.-Q. Liu, H.-J. Wang, N. Li, Y.-Z. Su, Y.-G. Jin, S.-Z. Qiao, *Chem. Eur. J.*, **21**, 15360 (2015)
- [9] P.-Y. Kuang, X.-J. Zheng, J. Lin, X.-B. Huang, N. Li, X. Li, Z.-Q. Liu, *ACS Omega*, **2**, 852 (2017)
- [10] Z.-Q. Liu, X.-H. Xie, Q.-Z. Xu, S.-H. Guo, N. Li, Y.-B. Chen, Y.-Z. Su, *Electrochim. Acta.*, **98**, 268 (2013)
- [11] R.-B. Wei, P.-Y. Kuang, H. Cheng, Y.-B. Chen, J.-Y. Long, M.-Y. Zhang, Z.-Q. Liu, *ACS Sustain. Chem. Eng.*, **5**, 4249 (2017)
- [12] P.-Y. Kuang, Y.-Z. Su, K. Xiao, Z.-Q. Liu, N. Li, H.-J. Wang, J. Zhang, *ACS Appl. Mater. Interfaces*, **7**, 16387 (2015)
- [13] G. Wang, X. Yang, F. Qian, J. Z. Zhang, Y. Li, *Nano Lett.*, **10**, 1088 (2010)
- [14] K.-S. Ahn, Y. Yan, S. Shet, K. Jones, T. Deutsch, J. Turner, M. Al-Jassim, *Appl. Phys. Lett.*, **93**, 163117 (2008)

-
- [15] Y.-Z. Su, K. Xiao, Z.-J. Liao, Y.-H. Zhong, N. Li, Y.-B. Chen, Z.-Q. Liu, *Int. J. Hydrog. Energy*, **38**, 15019 (2013)
- [16] P.-Y. Kuang, Y.-Z. Su, G.-F. Chen, Z. Luo, S.-Y. Xing, N. Li, Z.-Q. Liu, *Appl. Surf. Sci.*, **358**, 296 (2015)
- [17] F. Lei, Y. Sun, K. Liu, S. Gao, L. Liang, B. Pan, Y. Xie, *J. Am. Chem. Soc.*, **136**, 6826 (2014)
- [18] J. Gan, X. Lu, J. Wu, S. Xie, T. Zhai, M. Yu, Z. Zhang, Y. Mao, S. C. I. Wang, Y. Shen, Y. Tong, *Sci. Rep.*, **3**, 1021 (2013)
- [19] C. Zhu, C. Li, M. Zheng, J.-J. Delaunay, *ACS Appl. Mater. Interfaces.*, **7**, 22355 (2015)
- [20] G. Wang, Y. Ling, Y. Li, *Nanoscale*, **4**, 6682 (2012)
- [21] H. L. Tan, A. Suyanto, A. T. D. Denko, W. H. Saputera, R. Amal, F. E. Osterloh, Y. H. C. Ng, *Part. Part. Syst. Charact.*, **34**, 1600290 (2017)
- [22] G. Wang, H. Wang, Y. Ling, Y. Tang, X. Yang, R. C. Fitzmorris, C. Wang, J. Z. Zhang, Y. Li, *Nano Lett.*, **11**, 3026 (2011)
- [23] J. Wang, Z. Wang, B. Huang, Y. Ma, Y. Liu, X. Qin, X. Zhang, Y. Dai, *ACS Appl. Mater. Interfaces*, **4**, 4024 (2012)
- [24] J. L. G. Fierro, *Metal Oxides: Chemistry and Applications*, CRC Press, Boca Raton, FL, 2005
- [25] A. M. Mohamed, A. W. Amer, S. Y. Al Qaradawi, N. K. Allam, *Phys. Chem. Chem. Phys.*, **18**, 22217 (2016)
- [26] M. H. Mirfasih, C. Li, A. Tayyebi, Q. Cao, J. Yu, J.-J. Delaunay, *RSC Adv.*, **7**, 26992 (2017)
- [27] H. Tan, Z. Zhao, W.-b. Zhu, E. N. Coker, B. Li, M. Zheng, W. Yu, H. Fan, Z. Sun, *ACS Appl. Mater. Interfaces*, **6**, 19184 (2014)
- [28] M. Li, Y. Hu, S. Xie, Y. Huang, Y. Tong, X. Lu, *Chem. Commun.*, **50**, 4341 (2014)
- [29] A. Kushima, B. Yildiz, *ECS Trans.*, **25**, 1599 (2009)
- [30] S. Ghosh, G. G. Khan, A. Ghosh, S. Varma, K. Mandal, *CrystEngComm.*, **15**, 7748 (2013)

-
- [31] A. A. Peyghan, M. Noei, *Physica B*, **432**, 105 (2014)
- [32] J. J. Carey, M. Nolan, *J. Mater. Chem. A*, **5**, 15613 (2017)
- [33] A. Iwaszuk, M. Nolan, *J. Phys. Chem. C*, **115**, 12995 (2011)
- [34] M. Nolan, *J. Phys. Chem. C*, **115**, 6671 (2011)
- [35] P. R. L. Keating, D. O. Scanlon, G. W. Watson, *J. Mater. Chem. C*, **1**, 1093 (2013)
- [36] A. B. Kehoe, D. O. Scanlon, G. W. Watson, *Chem. Mater.*, **23**, 4464 (2011)
- [37] A. Iwaszuk, M. Nolan, *J. Phys.: Condens. Matter.*, **23**, 334207 (2011)
- [38] C. Chen, K. Xu, X. Ji, B. Zhang, L. Miao, J. Jiang, *J. Mater. Chem. A*, **3**, 12461 (2015)
- [39] G. K. Williamson, W. H. Hall, *Acta Metall.*, **1**, 22 (1953)
- [40] C. Suryanarayana, M. G. Norton, *X-Ray Diffraction: A Practical Approach*, Springer US, (1998)
- [41] C. D. Wanger, W. M. Riggs, L. E. Davis, J. F. Moulder, G. E. Muilenberg, *Handbook of X-ray Photoelectron Spectroscopy*, Perkin-Elmer Corp., Physical Electronics Division, Eden Prairie, Minnesota, USA, (1979)
- [42] A. Sarkar, K. Karmakar, G. G. Khan, *J. Phys. Chem. C*, **121**, 25705 (2017)
- [43] J. G. Lu, Y. Z. Zhang, Z. Z. Ye, Y. J. Zeng, H. P. He, L. P. Zhu, J. Y. Huang, L. Wang, J. Yuan, B. H. Zhao, X. H. Li, *Appl. Phys. Lett.*, **89**, 112113 (2006)
- [44] S. Ghosh, G. G. Khan, S. Varma, K. Mandal, *ACS Appl. Mater. Interfaces*, **5**, 2455 (2013)
- [45] Y. S. Rim, D. L. Kim, W. H. Jeong, H. J. Kim, *Appl. Phys. Lett.*, **97**, 233502 (2010)
- [46] C. Terrier, J. P. Chatelon, R. Berjoan, J. A. Roger, *Thin Solid Films*, **263**, 37 (1995)
- [47] Y. Zhao, G. Dong, L. Duan, J. Qiao, D. Zhang, L. Wang, Y. Qiu *RSC Adv.*, **2**, 5307 (2012)
- [48] X. P. Yang, J. G. Lu, H. H. Zhang, B. Lu, J. Y. Huang, C. L. Ye, Z. Z. Ye, *J. Appl. Phys.*, **112**, 113510 (2012)
- [49] T. Szörenyi, L. D. Laude, I. Bertóti, Z. Kántor, Z. Geretovszky, *J. Appl. Phys.*, **78**, 6211 (1995)
- [50] R. C. Wang, C. P. Liu, J. L. Huang, S.-J. Chen, *Appl. Phys. Lett.*, **86**, 251104 (2005)

-
- [51] K. Vanheusden, C. H. Seager, W. L. Warren, D. R. Tallant, J. A. Voigt *Appl. Phys. Lett.*, **68**, 403 (1996)
- [52] K. Vanheusden, W. L. Warren, C. H. Seager, D. R. Tallant, J. A. Voigt, B. E. Gnade, *J. Appl. Phys.*, **79**, 7983 (1996)
- [53] A. Janotti, C. G. Van de Walle, *Appl. Phys. Lett.*, **87**, 122102 (2005)
- [54] A. Janotti, C. G. Van de Walle, *Rep. Prog. Phys.*, **72**, 126501 (2009).
- [55] Y. Qiu, K. Yan, H. Deng, S. Yang, *Nano Lett.*, **12**, 407 (2012)
- [56] Y. -F. Xu, H. -S. Rao, X. -D. Wang, H. -Y. Chen, D. -B. Kuang, C. -Y. Su, *J. Mater. Chem. A*, **4**, 5124 (2016)
- [57] H. J. Lee, S.-H. Shin, K. T. Nam, J. Nah, M. H. Lee, *J. Mater. Chem. A*, **4**, 3223 (2016)
- [58] T. Majumder, K. Debnath, S. Dhar, J. J. L. Hmar, S. P. Mondal, *Energy Technol.*, **4**, 1 (2016)
- [59] R. Dom, L. R. Baby, H. G. Kim, P. H. Borse, *International Journal of Photoenergy*, **9**, 928321 (2013).

Chapter 5

The *p-n* CuFeO₂-ZnO Nano-Heterojunction Photoanode for Photoelectrochemical Water Oxidation

Here in this chapter fabrication process of *p-n* CuFeO₂-ZnO nano-heterojunction photoanode has been demonstrated. The study of photoelectrochemical properties of the photoanode by varying the nanolayer thickness of CuFeO₂ is the main focus of this chapter.

A part of this content of this chapter has been published in Nanotechnology [1] and is reproduced herein with permission from Institute of Physics (IOP).

5.1 Preamble

The photoelectrochemical (PEC) cells, which exhibit significant promise in the direct conversion of enormous solar energy into electricity and chemical fuels (hydrogen and hydrocarbons) is a remarkable approach to reduce environmental pollution caused by fossil fuels and the proper utilization of renewable and green solar energy. [2, 3] Recent studies on the PEC water splitting reveal that the electrical assembly of an *n*-type photoanode and a *p*-type photocathode in series, forming a tandem cell, provides immense promise to remarkably enhance the solar energy conversion efficiency. [4-6] Since the PEC water splitting property of titanium dioxide was reported, [7] various *n*-type metal oxides like TiO₂, ZnO, Fe₂O₃, WO₃ and BiVO₄ etc. have been extensively investigated as photoanode for water oxidation. [4, 8-14] Among them, ZnO is a very well-known photoanode having excellent photocatalytic and solar energy conversion property because of its favorable band edge energy position, remarkable electrochemical and thermal stability, non-toxicity and relatively low cost. [15-17] Instead of the high electron mobility and good stability, the poor light absorption only in the UV region of the solar spectra and high surface recombination of the charge carriers reduces the photocurrent density as well as the photocurrent to hydrogen conversion efficiency in ZnO. [17, 18] Hence, proper engineering is required to maximize the solar energy harvesting property of ZnO along with efficient charge carrier separation and transportation. [17, 19-22]

On the other hand, recently various copper oxide based *p*-type materials such as, CuAlO₂, CuFeO₂, CuRhO₂ and CuGaO₂ etc. have been explored as the promising photocathodes for water reduction. [23-27] Those novel *p*-type materials are found to exhibit superior performance over the conventional CuO and NiO based photocathodes. [25] Most interestingly, the CuFeO₂ has drawn intense interest as photocathode because of good light absorption properties (band gap energy ~1.5 eV), suitable band edge energy positions and good stability in aqueous medium. [24, 25, 28, 29] Still CuFeO₂ suffers from poor conductivity leading to recombination of

photogenerated holes and obvious poor electron–hole separation. [25] Hence, different strategies have been adopted to overcome those problems includes the doping and the formation of hybrid structure based on CuFeO₂. [25, 30]

In this context, here we have proposed a novel strategy to design an *n-p* type ZnO-CuFeO₂ nano-heterostructure, for the first time, by employing a facile low cost electrochemical technique to enhance the PEC property of the electrode material. The *p*-type CuFeO₂ nanolayer was electrodeposited on the ordered arrays of *n*-type ZnO nanorods (NRs) grown on FTO substrate. It is expected that, in this specially designed ZnO-CuFeO₂ nano-heterostructure, the low band gap *p*-type CuFeO₂ is suitable to absorb the whole range of the solar light to generate photoelectrons. Due to the formation of a favorable *n-p* junction at ZnO-CuFeO₂ interface the photogenerated electrons in the thin CuFeO₂ nanolayer will readily move towards the ZnO NRs core resulting efficient charge carrier separation. The electrons finally transfer towards the Pt electrode through the FTO and generate hydrogen by reducing protons. Because of the high generation rate of photo-carriers and low recombination rate of the same in this nano-engineered electrode the photogenerated holes in the CuFeO₂ will effectively diffuse to the electrode/electrolyte surface and oxidize water. As expected, the ZnO-CuFeO₂ nano-heterostructure photoanode exhibits enhanced PEC performance along with good stability and enhanced solar to hydrogen conversion efficiency because of the improved visible solar light absorption for electron–hole pair generation, better charge carrier separation, and reduced electron–hole recombination. The demonstration of the inherent PEC mechanism of this *p-n* type photoelectrode opens up new possibility to design such nanostructures for improved solar energy harvesting.

5.2 Experimental Section

5.2.1 Reagents

FTO (Fluorine doped tin oxide coated glass, Sigma Aldrich), Zinc acetate dihydrate (Zn(CH₃COO)₂·2H₂O, Loba Chemie), hexamethylenetetramine ((CH₂)₆N₄),

Loba Chemie), Ethanol (C₂H₅OH), Copper Nitrate (Cu(NO₃)₂, Loba Chemie) , Iron(III) perchlorate hydrate (Fe(ClO₄)₃.xH₂O , Alfa Aesar) , Potassium perchlorate (KClO₄ , Merck) and Dimethylsulfoxide (DMSO, Merck). All the chemicals are of analytical grade and were used without further purification.

5.2.2 Fabrication of ZnO NRs on FTO

ZnO NRs were synthesized by two step aqueous chemical growth process which was described in chapter 3 (Experimental Section).

5.2.3 Fabrication of *p-n* CuFeO₂/ZnO Nano-Heterojunction

The *p-n* CuFeO₂-ZnO nano-heterojunction was fabricated by electrochemically depositing the *p*-type CuFeO₂ on ZnO NRs at -0.4V using the ZnO NRs/FTO as working electrode, Ag/AgCl as reference electrode, and a platinum wire as counter electrode. In this cathodic electrodeposition process a DMSO solution containing 1 mM copper (II) nitrate, 3 mM iron (III) perchlorate and 100 mM potassium perchlorate were used as electrolyte. Here, CuFeO₂ was electrodeposited for 3, 6 and 10 minutes on different ZnO NRs substrates. Finally, the CuFeO₂/ZnO nano-heterojunction films were prepared by annealing at 600°C in argon atmosphere.

5.2.4 Material Characterizations

In order to find out the crystalline structure X-ray diffraction analysis was performed using grazing angle incidence (2°) of the Cu K_α line (λ =1.54 Å) with a step size of 0.15° (GIXRD, Panalytical X'pert pro diffractometer). The morphological of the nanostructures were examined by field emission scanning electron microscope (FESEM, FEI quanta 200) and the composition of the materials were analyzed by energy dispersive X-ray spectroscopy (EDAX) attached with the same instrument. The transmission electron microscopy (TEM) and high resolution TEM (HRTEM) were performed by JEOL JEM 2100 to get clear idea about the formation of heterojunction. Energy filtered TEM (EFTEM) was employed to get the elemental distribution in the as

prepared nano-heterojunction. The ionic state of the constituent materials was also examined by X-ray photoelectron spectroscopy (XPS, VG Microtech VGX 900-W) with Mg K_{α} beam line having resolution of 0.9 eV at a vacuum level of 2.2×10^{-10} mbar. Light absorption and band gap of the materials were determined by using UV-visible spectroscopy (PerkinElmer Lambda 1050 UV/vis spectrometer). The electronic transition of the materials and carrier recombination were analyzed by using PL spectroscopy (Horiba, FluoroLog-3 spectrometer).

5.2.5 Photoelectrochemical Studies

The photo-electrochemical performance of the photoelectrodes were studied using a three electrode electrochemical workstation (CHI 660E, CH Instruments) by using the as prepared material (*p-n* heterojunctions) as working electrode, platinum as counter electrode and Ag/AgCl as reference electrode in a 0.5 M aqueous Na_2SO_4 of pH 6.4. Linear sweep voltammetry was measured from 1.6 to 0V vs. Ag/AgCl with consecutive light on off cycle with a visible light ($\lambda > 420$ nm) source having intensity 10 mWcm^{-2} and sensitivity 10^{-1} . Photoswitching activity of the materials was envisioned by *I-t* amperometry curve at 0.5V external bias for all the samples with the same light source. The flat band potential was determined by Mott-Shottky measurement from 0 to 1 V vs. Ag/AgCl at 1 KHz frequency of the input signal for $\text{CuFeO}_2/\text{ZnO}$ electrode. Electrochemical impedance was recorded without applying external bias with 5mV ac perturbation.

5.3 Results and discussion

5.3.1 Morphology and Structural analysis

The top view FESEM image of the as prepared 1D arrays of ZnO and $\text{CuFeO}_2/\text{ZnO}$ (6 min) nano-heterojunction are shown in Fig. 5.1(a) and (b) respectively. It is very clear that ZnO NRs have hexagonal morphology which is also verified by XRD (given later). The as grown nano-heterostructures over a large surface area on FTO is

presented later (inset of Fig. 5.2) which clearly indicates well-ordered homogeneous arrays of the same. The coating of CuFeO_2 on the surface of ZnO NRs is evident from Fig. 5.1(b), which indicates the increase of surface roughness of $\text{CuFeO}_2/\text{ZnO}$ (6 min) after the coating of shell layer. The FESEM micrographs also signify the uniform fabrication of nano-heterojunction where the typical dimension of the 1D structure is about ~ 100 nm. Figure 5.1(c)-(f) shows the elemental distribution over a large area of the $\text{CuFeO}_2/\text{ZnO}$ nano-heterostructures (NHs) which indicates the uniform distribution of the constituent elements. Again, EDAX spectrum in Figure 5.2 shows the presence of constituent elements in the NHs over the FTO substrate and also their quantification has shown in the inset.

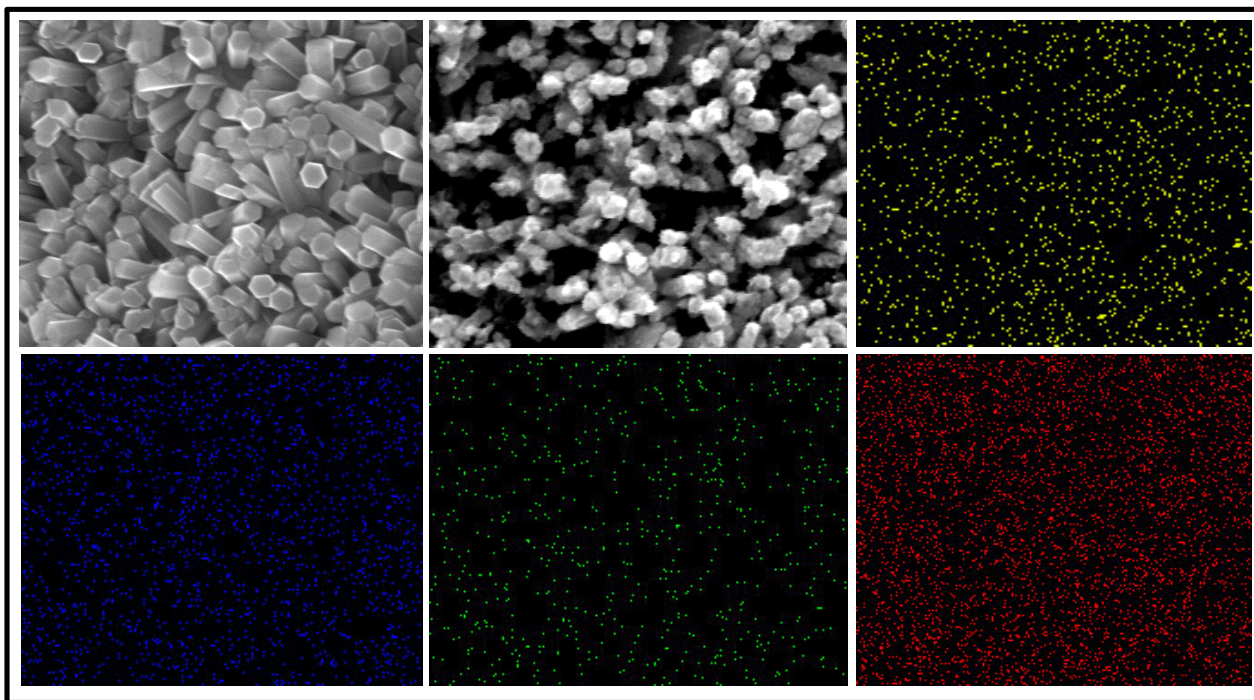


Figure 5.1: FESEM micrograph of (a) ZnO NRs, (b) $\text{CuFeO}_2/\text{ZnO}$ (6 min) nano-heterostructure and EDS elemental mapping of (c) Zn, (d) Cu, (e) Fe, (f) O.

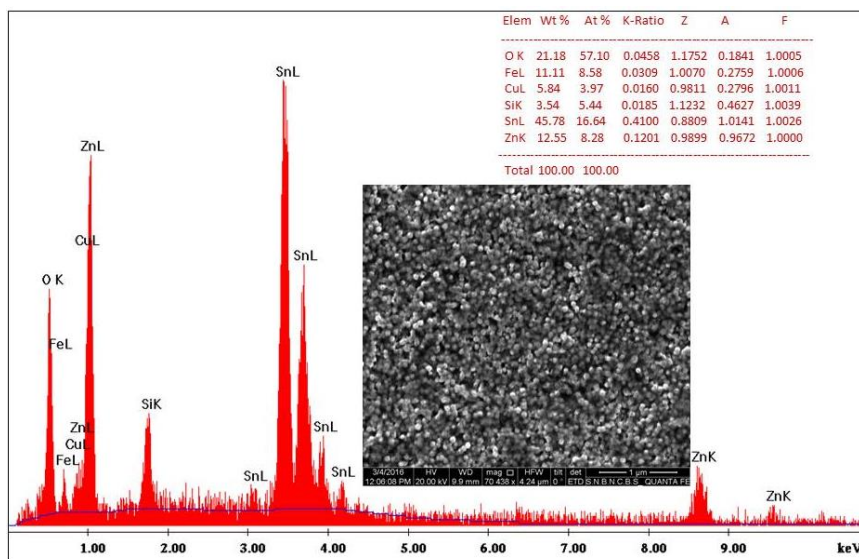


Figure 5.2: Energy dispersive X-ray (EDAX) data over a large area. Inset of figure, large scale FESEM image and elemental quantification data.

Figure 5.3(a) shows the TEM image of a mechanically broken part of the NHs, which confirms the retention of rod like structure even after electrodeposition of CuFeO_2 . The formation of crystalline nano-heterojunction is further clarified by HRTEM micrograph (Fig. 5.3(b)) and SAED pattern (Fig. 5.3(c)) recorded for the selected area of the TEM image. The thickness of CuFeO_2 on ZnO NRs is found to be about ~ 10 nm for $\text{CuFeO}_2/\text{ZnO}$ (6 min) sample. HRTEM image clearly depicts the polycrystalline nature of the nanostructure and the spacing between two adjacent crystal planes are 2.85, 2.59, and 1.91nm which corresponds to the distance between two crystal plane of CuFeO_2 (222), CuFeO_2 (100) and ZnO (102), respectively. The EFTEM images (Fig. 5.3(d)-(h)) of the nano-heterojunction again clearly demonstrate the uniform formation CuFeO_2 shell layer on ZnO NR core. The thin distribution of elemental 'Zn' confined at the core (Figure 5.3(d)) of the heterojunction clearly indicates the presence of ZnO NRs at the core. On the other hand the broad elemental distribution of O, Cu and Fe over Zn signify the well coverage of ZnO NR by CuFeO_2 . Figure 5.4 (a) shows the representative GIXRD pattern of the as prepared $\text{CuFeO}_2/\text{ZnO}$ (6 min) sample. It is to mention that for all the $\text{CuFeO}_2/\text{ZnO}$ samples the GIXRD pattern is found to be identical. It is evident

from Fig. 5.4(a), that both the ZnO and CuFeO₂ are polycrystalline in nature, where the ZnO NRs have a preferential growth direction of (002), which matches the hexagonal wurtzite structure of the ZnO (JCPDS file n. 89-1397) with $P6_3mc$ space group. The XRD pattern of CuFeO₂ coincides well with the hexagonal structure with R_3m space group (JCPDS file no. 85-0605). The broad nature of the diffraction peaks of the CuFeO₂ suggests the nanocrystalline nature of the material.

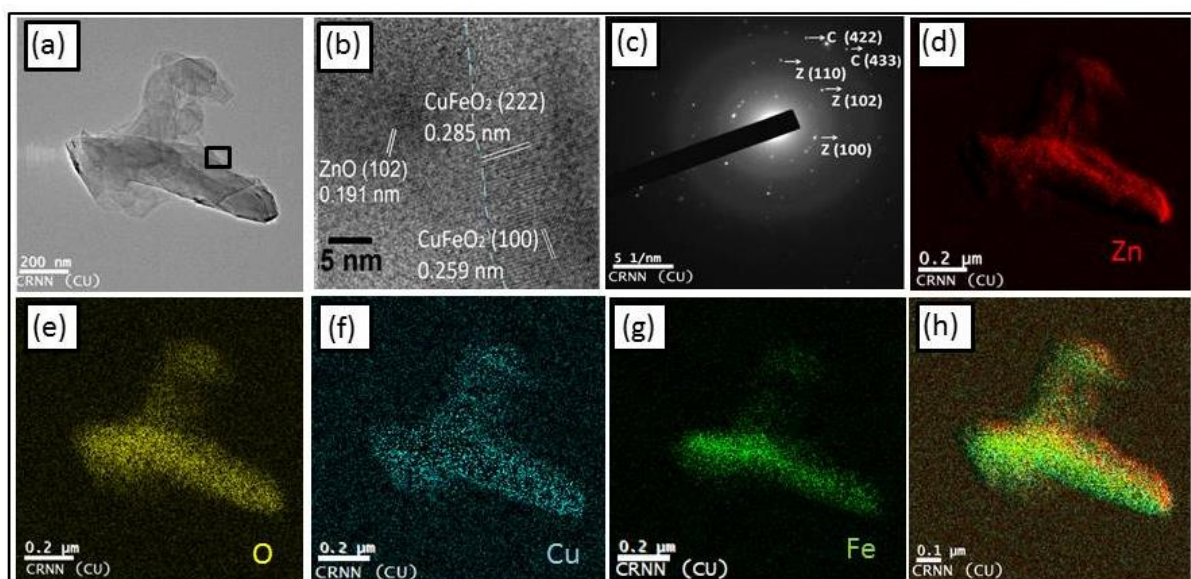


Figure 5.3: (a) TEM image of nano-heterostructure, (b) HRTEM image and (c) SAED pattern for the marked region of the heterostructure (C:CuFeO₂ and Z:ZnO). (d), (e), (f) and (g) EFTEM micrographs of nano-heterostructure showing the presence of elements like Zn, O, Cu, and Fe, respectively and (h) the overall elemental distribution.

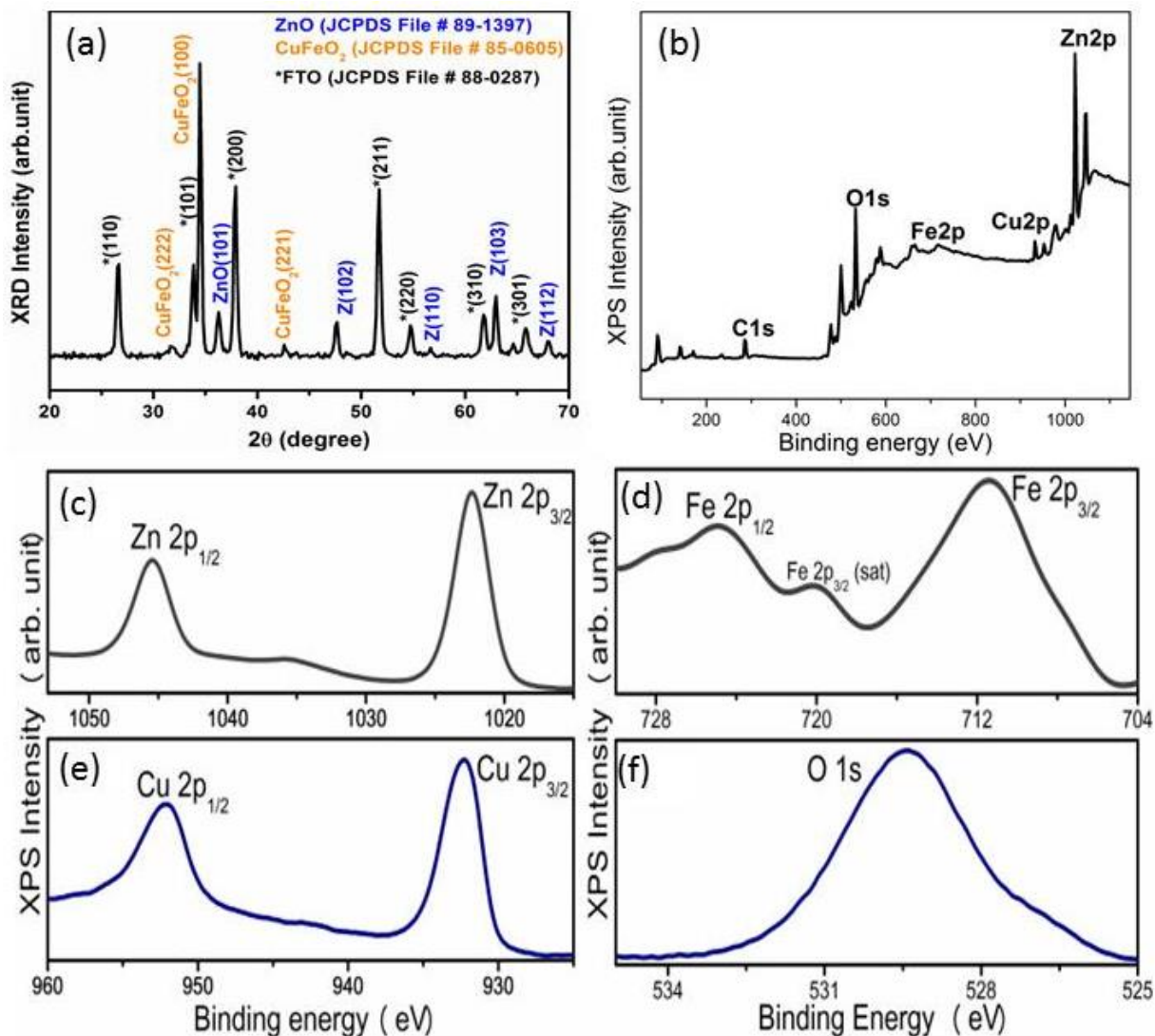


Figure 5.4: (a) GIXRD pattern of nano-heterostructure, (b) XPS surface survey of CuFeO₂/ZnO nano-heterostructure and (c), (d), (e), (f) are the XPS core level spectrum for Zn 2p, Cu 2p, Fe 2p and O 1s, respectively.

5.3.2 XPS Studies

The XPS core level spectra of the CuFeO₂/ZnO nano-heterostructures gives useful information about the chemical composition and oxidation state of the material. The surface survey of the NHs is shown in Fig 5.4(b). The Zn 2p core level XPS spectra (Fig. 5.4(c)) consists of doublets positioned at 1022.3 and 1045.4 eV having the spin orbit energy splitting of 23.1 eV, indicates +2 oxidation state of Zn. [31] However, the XPS

spectrum of Zn 2*p* core level of pristine ZnO NRs is found to be consists of a doublet positioned at 1021.8 and 1044.9 and eV (Chapter 3, see XPS core level spectra of Zn2*p*). Therefore, the shift of the Zn 2*p* core level spectrum towards the higher binding energy in CuFeO₂/ZnO nano-heterostructure compared to pristine ZnO NRs clearly indicates the change in the electronic structure of Zn because of the formation of the *p-n* heterojunction. [32, 33] The core level XPS spectra of Cu (Fig. 5.4(e)) shows two strong peaks positioned at 932 and 952 eV corresponds to Cu 2*p*_{3/2} and Cu 2*p*_{1/2}, respectively, indicates that the Cu ion only exists in +1 oxidation state. [34] The Fe 2*p* XPS spectra (Fig. 5.4(d)) of CuFeO₂ shows the presence of two distinct peaks situated at 710.5 eV for Fe 2*p*_{3/2} and 724.7 eV for Fe 2*p*_{1/2} and a weak satellite peak ~ 719.9 eV indicates the presence of Fe³⁺ in the material. [34] In Figure 5.4(f), the O 1*s* core level XPS spectra appears at 529.4 eV is attributed to O²⁻, which also signifies the binding of oxygen atom with Zn, Fe and Cu.

5.3.3 Photoelectrochemical Performance

The effect of the electrochemically deposited *p*-type CuFeO₂ on the PEC performance of the ZnO NRs photoanode is investigated using linear sweep voltammetry (LSV) under the illumination of visible light (10 mW.cm⁻², wavelength > 420 nm). The photocurrent density vs. potential (*J-V*) curve of the ZnO NRs and the different CuFeO₂/ZnO nano-heterostructures recorded in the potential window of 1.6 to 0 V at the scan rate of 100 mV.s⁻¹, under chopped-light is shown in Figure 5.5(a). The significantly enhanced photocurrent in the CuFeO₂/ZnO NHs samples compared to bare ZnO NRs under illumination suggests the improvement of visible light absorption, photo generation and conduction of carriers in the nano-heterostructures. Here, to maximize the collection of the photogenerated carriers and to minimize the recombination of the carriers in CuFeO₂/ZnO NHs, the thickness of the *p*-type CuFeO₂ nanolayer has been tailored by changing the electrodeposition time of CuFeO₂ on ZnO NRs. It is evident that the thickness of the *p*-CuFeO₂ nanolayer has a crucial role on controlling the photocurrent and this suggests the obvious influence of coating layer

thickness on the photogeneration of carriers and carrier collection. The dependence of the photocurrent density on the deposition time of the *p*-CuFeO₂ nanolayer on ZnO NRs is shown in Fig. 5.5(b), recorded at 0.6 and 1.2 V vs. Ag/AgCl. It is evident that with the increase of the thickness of the coating layer the photocurrent has increased significantly to 54 $\mu\text{A}\cdot\text{cm}^{-2}$ (CuFeO₂/ZnO (6 min)) from 12.34 $\mu\text{A}\cdot\text{cm}^{-2}$ (CuFeO₂/ZnO (3 min)), whereas the further increase in the photocurrent for CuFeO₂/ZnO (10 min) is not remarkable (59 $\mu\text{A}\cdot\text{cm}^{-2}$ only) compared to that of CuFeO₂/ZnO (6 min) NHs at a bias of 1.2V vs. Ag/AgCl. This indicates that there is a critical thickness of the coating layer above which the photocurrent cannot be improved and in our work we have found that the CuFeO₂ nanolayer grown beyond 12 min of electrodeposition reduces the photocurrent of the electrode. In general, the increasing CuFeO₂ thickness will enhance the photon absorption and hence contributes to the generation of more photocarriers. On the other hand, as the thickness of the outer layer increases over a critical limit, the charge carriers generated at the CuFeO₂/electrolyte interface would have to travel long path to reach the ZnO and FTO and this enhances the probability of recombination of the carriers as the driving force for carrier separation would gradually become weaker with the increase of the outer layer thickness. [9]

The photoconversion efficiency or solar to hydrogen (STH) efficiency, the measure of PEC water splitting performance of the photoelectrodes that requires an applied voltage upon the illumination of light is evaluated by the following equation: [35]

$$\eta\% = \frac{J_{ph} \times (1.229 - V)}{P_{in}} \times 100\% \quad (5.1)$$

Where J_{ph} is the photocurrent density at measured voltage, V is the applied voltage vs. Ag/AgCl, P_{in} is the power of the illuminated light (10 $\text{mW}\cdot\text{cm}^{-2}$). The photoconversion efficiency of the electrodes as a function of the applied voltage is shown in Fig. 5.5(c). The as prepared ZnO NRs show a maximum photoconversion efficiency of 0.02% at 0.7 V vs. Ag/AgCl, whereas the optimal conversion efficiency of the CuFeO₂/ZnO (10 min) nano-heterostructure is about 0.11%, which is ~450% higher than bare ZnO NRs.

Interestingly, the $\text{CuFeO}_2/\text{ZnO}$ (10 min) nano-heterostructure maintains a steady photoconversion efficiency ($\sim 0.11\%$) within the potential window of 0.4 to 0.8V vs. Ag/AgCl.

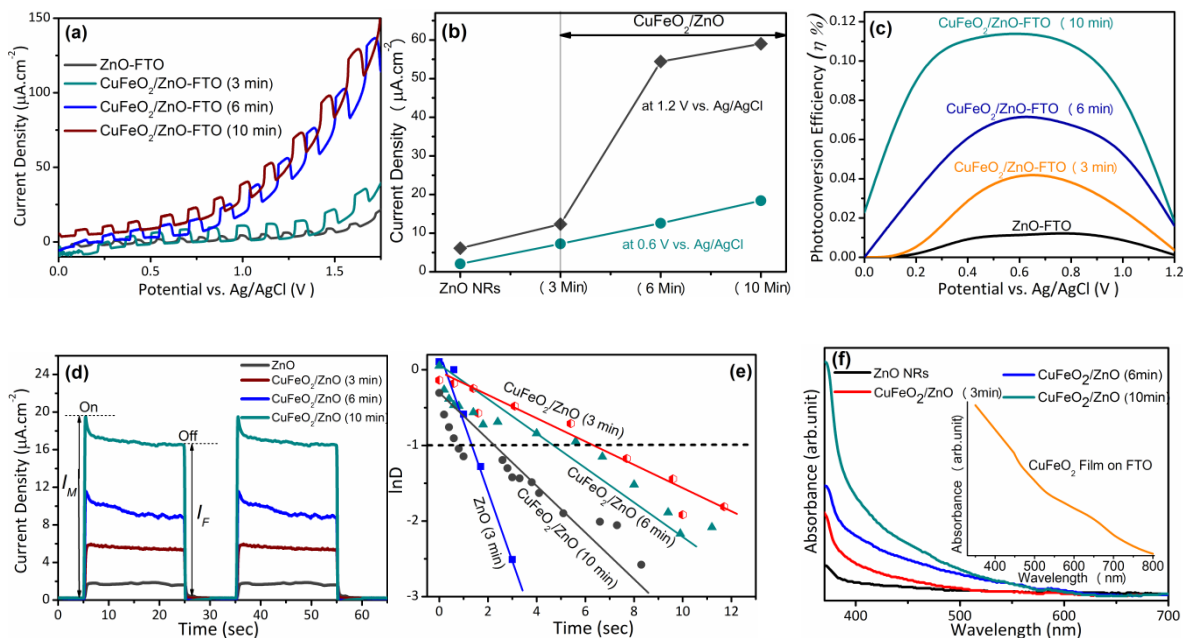


Figure 5.5: (a) Linear sweep voltammetry (LSV) curves for the photoelectrodes performed under chopped visible light, (b) The variation of photocurrent density with the thickness of the p-type shell layer for the as designed nano-heterostructures, (c) photoconversion efficiency of the electrodes under investigation, (d) photoswitching activity of the electrodes, (e) $\ln D$ vs. transient decay time plot and (f) UV-Vis absorption spectra of the as prepared electrodes.

The amperometric $I-t$ curves obtained from the ZnO NRs and different $\text{CuFeO}_2/\text{ZnO}$ NHs photoelectrodes with visible-light on/off cycles (2 cycles) at 0.5 V vs Ag/AgCl are shown in Fig. 5.5(d). The studies on the transient photocurrent decay occurring immediately upon light illumination in $I-t$ curves provide qualitative understanding about the charge recombination characteristics of the photoelectrodes. When the light is switched on, the photocurrent increases immediately with a spike because of the sudden generation of charge carriers due to absorption of light by the photoelectrodes. Immediately after the photocurrent spike, the photocurrent decay occurs, which is attributed to the recombination processes at the electrodes. The

transients in photocurrents in the NHs electrodes are thus attributed to the accumulation of electrons due to the poor electron conduction in CuFeO₂ and the electron-hole pair recombination occurs at the electrode surface. [11, 25, 36] Transient decay time can be evaluated from logarithmic plot of the parameter D , defined as: [11, 37, 38]

$$D = \frac{I_t - I_F}{I_M - I_F} \quad (5.2)$$

where, I_t is the photocurrent at any time t , I_M is the maximum photocurrent spike and I_F is the steady state photocurrent (when the recombination and charge generation reaches equilibrium). The transient decay time for the electrodes is defined as the time at which $\ln D = -1$. [11] Figure 5.5(e) shows the plots of the $\ln D$ vs. transient decay time for the different electrodes. The transient decay time for CuFeO₂/ZnO (3 min) NHs electrode is 6.3s, which is five times longer than the transient decay time of bare ZnO NRs (1.2s). For the CuFeO₂/ZnO NHs it is found that with the increase of the CuFeO₂ nanolayer thickness on ZnO NRs the transient decay time gradually decreases from 6.3s (CuFeO₂/ZnO (3 min)), to 4.6s (CuFeO₂/ZnO (6 min)) to 2.4 (CuFeO₂/ZnO (10 min)). However, the longer transient decay time observed for the CuFeO₂/ZnO NHs compared to the bare ZnO NRs indicates the lower charge carrier recombination rate of the NHs compared to the ZnO NRs, which is because of the reduction of surface states in ZnO due to the coating of CuFeO₂. The gradual decrease in the transient decay time in the NHs electrodes with the increase of CuFeO₂ layer thickness suggests the accumulation of electrons in the outer layer due to the increase of the thickness of poor conducting CuFeO₂ nanolayer on ZnO NRs.

To gain more clear idea about the charge carrier generation in the electrodes the light absorption property of the electrodes has been studied. Figure 5.5(f) shows the UV-Vis absorption spectra for the ZnO NRs and different CuFeO₂/ZnO NHs. It is evident that the ZnO NRs exhibit sharp band edge absorption in UV region ~ 381 nm (3.26 eV). All the CuFeO₂/ZnO NHs show very similar band-edge absorption like the bare ZnO NRs except significantly enhanced absorbance in the visible region,

particularly within the wavelength region of 400-600 nm. As usual, the visible light absorption behavior for the NHs increases with the increase of the thickness of the CuFeO₂ nanolayer. The CuFeO₂/ZnO (10 min) electrode exhibits six times higher light absorption than the bare ZnO NRs at the wavelength of 450 nm. The remarkably enhanced visible light absorption property of the CuFeO₂/ZnO (10 min) compared to other NHs electrodes confirms the generation of large number of charge carriers in the same. Although the charge carrier recombination rate in CuFeO₂/ZnO (10 min) electrode is higher compared to other electrodes (based on the transient decay time studies), still the generation of the largest numbers of carriers in the same due to visible light absorption makes it the most effective electrode with maximum photocurrent and STH efficiency. All the electrodes also exhibit sharp absorption edge in the UV region, which is found to be red shifted, compared to the pristine ZnO NRs and this is most expectedly because of the formation of shallow defect levels/interfacial states near the band edge as a result of the formation of heterojunction. [10, 39] The UV-Vis absorption spectra of the *p*-CuFeO₂ thin film grown on FTO substrate shown in the inset of Fig. 5.5(f) demonstrate the shape absorption edge of the same around ~800 nm, which corresponds to the band gap (~1.55 eV) of CuFeO₂. [24] This indicates that the CuFeO₂ having favorable optical band gap energy is suitable for enhanced visible light absorption to generate large concentration of electron-hole pairs.

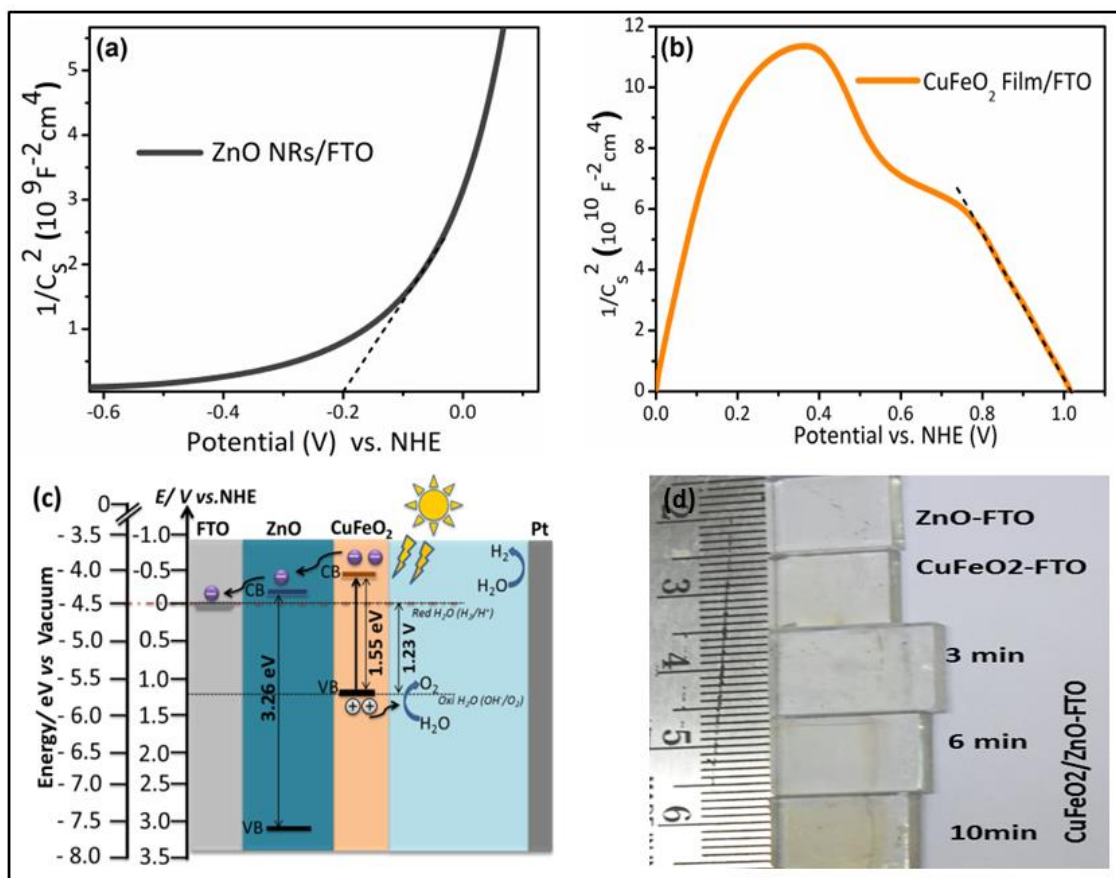


Figure 5.6: Mott-Schottky plots of (a) pristine ZnO NRs and (b) CuFeO₂ thin films grown on FTO. (c) The approximate band position of the FTO, ZnO and CuFeO₂ at pH 0 along with the charge carrier separation and transportation in the heterojunction electrode. (d) The photographs of the as prepared electrodes.

For detail understanding of the inherent mechanism of charge carrier generation, carrier separation and carrier transportation in the *p-n* type NHs electrode, the electronic energy levels of the as prepared ZnO and CuFeO₂ on FTO have been investigated using the electrochemical impedance measurements. The position of the flat-band potential (V_{fb}) for ZnO and CuFeO₂ grown on FTO has been determined from the Mott-Schottky plots (Fig. 5.6(a) and (b)) using the Mott-Schottky equation: [10, 22, 24, 25]

$$\frac{1}{C_s^2} = \frac{2}{e\epsilon\epsilon_0 A^2 N_d} \left(V - V_{fb} - \frac{kT}{e} \right) \quad (5.3)$$

where C_s is space charge layer capacitance, e is the electronic charge, ϵ is the dielectric constant of the semiconductor, ϵ_0 is the permittivity of the free space, V is applied potential, A is the area of the electrode, N_d is the majority carrier density and kT/e is a temperature dependent correction term. The V_{fb} can be determined by setting $\frac{1}{C_s^2}$ to be zero, which is extrapolation of X-axis intercepts in the Mott–Schottky plots. The positive slope for the ZnO NRs on FTO (Fig. 5.6(a)) indicates the n -type behavior of the semiconductors with electrons as majority charge carriers. The value of V_{fb} is -0.21 V vs. NHE, for the as prepared ZnO NRs, where $E(\text{NHE}) = E(\text{Ag}/\text{AgCl}) + 0.197$ (unit in V). [15] On the other hand, the Mott–Schottky plot for CuFeO₂ (Fig. 5.6(b)) indicates a typical p -type behavior, where the near zero value of $\frac{1}{C_s^2}$ in the first region (accumulation region) of the curve is because of the anodic voltages of the V_{fb} . [28] The second region the $\frac{1}{C_s^2}$ shows a negative slope from which the flat-band potential of CuFeO₂ is estimated to be +1.01 V vs. NHE, close to the reported value. [29] The position of the V_{fb} in the n -type semiconductors indicates the position of the bottom of the conduction band of the semiconductor. [41, 42] Similarly, the position of the valence band maxima edge in p -type semiconductors is assumed to be 0.1-0.2 eV (vs. vacuum) below the flat band potential [24, 43], Now, based on the calculated values of V_{fb} and the band gap energy for ZnO and CuFeO₂, obtained from UV-Vis absorption study, the position of the corresponding conduction and valence band edges are estimated and shown schematically in Fig. 5.6(c). Now, because of the formation of a favorable p - n CuFeO₂/ZnO junction the photogenerated electrons in the conduction band of the p -CuFeO₂ spontaneously transfer to the ZnO NRs and finally to the FTO. Generally, for p -type semiconductors the photogenerated electrons move into the electrolyte because of the favorable band bending at p -type electrode/electrolyte interface [25], but in this experiment the corresponding band position and band bending at the p - n heterointerface is more suitable for electron transport towards the ZnO NRs from the p -CuFeO₂ instead of the same towards the electrolyte from p -CuFeO₂ as shown in Fig. 5.6(c). Therefore, here the p -CuFeO₂/ n -ZnO NHs acts like a photoanode with enhanced

charge carrier separation, which considerably reduces the electron-hole pair recombination in p -CuFeO₂ along with its enhanced light absorption property. The photogenerated electron will finally reach Pt electrode via FTO and contribute in the H₂ generation. The photogenerated holes in the valence band of p -CuFeO₂ will easily reach the electrode surface and contribute in O₂ generation through water oxidation. Therefore, this unique strategy for designing the p - n type NHs photoanode provides enhanced photoelectrochemical performance based on the engineering of the band structure at nano-heterointerface.

More information about the charge transfer process at the semiconductor/electrolyte interface can be obtained from the EIS studies on the electrodes. [44] Figure 5.7(a) shows the Nyquist plots for the ZnO NRs and CuFeO₂/ZnO NHs photoanodes, plotted at a bias of 0 V vs Ag/AgCl, with 5mV ac perturbation over the frequency range of 10 Hz to 1MHz under the illumination of visible light. The EIS measurements vividly demonstrate the change in the interfacial charge carrier dynamics of the ZnO NRs after the coating of p -CuFeO₂ nanolayer. Generally, the shape of the Nyquist plots strongly depends upon the applied voltage used for the measurement and we also have noticed such variation in shape with applied voltage. However, from the J - V curve (Fig. 5.5(a)) it is also evident that the rate of charge transfer in the NHs photoanodes is significantly higher than the rate of charge recombination in the same compared to the pristine ZnO NRs. Hence, as expected, at the applied bias of 0 V vs Ag/AgCl the Nyquist plot of the photoanodes shows only one large arc (semicircle), [45] which corresponds to the charge transfer process at electrode/electrolyte interface and here the arc diameter in Nyquist plot is the measure of charge transfer rate. The gradual reduction of the arc diameter in EIS spectrum in the CuFeO₂/ZnO NHs compared to ZnO NRs indicates significant improvement in the charge transfer at the electrode/electrolyte interface due to the formation of p -CuFeO₂ nanolayer on ZnO NRs. The equivalent circuit corresponding to the Nyquist plots of the CuFeO₂/ZnO NHs electrodes is shown in the inset of Figure 5.7(a). Here, R_s is the resistance of the electrolyte solution between the working electrode and Pt electrode. R_{ct}

is the charge transfer resistance of CuFeO_2 nanolayers for the $\text{CuFeO}_2/\text{ZnO}$ NHs electrodes. For $\text{CuFeO}_2/\text{ZnO}$ NHs (10 min) electrode, R_{ct} is measured to be $18.05 \Omega \text{ cm}^2$. C_1 is the capacitance of CuFeO_2 layer. R_2 and C_2 are the resistance and capacitance of ZnO NRs, respectively.

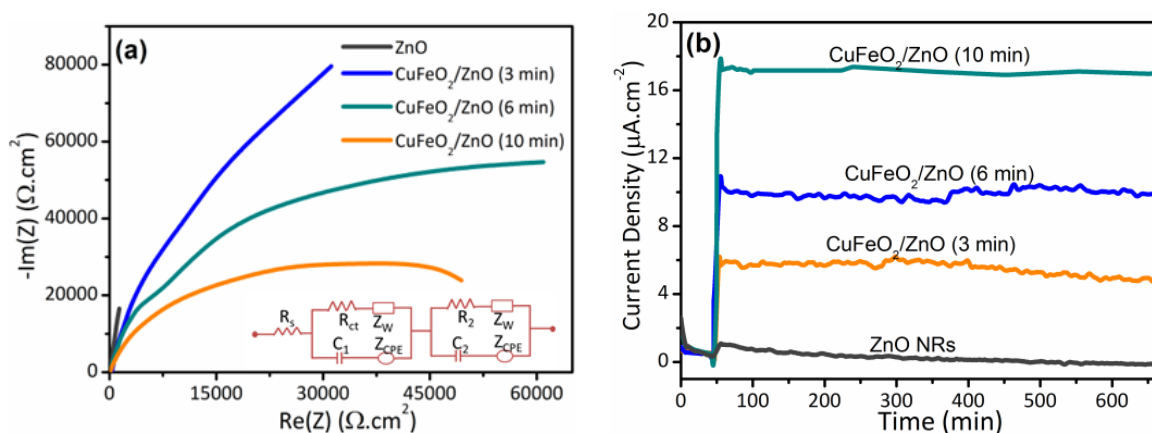


Figure 5.7: (a) Nyquist plots for different photoelectrodes recorded at 0V vs. Ag/AgCl. (b) The photocurrent stability of different photoelectrodes under the visible light illumination.

Considering the practical application of the photoanodes, the stability of the same has been tested for 10 hours as shown in Fig. 5.7(b). The as prepared ZnO NRs photoanode exhibits very unstable photocurrent where the photocurrent is found to decrease constantly over the time frame. This result indicates significant recombination of the photogenerated carriers at the surface of ZnO NRs because of the surface defects. On the contrary all the $\text{CuFeO}_2/\text{ZnO}$ NHs photoanodes show remarkably enhanced photocurrent stability and the photocurrent decreases only about 14%, 2% and 2% for the $\text{CuFeO}_2/\text{ZnO}$ (3 min), $\text{CuFeO}_2/\text{ZnO}$ (6 min), and the $\text{CuFeO}_2/\text{ZnO}$ (10 min), respectively, after 600 mins. Therefore, the p - CuFeO_2 nanolayer also improves the stability of the photoanodes remarkably. From Fig. 5.7(b), it is found that the photocurrent decreases after the initial peak current because of light illumination and this is due to the recombination of the photocarriers immediately after photo-generation. However, it is also found that after a long run, the photocurrent density of the $\text{CuFeO}_2/\text{ZnO}$ (6 min), and the $\text{CuFeO}_2/\text{ZnO}$ (10 min) electrodes increases a little and this might be because of thermal liberation of electrons from the available shallow

trap states near the conduction band edges upon long time light illumination. [46] In fact, it is found that the CuFeO₂/ZnO NHs electrodes contain more interfacial trap states than others as evidenced from the UV absorption studies.

5.4 Conclusion

In summary, this work demonstrates an effective strategy for the easy and cost effective fabrication of well-distributed regular array of a novel *p-n* CuFeO₂-ZnO nano-heterostructure by combining the electrodeposition and chemical synthesis for potential application in visible light PEC device. The thickness of the *p*-CuFeO₂ outer layer has a crucial role to control the PEC property of the photoelectrodes, where the electrodeposition of *p*-CuFeO₂ for 10 minutes provides the optimal thickness of the outer layer to maximize the PEC performance of the nano-heterostructure. The same sample exhibits the maximum light absorption efficiency and photocurrent density (58 μA. cm⁻² at 1.23 V vs Ag/AgCl). The photoconversion efficiency of the CuFeO₂/ZnO (10 min) nano-heterostructure photoanode is also maximum among the photoelectrodes and it is ~450% higher than the pristine ZnO NRs. The large transient decay time for the CuFeO₂/ZnO nano-heterostructures compared to the pure ZnO NRs indicates the lower charge carrier recombination rate in the nano-heterostructures compared to the pristine ZnO NRs leading to enhance charge carrier separation in the nano-heterostructures. The transient decay time for the CuFeO₂/ZnO NHs decreases with the increase of the thickness of CuFeO₂ nanolayer. Still the CuFeO₂/ZnO (10 min) shows the best PEC performance, mainly because of the improved light absorption resulting large number of photogenerated charge a carrier, where the number of the photogenerated electrons at the conduction band is still higher than other electrodes after the initial recombination of the electron-hole pair just after the illumination of the light. Furthermore, the EIS study demonstrates the most efficient charge transfer at the electrode/electrolyte interface for the CuFeO₂/ZnO (10 min) electrode. Based on the experimental results and the proposed *p-n* junction band engineering it is evident that the CuFeO₂-ZnO NHs exhibit excellent visible light absorption, large charge carrier

generation, low electron-hole recombination rate and good transportation of electron towards the Pt electrode because of favorable energy band tuning resulting the enhanced PEC performance for solar water oxidation. Overall, this nano-engineering design strategy could also be employed to other solar energy harvesting devices where large charge carrier generation, low carrier recombination and good charge transportation are the basic requirements to enhance the PEC efficiency.

Bibliography

- [1] K. Karmakar, A. Sarkar, K. Mandal and G. G. Khan. *Nanotechnology*, **28**, 325401 (2017)
- [2] M Grätzel, *Nature*, **414**, 338 (2001)
- [3] M. G. Walter, E. L. Warren, J. R. McKone, S. W. Boettcher, Q. Mi, E. A. Santori, N. S. Lewis, *Chem. Rev.*, **110**, 6446 ((2010)
- [4] J. Brillet, J-H. Yum, M. Cornuz, T. Hisatomi, R. Solarska, J. Augustynski M. Graetzel, K. Sivula , *Nature Photonics*, **6**, 824 (2012)
- [5] M. S. Prévot, K. Sivula, *J. Phys. Chem. C*, **117**, 17879 (2013)
- [6] X. Shi, H. Jeong, S. J. Oh, M. Ma, K. Zhang, J. Kwon, I. T. Choi, Y. Choi, H. K. Kim, J. K. Kim and J. H. Park, *Nature Communications*, **7**, 11943 (2016)
- [7] A. Fujishima and K. Honda , *Nature*, **238**, 37 (1972)
- [8] J. Li and N. Wu, *Catal. Sci. Technol*, **5**, 1360 (2015)
- [9] Y. Mi, L. Wen , R. Xu , Z. Wang , D. Cao , Y. Fang and Y. Lei , *Adv. Energy Mater.*, **6**, 1501496 (2016)
- [10] Moniz S J A, Zhu J and Tang J , *Adv. Energy Mater.*, **4**, 1301590 (2014)
- [11] L. Zhang, E. Reisner and J. J. Baumberg, *Energy Environ. Sci.*, **7**, 1402 (2014)
- [12] Wanhong H, Yang Y, Wang L, Yang J, Xiang X, Yan D and Li F , *ChemSusChem*, **8**, 1568 (2015)
- [13] Tang Y, Wang R, Yang Y, Yan D and Xiang X, *ACS Appl. Mater. Interfaces*, **8**, 19446 (2016)
- [14] W. He, R. Wang, L. Zhang, J. Zhu, X. Xiang and F. Li, *J. Mater. Chem. A*, **3**, 17977 (2015)
- [15] Yang X, Wolcott A, Wang G, Sobo A, Fitzmorris R C, Qian F, Zhang J Z and Li Y ,*Nano Lett.*, **9** (9), 2331 (2009)
- [16] J. Zhang, X. Jin, P. I. M. Guzman, X. Yu, H Liu, H Zhang, L. Razzari, J P Claverie, *ACS Nano*, **10**, 4496 (2016)

-
- [17] Wei Y, Ke L, Kong J, Liu H, Jiao Z, Lu X, Du H, Sun X W , *Nanotechnology*, **23**, 235401 (2012)
- [18] G. Wang, X. Yang, F. Qian, J.Z. Zhang and Y. Li , *Nano Lett.*, **10**, 1088 (2010)
- [19] K. Karmakar, A. Sarkar, K. Mandal and G. G. Khan, *ACS Sustainable Chem. Eng*, **4**, 5693 (2016)
- [20] Y. Li, Z. Lu, X. Xu, D. Yan and F. Li, *J. Mater. Chem. A*, **2**, 13250 (2014)
- [21] Xu. Xiang, L. Xie, Li. Zhiwei and F. Li, *Chemical Engineering Journal*, **221**, 222 (2013)
- [22] R. Wang, K. Pan, D. Han, J. Jiang, C. Xiang, Z. Huang, Lu Zhang and Xu. Xiang, *ChemSusChem*, **9**, 2470 (2016)
- [23] J. R. Smith, H. V. Steenkis Thomas and X. G Wang *Phys. Rev. B*. **79**, 041403 (2009)
- [24] C. G. Read, Y. Park and K. S. Choi, *J. Phys. Chem. Lett.*, **3**, 1872 (2012)
- [25] M. S. Prévot, Y. Li, N. Guijarro and K. Sivula, *J. Mater. Chem. A*, **4**, 3018 (2016)
- [26] J. Gu, Y. Yan, J. W. Krizan, Q. D. Gibson, Z. M. Detweiler, R. J. Cava and A. B. Bocarsly, *J. Am. Chem. Soc.*, **136**, 830 (2014)
- [27] I. H. Cardona, F. F. Santiago, A. Renaud, B. J. López, F. Odobel, L. Cario, S. Jobic and S. Giménez , *Electrochim. Acta*, **113**, 570 (2013)
- [28] M. S. Prévot, N. Guijarro and K. Sivula, *ChemSusChem*, **8**, 1359 (2015)
- [29] U. Kang, S. K. Choi, D. J. Ham, S. M. Ji, W. Choi, D. S. Han, A. Abdel-Wahab and H. Park, *Energy Environ. Sci.*, **8**, 2638 (2015)
- [30] J. Gu, A. Wuttig, J. W. Krizan, Y. Hu, Z. M Detweiler, R. J. Cava and A. B. Bocarsly, *J. Phys. Chem. C*, **117**, 12415 (2013)
- [31] C. D. Wanger, W. M. Riggs, L. E. Davis, J. F. Moulder and G. E. Muilenberg, *Handbook of X-ray Photoelectron Spectroscopy Physical Electronics Eden Prairie Minnesota USA* (1979)
- [32] Y. V. Kaneti, Q. M. D. Zakaria, Z. Zhang, C. Chen, J. Yue, M. Liu, X.Jiang and A. Yu , *J. Mater. Chem. A*, **2**, 13283 (2014)

-
- [33] L. Chen, Q. Gu, L. Hou, C. Zhang, Y. Lu, X. Wang and J. Long, *Catal. Sci. Technology*, **7**, 2039 (2017)
- [34] S. P. Pavunny, A. Kumar and R. S. Katiyar, *Journal of Applied Physics*, **107**, 013522 (2010)
- [35] M. G. Walter, E. L. Warren, J. R. McKone, S. W. Boettcher, Q. Mi, E. A. Santori and N. S. Lewis, *Chem. Rev.*, **110**, 6446 (2010)
- [36] X. Shi, K. Zhang and J. H. Park, *International Journal of Hydrogen Energy*, **38**, 12725 (2013)
- [37] A. Hagfeldt, H. Lindstroem, S. Soedergren and S. E. Lindquist, *J. Electroanal. Chem.*, **381**, 39 (1995)
- [38] N. J. Bell, Y. H. Ng, A. Du, H. Coster, S. C. Smith and R. Amal, *J. Phys. Chem. C*, **115**, 6004 (2011)
- [39] A. Sarkar, A. K. Singh, G. G. Khan, D. Sarkar and K. Mandal, *RSC Advances*, **4**, 55629 (2014)
- [40] Wolcott A, Smith W A, Kuykendall T R, Zhao Y and Zhang J Z, *Adv. Funct. Mater.*, **19**, 1849 (2009)
- [41] Aviles M A A and Wu Y, *J. Am. Chem. Soc.*, **131**, 3216 (2009)
- [42] J. L. White, M. F. Baruch, J. E. Pander III, Y. Hu, I. C. Fortmeyer, J. E. Park, T. Zhang, K. Liao, J. Gu, Y. Yan, T. W. Shaw, E. Abelev and A. B. Bocarsly, *Chem. Rev.*, **115**, 12888 (2015)
- [43] C. G. Morales-Guio, S. D. Tilley, H. Vrubel, M. Gratzel and X. L. Hu, *Nat. Commun.*, **5**, 1 (2014)
- [44] L. Bertoluzzi and J. Bisquert, *J. Phys. Chem. Lett.*, **3**, 2517 (2012)
- [45] J. R. Ran, J. Zhang, J. G. Yu, M. Jaroniec and S. Z. Qiao, *Chemical Society Reviews*, **43**, 7787 (2014)
- [46] A. Dekker, *J Solid State Physics, MacMillan India Ltd. India* (2011)

Chapter 6

1D-2D Nano-Heterojunction Photoanodes for Solar Fuel

This chapter describes the fabrication process of multidimensional nano-heterostructure based photoelectrodes by coupling the multilayered two-dimensional (2D) structure of MoS₂ and MoO₃ on the well aligned arrays of one-dimensional (1D) ZnO nanorods template expecting the effective synergic effects. This chapter also demonstrates the photoelectrochemical performances of the as fabricated photoelectrodes for the ZnO/MoS₂ heterostructures for the production of solar fuel through water splitting.

6.1 Preamble

Photoelectrochemical (PEC) water splitting using abundant solar energy is the most attractive way to produce solar fuel (hydrogen) with zero emission of carbon dioxide.[1,2] The PEC water splitting involves oxygen evolution reaction (OER) at the photoanode and hydrogen evolution reaction (HER) at the photocathode of the electrochemical cell.[3] The overall rate of water splitting is generally limited by sluggish kinetics for OER and the large overpotential resulting from the complex four-electron redox process at the photoanodes.[4] Hence, designing of photoanodes is a challenging task for efficient PEC water splitting. As the *n*-type semiconductors have shown promise as the photoanodes, hence, different *n-n* type or *n-p* type nano-heterostructures (NHs) photoelectrodes [3,5–10] have been designed based on the *n*-type semiconductors as the core material to boost the PEC water splitting. The nano-heterojunction based photoanodes are found to be effective for fast OER, offering enhanced light absorption and better photo-induced charge carrier separation and transportation required for enhanced PEC performance. [3,5–10] The studies have shown that the choice of appropriate electrode materials as well as the suitable architecture/design of the electrodes governs the performance of the electrode for water splitting.

Recently, two-dimensional (2D) graphene like transition metal oxides and dichalcogenides have attracted importance for energy related applications considering their superior physical and chemical properties.[11–13] The 2D materials have advantages like high specific area and unique in-plane electron transfer properties due to the confinement of electrons in their atomic layers.[14,15] The 2D layered crystal structures of molybdenum trioxide (MoO₃) and molybdenum disulfide (MoS₂) have been investigated as the promising material for electrodes.[12,14,16–18] Specially, the 2D layered structures of *n*-type semiconductor α -MoO₃ (band gap ~3.1 eV) has drawn attention because of its superior electrochemical and catalytic properties.[12,16] On the other hand, the nontoxic and earth abundant *p*-type layered MoS₂ (band gap ~1.85 eV)

has also been extensively studied both as the electrocatalytic and photocatalytic water splitting because of its unique electrochemical properties.[9,19,20] However, the fast recombination of photo-generated charge carriers and the poor conductivity of carries in 2D structure of MoS₂ and MoO₃ limit their applications in PEC cell.[9,21]

In this context, here we have designed a new type multidimensional 2D-1D nano-heterostructure (NHs) by anchoring 2D multilayered structure of MoS₂ and MoO₃ on the aligned arrays of 1D ZnO nanorods (NRs) template. An easy and scalable wet chemical method is employed for the 1D ZnO NRs template based growth of multilayered 2D structure of MoS₂ and MoO₃, which is found to provide ordered orientation and uniform thickness of the 2D nanolayers. Here, 1D ZnO NRs are chosen as core expecting the benefit of suitable band position of ZnO for water splitting, unidirectional charge transportation for 1D structure and better photocatalytic activity arising because of the large surface area.[20,22] Moreover, the NHs composed of layered 2D structure of MoS₂/MoO₃ and 1D ZnO NRs with the dangling bonds at their surface is expected to introduce novel functionality because of the nanoscale integration and the interfacial band alignment between the 2D-1D structures.[23,24] The synergistic effect of 2D layered MoS₂/MoO₃ and 1D ZnO NRs is expected to provide higher visible light absorption, efficient separation of interfacial photogenerated charge carriers and rapid charge transportation to the current collector leading to enhanced photoelectrochemical activity.[20,23,25,26] The 2D-1D NHs are found to exhibit excellent broadband light absorption, where the photocurrent density for ZnO/MoO₃ NHs and ZnO/MoS₂ NHs are found to be 0.67 and 2.04 mA cm⁻² at 1.23 V versus RHE, respectively, leading to the photoconversion efficiency as high as 0.3% and 0.67%, respectively, under applied bias. The 2D-1D interfacial band alignment also significantly suppresses the surface charge recombination of photogenerated excitons leading to photocarrier separation and rapid carrier transportation providing enhanced functionality for solar fuel production.

6.2 Experimental Section

6.2.1 Reagents

FTO (fluorine doped tin oxide, Sigma Aldrich) substrate, Zinc acetate dihydrate ($\text{Zn}(\text{CH}_3\text{COO})_2 \cdot 2\text{H}_2\text{O}$), hexamethylenetetramine ($(\text{CH}_2)_6\text{N}_4$), ethyl alcohol ($\text{C}_2\text{H}_5\text{OH}$), ammonium tetrathiomolybdate, *N, N*-dimethyl formamide.

6.2.2 Preparation of ZnO NRs

The 1D ZnO NRs over fluorine doped tin oxide (FTO) substrates were prepared following the previous work. Briefly, first of all the ZnO seed layer was prepared on FTO by spin coating (2000 rpm at 25°C) using the precursor of 0.1 M zinc acetate prepared in ethanol solution and the sample were annealed at 350°C for 2 hours in air. Afterwards, the ZnO NRs were grown by dipping this ZnO seed layered FTO in a precursor solution of zinc acetate and hexamethylenetetramine (1: 1) for 2 hours at 90°C.

6.2.3 Preparation of ZnO/MoS₂ and ZnO/MoO₃ NHs Photoanodes

The 2D layers of molybdenum oxide and chalcogenide were deposited over the 1D ZnO NRs array using simple wet chemical method through spin coating at 2000 rpm for 1 minute at 25°C. The ammonium tetrathiomolybdate (0.1 M) dissolved in *N, N*-dimethyl formamide was used as precursor solution. Finally, the ZnO/MoO₃ and ZnO/MoS₂ NHs samples were prepared by annealing at 400°C for one hour in air and argon atmosphere separately, respectively.

6.2.4 Material Characterizations

The morphology of the as prepared ZnO NRs and ZnO/MoO₃ and ZnO/MoS₂ NHs photoanodes were characterized by field emission scanning electron microscope (FESEM, FEI Quanta-200 Mark-2) and transmission electron microscopy (TEM, JEOL JEM 2100). The crystal structure of the samples were investigated with grazing incidence X-ray diffraction (GIXRD, Panalytical X'Pert Pro diffractometer) using the Cu K_α radiation ($\lambda = 1.54 \text{ \AA}$) with a step size of 0.15° and high resolution TEM (HRTEM). The elemental composition of the samples was studied with energy dispersive X-ray

spectroscopy (EDS, Oxford Instruments) equipped with the FESEM and energy filtered TEM. The chemical composition and states of the sample surface were investigated by X-ray photoelectron spectroscopy (XPS) with an Al K_{α} ($h\nu = 1253.6$ eV) radiation. The UV-Vis absorption spectra of the electrodes were recorded using a Perkin Elmer Lambda 1050 UV/Vis spectrophotometer in the spectral range of 250-700 nm. The room temperature steady state photoluminescence (PL) and the time-resolved photoluminescence (TRPL) were recorded using a Horiba, FluoroLog-3 spectrophotometer.

6.2.5 PEC Measurements

PEC studies of the as prepared electrodes were conducted using a typical three-electrode electrochemical workstation (CHI660E, with working electrode: photoanodes, counter electrode: Pt; reference electrode: Ag/AgCl) under the illumination of 100 mWcm⁻² solar light coming from a 100 W Xe lamp coupled with an AM 1.5 G filter available from a LCS-100 solar simulator (Newport, Model 94011A). The linear sweep voltammetry (LSV), $i-t$ amperometry, open-circuit potential vs. time plot, Tafel plot and the Nyquist plot of the electrochemical impedance spectroscopy (EIS) studies were performed in the 0.5 Na₂SO₄ electrolyte of pH 6.4. To study the overall PEC water splitting, the PEC studies of the photoelectrodes were conducted in an air-tight cell at 1.23 V versus RHE under AM 1.5 G illumination and the amount of gases was measured with a gas chromatograph. The potentials versus RHE were converted from the potentials versus Ag/AgCl by using the following equation: [27]

$$E_{RHE} = E_{Ag/AgCl} + 0.059 \times \text{pH} + E_{Ag/AgCl}^0 \quad (6.1)$$

where, E_{RHE} and $E_{Ag/AgCl}$ are the converted potential versus RHE and the measured potential versus Ag/AgCl, respectively, and the value of $E_{Ag/AgCl}^0$ is 0.197 V at 25 °C. The ABPE can be calculated using the following equation: [28]

$$\eta\% = \frac{J_{ph} \times (1.229 - V)}{P_{in}} \times 100\% \quad (6.2)$$

where, J_{ph} refers to the photocurrent density (mA cm⁻²) obtained from the different photoelectrodes. V represents the applied bias versus RHE (V), and P_{in} represents the

total incident light intensity of AM 1.5 G (100 mW cm^{-2}). The EIS spectra were recorded with an AC voltage amplitude of 10 mV at the open circuit potentials of the electrodes under AM 1.5 G illumination in the frequency range of 1 Hz-100 kHz.

6.3 Results and Discussion

6.3.1 Morphology and Crystallography Study

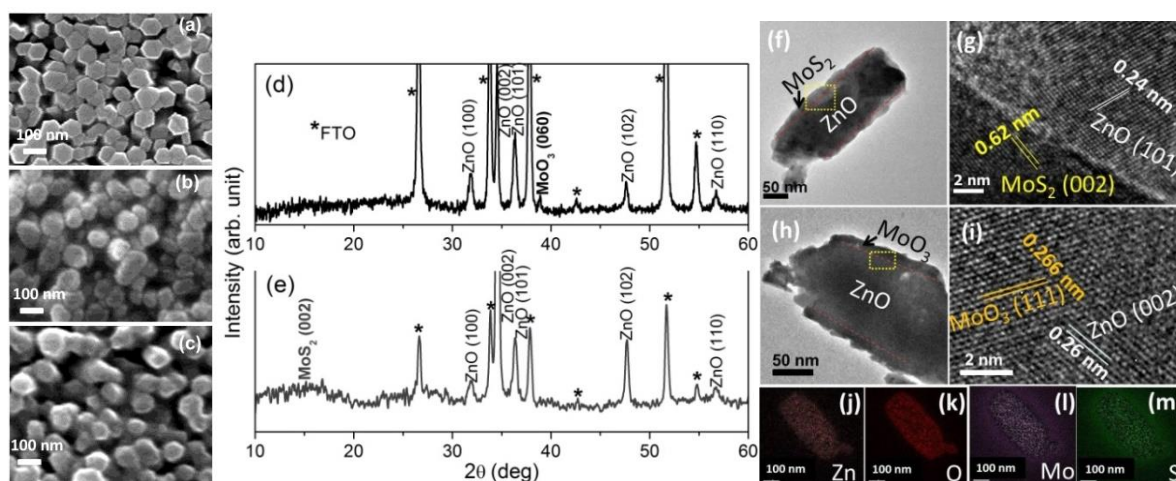


Figure 6.1: FESEM images of (a) ZnO NRs, (b) ZnO/MoO₃ NHs and (c) ZnO/MoS₂ NHs as grown on FTO substrate. Grazing Incidence X-ray diffraction (GIXRD) pattern of (d) ZnO/MoO₃ NHs and (e) ZnO/MoS₂ NHs. (f) TEM micrograph and (g) HRTEM micrographs of ZnO/MoS₂ NHs. (h) TEM micrograph and (i) HRTEM micrograph of ZnO/MoO₃ NHs. (j)-(m) EFTM color mapping for different elements present in ZnO/MoS₂ NHs.

Figure 6.1(a)-(c) show the top view FESEM micrographs of the as fabricated ZnO NRs, ZnO/MoO₃ NHs and ZnO/MoS₂ NHs grown on FTO substrate, respectively. Fig. 1(a) shows that the arrays of ZnO NRs of hexagonal shape having dimension $\sim 100 \text{ nm}$ have grown vertically on FTO. It is evident from Fig. 6.1(b) and (c), that the original hexagonal shape of the ZnO NRs is distorted because of the coating of MoO₃ and MoS₂ on ZnO NRs. However, the smoothness and the distinct nature of the individual ZnO/MoO₃ and ZnO/MoS₂ NHs designate that both the MoO₃ and MoS₂ have grown uniformly following the surface of 1D ZnO NRs. The GIXRD pattern of the ZnO/MoO₃

and ZnO/MoS₂ NHs are shown in Fig. 6.1(d) and (e), respectively. It is evident that both the as grown MoO₃ and MoS₂ are exhibiting single crystalline nature with unidirectional growth along [060] and [002] direction, respectively, on the ZnO NRs surface. It is found that the crystal structure of the as grown MoO₃ is matching with α -MoO₃ (orthorhombic structure, JCPDS No. 05-0508), which is reported to grow in the form of a layered structure.[29,30] In Fig. 6.1(e), the broad XRD peak around 14° correspond to the (002) peak of layered MoS₂ structure with lattice spacing of 0.62 nm (JCPDS 37-1492).[31-33] The as grown ZnO NRs are found to be polycrystalline in nature with preferred orientation along [002] direction (see previous chapters).

The structure of the as grown NHs was further probed by TEM and HRTEM. The TEM micrographs for both the ZnO/MoS₂ and ZnO/MoO₃ NHs shows the rod like 1D structure of the NHs having well covered uniform coating of MoS₂/MoO₃ on ZnO NRs (Fig. 6.1(f) & (h)). The HRTEM images for both the ZnO/MoS₂ and ZnO/MoO₃ clearly indicate the growth of layered structure of MoS₂ and MoO₃ on ZnO NRs (Fig. 6.1(g) & (i)). Fig. 6.1(g) also shows the heterojunction of ZnO and MoS₂ where, the interplanar spacing of 0.24 and 0.62 nm corresponds to (101) plane of ZnO NRs and (002) plane of MoS₂, respectively.[31] Hence, the HRTEM study of ZnO/MoS₂ NHs indicates the single crystalline 2D layered structure of MoS₂. However, the HRTEM image of ZnO/MoO₃ NHs (Fig. 6.1(i)) indicates that the interplanar spacing of 0.266 and 0.26 nm corresponds to the MoO₃ (111) and ZnO (002) crystallographic planes, respectively. However, this result demonstrates that the as grown MoO₃ layers on ZnO NRs is not single crystalline in nature as indicated from the GIXRD pattern. The energy filtered TEM (EFTEM) colour images for the ZnO/MoS₂ NHs (Fig. 6.1(j)-(m)) show the elemental distribution of zinc, oxygen, molybdenum and sulphur, respectively, which essentially proves that the core of ZnO/MoS₂ NHs contains only zinc and oxygen whereas, molybdenum and sulphur are present throughout the surface of the NHs.

6.3.2 XPS Analysis

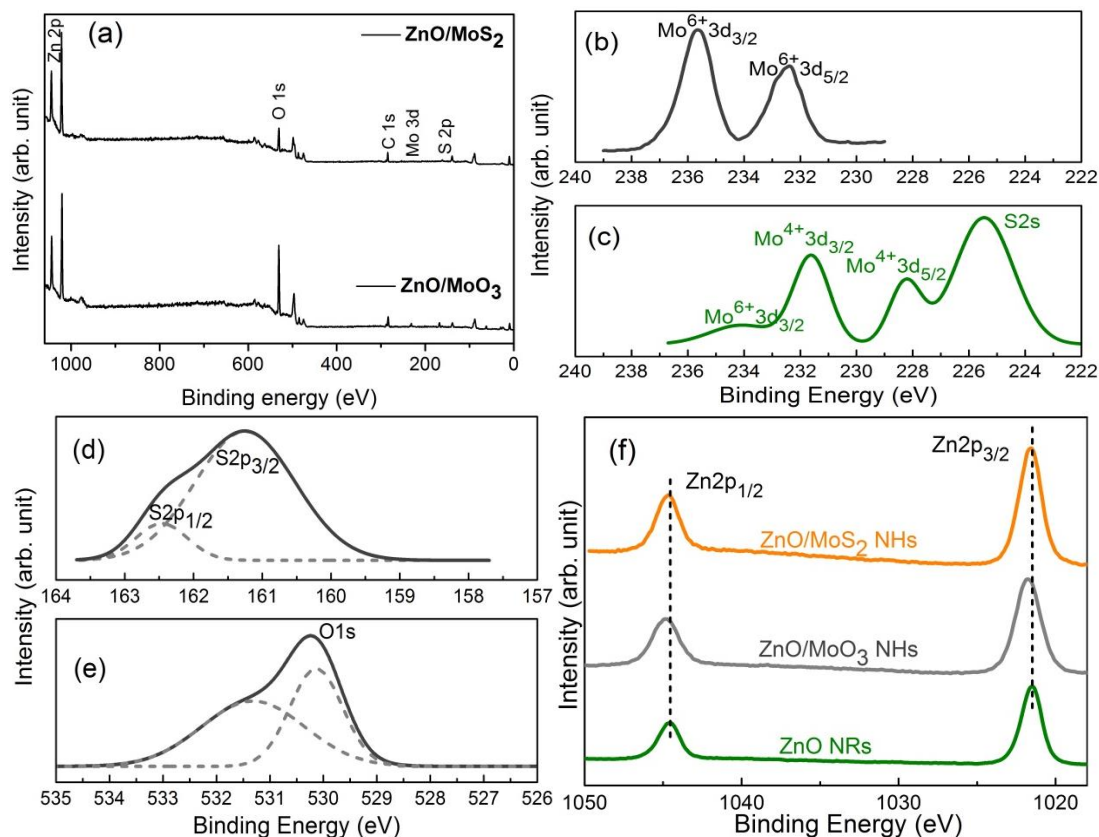


Figure 6.2: XPS (a) survey scan for ZnO/MoS₂ and ZnO/MoO₃ NHs, (b) Mo3d, (c) Mo3d and S2s, (d) S2p (e) O1s and (f) Zn2p core levels.

Figure 6.2(a) shows the XPS surface survey spectra of ZnO/MoO₃ and ZnO/MoS₂ NHs. Figure 6.2(b) and (c) show the core level XPS spectra of Mo 3d obtained from the ZnO/MoO₃ and ZnO/MoS₂ NHs, respectively. In Fig. 6.2(b), the doublet peak appear at 235.5 and 232.4 eV correspond to the Mo 3d_{3/2} and Mo 3d_{5/2}, respectively, attributing to the +6 oxidation state of Mo in MoO₃. [34,35] The core level spectra of Mo 3d in Fig. 6.2(c) shows three peaks positioned at 234.7, 231.5 and 228.2 eV, respectively. The doublet peak appears in the middle at 231.5 and 228.2 eV corresponds to the Mo 3d_{3/2} and Mo 3d_{5/2}, respectively, correlating to the +4 oxidation state of Mo in MoS₂. [34–36] The low intensity Mo 3d core level peak at 234.7 eV (Fig. 6.2(c)) indicates +6 oxidation state Mo in MoO₃. This result indicates the existence of

molybdenum oxide phase in MoS₂. The presence of MoO₃ might be because of the formation of sulphur vacancy defects during the growth of MoS₂. The sulphur vacancies can react with atmosphere oxygen and the MoO₃ phase might be formed.[34] Moreover, the presence of oxygen gas as inclusion with Ar may also be responsible for the formation of MoO₃. [34] In Fig. 6.2(c), the sharp peak appears at 225.4 eV is attributed to the binding energy of S 2s core level spectra indicating the presence of sulfur in MoS₂. [35] Again, in Fig. 6.2(d), the presence of S 2p peaks positioned at 161.2 and 162.4 eV confirm the -2 oxidation state of sulfur present in MoS₂. [37] The deconvolution of O1s core level spectra (Fig. 2(e)) suggests doublet peak with corresponding binding energy of 529.9 and 531.3 eV, which indicate -2 oxidation state of oxygen and oxygen vacancy defects or adsorbed -OH species in the NHs, respectively. [38,39] Fig. 6.2(f) shows the core level XPS spectra of Zn 2p, where the doublet peak positioned at 1044.4 and 1021.3 eV correspond to the Zn 3p_{1/2} and Zn 3p_{3/2}, respectively, indicating the +2 oxidation state of Zn in the ZnO NRs. [10,38] Furthermore, the shift of the Zn 2p doublet peak towards the higher binding energy in the ZnO/MoO₃ and ZnO/MoS₂ NHs designates the charge transfer between the ZnO and MoO₃ or MoS₂ because of the formation of nano-heterojunction. [37,40]

6.3.3 Photoelectrochemical Performance

The photoelectrochemical performance of the as prepared ZnO/MoO₃ NHs, ZnO/MoS₂ NHs and the pristine ZnO NRs photoelectrodes has been investigated under standard simulated solar light (AM 1.5 G, 100 mW.cm⁻²). The photocurrent density versus applied potential curves (Fig. 6.3(a)) clearly show the enhanced photocurrent density because of the incorporation of 2D layered structure of MoS₂ and MoO₃ on the 1D ZnO NRs. As shown in Fig. 6.3(a), the ZnO NRs photoelectrode shows a photocurrent density of 0.47 mA cm⁻² at 1.23 V vs. RHE with an onset potential of 0.44 V. On the other hand, for the ZnO/MoO₃ and ZnO/MoS₂ NHs, the photocurrent densities are increased drastically by 43% and 334%, reaching the values of 0.67 and 2.04 mA cm⁻² at 1.23 V versus RHE, respectively. Moreover, 30 and 70 mV cathodic shift

(Fig. 6.3(b)) of the photocurrent onset potential is also observed for ZnO/MoO₃ and ZnO/MoS₂ NHs, respectively, denoting the improved charge carrier separation efficiency at the nano-heterojunction at low voltage.[3]

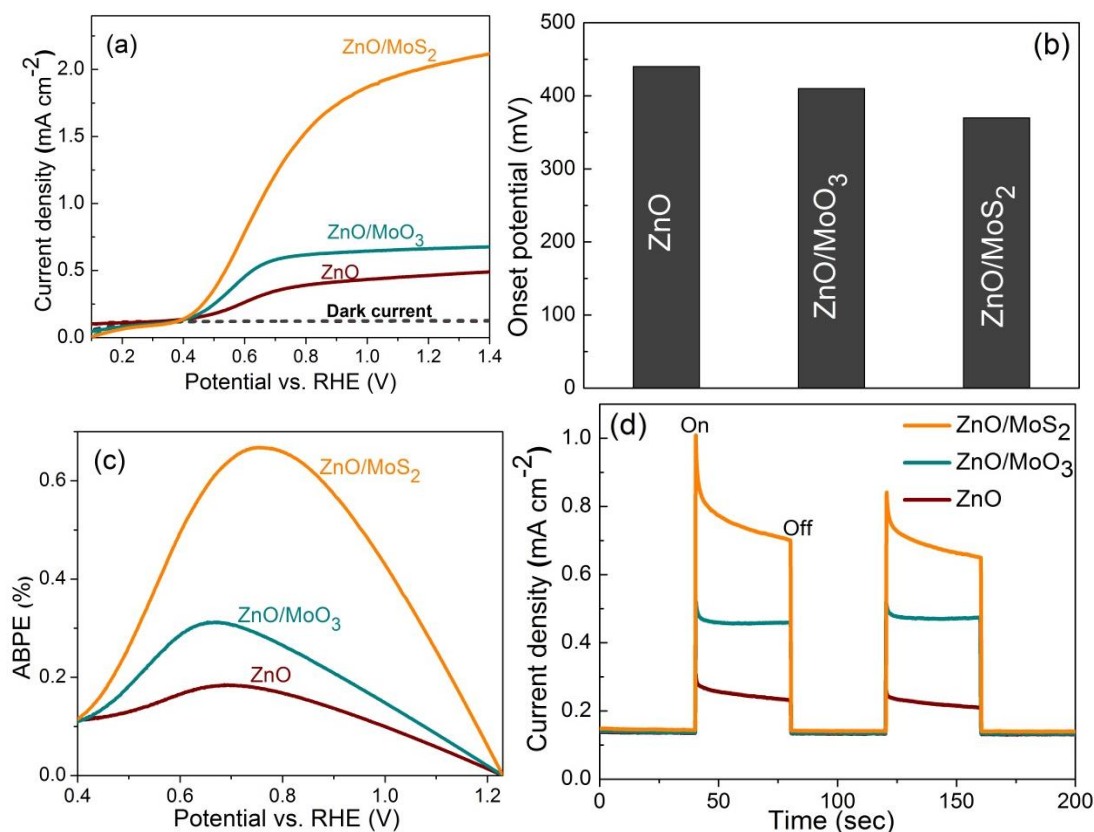


Figure 6.3: (a) Linear sweep voltammogram photocurrent density versus applied potential curves, (b) photocurrent onset potential, (c) ABPE curves, (d) current density versus time plots under chopped illumination.

However, the increase of photocurrent density with the increase of applied bias also indicates the *n*-type nature of the as prepared photoelectrodes. The above studies indicate that the 2D layered MoS₂ is more efficient than the MoO₃ to reduce the surface charge recombination in the NHs and hence, it effectively enhances the photocurrent densities of the NHs electrode. The calculated applied bias photon-to-current conversion efficiency (ABPE) values of the ZnO NRs, ZnO/MoO₃ and ZnO/MoS₂ NHs are shown in Fig. 6.3(c). The as prepared ZnO NRs photoanode shows the ABPE peak of only 0.18% at around 0.67 V versus RHE, whereas, both the ZnO/MoO₃ and ZnO/MoS₂ NHs exhibit enhanced ABPE at a lower applied bias. The ZnO/MoS₂ NHs exhibits

ABPE as high as 0.67%, which is over threefold and twofold than that of the pristine ZnO NRs and ZnO/MoO₃ NHs, respectively. The amperometry curve (Fig. 6.3(d)), of the electrodes recorded at an applied potential of 0 V vs Ag/AgCl (0.57 V vs. RHE) depicts the obvious transient response of photocurrent density upon the illumination. It is evident that all the photoanodes exhibit sharp photoresponse upon light 'on' and 'off', however, the ZnO/MoS₂ NHs exhibits highest photocurrent density of 0.71 mA cm⁻², which is threefold higher than that of ZnO NRs. This result also indicates that the ZnO/MoS₂ nano-heterojunction structure is promoting the separation and transportation of photogenerated charge carriers.

The PEC water splitting performance of the as prepared photoelectrodes were recorded under AM 1.5 G illumination only and the hydrogen gas evolution was measured by gas chromatography. Figure 6.4 shows the plot of hydrogen produced at the Pt electrode at different time for the ZnO/MoS₂ NHs photoanode. Inset of Fig. 6.4 shows the amount of hydrogen produced at Pt electrode for the different photoanodes after 60 min under AM 1.5 G light illumination without applied bias. It is evident from Fig. 6.4, that 2.01, 4.90 and 7.76 μmol cm⁻² of hydrogen has been generated for ZnO, ZnO/MoO₃, and ZnO/MoS₂ NHs photoanode, respectively, after one hour under the solar light illumination. Here, the higher ABPE efficiency and higher hydrogen production from ZnO/MoS₂ NHs is due to the increase of photocurrent density of this photoelectrode.

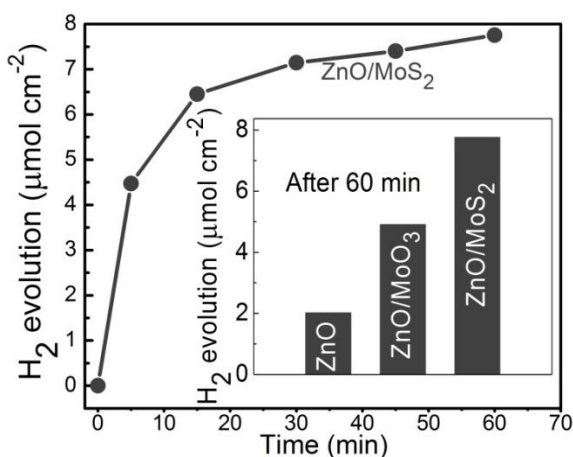


Figure 6.4: The hydrogen evolution data for the different as prepared photoanodes.

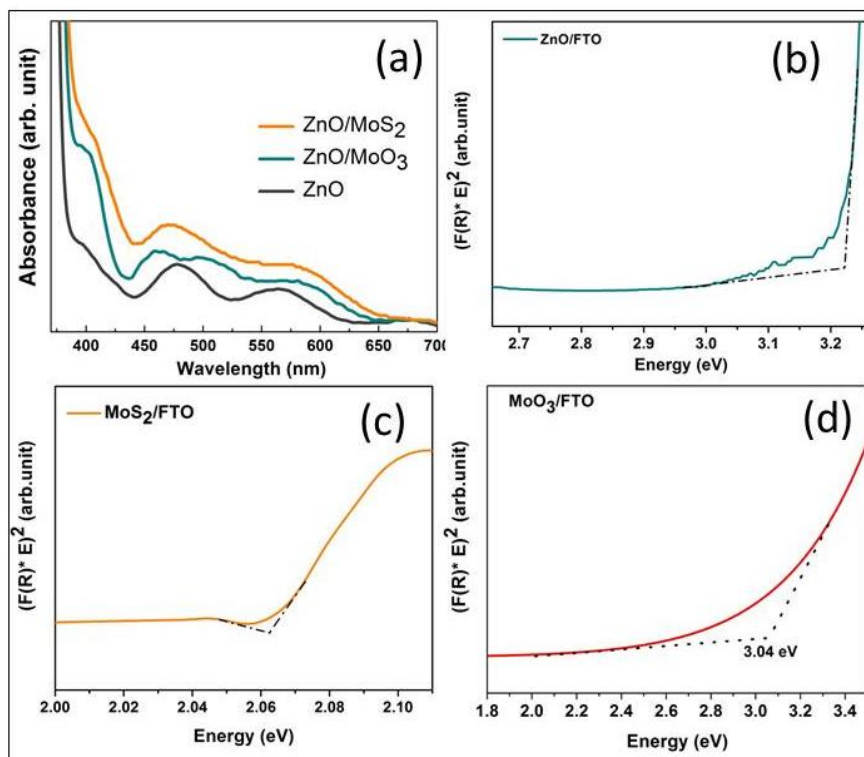


Figure 6.5: (a) UV-vis absorption spectra of the as-fabricated samples, Kubelka-Munk plot of (b) ZnO/FTO, (c) MoS₂/ZnO and (d) MoO₃/FTO.

The light harvesting property of the as prepared electrodes was studied by recording the UV-Vis absorption spectra (Figure 6.5(a)) of the electrodes. The intense absorption band below 387 nm could be attributed to the interband absorption (band-gap absorption) for ZnO NRs.[41] It is evident from Fig. 6.5(a), that the coating of 2D layered MoS₂ and MoO₃ over ZnO NRs definitely promotes the visible-light absorption of the NHs over the pristine ZnO NRs. Furthermore, the formation of ZnO/MoO₃ and ZnO/MoS₂ NHs results in a red-shift of the absorption edge of the NHs, which eventually leads to decrease of the band-gap energy.[42] The ZnO/MoS₂ NHs exhibits 300 and 100-fold enhancement in absorbance in between the wavelength range of 400–440 nm and 450–650 nm, respectively, as compared with pristine ZnO NRs. However, these results imply that the formation of nano-heterojunction significantly enhances the visible-light absorption of the photoanodes. The band gap of the individual samples i.e, ZnO, MoO₃ and MoS₂ are also calculated by Kubelka-Munk plot (Fig. 6.5 (b)-(d)) and it is found that the band gap of ZnO, MoO₃ and MoS₂ samples are 3.22, 3.04 and 2.06 eV,

respectively. As a consequence of enhanced light absorption the photo excitation generation also increases which boosts the photocurrent density after successful charge separation and transportation across the nano-heterojunction.

Along with the light absorption, the photo carrier separation/transfer and excitation lifetime are also crucial factors to determine the PEC performance of the electrodes. Hence, to further investigate the photocarrier dynamics of the electrodes, steady state photoluminescence (PL) and time-resolved photoluminescence (TRPL) properties of the electrodes are studied. Inset of Fig. 6.6 shows that the ZnO NRs grown on FTO exhibits major PL emission peaks at 380 nm and broad emission peak in between 400-500 nm, which can be attributed to near band edge transition and defect state transitions, respectively.[43,44] It is evident that the PL intensity of ZnO NRs has strongly quenched due to the anchoring of 2D MoS₂ or MoO₃ layers on ZnO NRs under an excitation energy of 3.75 eV (330 nm). The quenching effect is quantified by calculating the quenching factor ($Q = I_{\text{ZnO}}/I_{\text{ZnO/MoS}_2 \text{ or MoO}_3}$), where I_{ZnO} and $I_{\text{ZnO/MoS}_2 \text{ or MoO}_3}$ are the heights of PL emission peaks for ZnO NRs and ZnO/MoS₂ or ZnO/MoO₃ NHs.[45] The as calculated quenching factor for ZnO NRs due to the anchoring of 2D layered MoS₂ and MoO₃ are 6.5 and 2, respectively, which indicates that the recombination of photo-induced charge carriers is reduced significantly due to the formation of nano-heterojunctions. The pronounced PL quenching in nano-heterostructures qualitatively demonstrates enhanced interfacial charge transfer across the heterojunction.[45-47] Hence, the above result indicates that upon illumination, the photo-generated electrons can effectively transfer from 2D layered structure to 1D structure, where the charge transfer between 2D MoS₂ to 1D ZnO is found to be significantly higher than that of 2D MoO₃ to 1D ZnO. Generally, the transferred electrons try to bound with the excitations forming large binding energy trions leading to suppressed PL intensity.[45] However, it is evident that the as fabricated 2D-1D NHs facilitate efficient electron-hole separation by suppressing the surface charge recombination.

The dynamics of the photoinduced exciton formation and carrier migration of the electrodes have been investigated by TRPL spectroscopy at 430 nm emission to estimate the excitation lifetime (Fig. 6.6). The TRPL emission decay curves were fitted by a bi-exponential decay model [45,48-50] with the decay kinetics function expressed as: $I(t) = \sum A_i e^{-t/\tau_i}$, where $i = 1, 2$ and the calculated slow decay time (τ_1), fast decay time (τ_2). The average PL emission lifetime, reflecting the overall emission decay behavior of the electrode samples, was calculated as: [45]

$$\tau_{\text{avg}} = \frac{\sum A_i \tau_i^2}{\sum A_i \tau_i}, \quad \text{where } i = 1, 2 \quad (6.3)$$

The slow decay time (τ_1), fast decay time (τ_2), average lifetime (τ_{avg}) and other parameters are summarized in Table 6.1. The short decay time component is related to trap-assisted nonradiative recombination of charge carriers in the defect states of the electrode, whereas the long decay component is related to the radiative recombination because of the recombination of free excitons.[45,48-50] The emission lifetimes components for ZnO/MoS₂ NHs ($\tau_1 = 0.26$ ns, $\tau_2 = 2.8$ ns) and ZnO/MoO₃ NHs ($\tau_1 = 0.28$ ns, $\tau_2 = 3.3$ ns) are shorter than that of the corresponding ZnO NRs ($\tau_1 = 0.33$ ns, $\tau_2 = 3.5$ ns). Moreover, the average decay lifetime, which reflects the overall emission decay behaviour of the electrodes, is also found to decrease for ZnO/MoS₂ NHs ($\tau_{\text{av}} = 2.2$ ns) and ZnO/MoO₃ NHs ($\tau_{\text{av}} = 2.8$ ns) compared to the pure ZnO NRs ($\tau_{\text{av}} = 3$ ns). The decrease in the values of lifetime for NHs electrode compared to ZnO NRs indicates the appearance of a nonradiative pathway, that is the establishment of an electron transfer channel from MoS₂ or MoO₃ to ZnO.[46,49] Both the quenched PL emission and the reduced decay lifetime indicate efficient interfacial charge carrier transfer/separation and suppression of photoexcited charge carrier recombination in the nano-heterostructure because of the formation of nano-heterojunction.[46,49,51] The results show that the ZnO/MoS₂ NHs electrode exhibits the most effective photo-induced excitation separation and reduced surface charge carrier recombination among the as fabricated electrodes .

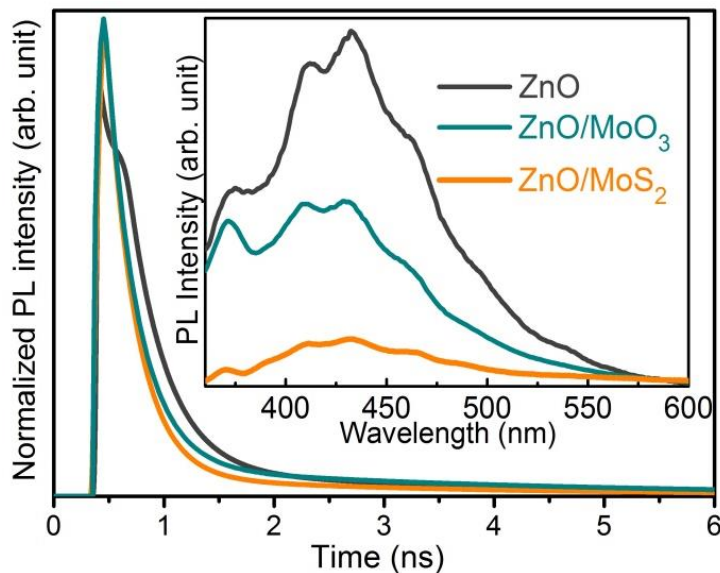


Figure 6.6: Time-resolved transient photoluminescence decay of the as prepared electrodes (excitation at 400 nm and emission at 430 nm). Room temperature steady-state PL emission spectra of ZnO NRs, ZnO/MoO₃ and ZnO/MoS₂ NHs under the excitation of 330 nm (Inset of the Fig.6.6).

Table 6.1: Dynamics analysis of PL emission decay for the different electrode sample.

Photoelectrodes	τ_1 (ns)	τ_2 (ns)	A ₁ (%)	A ₂ (%)	τ_{avg} (ns)	χ^2
ZnO	0.33	3.5	70	30	3	1.01
ZnO/MoO ₃	0.28	3.3	65	35	2.8	0.88
ZnO/MoS ₂	0.26	2.8	74	26	2.2	0.84

The charge carrier dynamics of the photoelectrodes were further studied by recording the change of open-circuit potential (V_{oc}) over time under chopped illumination condition. In Fig. 6.7 (a), the V_{oc} for all the as prepared electrodes is found to decrease sharply when the illumination is switched on. Similarly, the V_{oc} for all the samples increases when the illumination is switched off. Generally, when the illumination is switched off, the electrons density of the conduction band decreases because of the carrier recombination which results in decrease of V_{oc} . Hence, here the increase in V_{oc} upon the switch off of the illumination can be interpreted as the ‘hole’

transportation at electrode/electrolyte interface.[8] Therefore, the large increase in V_{oc} for ZnO/MoS₂ NHs (~120%) compared to that of ZnO/MoO₃ NHs (~110%) and ZnO NRs (~100%) indicates effective transportation of large amount of photogenerated 'holes' at ZnO/MoS₂ NHs/electrolyte interface.

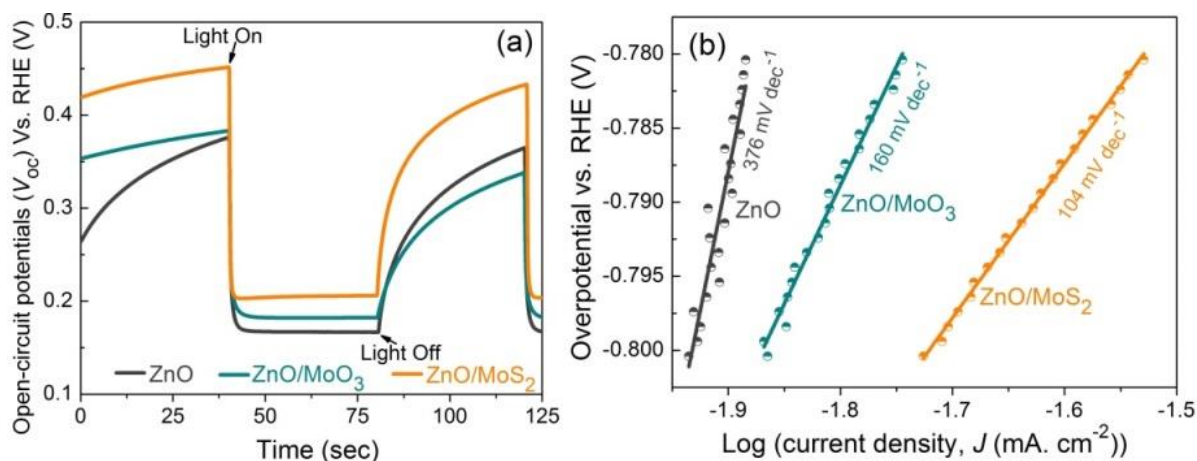


Figure 6.7: (a) Open-circuit potential vs. time plot, (b) Tafel plot.

The reaction kinetic parameters of the OER activity of the different photoanodes have also been determined from the Tafel plots (Fig. 6.7(b)) by plotting the overpotential (η) against $\log(\text{current density}, J)$. [52–54] As the slopes of the Tafel plots are subjective to the mass transport and electron transport, hence, the Tafel slopes can also be used to analysis the mechanism of OER activity of the photoanodes. [27,52,54] It is evident from Fig. 6.7(b), that the value of Tafel slope decreases significantly for ZnO/MoO₃ NHs (160 mV decade⁻¹) and ZnO/MoS₂ NHs (104 mV decade⁻¹) compared to the pristine ZnO NRs (376 mV decade⁻¹). It has been reported that the intrinsic semiconductors like ZnO are expected to exhibit higher value of Tafel slops because of the slow electron transportation at the surface. [55] Therefore, the remarkable decrease in the value of the Tafel slops after the formation of 2D-1D MoS₂ or MoO₃-ZnO NHs signifies the faster and effective electron transportation through the heterointerface. [27,54,55] The lowest value of the Tafel slope for ZnO/MoS₂ NHs indicates its superior carrier transportation characteristics.

The charge carrier dynamics (charge transport phenomena) in the bulk and at the electrode surface/electrolyte interface of the as prepared photoanodes has also been

examined by electrochemical impedance spectroscopy (EIS) measurements. The semicircle of the Nyquist plot (Fig. 6.8) of the EIS analysis of the photoanodes obtained under AM 1.5 G illumination have been fitted to the Randles equivalent circuit (inset of Fig. 6.8) [56,57], where R_s represents the equivalent series resistance, R_{ct} is attributed to the interfacial charge transfer resistance at the photoanode/electrolyte interface, and the CPE is the constant phase element at the electrode/electrolyte interface, respectively. The diameter of the semicircle of the EIS curve is the measure of the R_{ct} , which is directly related to the photo-induced charge carrier transfer kinetics at the photoelectrode/electrolyte interface.[3,58,59] Hence, the significant reduction of the diameter of the semicircle as shown in the Nyquist plot for the NHs photoanodes compared to the pristine ZnO NRs indicates remarkable decrease of the charge transfer resistance at photoanode/electrolyte interface resulting faster charge transportaion. [27] The smallest value of R_{ct} (see Table 6.2) for ZnO/MoS₂ NHs also signifies superior charge transfer ability and faster interfacial reaction kinetics for the NHs photoanodes leading to improved photocatalytic efficiency. [3,58]

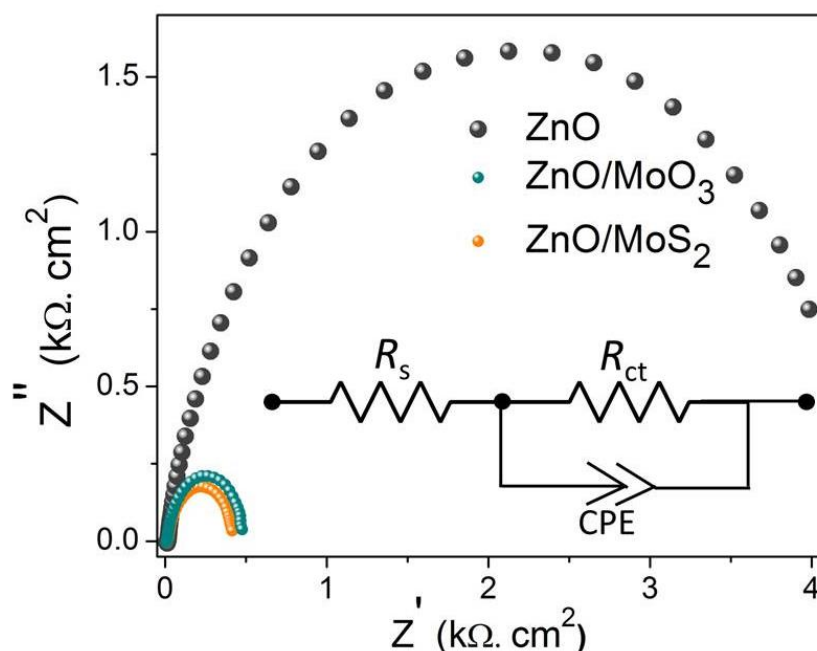


Figure 6.8: Nyquist plot of the EIS analysis of the photoanodes. Inset of the Fig.6.8 shows the fitted equivalent circuit for the impedance spectra.

Table 6.2: Electrochemical impedance parameters obtained from equivalent obtained from the EIS curves in Figure 6.8.

Photoelectrodes	R_s (Ω)	R_{ct} (Ω)
ZnO NRs	14	2979
ZnO/MoO ₃ NHs	16	1128
ZnO/MoS ₂ NHs	9	506

The above studies show that the formation of 2D-1D NHs helps to achieve increased specific surface area effective for enhanced broadband light absorption and surface chemical reactions the most important factors for water splitting. Alongwith the enhanced photo-generation of excitons the interfacial band alingment at interface promotes the rapid separation and tranfer of the photo-induced charge carriers at nano-heterojunction through the 1D ZnO NRs towards to current collector (FTO) resulting enhanced photocurrent. Therefore, the enhanced photoelectrochemical activities of the multidimensional NHs may be attributed to enhanced light absorption, rapid charge separation and transportation, and effective surface OER.

6.4 Conclusion

In conclusion, multidimensional 2D-1D nano-heterostructure photoanodes have been fabricated by designing multilayered 2D structures of MoS₂ and MoO₃ on 1D ZnO NRs by easy and scalable wet chemical route. The NHs photoanodes exhibit significantly enhanced OER activity compared to the pristine ZnO NRs photoelectrode. The as prepared ZnO/MoS₂ and ZnO/MoO₃ NHs show improved broadband solar light absorption, whereas the effective band gap of the NHs is found to decrease compared to the pristine ZnO NRs. The ZnO/MoS₂ NHs offers the lowest onset potential (370 mV), whereas its photocurrent density has increased by 334%, reaching the values of 2.02 mA cm⁻² at 1.23 V versus RHE compared to ZnO NRs photoanode. It is expected that the excellent contact and band alignment between ZnO and MoS₂ or

MoO₃ are the key factors to promote the effective photo-induced charge carrier separation, which is evident from the carrier lifetime study and the small value of Tafel slopes of the NHs photoanodes. The increase of the value of open-circuit potential and the decrease of the value of interfacial charge transfer resistance for the NHs photoanodes compared to the pristine ZnO NRs photoelectrode upon illumination indicate superior photo-induced charge carrier transfer ability and faster interfacial reaction kinetics of the NHs photoanodes. The as prepared 2D-1D nano-heterostructures are found to be effective photoanodes for water oxidation reaction to harvest solar energy.

Bibliography

- [1] Y. Zheng, Y. Jiao, Y. Zhu, L.H. Li, Y. Han, Y. Chen, A. Du, M. Jaroniec, S.Z. Qiao, *Nat. Commun.*, **5** 1, (2014)
- [2] T. Hisatomi, J. Kubota, K. Domen, *Chem. Soc. Rev.*, **43**, 7520 (2014)
- [3] S. Wang, T. He, J.H. Yun, Y. Hu, M. Xiao, A. Du, L. Wang, *Adv. Funct. Mater.* **28**, 1 (2018)
- [4] B. Zhang, X. Zheng, O. Voznyy, R. Comin, M. Bajdich, M. García-Melchor, L. Han, J. Xu, M. Liu, L. Zheng, F.P.G. De Arquer, C.T. Dinh, F. Fan, M. Yuan, E. Yassitepe, N. Chen, T. Regier, P. Liu, Y. Li, P. De Luna, A. Janmohamed, H.L. Xin, H. Yang, A. Vojvodic, E.H. Sargent, *Science*, **352**, 333 (2016)
- [5] D. Barreca, G. Carraro, A. Gasparotto, C. Maccato, M.E.A. Warwick, K. Kaunisto, C. Sada, S. Turner, Y. Gönüllü, T.P. Ruoko, L. Borgese, E. Bontempi, G. Van Tendeloo, H. Lemmetyinen, S. Mathur, *Adv. Mater. Interfaces.*, **2**, 1 (2015)
- [6] J. Resasco, H. Zhang, N. Kornienko, N. Becknell, H. Lee, J. Guo, A.L. Briseno, P. Yang, *ACS Cent. Sci.*, **2**, 80 (2016)
- [7] C.F. Chi, Y.L. Lee, H.S. Weng, *Nanotechnology*, **19**, 125704 (2008)
- [8] A. Sarkar, K. Karmakar, G.G. Khan, *J. Phys. Chem. C*, **121**, 25705 (2017)
- [9] F. Meng, J. Li, S.K. Cushing, M. Zhi, N. Wu, *J. Am. Chem. Soc.*, **135**, 10286 (2013)
- [10] K. Karmakar, A. Sarkar, K. Mandal, G.G. Khan, *Nanotechnology*, **28**, 325401 (2017)
- [11] L. Peng, P. Xiong, L. Ma, Y. Yuan, Y. Zhu, D. Chen, X. Luo, J. Lu, K. Amine, G. Yu, *Nat. Commun.*, **8**, 151139 (2017)
- [12] A.S. Etman, H.N. Abdelhamid, Y. Yuan, L. Wang, X. Zou, J. Sun, *ACS Omega*. **3**, 2201 (2018)
- [13] M.Y. Li, C.H. Chen, Y. Shi, L.J. Li, *Mater. Today*, **19**, 322 (2016)
- [14] Y. Wu, F. Li, W. Chen, Q. Xiang, Y. Ma, H. Zhu, P. Tao, C. Song, W. Shang, T. Deng, J. Wu, *Adv. Mater.* **30**, 1 (2018)
- [15] H. Li, Y. Li, A. Aljarb, Y. Shi, L.J. Li, *Chem. Rev.*, **118**, 6134 (2018)

-
- [16] H. Yin, Y. Kuwahara, K. Mori, H. Cheng, M. Wen, H. Yamashita, *J. Mater. Chem. A*, **5**, 8946 (2017)
- [17] J. Ding, S. Du, Z. Zuo, Y. Zhao, H. Cui, X. Zhan, *J. Phys. Chem. C*, **121**, 4917 (2017)
- [18] S. Wei, X. Cui, Y. Xu, B. Shang, Q. Zhang, L. Gu, X. Fan, L. Zheng, C. Hou, H. Huang, S. Wen, W. Zheng, *ACS Energy Lett.*, **4**, 368 (2019)
- [19] J. Liu, J. Wang, B. Zhang, Y. Ruan, H. Wan, X. Ji, K. Xu, D. Zha, L. Miao, J. Jiang, *J. Mater. Chem. A*, **6**, 2067 (2018)
- [20] S. Kumar, V. Sharma, K. Bhattacharyya, V. Krishnan, *Mater. Chem. Front.*, **1**, 1093 (2017)
- [21] J. Qiu, Z. Yang, Y. Li, *J. Mater. Chem. A*, **3**, 24245 (2015)
- [22] X. Zhang, J. Qin, Y. Xue, P. Yu, B. Zhang, L. Wang, R. Liu, *Sci. Rep.*, **4**, 4 (2014)
- [23] B. Xu, P. He, H. Liu, P. Wang, G. Zhou, X. Wang, *Angew. Chemie - Int. Ed.*, **53**, 2339 (2014)
- [24] S.-H. Bae, H. Kum, W. Kong, Y. Kim, C. Choi, B. Lee, P. Lin, Y. Park, J. Kim, *Nat. Mater.*, **18**, 550 (2019)
- [25] S. Wang, C. Ren, H. Tian, J. Yu, M. Sun, *Phys. Chem. Chem. Phys.*, **20**, 13394 (2018)
- [26] Y.H. Tan, K. Yu, J.Z. Li, H. Fu, Z.Q. Zhu, *J. Appl. Phys.*, **116**, (2014)
- [27] K. Fan, H. Chen, Y. Ji, H. Huang, P.M. Claesson, Q. Daniel, B. Philippe, H. Rensmo, F. Li, Y. Luo, L. Sun, *Nat. Commun.*, **1**, 119181 (2016)
- [28] D. Maity, K. Karmakar, K. Mandal, *J. Alloys Compd.* **791**, 739 (2019)
- [29] Z. Luo, R. Miao, T.D. Huan, I.M. Mosa, A.S. Poyraz, W. Zhong, J.E. Cloud, D.A. Kriz, S. Thanneeru, J. He, Y. Zhang, R. Ramprasad, S.L. Suib, *Adv. Energy Mater.*, **6**, 1600528 (2016)
- [30] H. Cheng, T. Kamegawa, K. Mori, H. Yamashita, *Angew. Chemie - Int. Ed.*, **53**, 2910 (2014)
- [31] H. Li, K. Yu, H. Fu, B. Guo, X. Lei, Z. Zhu, *J. Phys. Chem. C*, **119**, 7959 (2015)
- [32] T.S. Sahu, S. Mitra, *Sci. Rep.*, **5**, 1 (2015)

-
- [33] S. Hu, W. Chen, J. Zhou, F. Yin, E. Uchaker, Q. Zhang, G. Cao, *J. Mater. Chem. A*, **2**, 7862 (2014)
- [34] Y.T. Ho, C.H. Ma, T.T. Luong, L.L. Wei, T.C. Yen, W.T. Hsu, W.H. Chang, Y.C. Chu, Y.Y. Tu, K.P. Pande, E.Y. Chang, *Phys. Status Solidi - Rapid Res. Lett.*, **9**, 187 (2015)
- [35] X.L. Yin, L.L. Li, W.J. Jiang, Y. Zhang, X. Zhang, L.J. Wan, J.S. Hu, *ACS Appl. Mater. Interfaces*, **8**, 15258 (2016)
- [36] P. Cheng, K. Sun, Y.H. Hu, *Nano Lett.*, **16**, 572 (2016)
- [37] H.S. Woo, C.H. Kwak, I.D. Kim, J.H. Lee, *J. Mater. Chem. A*, **2**, 6412 (2014)
- [38] K. Karmakar, A. Sarkar, K. Mandal, G.G. Khan, *ACS Sustain. Chem. Eng.*, **4**, 5693 (2016)
- [39] F. Liu, C. Chen, H. Guo, M. Saghayezhian, G. Wang, L. Chen, W. Chen, J. Zhang, E.W. Plummer, *Surf. Sci.*, **655**, 25 (2017)
- [40] Y. Chen, S. Huang, X. Ji, K. Adepalli, K. Yin, X. Ling, X. Wang, J. Xue, M. Dresselhaus, J. Kong, B. Yildiz, *ACS Nano*, **12**, 2569 (2018)
- [41] Q. Xiang, J. Yu, M. Jaroniec, *J. Am. Chem. Soc.*, **134**, 6575 (2012)
- [42] S. Kumar, N.L. Reddy, H.S. Kushwaha, A. Kumar, M.V. Shankar, K. Bhattacharyya, A. Halder, V. Krishnan, *ChemSusChem.*, **10**, 3588 (2017)
- [43] V. Ischenko, S. Polarz, D. Grote, V. Stavarache, K. Fink, M. Driess, *Adv. Funct. Mater.*, **15**, 1945 (2005)
- [44] Z. Zheng, Z.S. Lim, Y. Peng, L. You, L. Chen, J. Wang, *Sci. Rep.*, **3**, 1 (2013)
- [45] H. Wu, Z. Kang, Z. Zhang, Z. Zhang, H. Si, Q. Liao, S. Zhang, J. Wu, X. Zhang, Y. Zhang, *Adv. Funct. Mater.*, **28**, 1 (2018)
- [46] I. Shown, S. Samireddi, Y.C. Chang, R. Putikam, P.H. Chang, A. Sabbah, F.Y. Fu, W.F. Chen, C.I. Wu, T.Y. Yu, P.W. Chung, M.C. Lin, L.C. Chen, K.H. Chen, *Nat. Commun.*, **9**, 169 (2018)
- [47] X. Hong, J. Kim, S.F. Shi, Y. Zhang, C. Jin, Y. Sun, S. Tongay, J. Wu, Y. Zhang, F. Wang, *Nat. Nanotechnol.*, **9**, 682 (2014)

-
- [48] C. Wolf, C.-L. Lee, S.H. Im, J.H. Heo, S.-H. Jeong, N. Myoung, A. Sadhanala, M.-H. Park, S. Yoo, T.-W. Lee, R.H. Friend, Y.-H. Kim, H. Cho, *Science*, **350**, 1222 (2015)
- [49] M.Q. Yang, Y.J. Xu, W. Lu, K. Zeng, H. Zhu, Q.H. Xu, G.W. Ho, *Nat. Commun.*, **8**, 1 (2017)
- [50] Z. Ning, X. Gong, R. Comin, G. Walters, F. Fan, O. Voznyy, E. Yassitepe, A. Buin, S. Hoogland, E.H. Sargent, *Nature*, **523**, 324 (2015)
- [51] Z. Zhang, Y. Huang, K. Liu, L. Guo, Q. Yuan, B. Dong, *Adv. Mater.*, **27**, 5906 (2015)
- [52] T.Y. Ma, S. Dai, M. Jaroniec, S.Z. Qiao, *Angew. Chemie - Int. Ed.*, **53**, 7281–7285 (2014)
- [53] H. Dau, C. Limberg, T. Reier, M. Risch, S. Roggan, P. Strasser, *ChemCatChem.*, **2**, 724 (2010)
- [54] F. Song, X. Hu, *J. Am. Chem. Soc.*, **136**, 16481 (2014)
- [55] H. Vrubel, T. Moehl, M. Gratzel and X. Hu, *Chem. Commun.*, 2013, **49**, 8985 (2013)
- [56] J.K. Kim, Y. Cho, M.J. Jeong, B. Levy-Wendt, D. Shin, Y. Yi, D.H. Wang, X. Zheng, J.H. Park, *ChemSusChem.*, **11**, 933 (2018)
- [57] B. Klahr, S. Gimenez, F. Fabregat-Santiago, T. Hamann, J. Bisquert, *J. Am. Chem. Soc.*, **134**, 4294 (2012)
- [58] Y. Teng, X.D. Wang, J.F. Liao, W.G. Li, H.Y. Chen, Y.J. Dong, D. Bin Kuang, *Adv. Funct. Mater.*, **28**, 1 (2018).
- [59] M. Li, W. Luo, D. Cao, X. Zhao, Z. Li, T. Yu, Z. Zou, *Angew. Chemie - Int. Ed.*, **52**, 11016 (2013)

Chapter 7

Cobalt Oxide - Manganese Dioxide -Nickel Oxide Ternary 1D Hybrid Nanotubes for Supercapacitor Electrode

This chapter presents a facile electrodeposition and post annealing techniques to design the unique $\text{Co}_3\text{O}_4\text{-MnO}_2\text{-NiO}$ ternary hybrid one dimensional (1D) nanotube arrays for their application as an active material for high-performance supercapacitor electrode.

A part of the content of this chapter has been published in the journal of *ACS Appl. Mater. Interfaces* [1] and is reproduced herein with permission from American Chemical Society (ACS).

7.1 Preamble

Since last few years, the hassle of clean, efficient, and renewable energy sources is remarkable and thereby driving intense scientific concern in the production, storage and management of this precious energy. [2,3] Among variety of electrical energy storage devices, supercapacitors (SCs), also known as electrochemical capacitors have drawn enormous research and industrial attention because of their high power density and very long cycle stability as compared to their counterparts such as batteries, fuel cells and conventional capacitors etc. [4,5] SCs are very promising concept for next-generation consumer applications in hybrid electric vehicles, miniaturized electronic circuits, portable electronic devices and backup power sources.

Various materials and electrode structures have been investigated to improve the performance of SCs. Initially, some carbon-based electrode materials like activated carbon, carbon nanotubes, and graphene [4,6,7] have been used as electrode materials which come under the category of electric double layer capacitors (EDLC) because of their charge storage mechanism (electrostatic gathering of charges at the electrode-electrolyte interface). Later, transition metal oxides (TMOs) like RuO_2 , MnO_2 , Fe_2O_3 , NiO , and Co_3O_4 , etc. and conducting polymers specially PANI [4,6,7] have been investigated thoroughly because of their very high specific capacitance resulting from unique redox (reduction/oxidation) reactions at the electrode-electrolyte interface and thus categorized as pseudocapacitors. In particular, Co_3O_4 , MnO_2 , and NiO have exhibited immense potential as electro-active material in improving the performance of SCs because of their high theoretical specific capacitances, environment compatibility and mechanical and thermal stability. Moreover, their natural abundance makes them economic as compared to other TMO's like RuO_2 . [4,8] Recently, various nanostructured morphologies such as nano-hollow-spheres, nano-rods, nano-belts, nano-needles, nano-sheets, nano-flowers, nanowires, and nanotubes (NTs) [4,6-8] of different single or composite TMOs have also been designed to enhance the electrochemical performance of the SC electrodes having the benefits of different nanostructures. However, among

all the morphologies mentioned, nanotubes (NTs) have shown tremendous superiority because of their unique 1D structure having large accessible inner and outer surfaces which serve as a feasible platform for redox reactions to happen during the functionalization of SCs and also the thin shell of the nanotubes (comparable to the ion diffusion depth) boosts the performance of the active material helping in fast charge transportation. [9-11] Significant attempts have been made to improve the performance of SCs using TMOs based nanostructures and it brings the challenges like the poor electrical conductivity and low cycle life to overcome. However, the electrical conductivity of TMOs can be improved significantly, on the basis of previous reports, by introducing vacancies or impurities, via sintering in the selected gaseous environment or through doping. [12-15] These mechanism boost up charge transportation at the electrode/electrolyte interface during redox reactions and also through the active material towards the current collector improving their electrochemical performance.

In this backdrop, we have proposed a facile technique to grow freestanding vertically aligned arrays of highly porous 1D $\text{Co}_3\text{O}_4\text{-MnO}_2\text{-NiO}$ composite NTs on conducting (Au) substrate for the fabrication of SC electrode. Such unique design and selection of component materials have several scientific advantages: (i) 1D structure having large surface area with proper use of both of the inner and outer surfaces of the NTs; as well as their highly porous walls would enhance the effective accessible surface area of electrodes providing huge platform for surface based faradaic reactions; (ii) thin walls of NTs would provide short ion diffusion path; (iii) combination of three highly redox active oxides (Co_3O_4 , MnO_2 and NiO) in a single nanostructure would definitely improve the charge storing capacity of the whole system because of synergistic effect; and (iv) direct growth of NTs on current collector (Au) would significantly improve the electrical conductivity of the entire electrode by reducing contact resistance and also eliminates the use of expensive and resistive binders, which causes extra weight to the electrode. Therefore, SC electrode containing highly ordered, vertically aligned, porous 1D ternary hybrid NTs arrays having above mentioned advantages are expected to

exhibit enhanced electrochemical performance. The hybrid NTs demonstrate superior electrochemical performance with high specific capacitance ($\sim 2525 \text{ Fg}^{-1}$ within 0.8V potential window), excellent long cycle stability, high energy and power density, which are because of the unique design of the nanostructure electrode material together with the peculiar combination of the component elements in a single unit.

7.2 Experimental Section

7.2.1 Chemicals and Materials

Aluminium foil (99.99+% pure, 0.2 mm thick), Oxalic acid (99.9+% pure), Cobalt sulphate heptahydrate ($\text{CoSO}_4 \cdot 7\text{H}_2\text{O}$, 99.95+% pure), Nickel sulphate hexahydrate ($\text{NiSO}_4 \cdot 6\text{H}_2\text{O}$, 99.9+% pure), Manganese sulphate monohydrate ($\text{MnSO}_4 \cdot \text{H}_2\text{O}$, 99.9+% pure), Boric acid (H_3BO_3 , 99.9+% pure), Sodium hydroxide (NaOH, 99.9+% pure) and Potassium hydroxide (KOH, 99.9+% pure) were purchased from SIGMA-ALDRICH. All chemicals were of analytical grade and were used without further purification.

7.2.2 Synthesis of $\text{Co}_3\text{O}_4\text{-MnO}_2\text{-NiO}$ Ternary Hybrid Nanotubes

Highly ordered nanoporous anodic aluminium oxide (AAO) templates were fabricated by the controlled two-stage electrochemical anodization of high-purity aluminium foil in oxalic acid solution as described in chapter 2. The software controlled three electrode electrodeposition unit (potentiostat AutoLab-30) equipped with power supply was used to synthesize high-density arrays of Co-Mn-Ni alloy nanotubes with the help of AAO template with one side coated with a conductive gold (Au) layer grown by the thermal evaporation technique. Figure 7.1 displays the schematic of the fabrication process of 1D $\text{Co}_3\text{O}_4\text{-MnO}_2\text{-NiO}$ ternary hybrid NTs arrays by using nanoporous anodic aluminium oxide (AAO) template. A high-purity Pt wire and an Ag/AgCl electrode were used as the counter and reference electrodes, respectively. The arrays of Co-Mn-Ni alloy nanotubes were grown in the pores of AAO using the aqueous solution of $40 \text{ g L}^{-1} \text{ CoSO}_4 \cdot 7\text{H}_2\text{O}$, $45 \text{ g L}^{-1} \text{ MnSO}_4 \cdot \text{H}_2\text{O}$, $50 \text{ g L}^{-1} \text{ NiSO}_4 \cdot 6\text{H}_2\text{O}$ and $30 \text{ g L}^{-1} \text{ H}_3\text{BO}_3$ as the electrolyte at room temperature. Here, boric acid and NH_4OH

were used as a buffer to maintain the pH of the electrolyte around 3.5 and also to control the electrodeposition process. The deposition of the arrays of Co-Mn-Ni alloy nanotubes was conducted for 30 minutes by using a dc voltage of -0.78 V, following the linear sweep voltammetry (LSV) results. After the growth of the Co-Mn-Ni alloy nanotubes the template was removed by dissolving it in 2 M NaOH aqueous solution. The open arrays of Co-Mn-Ni alloy nanotubes grown on Au layer were finally oxidized to form Co_3O_4 - MnO_2 -NiO ternary hybrid nanotubes by annealing at 600°C for 5 hours in air atmosphere. The mass of the active electrode material was measured by using a microbalance having an accuracy of 0.1 μg . The mass of the active electrode materials was calculated by subtracting the mass of the equal area Au foil layer, on which the hybrid nanotubes were grown, from the total mass of the cathode (hybrid nanotubes material and the Au layer). The loading density of the Co_3O_4 - MnO_2 -NiO ternary hybrid nanotubes was found to be 0.182 mg cm^{-2} .

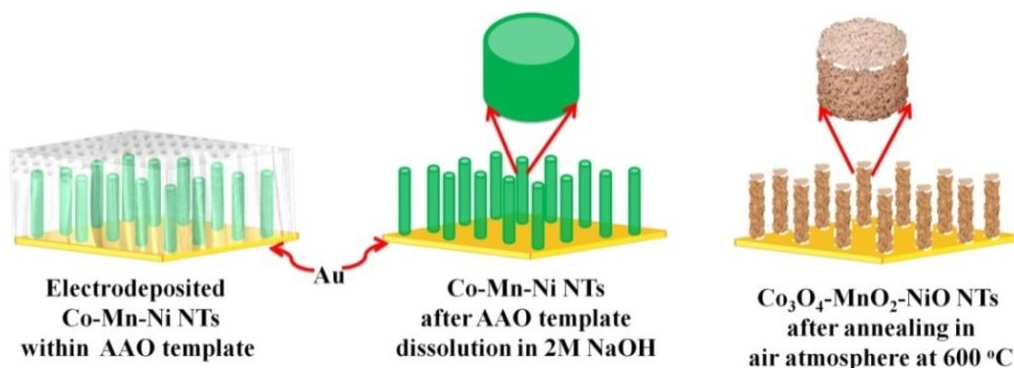


Figure 7.1: Schematic of the fabrication of ordered arrays of 1D Co_3O_4 - MnO_2 -NiO hybrid nanotubes.

7.2.3 Structural Characterizations

The crystal structures of the as prepared 1D Co_3O_4 - MnO_2 -NiO ternary hybrid nanotubes were analyzed by X-ray diffraction (XRD, Panalytical X'Pert Pro diffractometer). The chemical composition and elemental composition of the Co_3O_4 - MnO_2 -NiO ternary hybrid nanotubes were investigated by energy dispersive X-ray (EDAX). The morphology and the structure of the arrays of Co-Mn-Ni alloy nanotubes

and Co_3O_4 - MnO_2 - NiO ternary hybrid nanotubes were studied using field emission scanning electron microscope (FESEM, FEI Quanta-200 Mark-2), transmission electron microscope (TEM, FEI TECNAI G2 TF20ST) and energy filtered transmission electron microscope (EFTEM). The crystalline structure of the hybrid nanotubes was further investigated by high-resolution TEM (HRTEM).

7.2.4 Electrochemical Measurements

The electrochemical properties of the samples were investigated by cyclic voltammetry (CV) and galvanostatic (GV) charge/discharge tests by using a software controlled conventional three-electrode electrochemical cell (potentiostat AutoLab-30) consisting of the as-prepared samples as the working electrode, Ag/AgCl as the reference electrode, a Pt wire as the counter electrode and 1 M KOH solution as the electrolyte, at room temperature. The CV measurements were performed at different scan rates varying from 2 to 100 mV s^{-1} . Galvanostatic charge/discharge measurements were conducted at various current densities varying from 2.6 to 45.7 Ag^{-1} to evaluate the specific capacitance, areal capacitance, power density and energy density. A potential window in the range from -0.2 V to +0.6 V was used in all the measurements. Electrochemical impedance spectroscopy (EIS) was carried out to prove the capacitive performance at open circuit potential in 1 M KOH within a frequency range of 1– 10^5 Hz.

7.3 Results and discussion

7.3.1 Structural and Morphological Analysis

The XRD data in Fig. 7.2(a) shows the individual crystalline phases of Co_3O_4 , MnO_2 -and NiO . It is also evidenced that the as synthesized metal oxides are of polycrystalline in nature. Field emission scanning electron microscope (FESEM) image of the as-prepared 1D Co_3O_4 - MnO_2 - NiO ternary hybrid NTs arrays is shown in Fig. 7.2(b). From the figure, it is evident that high density well aligned arrays of NTs have

been formed uniformly throughout the whole substrate during the electrodeposition process. Average length and outer diameter of these NTs are uniform and found to be approximately 2 μm and 125 nm, respectively. The elemental compositions are studied by EDAX as shown in Fig. 7.2(c) and it is found that the weight ratio of Co, Mn and Ni is found to be 1.1:1.2:1. Again the porous nature of the NTs wall is evidenced by cross sectional FESEM with higher resolution which is shown in Fig. 7.2(d).

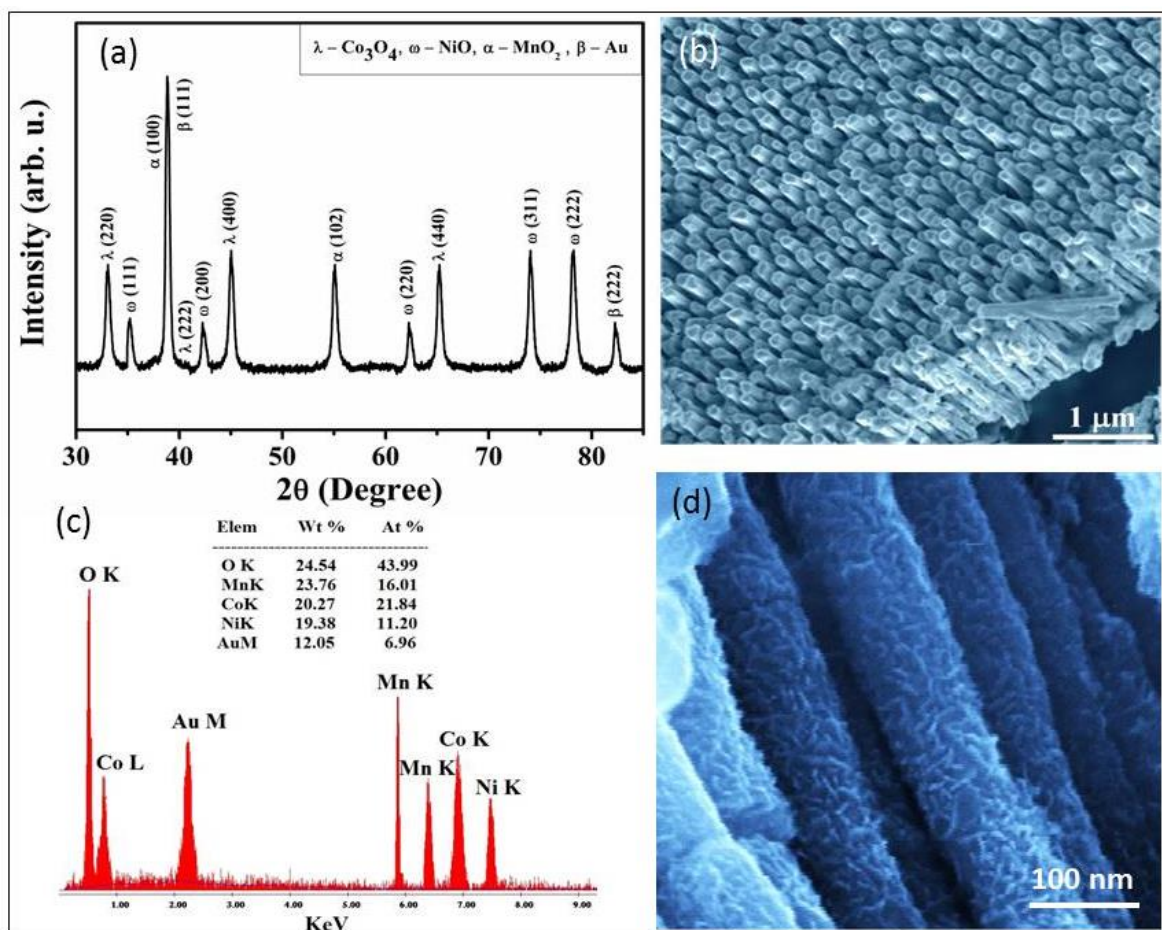


Figure 7.2: (a) XRD pattern, (b) large area FESEM micrograph, (c) EDAX spectrum and (d) porous wall of Co_3O_4 - MnO_2 - NiO ternary hybrid nanotubes.

Again, the high resolution FESEM image is also provided in Fig. 7.3(a) which clearly shows the nano-tubular nature of the hetero-structures. The tubular nature of the as-prepared hybrid NTs is further explored by transmission electron microscope

(TEM) and the corresponding micrograph for the hybrid NTs is shown in Fig. 7.3(b). TEM image displays solid tube wall (dark contrast) and void center of the tubes (bright contrast), clearly confirms the formation of NTs (wall thickness $\sim 12\text{-}15\text{ nm}$) with huge surface roughness, which would enlarge the active surface area of the electrode, as discussed later. Three different sets of lattice fringes can be observed in the HRTEM image (Fig. 7.3(c)) with lattice spacing nearly ~ 0.28 , 0.268 and 0.24 nm , which correspond to the d -spacing of the (111) planes of NiO, (102) planes of MnO_2 and (220) planes of Co_3O_4 , respectively. Moreover, the XRD pattern illustrates diffraction peaks that can be indexed perfectly with corresponding lattice planes of NiO, MnO_2 , and Co_3O_4 conforming the formation of ternary hybrid of TMOs NTs. However, the Au peak in the XRD pattern comes from metallic Au substrate underneath the hybrid NTs.

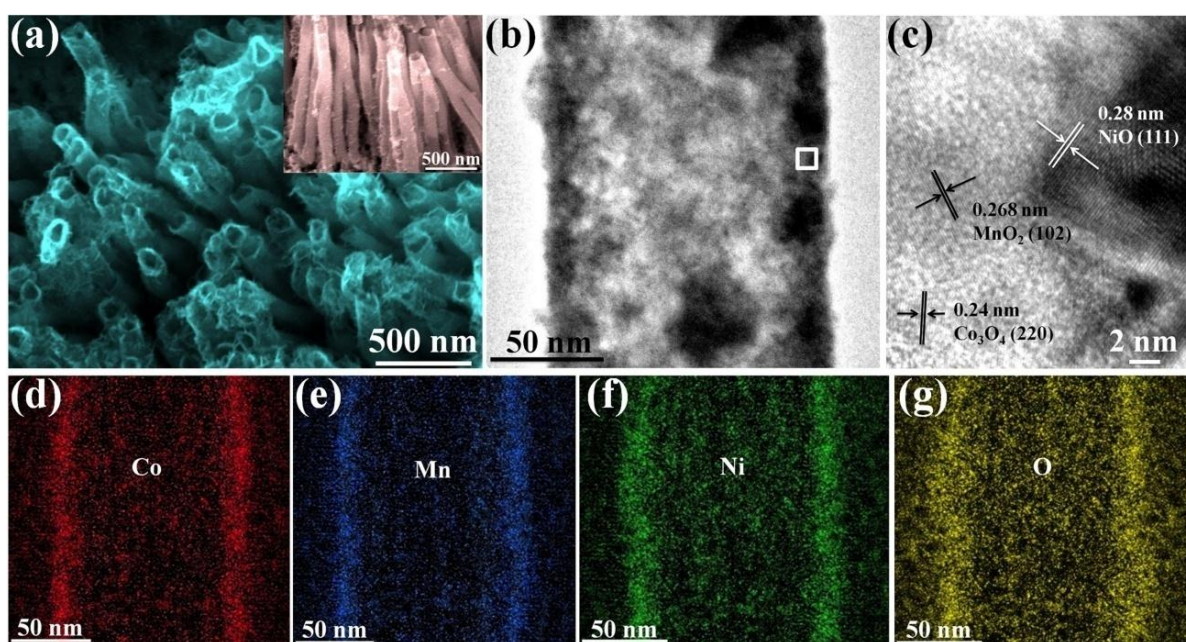


Figure 7.3: (a) and inset of (a): FESEM micrograph, (b) TEM image, (c) HRTEM image and (d)-(g) energy filtered TEM (EFTEM) images (color mapping of Co, Mn, Ni and O) of the as-prepared $\text{Co}_3\text{O}_4\text{-MnO}_2\text{-NiO}$ ternary hybrid NTs.

Furthermore, elemental distribution throughout the 1D $\text{Co}_3\text{O}_4\text{-MnO}_2\text{-NiO}$ hybrid NTs has been examined by energy-filtered TEM (EFTEM), as shown in Fig. 7.3(d)-(g), which clearly indicates uniform distribution of metallic components and also oxygen

ion present in the NTs. However, higher intensity of the Co, Mn, Ni and O at the surface as compared to the central portion of the nanostructure confirms the formation of uniform hybrid NTs.

7.3.2 XPS Analysis

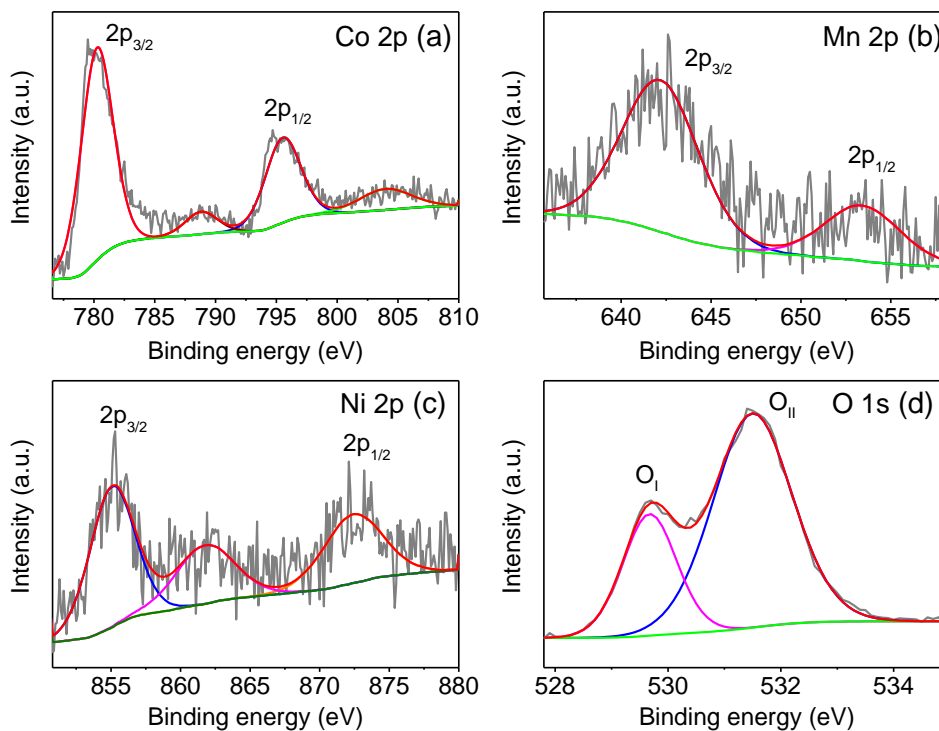


Figure 7.4: XPS spectrum of (a) Co 2p, (b) Mn 2p, (c) Ni 2p and (d) O 1s, respectively, in Co_3O_4 - MnO_2 - NiO ternary hybrid nanotubes.

We also have employed the x-ray photoelectron spectroscopy (XPS) to verify the elemental composition and chemical states of the as-synthesized 1D Co_3O_4 - MnO_2 - NiO ternary hybrid NTs, respectively. Core level XPS spectrum of Co 2p (Fig. 7.4(a)) shows two peaks of Co $2p_{3/2}$ and Co $2p_{1/2}$ observed at the binding energies of 780.4 and 795.5 eV, respectively, suggests the Co^{2+} state, whereas two small peaks at 788.9 and 804 eV could be attributed to $2p_{3/2}$ and $2p_{1/2}$ of Co^{3+} , respectively, indicating the presence of Co_3O_4 phase in this hybrid nanotube. [16,17] Deconvolution of Mn 2p core level

spectrum (Fig. 7.4(b)) gives two distinct peaks at 642.1 and 653.4 eV with a spin-orbital splitting of 11.3 eV, which corresponds well to Mn $2p_{3/2}$ and Mn $2p_{1/2}$ of MnO₂, respectively. [16, 18] Similarly, Ni $2p$ core level spectrum (Fig. 7.4(c)) displays Ni $2p_{3/2}$ and Ni $2p_{1/2}$ peaks at binding energies of 855 and 872 eV, respectively, with the spin-orbital splitting of ~ 17 eV, confirming the divalent (+2) oxidation state of Ni in 1D Co₃O₄-MnO₂-NiO hybrid NTs. [19] Moreover, the presence of the satellite peak at ~ 861 eV again indicates 2+ oxidation state of Ni. The O 1s core level XPS spectrum (Fig. 7.4(d)) has two distinct component peaks at ~ 529.6 and 531.5 eV, which could be assigned to the oxygen present in the oxides of Co₃O₄, MnO₂, and NiO and the oxygen atoms in hydroxyl groups or oxygen vacancy defects incorporated on the surface of NTs, respectively.

7.3.3 Electrochemical Performance

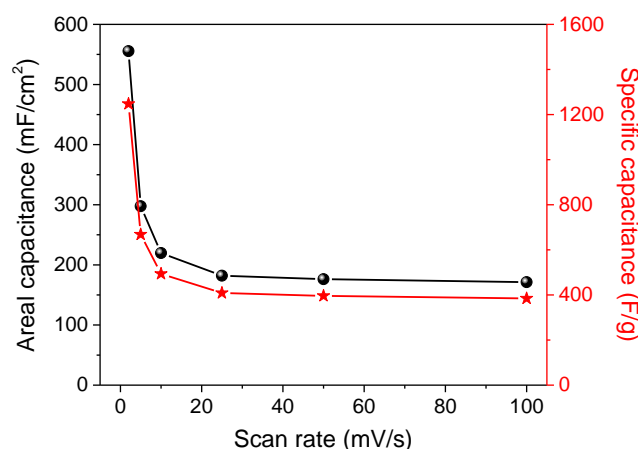


Figure 7.5: Variation of Areal and specific capacitance for the ternary hybrid nanotube electrode as a function of potential scan rate.

Electrochemical performance of the as-prepared 1D Co₃O₄-MnO₂-NiO hybrid NTs, was investigated in three-electrode electrochemical cell system by cyclic voltammetry (CV) and galvanostatic charge/discharge methods. The typical three-electrode cell consisted of the 1D Co₃O₄-MnO₂-NiO ternary hybrid nanotubes,

Ag/AgCl, and Pt electrodes as working, reference and counter electrodes, respectively, dipped in 1 M aqueous KOH solution at room temperature. The value of specific capacitance and areal capacitance (Fig. 7.5) are calculated at different scan rates from CV curves (Fig. 7.6(a)). The CV curves of the as-prepared Co₃O₄-MnO₂-NiO ternary hybrid NTs electrode at different scan rates are shown in Fig. 7.6(a), where the current increases sharply with increasing scan rate. However, the shape of the CV curve, remains almost similar at all scan rates, suggesting good reversibility nature of the hybrid NTs electrode. The shape of the CV curves as observed in each CV curve suggests charge storage mechanism of Co₃O₄-MnO₂-NiO ternary hybrid NTs electrode via surface bound faradaic reactions governed by inter conversion of various oxidation states of metal ions together with K⁺ ion intercalation/deintercalation process into/from oxide nanostructure. [20, 21] The area under the CV curve represents total charge originating through faradaic and non-faradaic processes; faradaic contribution involves ion intercalation together with surface bound redox pseudocapacitance whereas non-faradaic process arises from double layer effect. [22] These effects can be explained by analysing CV curves at different scan rates (ν) using the power law: $i = a\nu^b$, where a and b are two adjustable parameters [22,23] and accordingly parameter b can be calculated from the slope of the plot of $\log i$ vs $\log \nu$. Generally, for ideal diffusion controlled faradaic process, slope $b = 1/2$ and it satisfies Cottrell's equation: $i = \nu^{1/2}$, [23] whereas slope $b = 1$ represents purely capacitive response (redox pseudocapacitance plus double layer capacitance) because the capacitive current is proportional to the potential sweep rates: $i = \nu C_d A$, C_d being the capacitance and A is the surface area of the electrode. [24] Hence, one can expect dominant capacitive charging at higher scan rates because of stronger linear dependence, whereas diffusion process will dominate more at lower sweep rates. Moreover, slope b , as obtained by plotting $\log i$ against $\log \nu$ at different voltages (V), shows a value ~ 0.5 at peak potentials suggesting dominance of diffusion-limited charge storage process, whereas at other potentials slope value is ~ 1 indicating that the current is predominantly capacitive, as shown in Fig. 7.6(b). Now, from CV

curves capacitance (C) values are calculated using the equation: $C = q/V = \int idt/V$, where q is the charge stored, I the current and V is the potential window. In accordance with our arguments, we have observed a sharp increase in capacitance with decreasing sweep rates, a maximum value of $\sim 1247 \text{ Fg}^{-1}$ ($\sim 555.5 \text{ mFcm}^{-2}$) being attained at a scan rate of 2 mVs^{-1} (as shown in Fig. 7.5). It is mainly because of the formation of the porous and spongy surface of this $\text{Co}_3\text{O}_4\text{-MnO}_2\text{-NiO}$ ternary hybrid NTs arrays that provide enormous and accessible inner surfaces of the nanostructure for effective diffusion controlled faradaic reactions at lower sweep rates. However, at higher scan rates, only non-diffusion controlled capacitive charging process dominates over intercalation capacity, that reduces overall capacitance of hybrid NTs electrodes ($\sim 384.5 \text{ Fg}^{-1}$ at a scan rate of 100 mVs^{-1}).

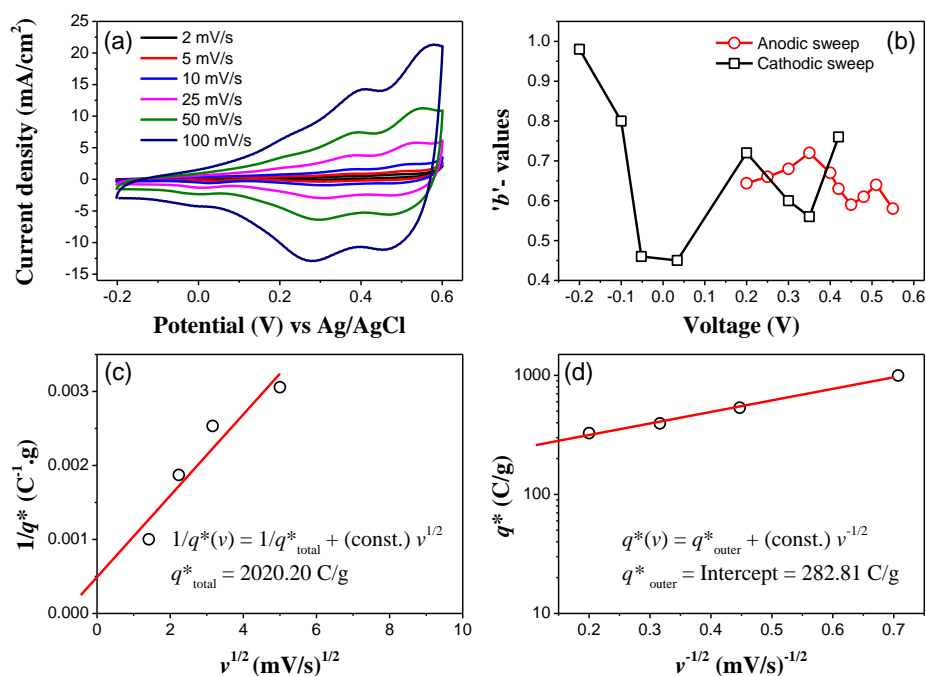


Figure 6: (a) Cyclic voltammetry curves recorded at various scan rates, (b) variation of slope 'b' as a function of voltage (V) for cathodic and anodic sweeps of CV cycles, and Trasatti plots: (c) plot of $1/q^*$ against $v^{1/2}$ to find the total charge (q^*_{total}) stored by the electrode material. (d) shows the plot of q^* against $v^{-1/2}$ to quantify the charge stored only on the outer surface of the electrode material (q^*_{outer}).

Now, as ion intercalation at lower sweep rates enhances charge storage capacity drastically, so it would be interesting to investigate the maximum charge that can be stored in this ternary hybrid NTs arrays and also the actual electrochemical surface area leading to total charge storage. The overall or complete charge stored in the electrode material can be calculated using procedure given by Trasatti et al.,²⁵ which involves the determination of total charge stored (q^*_{total}) from the intercept of the linear plot of $1/q^*$ against $v^{1/2}$, as shown in Fig. 6(c). This procedure can also be used to determine the charge stored only at the outer surface (q^*_{outer}) of the electrode material from the intercept of the linear plot of q^* against $v^{-1/2}$, [22] as shown in Fig. 7.6(d). Interestingly, the value of maximum charge that can be stored within this ternary hybrid nanostructure is found to be 2020.20 Cg^{-1} , equivalent to a specific capacitance of 2525.25 Fg^{-1} for a potential window of 0.8 V. Similarly, the charge stored on the outer surface is found to be 282.8 Cg^{-1} with an equivalent capacitance of 353.5 Fg^{-1} . Moreover, the charge stored in the inner surface (q^*_{inner}) is the difference between total charge (q^*_{total}) and charge stored on outer surface (q^*_{outer}), is found to be 1737.4 Cg^{-1} ($\sim 2171.8 \text{ Fg}^{-1}$). The high charge storage capacity of the electrode can be attributed to the porous, spongy and tubular structure of these ternary NTs that provides enormous inner and outer surface for both faradaic and non-faradaic processes at lower as well as at higher potential sweep rates, as discussed earlier.

To further illustrate the capacitive performance of the $\text{Co}_3\text{O}_4\text{-MnO}_2\text{-NiO}$ ternary hybrid NTs, galvanostatic charge/discharge was performed within the potential window between -0.2 and 0.6V at different current densities and corresponding charging/discharging curves at some selected current densities are shown in Fig. 7.7(a). At lower current densities, charging profile shows non-linear and sluggish behavior, which is due to the diffusion-controlled faradaic process together with purely capacitive charging. Interestingly, discharge profile shows two prominent regions, the first one after the IR -drop characterized by a linear discharge region can be attributed to the release of charges from the surface or near surface regions of the electrode material, i.e. capacitive discharge. However, the second region that is characterized by a very slow

and extended discharge tail is mainly because of de-intercalation of diffused ions from the innermost portions of electrode material, i.e. diffusion controlled discharge profile. Such behavior of charging/discharging curves is consistent with their CV profiles at lower potential sweep rates. Moreover, at higher discharge currents, although the discharge profile shows the first linear region, however, slow discharge tail has been reduced significantly which is mainly because of the availability of only surface or near-surface regions of the electrode material at higher currents, i.e. discharge becomes non-diffusion controlled and more capacitive with the increase in current. From the discharge profiles of charging/discharging curves, capacitance values for this $\text{Co}_3\text{O}_4\text{-MnO}_2\text{-NiO}$ ternary hybrid nanotubes electrode have been calculated using equation: $C = i\Delta t / \Delta V$, (where, I is the discharge current, and Δt be the discharge time for potential window ΔV) and found to be $\sim 1224.5 \text{ F/g}$ ($\sim 544.9 \text{ mF/cm}^2$) at a current density of 12.2 A/g ($\sim 5.4 \text{ mA/cm}^2$) and retains a value of 397.5 F/g ($\sim 176.9 \text{ mF/cm}^2$) as the current density reaches at $\sim 18.4 \text{ A/g}$ ($\sim 8.2 \text{ mA/cm}^2$). The value of capacitances for this hybrid nanotubes electrode are higher than previously reported transition metal oxides and their mixed composites incorporated with conductive polymers and carbon-based materials. [9-11,20,21, 26-37]

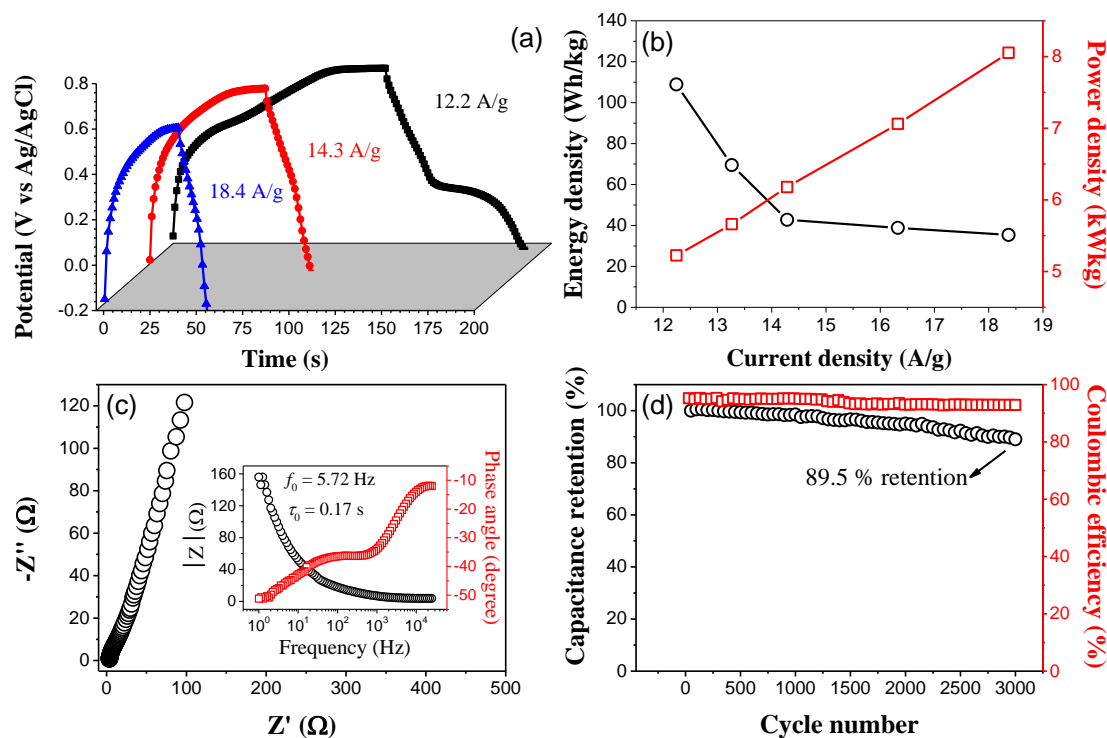


Figure 7.7: (a) Galvanostatic charge/discharge curves for $\text{Co}_3\text{O}_4\text{-MnO}_2\text{-NiO}$ hybrid NTs electrode within voltage window of -0.2 to 0.6 V; (b) variation of energy and power densities with current densities, calculated from the discharge profile; (c) Nyquist plot ($-Z''$ vs. Z') plot for the hybrid electrode within the frequency range of 1 Hz to 100 kHz, inset shows the Bode plot to find out response time of this hybrid NTs electrode and (d) cycling performance and coulombic efficiency during 3000 charge/discharge cycles.

Energy (E) and power (P) densities for the ternary hybrid NTs electrode have been calculated using equations $E = 1/2CV^2$ and $P = E/\Delta t$, respectively, where the parameters have their usual meanings, are plotted against current densities in Figure 7.7(b). This nanostructured electrode demonstrates an energy density as high as 108.8 Whkg^{-1} at a current density of 12.2 Ag^{-1} . Moreover, maximum power density that has been achieved is $\sim 8 \text{ kWg}^{-1}$ with a corresponding energy density of 35.3 Whkg^{-1} when current density reaches at 18.4 Ag^{-1} , thus showing remarkable energy and power performance of the hybrid NTs electrode. We have also performed electrochemical impedance spectroscopy and corresponding Nyquist plot ($-Z''$ vs Z') plot is depicted in

Fig. 7.7(c). The intercept of the Nyquist curve with the real axis at high-frequency regime provides equivalent series resistance (ESR) which is found to be $\sim 3.55 \Omega$ for this hybrid NTs electrode, showing the low resistance of the electrolyte and good electrical contact between the electrode material and the substrate. Moreover, the capacitive response frequency (f_0) for this electrode as calculated from the Bode plot (as shown in the inset of Fig. 7.7(c)) at a phase angle of -45° is found to be 5.72 Hz, gives a response time ($\tau_0 = 1/f_0$) as small as 0.17s, again suggesting fast charge/discharge characteristics of this ternary hybrid NTs electrode.

The cycling stability and coulombic efficiency of the $\text{Co}_3\text{O}_4\text{-MnO}_2\text{-NiO}$ ternary hybrid NTs electrode were investigated at a current density of 15 Ag^{-1} during 3000 charge/discharge cycles are shown in Fig. 7.7(d). The electrode exhibits an exceptional cycling stability with 89.5% retention of its initial capacitance and a coulombic efficiency of almost 95% after 3000 cycles, suggesting stable electrochemical behavior of the hybrid NTs electrode during long cycle test. A little drop in the specific capacitance following 3000 charge/discharge cycles might be due to the bulging of the electrode material resulted from continual ion intercalation/deintercalation process during long charge/discharge cycles. Nonetheless, such high specific capacitance, high energy/power density and fast response time, i.e. worthy capacitive performance of the $\text{Co}_3\text{O}_4\text{-MnO}_2\text{-NiO}$ hybrid NTs electrode can mostly be attributed to the well planned nano-architectural designing of electrode based on three highly electroactive materials that offers huge surface area (having highly porous inner and outer surface of the NTs) for fast faradaic and non-faradaic process. Additionally, direct growth of electroactive materials on conducting substrate provides enough structural integrity to sustain long charge/discharge cycles and also reduces the internal resistance to facilitate electron transfer towards the current collector boosting the performance of the electrode.

7.4 Conclusion

In conclusion, novel 1D architecture of $\text{Co}_3\text{O}_4\text{-MnO}_2\text{-NiO}$ ternary hybrid NTs arrays with remarkable capacitive performance has been demonstrated. These hybrid

nanotubes are fabricated by combining simple template based electrochemical deposition of Co-Mn-Ni alloy NTs followed by controlled oxidation. The unique nano-architectural design of this hybrid NTs electrode having large accessible inner and outer surface area and small ion diffusion path coupled with synergy effects from three highly redox active materials grown on a highly conducting metal substrate facilitating fast charge transport helps to achieve enhanced electrochemical properties of this hybrid NTs arrays suitable for supercapacitor applications.

Bibliography

- [1] A. K. Singh, D. Sarkar, K. Karmakar, K. Mandal and G. G. Khan. *ACS Appl. Mater. Interfaces*, **8**, 20786 (2016)
- [2] J. R. Miller and P. Simon, *Science*, **321**, 651 (2008)
- [3] J. Chmiola, C. Largeot, P. L. Taberna, P. Simon, and Y. Gogotsi, *Science*, **328**, 480 (2010)
- [4] P. Simon, and Y. Gogotsi, *Nat. Mater.*, **7**, 845 (2008)
- [5] G. Guo, L. Huang, Q. Chang, L. Ji, Y. Liu, Y. Xie, W. Shi, and N. Jia, *Appl. Phys. Lett.*, **99**, 083111 (2011)
- [6] G. Wang, L. Zhang and J. Zhang, *Chem. Soc. Rev.*, **41**, 797 (2012)
- [7] M. Zhi, C. Xian, J. Li, M. Li and N. Wu, *Nanoscale*, **5**, 72 (2013)
- [8] G. Zhang and X. W. Lou, *Sci. Rep.* **3**, 1470 (2013)
- [9] D. W. Wang, H. T. Fang, F. Li, Z. G. Chen, Q. S. Zhong, G. Q. Lu, and H. M. Cheng, *Adv. Funct. Mater.*, **18**, 3787 (2008)
- [10] F. Grote, R. S. Kuhnel, A. Balducci and Y. Lei, *Appl. Phys. Lett.*, **104**, 053904 (2014)
- [11] X. Lu, G. Wang, T. Zhai, M. Yu, J. Gan, Y. Tong and Y. Li, *Nano Lett.*, **12**, 1690 (2012)
- [12] M. T. Greiner, L. Chai, M. G. Helander, W. Tang and Z. Lu, *Adv. Funct. Mater.*, **22**, 4557 (2012)
- [13] M. Park, J. Li, A. Kumar, G. Li, and Y. Yang, *Adv. Funct. Mater.*, **19**, 1241 (2009)
- [14] J. Meyer, P. R. Kidambi, B. C. Bayer, C. Weijtens, A. Kuhn, A. Centeno, A. Pesquera, A. Zurutuza, J. Robertson and S. Hofmann, *Sci. Rep.*, **4**, 5380 (2014)
- [15] A. Hirata, L. Kang, X. Zhang, Y. Hou, L. Chen, C. Li, T. Fujita, K. Akagi, M. Chen, *Angew. Chem. Int. Ed.*, **52**, 1664 (2013)
- [16] H. Xia, D. Zhu, Z. Luo, Y. Yu, X. Shi, G. Yuan and J. Xie, *Sci. Rep.*, **3**, 2978 (2013)
- [17] N. Yan, L. Hu, Y. Li, Y. Wang, H. Zhong, X. Hu, X. Kong, and Q. Chen, *J. Phys. Chem. C*, **116**, 7227 (2012)

-
- [18] A. L. M. Reddy, M. M. Shaijumon, S. R. Gowda and P. M. Ajayan, *Nano Lett.* **9**, 1002 (2009)
- [19] G. Tan, F. Wu, J. Lu, R. Chen, L. Li and K. Amine, *Nanoscale*, **6**, 10611 (2014)
- [20] R. B. Rakhi, W. Chen, D. Cha, and H. N. Alshareef, *NanoLett.*, **12**, 2559 (2012)
- [21] M. Toupin, T. Brousse, and D. Belanger, *Chem. Mater.*, **16**, 3184 (2004)
- [22] M. Sathiya, A. S. Prakash, K. Ramesha, J. - Tarascon, and A. K. Shukla, *J. Am. Chem. Soc.*, **133**, 16291 (2011)
- [23] Lindstrom, H.; Soldergren, S.; Solbrand, A.; Rensmo, H.; Hjelm, J.; Hagfeldt, A.; Lindquist, S. E. *J. Phys. Chem. B*, **101**, 7717 (1997)
- [24] Wang, J.; Polleux, J.; Lim, J.; Dunn, B. J. *Phys. Chem. C*, **111**, 14925 (2007)
- [25] Ardizzone, S.; Fregonara, G.; Trasatti, S. *Electrochim. Acta*, **35**, 263 (1990)
- [26] C. Yuan, J. Li, L. Hou, X. Zhang, L. Shen, and X. W. Lou, *Adv. Funct. Mater.*, **22**, 4592 (2012)
- [27] J. Du, G. Zhou, H. Zhang, C. Cheng, J. Ma, W. Wei, L. Chen, and T. Wang, *ACS Appl. Mater. Interfaces*, **5**, 7405 (2013)
- [28] F. Yang, J. Yao, F. Liu, H. He, M. Zhou, P. Xiao, and Y. Zhang, *J. Mater. Chem. A*, **1**, 594 (2013)
- [29] A. K. Singh, D. Sarkar, G. G. Khan, and K. Mandal, *Appl. Phys. Lett.*, **104**, 133904 (2014)
- [30] L. Yang, S. Cheng, Y. Ding, X. Zhu, Z. L. Wang, and M. Liu, *NanoLett.*, **12**, 321 (2012)
- [31] G. Q. Zhang, H. B. Wu, H. E. Hoster, M. B. Chan-Park, and X. W. Lou, *Energy Environ. Sci.*, **5**, 9453 (2012)
- [32] H. Jiang, J. Mab, and C. Li, *Chem. Commun.*, **48**, 4465 (2012)
- [33] H. L. Wang, Q. M. Gao, and L. Jiang, *Small*, **7**, 2454 (2011)
- [34] A. K. Singh, D. Sarkar, G. G. Khan, and K. Mandal, *J. Mater. Chem. A*, **1**, 12759 (2013)
- [35] H. L. Wang, H. S. Casalongue, Y. Y. Liang, and H. J. Dai, *J. Am. Chem. Soc.*, **132**, 7472 (2010)

- [36] X. H. Xia, J. P. Tu, Y. J. Mai, X. L. Wang, and C. D. Gu, *J. Mater.Chem.*, **21**, 9319 (2011)
- [37] J. Jiang, J. P. Liu, R. M. Ding, J. H. Zhu, Y. Y. Li, A. Z. Hu, X. Li, and X. T. Huang, *ACS Appl. Mater. Interfaces*, **3**, 99 (2011)

Chapter 8

Conclusion and Future Scope of The Work

This chapter presents an overall conclusion of the work described so far and the scopes for further work in this specific field.

8.1 Conclusion

In this modern era, energy supply is highly required in order to maintain this industrially revolutionized society. Sustainable development of the society needs energy infrastructure based on environmentally acceptable sources of supply by replacing the principle energy resources available today, the fossil fuels. The utilization of clean and renewable energy resources, mainly solar energy will not only provide the total energy need in future but it will prevent severe anthropogenic impact on the environment. Also, owing to tremendous use of portable electronics, investigation of supercapacitive materials has huge importance.

This thesis has been mainly focusd on the fabrication of oxide materials based electrodes for solar energy conversion via water splitting in a photoelectrochemical cell as well as for supercapacitor devices. In particular, we have fabricated 1D ZnO nanorods array over fluorine doped tin oxide (FTO) glass substrate as prinstine photoelectrode material for PEC cell. After that, several strategies such as surface functionalization, doping, heterojunction fabrication etc. have been adopted to improve the photoelectrochemical performance and their photoconversion efficiency. On the other hand, for supercapacitor we have fabricated transition metal oxide based hybrid nanotubes ($\text{Co}_3\text{O}_4\text{-MnO}_2\text{-NiO}$ ternary hybrid 1D nanotubes array) electrode.

First of all, we have fabricated highly oriented arrays of C, N and S surface functionalized/surface doped ZnO nanorods (NRs) by a simple chemical bath deposition followed by wet chemical method. Surface functionalization significantly improves both the photocurrent and photostability of the ZnO NRs electrodes under visible-light irradiation along with the reduction in onset potential for water oxidation. The C-ZnO, N-ZnO and S-ZnO NRs photoanodes exhibite 6.5, 5.5 and 3 times increased photoconversion efficiency, respectively, as compared to that measured for pure ZnO NRs (0.02%) under visible-light illumination ($10 \text{ mW}\cdot\text{cm}^{-2}$, $\lambda > 420 \text{ nm}$, $0.5 \text{ M Na}_2\text{SO}_4$). The study demonstrated that the surface functionalization could be a facile and general

approach for oxide semiconductors to achieve an effective solution for high performance solar light-driven water splitting.

Afterwards, we have fabricated alkali metal (Li, Na and K) doped ZnO NRs array photoanodes. Li-ZnO, Na-ZnO and K-ZnO NRs photoanodes show enhanced photoconversion efficiency (0.69%, 0.73% and 0.70% respectively) than the pristine ZnO NRs photoanode under visible-light illumination (10 mW.cm⁻², $\lambda > 420$ nm, 0.5 M Na₂SO₄). This work basically demonstrates the significance of defect engineering in tuning the visible light driven photoelectrochemical properties of the alkali metal (Li, Na and K) doped ZnO NRs. Large concentration of oxygen vacancies introduced in the sub-bandgap because of alkali doping serve as the light absorbing donor sites and also photoelectron recombination centres resulting enhanced photocurrent and hole separation in the valance band, respectively. The lattice strain developed in the nanorods due to doping contributes in easy electron transportation and mobility. Defect engineering also tunes the electronic structure of the photoanodes resulting in the band gap modification and band edge engineering, boosting charge carrier migration and reduced electron-hole pair recombination for enhanced oxygen evolution reaction.

Again, a novel efficient strategy for designing of *p-n* type nano-heterojunction photoanode is demonstrated for empowering the water splitting efficiency by growing low band-gap *p*-CuFeO₂ nanolayer on *n*-ZnO Nanorods by an easy and scalable route. The photoconversion efficiency of *p-n* CuFeO₂/ZnO photoanode is found to be 5.5 times higher than that of the pristine ZnO Nanorods electrode under visible-light illumination ($\lambda > 420$ nm, intensity 10 mWcm⁻², 10 mW.cm⁻², 0.5 M Na₂SO₄). The *p-n* CuFeO₂/ZnO nano-engineering not only boosts the visible light absorption but also resolve the limitations regarding effective charge carrier separation and transportation because of interfacial band alignment. This photoanode also shows remarkably enhanced stability where the formation of *p-n* nano-heterojunction enhances the easy migration of holes to the electrode/electrolyte interface and the electrons to the counter electrode (Pt) for hydrogen generation.

Finally, the design of a novel architecture of multidimensional nano-heterostructures based photoelectrode is demonstrated by coupling the multilayered two-dimensional (2D) structure of MoS₂ and MoO₃ on the well aligned arrays of one-dimensional (1D) ZnO nanorods template expecting the effective synergic effects. The advantages of catalytically active sites of 2D layered structure of transition metal dichalcogenides/oxides is integrated with the distinctive dimensionality dependent phenomena of 1D structure to achieve enormous surface area for light harvesting and photoelectrochemical reaction along with favorable photocarrier dynamics required for water splitting. The new ZnO/MoS₂ and ZnO/MoO₃ nano-heterostructures photoanodes exhibit low onset potential and enhanced broadband light absorption resulting high photocurrent density of 2.04 and 0.67 mA cm⁻² at 1.23 V versus reversible hydrogen electrode under AM 1.5 G illumination, which correspond to 334% and 43% increase of photocurrent, respectively, compared to that of pure ZnO nanorods. The nano-heterostructures photoanodes also exhibit enhanced applied bias photon-to-current conversion efficiency and superior spatial photo-induced exciton separation and transportation because of the favorable interfacial band alignment at 2D-1D nano-heterointerface and suppress in the surface charge recombination, which promotes the hole transportation at nano-heterostructure/electrolyte interface and boost the surface oxygen evolution reaction leading to enhanced photoelectrochemical performance.

On the other hand, we have adopted electrodeposition technique to design Co₃O₄-MnO₂-NiO ternary hybrid 1D nanotubes array for their application as an active material for high-performance supercapacitor electrode. This as-prepared novel supercapacitor electrode can store charge as high as ~ 2020 Cg⁻¹ (equivalent specific capacitance ~ 2525 Fg⁻¹) for a potential window of 0.8V, has long cycle stability (nearly 89.5% specific capacitance retains after successive 3000 charge/discharge cycle), significantly high coulombic efficiency and fast response time (~0.17s). The remarkable electrochemical performance of this unique electrodematerial is the outcome of its enormous reaction platform provided by its special nanostructure morphology and

conglomeration of the electrochemical properties of three highly redox active materials in a single unit.

8.2 Future Scope

The research works which have so far been described in this thesis set the stage for further research in the field of solar energy conversion and clean fuel generation in PEC cell by designing effective oxide semiconductors owing to their low fabrication cost, faster reaction kinetics, stability in electrolyte medium and possibility of large scale integration. Particularly, ZnO based nanostructures have been showed enormous potential for solar energy harvesting in PEC cell by water splitting from the last several decades owing to the excellent carrier density, conductivity, different electronic and energy properties, large scale economical productivity, etc. Basically, to further improve the photconversion efficiency by minimizing the limiting parameters of the photoelectrodes fabrication and to meet the current challenges of energy requirement enormous research on oxide semiconductors based nanostructures should be required. Furthermore, the physics behind various peculiar electrochemical aspects and electronic properties, which often arise but are not properly studied in detail, has been explored in some of the present research works and this will certainly help to build better concepts on these matters and will encourage others to do research in these fields. One important aspect, we have found out that the lattice strain and oxygen vacancies developed in ZnO NRs due to alkali metal (Li, Na and K) doping significantly enhance the photocurrent level and hence the photoconversion efficiency. Therefore, research on proper defect engineering in oxide semiconductors might be a solution for effective photoelectrodes fabrication. However, all our research works have been done in laboratory scale and to make our materials to be used in the real field applications, a thorough research in engineering is needed.

On the other hand, the supercapacitive performances shown by the $\text{Co}_3\text{O}_4\text{-MnO}_2\text{-NiO}$ ternary hybrid 1D nanotubes array is quite promising due to accessible inner and outer surfaces of the NTs for enormous reaction platform and short hole-diffusion

length and the integrability of several metal oxide phases into a single platform. Apart from making a real supercapacitor from the $\text{Co}_3\text{O}_4\text{-MnO}_2\text{-NiO}$ ternary hybrid 1D nanotubes array, investigation of other ternary hybrid oxide based NTs might provide a convenient way to make high performance supercapacitor devices.